



UNIVERSITY OF  

---

LIVERPOOL

**Targeting Photoresponsive Porous Organic Cages,  
Porous Liquids and Glass Phases**

Thesis submitted in accordance with the requirements of the  
University of Liverpool for the degree of Doctor of Philosophy

Michael Christopher Brand

Department of Chemistry

July 2022



## **Acknowledgements**

Firstly, I would like to thank Prof Andy Cooper for giving me the opportunity to undertake a PhD within his research group and providing knowledge and supervision. Secondly, huge thanks go to Dr Becky Greenaway who provided ongoing guidance and support throughout my time in Liverpool, while also securing a Royal Society Fellowship and lectureship at Imperial College. I wish you the best of luck and I know your future students are in good hands.

Collaboration is such a key part of science and without these collaborations many of these projects would not be where they are today. Thank you to our computational collaborators Dr Kim Jelfs, Dr James Pegg, and Dr Austin Mroz, Rob Clowes and Nicola Rankin for continuous technical support, Dr Marc Little for x-ray diffraction, Dr Jake Greenfield for assistance with photophysical experiments, Dr Tom Bennett for his glass expertise, Dr Ben Egleston and Aiting Kai for electron microscopy images, and countless others for useful discussions.

Studying for a PhD is not easy and when things get tough having good people around you make things a whole lot easier. So, I would like to thank Andy, Becky, Nicola, Ben, Rich, Alex, Zack, Aly, and so many others. The smiles, laughs, and endless coffees have certainly made this journey so much more enjoyable.

To Mum, Dad, Nan, and Les, thank you for your never-ending encouragement and love. Without your support I would not be where I am today. Thank you for believing in me. I hope I have made you proud.

Finally, thank you to my future wife, Lydia. You have stood by me and supported every decision I have made, even when that meant moving to the opposite side of the world. You have been with me through the highs, and your love and support has always picked me up from the lows. The past few years have been tough, but your love, continued support, and frequent visits from the neighbourhood cat have made this time so much easier. I could not have done this without you.



## Abstract

Porous materials play a vital role within industry and the domestic market, and with the current global climate crisis there is certainly the need to develop and produce new materials that may assist in tackling this issue. Whilst a large amount of research into materials such as metal-organic frameworks and zeolites has proven to be successful, there are more recently discovered materials such as porous organic cages and porous liquids which have shown promising results over a wide range of applications such as gas storage and separations, catalysis, and molecular sensing. In this thesis, a new class of light responsive organic cages have been investigated with the aid of computational models. These organic cages have been successfully synthesised and their properties have been explored. They have shown the ability to undergo a structural change resulting in a change in shape upon irradiation with UV light, creating the possibility of a low energy release mechanism that avoids the energy demand of temperature and pressure swings. With that type of system in mind, a new photoresponsive porous liquid has also been developed which incorporates the use of a known photoresponsive metal-organic framework and an ionic liquid, which has been shown to increase the carbon dioxide capacity over that of the neat liquid. It has also been demonstrated to have excellent selectivity for carbon dioxide over methane, making it one of the most selective porous liquids to date. This porous liquid has the ability to release CO<sub>2</sub> when irradiated with UV light, which is comparable to other mechanisms of release including heating, sonication, and chemical displacement. Finally, the incorporation of porous organic cages into type II (solutions) and type III (dispersions) porous liquids has previously been reported, though they have not yet been successfully implemented as type 1 (neat) porous liquids. To explore the potential of a type 1 porous liquid based on organic cages, an investigation into the melting of organic cages has also been carried out, which found the possibility of forming several organic cage glasses. Of the molecular organic cage glasses found, one was found to exhibit improved gas uptake for carbon dioxide and methane compared to that of the parent cage, creating a more porous, stable and less soluble material.



## Table of Contents

Acknowledgements .....	2
Abstract.....	4
Abbreviations .....	9
Chemical Abbreviations.....	10
List of Publications .....	11
<b>Chapter 1 Introduction .....</b>	<b>12</b>
1.1 Porous Materials.....	13
1.2 Porous Organic Molecules.....	15
1.2.1 Porous Organic Cages .....	15
1.3 Porous Frameworks.....	24
1.3.1 Metal-Organic Frameworks .....	25
1.4 Porous Liquids.....	27
1.4.1 Type 1 Porous Liquids.....	29
1.4.2 Type 2 Porous Liquids.....	31
1.4.3 Type 3 Porous Liquids.....	34
1.4.4 Type 4 Porous Liquids.....	37
1.5 Photochromism.....	37
1.6 Photoresponsive Materials.....	40
1.7 Incorporation of Photoresponsive Moieties .....	41
1.8 Thesis Summary.....	46
1.9 References.....	47
<b>Chapter 2 Synthesis of Azobenzene-Derived Organic Cages .....</b>	<b>56</b>
2.1 Preface.....	57
2.2 Discovery of Organic Cages .....	58
2.3 Azobenzene-Derived Organic Cages.....	60
2.3.1 Designing an Azobenzene-Derived Organic Cage.....	60
2.3.2 Screening of Modelled Organic Cages .....	63
2.3.3 Synthesis of Azobenzene-Derived Precursors.....	66

2.3.4	Screening and Synthesis of Azobenzene-Derived Cages .....	68
2.3.5	Photophysical Properties of Azobenzene-Derived Organic Cages ....	82
2.3.6	NMR Studies of Azobenzene-Derived Organic Cages .....	95
2.4	Conclusions .....	109
2.5	Experimental.....	110
2.6	References .....	138
<b>Chapter 3 Photoresponsive Type III Porous Liquids.....</b>		<b>142</b>
3.1	Preface .....	143
3.2	Type III Porous Liquids .....	144
3.3	Developing a Photoresponsive Porous Liquid .....	146
3.3.1	Choice of Material.....	146
3.3.2	Designing a Photoreactor for Gas Sorption of Porous Liquids.....	148
3.3.3	Solvent Screening.....	152
3.3.4	Photoresponsive Gas Sorption Experiments.....	155
3.3.5	Gas Displacement Measurements .....	169
3.4	Conclusions .....	172
3.5	Experimental Details .....	174
3.5.1	General Synthetic and Analytical Methods.....	174
3.5.2	Synthesis and Characterisation .....	175
3.5.3	Light-Responsive Porous Liquid Gas Adsorption Experimental Setup 176	
3.5.4	Gas Evolution Experimental Setup.....	177
3.6	References .....	179
<b>Chapter 4 Melt-Quenched Porous Organic Cage Glasses .....</b>		<b>182</b>
4.1	Preface .....	183
4.2	Glasses.....	184
4.3	Type 1 Porous Liquids .....	186
4.4	Melt-Quenched Porous Organic Cage Glasses.....	189
4.4.1	Screening the Thermal Properties of Porous Organic Cages .....	189



4.4.2	High-Throughput Gas Sorption of Cage Glasses .....	202
4.4.3	The Curious Case of CC3.....	210
4.5	Conclusions.....	226
4.6	Experimental Details.....	227
4.6.1	General Synthetic and Analytical Methods.....	227
4.6.2	Synthesis and Characterisation of Organic Cages.....	229
4.7	References .....	235
<b>Chapter 5 Conclusions and Future Outlook .....</b>		<b>238</b>
5.1	Conclusions.....	239
5.2	Future Work.....	240
5.3	References .....	243

## Abbreviations

CFCs	Chlorofluorocarbons
COF	Covalent Organic Framework
COSY	Correlation Spectroscopy
DFT	Density Functional Theory
DSC	Differential Scanning Calorimetry
EDA	1,2-ethylenediamine
HCP	Hyper-Cross-Linked Polymer
HPLC	High-Performance Liquid Chromatography
HRMS	High-Resolution Mass Spectroscopy
HSQC	Heteronuclear Single Quantum Coherence
IUPAC	International Union of Pure and Applied Chemistry
MD	Molecular Dynamics
MOC	Metal Organic Cage
MOF	Metal Organic Framework
MS	Mass Spectrometry
NMR	Nuclear Magnetic Resonance
PIM	Polymer of Intrinsic Microporosity
POC	Porous Organic Cage
PSD	Pore-Size Distribution
PSM	Post-Synthetic Modification
PXRD	Powder X-ray Diffraction
scXRD	Single Crystal X-ray Diffraction
SEM	Scanning Electron Microscopy
$T_g$	Glass Transition Temperature
TGA	Thermogravimetric Analysis
$T_m$	Melting point
ZIF	Zeolitic Imidazolate Framework

## Chemical Abbreviations

[BMIM][NTf <sub>2</sub> ]	1-Butyl-3-methylimidazolium bis(trifluoromethylsulfonyl)imide
[BPy][NTf <sub>2</sub> ]	1-Butylpyridinium bis(trifluoromethanesulfonyl)imide
[EtHPy][EtS]	1-Ethyl-3-(hydroxymethyl) pyridinium ethyl sulfate
CHDA	Cyclohexanediamine
DCM	Dichloromethane
DMF	Dimethylformamide
MIm	2-Methylimidazole
TFB	1,3,5-Triformylbenzene
TREN	Tris(2-aminoethyl)amine

## List of Publications

Parts of this thesis contains research published in the following articles:

- 1) M. C. Brand, F. Greenwell, R. Clowes, B. D. Egleston, A. Kai, A. I. Cooper, T. D. Bennett and R. L. Greenaway, Melt-quenched Porous Organic Cage Glasses, *J. Mater. Chem. A*, 2021, **9**, 19807-19816.
- 2) M. C. Brand, N. Rankin, M. A. Little, A. I. Cooper and R. L. Greenaway, Shining a Light on Photoresponsive Type III Porous, ChemRxiv, **2022**, DOI: 10.26434/chemrxiv-2022-mgwnm (pre-print).
- 3) M. C. Brand, J. T. Pegg, J. L. Greenfield, M. A. Little, N. Rankin, M. J. Fuchter, A. I. Cooper, K. E. Jelfs and R. L. Greenaway, Photoresponsive Organic Cages – Computationally Driven Discovery of Azobenzene-Derived Organic Cages, 2022 (in preparation).
- 4) M. C. Brand, A. Mroz, F. Greenwell, T. D. Bennett, K. E. Jelfs, A. I. Cooper and R. L. Greenaway, Thermal Conversion of a Porous Organic Cage into a Polymeric Organic Glass or Covalent Organic Framework, 2022 (in preparation).

Contributions towards the following publications during the PhD studentship:

- 5) B. D. Egleston, K. V. Luzyanin, M. C. Brand, R. Clowes, M. E. Briggs, R. L. Greenaway, A. I. Cooper, Controlling Gas Selectivity in Molecular Porous Liquids by Tuning the Cage Window Size, *Angew. Chem. Int. Ed.*, 2020, **59**, 7362 – 7366.
- 6) B. D. Egleston, M. C. Brand, F. Greenwell, M. E. Briggs, S. L. James, A. I. Cooper, D. E. Crawford and R. L. Greenaway, Continuous and Scalable Synthesis of a Porous Organic Cage by Twin Screw Extrusion (TSE), *Chem. Sci.*, 2020, **11**, 6582-6589.
- 7) R. J. Kearsey, A. Tarzia, M. A. Little, M. C. Brand, R. Clowes, K. E. Jelfs, A. I. Cooper and R. L. Greenaway, Competitive Amino Formation during the Synthesis of an Isopropyl-Decorated Imine Porous Organic Cage, 2022 (in preparation).
- 8) J. L. Borioni, S. Fonrouge, B. D. Egleston, M. C. Brand, D. T. Bowron, S. L. James, A. I. Cooper, T. Y. A. Youngs, R. L. Greenaway, M. G. Del Pópolo, Understanding the Mesoscale Assembly of Organic Cages in Porous Liquids, 2022 (in preparation).

# **Chapter 1**

## **Introduction**

## 1.1 Porous Materials

Porosity is defined by the empty space within a material. This can exist as intrinsic porosity within the material through empty pores or cavities, or as extrinsic porosity where empty spaces exist between molecules, which can be a result of how individual molecules pack together.<sup>1</sup> The field of porous materials research is rapidly expanding,<sup>2</sup> with continuing interest in established classes such as metal-organic frameworks (MOFs),<sup>3,4</sup> covalent organic frameworks (COFs),<sup>5</sup> sitting alongside an increasing focus on porous organic cages (POCs),<sup>6,7</sup> and porous liquids (Figure 1.1).<sup>8</sup> These materials can be classified according to their pore size, defined by IUPAC: (i) pores with widths not exceeding ~ 2 nm are called microporous; (ii) pores with widths between 2 nm and 50 nm are called mesoporous; and (iii) pores with widths exceeding 50 nm are called macroporous.<sup>9,10</sup>

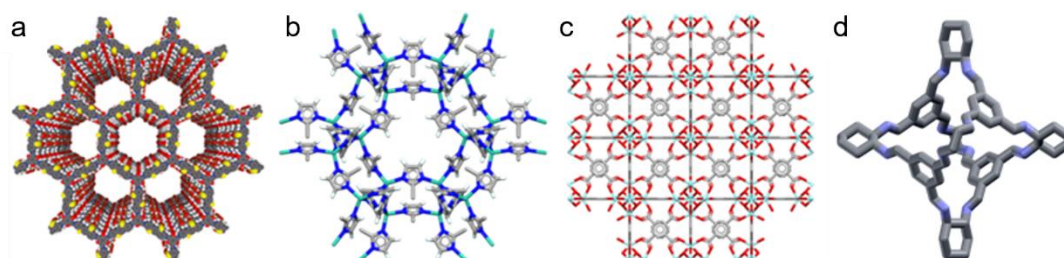


**Figure 1.1** Examples of porous materials: a) Covalent organic framework (FS-COF, fused sulfone); b) Zeolitic imidazolate framework (ZIF-8); c) Metal-organic framework (UiO-66); d) Porous organic cage (**CC3-R**).

Porous materials have been well known for many millennia, where the use of activated carbon dates back as far as 3750 BC, and is still widely used within industry today.<sup>11</sup> One of the earliest known applications of activated carbon was in the form of charred wood, which was used on the inner side of wooden barrels to store drinking water. They note the decolourising effect that the barrels had on the water, showing a reduction in particulates and impurities in the water.<sup>12</sup> Of course, charring organic material is one of the simplest forms of producing activated carbon. Activated carbon is now typically synthesised by thermal decomposition or pyrolysis of carbon rich materials, such as wood, followed by activation with steam or carbon dioxide at elevated temperatures (>800 °C).<sup>13</sup> Other early applications of the adsorption properties of activated carbon were also discovered by the Egyptians, where it is noted that odorous vapours, such as putrefying wounds and matter, could be removed using charcoal, and was also used to reduce the effects of food poisoning.<sup>11</sup> We now know that activated carbon is a stable, cheap, and reliable material that has a high surface to volume ratio capable of a wide range of applications.<sup>14</sup> One of its

earliest known applications is still widely used around the world today, in treating drinking water and wastewater.<sup>15</sup> More modern applications utilise this porous material in catalysis.<sup>16</sup> The large surface area and pore system allows for a high dispersion of catalytic sites, making them excellent candidates for heterogeneous catalyst loading, and they continue to be widely used within the fine chemical and petrochemical industries.<sup>17</sup>

Porous materials maintain their popularity due to their, what seems to be, never-ending array of applications.<sup>18,19</sup> At present, microporous materials are of interest due to their compatibility with small gas molecules such as H<sub>2</sub>, He, N<sub>2</sub>, CO<sub>2</sub>, and CH<sub>4</sub>, and their ability to store, separate, and selectively release the desired gases. The large array of applications is also in part due to the ability of researchers to tune the pore size along with its scaffold, allowing specific properties to be targeted, whether that is to allow for a large internal volume to store gases, or to tweak the 'window' size to allow certain gases to pass through while preventing larger gases from fitting.<sup>20</sup> However, in reality, the ability to tune the pore size and the properties of these materials can prove difficult, as it may be problematic to synthetically produce novel microporous materials, along with their predicted properties.<sup>21</sup> Recently, to reduce the amount of laboratory hours spent researching materials, which may not even be suitable for their target application, the use of computational approximations and modelling has been incorporated into materials research.<sup>22</sup>

Two important features of microporous materials are their surface area, and selectivity. This thesis will focus on two subgroups of microporous material: (i) discrete organic cage molecules, and (ii) extended framework materials, and how they can be incorporated into porous liquids.

## 1.2 Porous Organic Molecules

### 1.2.1 Porous Organic Cages

Porous organic cages (POCs) are discrete organic molecules that contain a permanent cavity, which is accessible through gaps or windows in the cage structure.<sup>23</sup> The synthesis of POCs often uses reversible chemistries, which provides a degree of error correction and allows the thermodynamic product to be isolated (Figure 1.2). The first POCs were reported by Tozawa *et al.* in 2009.<sup>6</sup> Here they carried out a series of imine condensations in which they combined 4 equivalents of 1,3,5-triformylbenzene (TFB) with 6 equivalents of three different diamines, 1,2-ethylenediamine (EDA, **CC1**), 1,2-propylenediamine (**CC2**), and (*R,R*)-1,2-cyclohexanediamine (CHDA, **CC3**), resulting in a 10-component imine polycondensation to form Tri<sup>4</sup>Di<sup>6</sup> cages (Figure 1.3). All three cages were successfully isolated and were found to have an octahedral structure which was confirmed by single crystal X-ray diffraction (scXRD). These cages were all found to contain a permanently open structure with an intrinsic cavity. The crystal packing was also identified as being different between the cage species, where **CC1** was found to pack window-to-face and therefore lacked void connectivity, **CC2** had undulated packing with non-interconnecting pores, and **CC3** was found to pack window-to-window leading to an interconnected pore network. This variation in packing also explained the observed N<sub>2</sub> uptakes, where **CC1** was found to be non-porous, and **CC2** and **CC3** were found to be porous, with BET surface areas of 533 and 624 m<sup>2</sup> g<sup>-1</sup> respectively. They also indicated that the addition of cyclohexyl functionality on the cage vertices creates additional space between discrete cage molecules, resulting in increased extrinsic porosity within the bulk material.

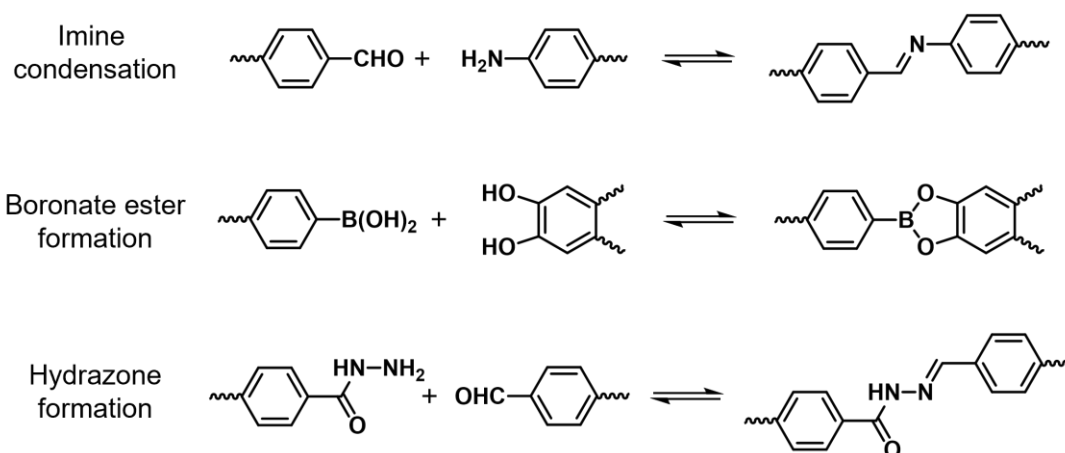


**Figure 1.2** Reversible chemistries that have been utilised in the synthesis of organic cage materials.



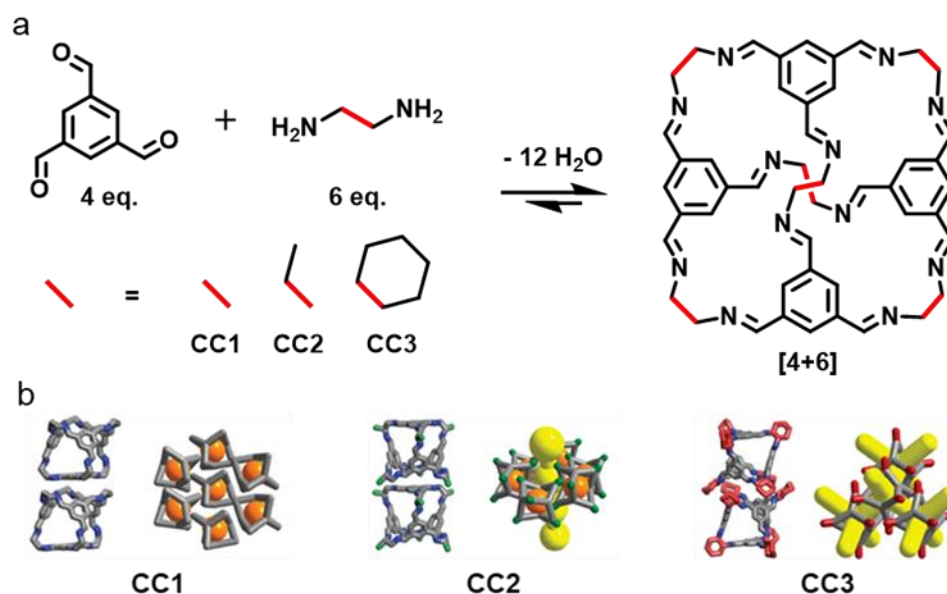


**Figure 1.3** a) Reaction scheme for the synthesis of cages **CC1** – **CC3**. b) Schematic of cage-to-cage packing in the crystal structure of **CC1** – **CC3**, with differing properties arising from a change in vertex functionality. The isolated void volumes are shown in orange, and pore channels are shown in yellow. Reproduced with permissions from ref (6).

On summarising this work, the authors also questioned how the introduction of even bulkier groups on the cage exterior would affect the pore volume and porosity. Shortly after the initial report of **CC3**, Bojdys *et al.* demonstrated the synthesis of structurally analogous covalent organic cages with diphenylethylenediamine derivatives and TFB (Figure 1.4).<sup>24</sup> Here, they report the synthesis of two new cages, **CC9** and **CC10**, where (*R,R*)-1,2-diphenylethylenediamine and (*R,R*)-1,2-bis(4-fluorophenyl)ethane-1,2-diamine were used respectively, both forming  $\text{Tri}^4\text{Di}^6$  cages. Though very similar in size, both building blocks behaved rather differently. **CC9** was found to contain two different polymorphs, where cage molecules favoured a window-to-face packing, creating two types of extrinsic pore surrounding the cage, whereas **CC10** was found to pack in alternating window-to-window and face-to-face arrangements, resulting in very little extrinsic porosity. The increase in external cavities in **CC9** had a favourable effect on the porosity of the material, with a BET surface area of  $854 \text{ m}^2 \text{ g}^{-1}$ , and a loss of porosity was observed in **CC10** with a reported surface area of  $460 \text{ m}^2 \text{ g}^{-1}$ .

A study by Giri *et al.* also investigated the effect of the addition of alkyl groups to the exterior of organic cages.<sup>25</sup> They reported the successful synthesis of four  $\text{Tri}^4\text{Di}^6$  cages, with varying exterior alkyl functionality, including *n*-hexyl, *n*-pentyl, isohexyl and *n*-octyl, with the aim of producing neat porous liquids. Cages with the *n*-alkyl chains showed a complete loss in porosity, with a later computational study

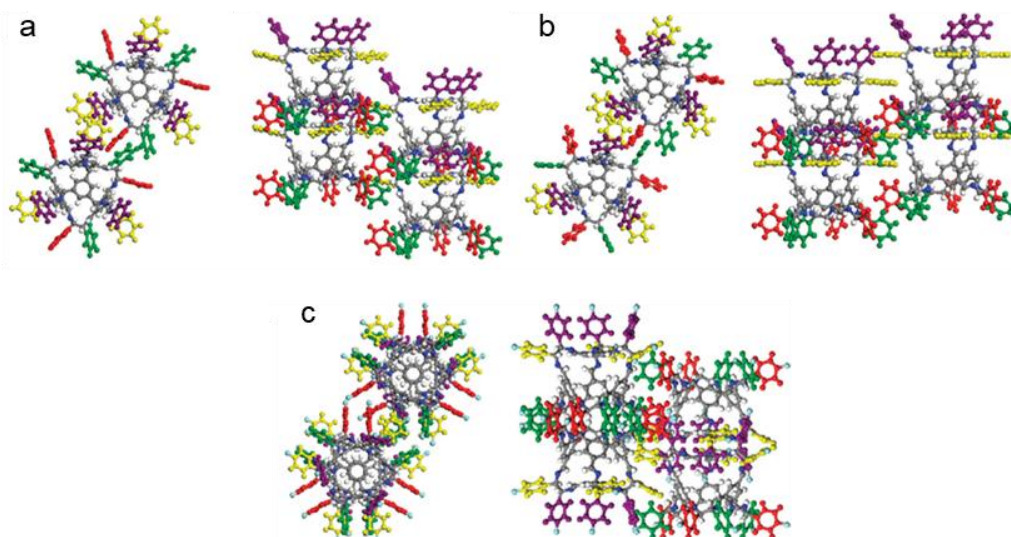


**Figure 1.4** Solid state packing of cages, where a) **CC9** in one polymorph; b) **CC9** in its second polymorph; c) **CC10**. Reproduced with permissions from ref (24).

postulating that unbranched chains are capable of rapidly entering the internal cavity of the cage.<sup>26</sup> Free energy calculations show that interpenetration is thermodynamically favourable, resulting in partly filled pores and leading to the material being non-porous. The branched isohexyl derivative was found to be less favourable for entering adjacent cage molecules, when compared to the non-branched alkyl chains, and consequently had some porosity in the solid state with a reported BET surface area of  $289 \text{ m}^2 \text{ g}^{-1}$ .

In more recent years, studies involving **CC3** have increased. Variations of the cage and its packing have been researched, for example, the work by Jones *et al.* demonstrated how POCs could undergo self-sorting by chiral recognition to form highly crystalline materials.<sup>27</sup> One method to increase the porosity in **CC3** was to combine **CC3-S** (formed using the *S,S* enantiomer of CHDA) and **CC3-R** (formed using the *R,R* enantiomer of CHDA), to produce a racemic porous material (Figure 1.5, b), increasing the BET surface area to  $873 \text{ m}^2 \text{ g}^{-1}$ . Combining **CC3-R** with either **CC1** (Figure 1.5, a), or the opposite enantiomer of **CC4** (formed using TFB and (*S,S*)-1,2-cyclopentdiamine) (Figure 1.5, c), again created a porous quasi-racemic material, with surface areas of  $437 \text{ m}^2 \text{ g}^{-1}$  and  $980 \text{ m}^2 \text{ g}^{-1}$  respectively. Similar work was also reproduced and developed further by Hasell *et al.*, where they investigated how different size particles and morphologies of **CC3-rac** could be formed by changing the reaction conditions.<sup>28</sup> Both the rate of addition, *i.e.*, the rate at which solutions of both cage enantiomers were mixed together, and the temperature, had a direct effect on the size and morphology of the particle. When mixed at  $20 \text{ }^\circ\text{C}$ , the

highest temperature tested, the largest particle size was produced, creating a material with the highest BET surface area of  $696 \text{ m}^2 \text{ g}^{-1}$ , although it produced the lowest  $\text{N}_2$  uptake. In contrast, the smallest particles formed at the lowest temperature tested,  $-80 \text{ }^\circ\text{C}$ , produced the highest  $\text{N}_2$  uptake while having the smallest BET surface area of  $507 \text{ m}^2 \text{ g}^{-1}$ . The rate at which enantiomers were introduced to each other also influenced the surface area and gas uptake. Slow addition at  $0.5 \text{ mL min}^{-1}$  created a material with both a low surface area and the lowest gas uptake, whereas the fastest addition of  $20 \text{ mL min}^{-1}$  produced the highest surface area and the highest gas uptake. The authors rationalise that this behaviour is due to reduced crystallinity from the rapid crystallisation, resulting in a less crystalline amorphous material, as opposed to a highly ordered crystalline material, creating a large number of defects leading to a high surface area.

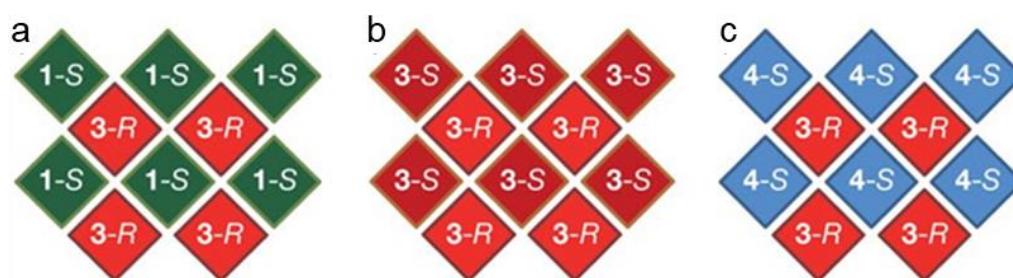


**Figure 1.5** Packing of isostructural POCs in their window-to-window configuration in various quasiracemic (a, c) and racemic (b) co-crystals. Reproduced with permissions from ref (27).

Intentional disruption of the crystal packing in POCs was reported by Jiang *et al.*, where they utilise dynamic covalent ‘scrambling’. This involves employing two differing diamines (EDA and CHDA), in combination with TFB, to create a statistical distribution ranging from **CC1** to **CC3**, and including a whole range of intermediate cages with varying vertices, denoted by  $1^x3^y$  where x and y are the number of EDA and CHDA vertices on the individual cage species (Figure 1.6).<sup>29</sup> A range of different product distributions were also possible by using different starting ratios of diamine, which could be determined using HPLC. For comparison, both the parent cages, **CC1** and **CC3**, were produced, and their surface areas measured, with BET surface areas of  $40 \text{ m}^2 \text{ g}^{-1}$  and  $624 \text{ m}^2 \text{ g}^{-1}$ , respectively. From pure **CC1**, increasing the CHDA ratio in the scrambled mixture overall had a positive effect on the surface area, and a dramatic increase was noticeable when a 3:3 ratio of EDA:CHDA was used. This trend continued with both a 2:4 and 1:5 ratio, which demonstrated increasing BET surface areas up to  $704 \text{ m}^2 \text{ g}^{-1}$ . This demonstrates how the introduction of different vertices on the same cages in a mixture disrupts the molecular packing, resulting in

higher surface areas through the creation of extrinsic porosity between cage molecules.

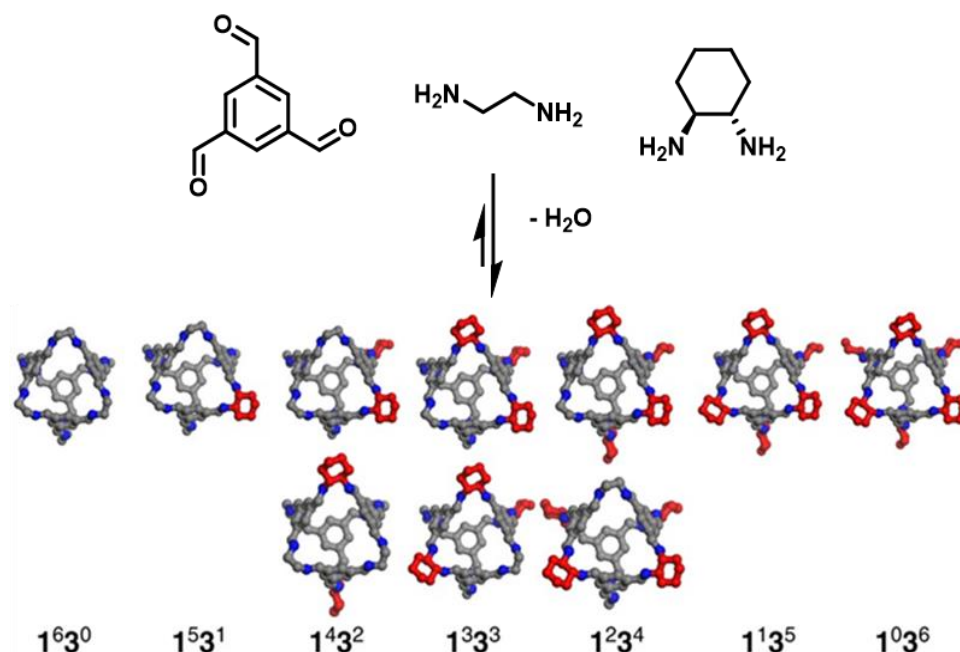


**Figure 1.6** Dynamic covalent scrambling - the combination of two different diamines, ethylenediamine (EDA) and 1,2-cyclohexanediamine (CHDA) with 1,3,5-triformylbenzene (TFB), results in a variety of cages being formed in the same mixture with mixed vertices. Reproduced with permissions from ref (29).

As with many framework materials, adjusting the size and shape of the precursor can allow for the cages and the resulting material to be finely ‘tuned’ for their specific needs.<sup>30</sup> In frameworks, this can be done through altering the physical and chemical properties of the material, for example, by introducing functional groups, or through changing the geometry and/or topology of the material.<sup>31,32</sup> The same basis can be applied to organic cages.<sup>33,34</sup> For example, Jelfs *et al.* report the synthesis of a large Tri<sup>8</sup>Di<sup>12</sup> cage (**CC7**) using a tritopic aldehyde precursor, tris(4-formylphenyl)amine, and the same diamine used in the synthesis of **CC3**, *R,R*-CHDA (Figure 1.7).<sup>35</sup> However, they found that increasing the size of the cage also dramatically reduced its stability, resulting in the cage collapsing upon isolation. This was due to the nature of the reversible chemistries involved in combination with the steric strain imposed by increasing the size of the cage.

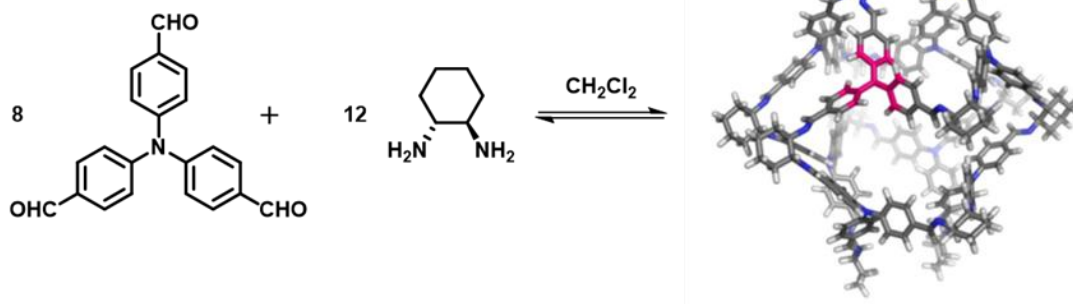


**Figure 1.7** Reaction scheme for the synthesis of the Tri<sup>8</sup>Di<sup>12</sup> cage, **CC7**, from tris(4-formylphenyl)amine and (*R,R*)-CHDA. Reproduced with permissions from ref (35).

Generally, the synthesis of these materials depends largely on the starting materials and whether they have the correct connecting geometry to create a cage.<sup>23</sup> Even small changes in precursor geometry can result in different cages being formed, leading to changes in topology or geometry.<sup>36</sup> Another factor which needs to be considered is whether the cage can be isolated. In some cases, if the formed structure becomes too strained, isolation may not be possible, resulting in decomposition of the resulting cage.<sup>37</sup> This may also happen if the resulting cage is not rigid enough, leading to collapse upon desolvation, resulting in a complete loss of porosity.<sup>38</sup>

One of the most cited pieces of work in the MOF field is by Eddaoudi *et al.*, and is based on how the pore size of a framework can be controlled by using similar precursors of varying lengths to produce an isorecticular series, *i.e.*, one that has the same framework topology.<sup>30</sup> In 2017, Slater *et al.* reported the first series of reticular organic cages, named tubular covalent cages (**TCC**).<sup>39</sup> This series of cages, **TCC 1-3**, are synthesised using tetratopic aldehyde precursors of varying lengths in combination with CHDA, as in **CC3** (Figure 1.8). Each of the three cages produced had a similar window-size and shape as those present in **CC3**, on the 'top' and 'bottom' end, with the 'side' windows being rectangular in shape. Each of the tubular cages was found to have a higher surface area than **CC3**, with reported values of 2,037 m<sup>2</sup> g<sup>-1</sup>, 627 m<sup>2</sup> g<sup>-1</sup>, and 834 m<sup>2</sup> g<sup>-1</sup> for **TCC 1-3**, respectively. Interestingly, the authors mention that although the **TCC** series has similar **CC3** windows, they do not pack in a window-to-window configuration, which they mention is due to **CC3** being able to propagate in four directions. The structures of these cages are more similar to nanotubes and hence pack together with a longitudinal offset.

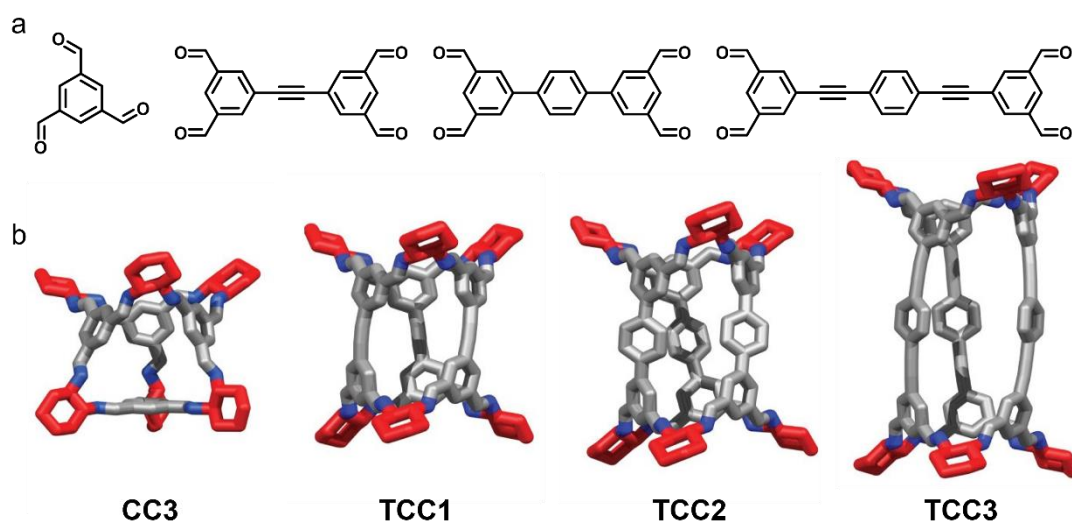


**Figure 1.8** Reticular organic cages, where: a) tritopic and tetratopic aldehyde precursors used for the synthesis of **CC3** and the tubular covalent cages (**TCC**) series; b) single-crystal X-ray structures of **CC3** and the **TCC** series of cages. Reproduced with permissions from ref (39).

Another example of producing different topologies, and also geometries of organic cages, was demonstrated in 2013 by Briggs *et al.*, where different shapes were predicted for the combination of the same precursors using computational chemistry (Figure 1.9).<sup>37</sup> They predicted two topological outcomes from the same tritopic aldehyde, tris(4-formylphenyl)amine, and a tritopic amine, tris(2-aminoethyl)amine, when combined in a 1:1 ratio. Computational predictions suggested that a  $\text{Tri}^4\text{Tri}^4$  topological cage is the lowest energy configuration, but this had two competing geometries of either a cube or a tetrapodal structure, where one would have a large internal cavity and the other would be completely non-porous. Unfortunately, one of the inherent problems with reversible chemistries can be their stability. The authors found this to be apparent with these cage systems, where the  $\text{Tri}^4\text{Tri}^4$  cages could not be isolated as bulk material and had to be characterised in solution. Additionally, they note they had difficulty producing single crystals for X-ray diffraction through slow evaporation and precipitation, though they successfully managed to produce a single crystal to confirm the favoured tetrapod structure. This is likely due to the flexibility and degrees of freedom of the tritopic amine used, producing a very flexible, and unstable cage, unlike the more rigid CHDA which is highly pre-configured in a chair structure, and is known to produce stable cages.

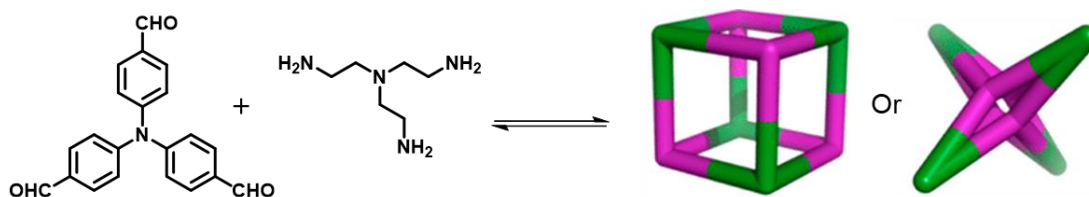


**Figure 1.9** Reaction scheme for the synthesis of possible Tri<sup>4</sup>Tri<sup>4</sup> cages, from the reaction of tris(4-formylphenyl)amine and tris(2-aminoethyl)amine. Reproduced with permissions from ref (37).

One method used to increase the stability of imine-based organic cages is to post-synthetically remove the reversible nature of the imine bonds.<sup>40</sup> This can be achieved through reduction to secondary amines, removing the sensitivity to water and eradicating the reversibility.<sup>41,42</sup> However, one of the issues found when the imines are reduced in **CC3** is that there is an increase in flexibility, which leads to a loss of the internal cavity and a complete loss of porosity. A workaround was found by Liu *et al.*, which was to combine **RCC3** (reduced **CC3**), with acetone (Figure 1.10, top and middle).<sup>43</sup> **RCC3** was found to be readily soluble in acetone, and after leaving the solution for around 30 minutes, small crystals started to form. SCXRD confirmed the formation of a new species, **AT-RCC3** (acetone tied-reduced **CC3**), where a single acetone molecule bridges the location of two former imine bonds, creating a 5-membered imidazolidine ring. Only a single acetone tie is possible, as the initial acetone molecule prevents a second acetone molecule from reacting with the cage, because of steric inhibition of intermediates. The addition of acetone into the cage structure increases the porosity, allowing a small amount of nitrogen adsorption. To explain this change, the authors describe how the addition of acetone would prop the cage open, maintaining an internal cavity, however the two methyl groups within the cage prevent a high gas uptake. This issue was mitigated by substituting acetone with formaldehyde to produce **FT-RCC3** (formaldehyde tied-reduced **CC3**). In this case, all positions are accessible by formaldehyde and allow for addition at each amine pair. This produces a rigid, stable cage with a high BET surface area, just shy of what is displayed by **CC3** (377 vs 409 m<sup>2</sup>/g).

Another method that can be used to remove the reversible nature of the imine bonds, is the oxidation of imine bonds. This can be achieved through a Pinnick oxidation, which uses sodium chlorite under mild acidic conditions. While this reaction is typically known for the oxidation of aldehydes, they can also be applied to imines (Figure 1.10, bottom).<sup>44</sup> Applying this chemistry to imine-derived cages was demonstrated by Bhat *et al.*, who demonstrated the synthesis of a Tri<sup>4</sup>Di<sup>6</sup> imine cage, before oxidising the cage to the amide variant.<sup>45</sup> During this study they also attempt to produce the amide

cage directly from the triamine with a bis(acidchloride) which produces a wide range of products, observed by HPLC, though the synthesis via the imine cage produced significantly fewer products, yielding a high purity amide cage, albeit with a low isolated yield of 21% after purification. The transformation of the imine to the amide significantly increases the stability of the cage, which is demonstrated by stirring the cage in a range of acidic and basic conditions, before obtaining  $^1\text{H}$  NMR spectra of the material, where only concentrated  $\text{H}_2\text{SO}_4$  (36 M) showed a change to the  $^1\text{H}$  NMR spectra. While there is not a dramatic change in shape or size, the amide variant of the cage produces a significantly lower BET surface area of  $275\text{ m}^2\text{g}^{-1}$  versus the  $1377\text{ m}^2\text{g}^{-1}$  of the previous reports of the imine cage.<sup>46</sup>

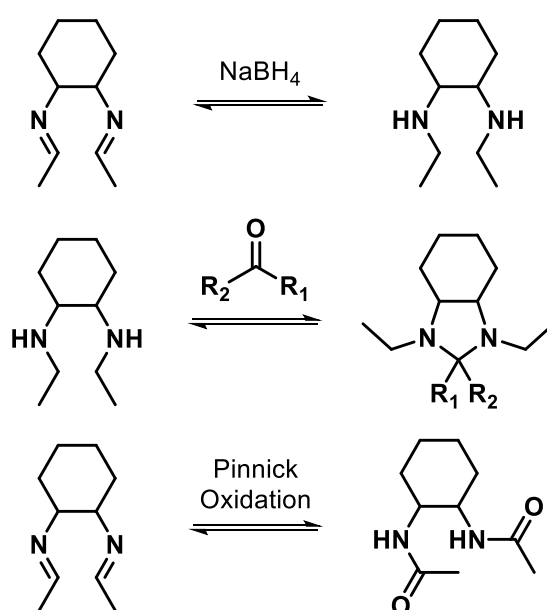


**Figure 1.10** Reaction schemes demonstrating possible routes to remove the imine functionality to improve organic cage stability.<sup>48,49</sup>

Since their discovery, POCs have been shown to have many uses arising from their discrete internal cavity and cage windows. At present, POCs have been shown to separate gases, with selective uptake of  $\text{CO}_2$  over  $\text{CH}_4$ <sup>47</sup> and  $\text{N}_2$ .<sup>48,49</sup> They have also shown success in including quantum sieving of hydrogen isotopes<sup>50</sup> and have the ability to trap rare gases such as Kr and Rn, as well as the separation of Xe and Kr.<sup>51,52</sup> Some POCs have also been shown to selectively bind chiral substrates depending on their chirality, demonstrating their ability to be applicable to a wide range of chiral and molecular separations.<sup>53</sup> Whilst being able to adsorb and trap gases, cages also have the potential for being used as molecular sensors, for example, Acharyya *et al.* have demonstrated how fluorescent POCs can be used as molecular sensors for picric acid detection.<sup>54</sup>



Overall, one major advantage porous organic molecules, such as POCs, have over typical framework materials is their ability to be solution processable.<sup>23</sup> The synthesis of POCs allows for molecules to be synthesised under mild conditions, including reduced temperatures and less hazardous solvent choices, rather than those typically required to produce framework materials.<sup>55</sup> Their ability to dissolve also allows for a wide range of standard characterisation techniques to be used on the material, such as solution NMR, mass spectrometry, and HPLC, in addition to solid state techniques which can be used for framework and polymer materials, such as IR spectroscopy, UV-Vis spectroscopy, and X-ray diffraction. In addition, they can be purified using standard procedures such as recrystallisation and preparative chromatography.<sup>56</sup> With this in mind, POCs are particularly attractive because of vast amounts of possible precursors to develop and produce novel cages, which produces new and exciting applications. POCs have also been shown to be readily scalable using solvent free methods, such as mechanochemistry using twin screw extrusion,<sup>57</sup> and continuous flow methods.<sup>58</sup>

### **1.3 Porous Frameworks**

One of the major differences between POCs and porous frameworks is the extended structure creating long-range networks, whereas cages are discrete molecules. Like POCs, porosity can arise through intrinsic porosity created by a 3D structure creating pores. Channels can also be created through the material which can occur with a regular array of cavities within the framework material, such as crystalline frameworks such as covalent organic frameworks (COFs), metal-organic frameworks (MOFs), and zeolites, rather than the packing of POCs which can produce channels within that material. Porous frameworks are also typically non-soluble, though they can be characterised through standard solid-state techniques. More recently, the melting of some framework materials has been discovered,<sup>59</sup> leading to the formation of melt-quenched glass MOFs<sup>60</sup> and polymers of intrinsic porosity (PIMs).<sup>61</sup> Both POCs and framework materials have been fundamental in the discovery of type II (solutions) and type III (dispersions) porous liquids, which are discussed in more detail later in this chapter, along with the discovery of a new MOF-based type III porous liquid discussed in Chapter 3.

### 1.3.1 Metal-Organic Frameworks

Porous co-ordination polymers started to appear in the early 1960s,<sup>62</sup> which had very similar features to what were later named metal-organic frameworks (MOFs) in the late 1990's (Figure 1.11).<sup>63</sup> MOFs are a class of co-ordination polymer, which consists of metal ions or metal clusters acting as nodes, connected by organic ligands, known as the 'linkers'. These co-ordination polymers can be one-, two- or three-dimensional, depending on the number, orientation, and availability of co-ordination sites, allowing these molecular building blocks to extend over the entire material.<sup>64</sup> In some cases, such three-dimensional materials can be porous, creating large internal surface areas in these frameworks, with reports of BET surface areas exceeding  $10,000 \text{ m}^2 \text{ g}^{-1}$ .<sup>65</sup> While MOFs incorporate reversible chemistries (which also allows for error correction, similar to that of POCs), through co-ordination bonds, they have been shown to exhibit high stabilities, and are able to maintain their structure over a wide range of temperatures and conditions.<sup>66</sup>

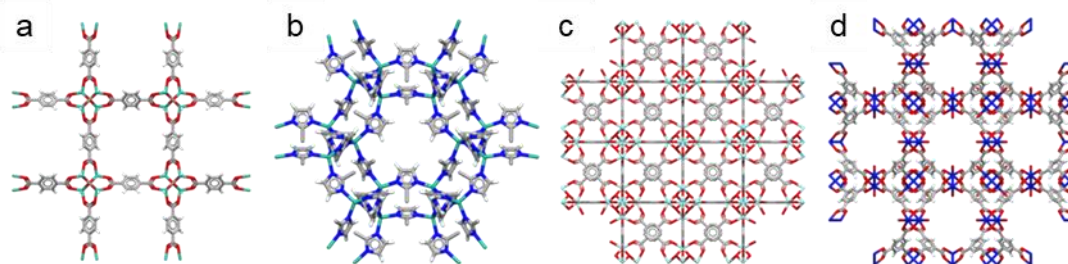


**Figure 1.11** Examples of metal-organic frameworks: a) MOF-5; b) ZIF-8; c) UIO-66; d) HKUST-1.

Rapid advances in the fields of synthesis and catalysis has led to over 100,000 MOF structures being reported on the Cambridge Structural Database (CSD) to date (which does not include amorphous materials), and over 500,000 predicted structures,<sup>67</sup> making MOFs one of the fastest growing fields in chemistry. This is likely due to the multitude of possible precursors that MOFs can be created from, where the pore size of such materials can be altered or tuned by using the 'node-and-linker' approach, which can control the cavity size by combining certain metal nodes with organic linkers, allows the volume to be adjusted according to its desired purpose (Figure 1.12).<sup>68</sup> This can also be achieved by altering the organic linker and keeping the same metal node, which can maintain the same framework topology – this approach can be referred to as isorecticular MOFs (Figure 1.13).<sup>30</sup> The organic linkers and nodes can also be functionalised, either as precursors or post-synthetically modification, to finely tune the cavity towards targeting guest interactions, or can allow for dynamic

changes to the material through the incorporation of stimuli-responsive components resulting in the change of cavity size (described in 1.5 Photochromism).

MOFs are typically synthesised through solvothermal synthesis, which often requires high-temperatures and harmful solvents such as dimethylformamide (DMF), which often limits the scale-up possibilities of MOFs.<sup>55</sup> Due to the reversible nature of coordination bonds, the high-temperatures provide a higher degree of error correction, which in theory, limits the amount of oligomers and side-products, and favours the MOF and the most thermodynamically stable product. There are new methodologies that incorporate continuous flow processes,<sup>69</sup> however, given the materials produced are solid this can lead to regular blocking of the flow reactor, whereas solvent-free approaches allow the continuous synthesis of these materials without the need for solvents,<sup>70</sup> although there are few examples of the approach.

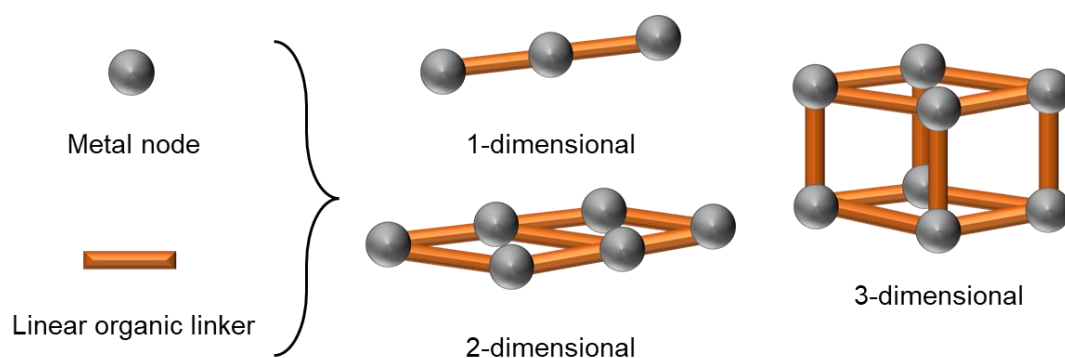


**Figure 1.12** The node-and-linker approach applied to metal-organic frameworks.

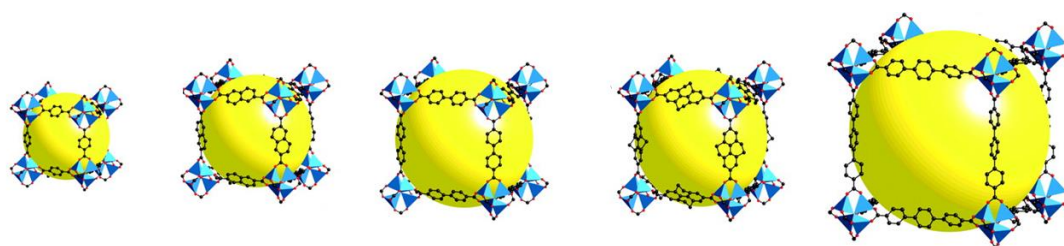


**Figure 1.13** Series of isoreticular MOFs with increasing ligand (ditopic carboxylate) lengths, where the yellow spheres represent the Van Der Waals spheres that would fit in the cavity. Reproduced with permissions from ref (30)

The interest in MOFs has extensively gone beyond the synthesis, where there have been rapid developments with the potential applications of these materials, such as gas storage and separation, sensing, catalysis, drug delivery, and light harvesting.<sup>71</sup> Given the mass popularity of MOFs, it is unsurprising that such materials have become commercially available, including MOF-5, ZIF-8, UIO-66, HKUST-1 and MIL-

53.<sup>72</sup> However, one of the limitations of MOFs is the solid nature of these materials, which prevents them from being implemented into existing infrastructure within industry, which often sides towards liquid materials because of their ability to flow. While 'liquid MOFs' have been achieved through melting, they require high temperatures to maintain their liquid state, which makes them impractical for industrial processes,<sup>59</sup> though the ability to melt MOFs gives access to melt-quenched glass MOFs and also occurs the ability of these materials to be cast directly into membranes and other materials, reducing the need for liquid processing. Another method that can be used to incorporate MOFs as liquids, is by utilising them as a component with porous liquids, where they have shown promising results as type III porous liquids, as a porous material dispersed in a size-excluded solvent.<sup>73</sup>

#### **1.4 Porous Liquids**

Until recently, the occurrence of porosity was predominantly observed in solid materials. However, the concept of a 'porous liquid' (PL) was first introduced by James in 2007, which outlined a system that utilises molecules with permanent intrinsic pores within a liquid, rather than a conventional liquid which contains extrinsic and transient cavities.<sup>74</sup> Three different types of porous liquid were initially proposed, while recently expanding to a fourth type<sup>75</sup> (Figure 1.14):

- Type 1 – neat liquids consisting of molecules containing an internal cavity, and rigidity, to prevent the collapse and loss of porosity
- Type 2 – empty hosts dissolved in a cavity-excluded solvent (rigid discrete molecules are required to prevent the collapse of the pore)
- Type 3 – solid microporous materials dispersed within a cavity-excluded solvent to produce a fluidised porous material
- Type 4 - neat microporous hosts that form transient, strongly associated liquid, *i.e.* neat meltable microporous extended frameworks

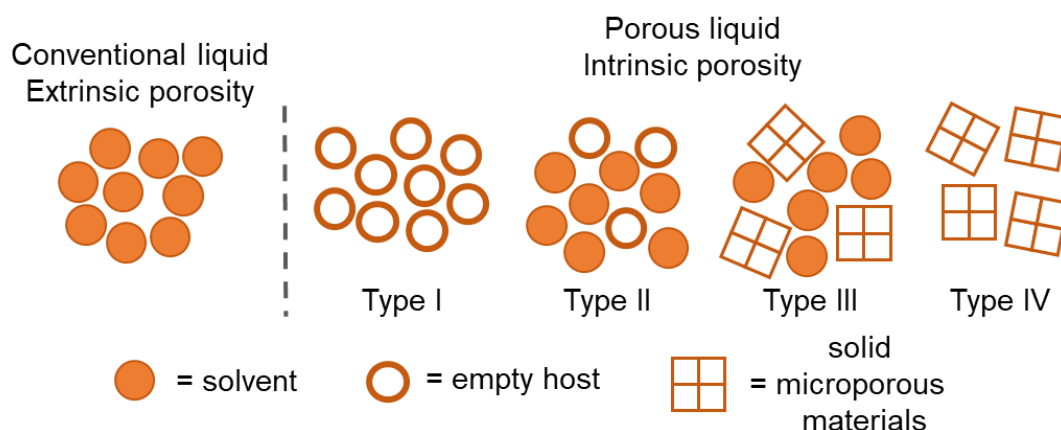


**Figure 1.14** Schematic representing the four types of porous liquids.

One of the first Type 3 PLs were reported by Wang and co-workers in 2014, though was described as a ‘hybrid absorption–adsorption’ method, which involved the dispersion of a zeolite, ZIF-8, in a mixture of glycol solutions. The first molecular microporous liquids were realised by Cooper, James and co-workers, who reported the synthesis of Type 2 porous liquids in 2015.<sup>8</sup> In this work, they demonstrated the use of highly soluble POCs dissolved in a variety of size-excluded solvents. Within the same year, Dai and co-workers also reporting the first type 3 system in 2015.<sup>76</sup> In subsequent years, the field has gained more popularity and examples of all four different types of PLs have now been reported, formed using a range of porous materials including MOFs, zeolites, POCs, and porous organic polymers in a variety of organic solvents, oils and ionic liquids. They have also been investigated for their applications in gas uptake, gas retention, and gas release, along with shape and size-selectivity.<sup>76–78</sup> Due to their definition, there may also be systems that could be classified as porous liquids prior to their conceptualisation.

To remain functionally useful, all types of porous liquid require the cavity to remain empty. This imposes limitations, preventing the use of long flexible derivatives such as alkyl groups, and the use of a wide range of solvents, which can be too small and subsequently occupy the cavity. Another factor that also needs to be taken into consideration when designing a porous liquid is its viscosity. For example, if a type 2 or type 3 porous liquid is based on dissolving or dispersing a porous organic cage in a solvent, the amount of cage that can be used can be significantly high. However, this is somewhat mitigated if a very high loading results in a porous liquid that is unable to flow like a conventional liquid, and instead is on the borderline of being a gel or wet solid.

As this field has dramatically increased in popularity, there are examples of each type of PL. In the next sections a few of the key milestones will be introduced.

### 1.4.1 Type 1 Porous Liquids

At present, there are very few examples of type 1 porous liquids. An early example of a porous liquid type of material was developed by Giannelis and co-workers.<sup>79</sup> This work demonstrated how hollow silica nanospheres could be functionalised with positively charged organosilanes, by reacting them with hydroxyl groups bound to the silica shell. The use of chloride as the counter ion produced a high melting solid, which when exchanged with poly(ethylene glycol)-tailed sulfonate groups (PEGs), became liquid at room temperature (Figure 1.15). Although the material is porous and adsorbs gas, it deviates from the initial definition of a type 1 porous liquid, as the hollow silica liquid does not contain a single cavity, but rather consists of a porous shell which is accessible through small micropores, similar to that of molecular sieves.<sup>80</sup>

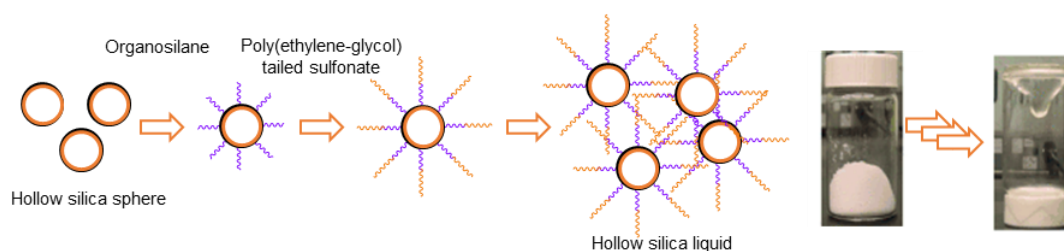


**Figure 1.15** Preparation used to convert hollow silica spheres into a hollow silica ‘type 1’ liquid. Reproduced with permissions from ref (80).

Another notable attempt towards a true type 1 porous liquid was reported by Giri *et al.*, which was based around functionalisation of imine-based POCs (in particular **CC1**) with long alkyl substituents.<sup>25</sup> They demonstrated that increasing the length of the alkyl chain functionality resulted in a decrease in the melting point of the material, down to a minimum of 50 °C, while the parent non-alkylated cages would decompose before melting at 300 °C (Figure 1.16). This approach was designed to allow a type 1 porous liquid to become a reality, at slightly above ambient temperatures. However, the addition of long alkyl chains resulted in a significant loss in gas uptake and porosity. This was due to the alkyl chains entering and occupying the cavities of neighbouring cage molecules. In an attempt to mitigate these effects, Giri *et al.* tried to incorporate bulkier chains using branched tails on the alkyl groups, such as isopropyl, in the hope that this would make them sterically unfavourable and unable to fit through the neighbouring cage windows and occupy the cavities. Unfortunately, they found that this had an inverse effect, with the tertiary groups being more favoured

than the originally attempted alkyl groups. Furthermore, it also had a negative impact on the melting point, with it being higher than the original alkylated cages.

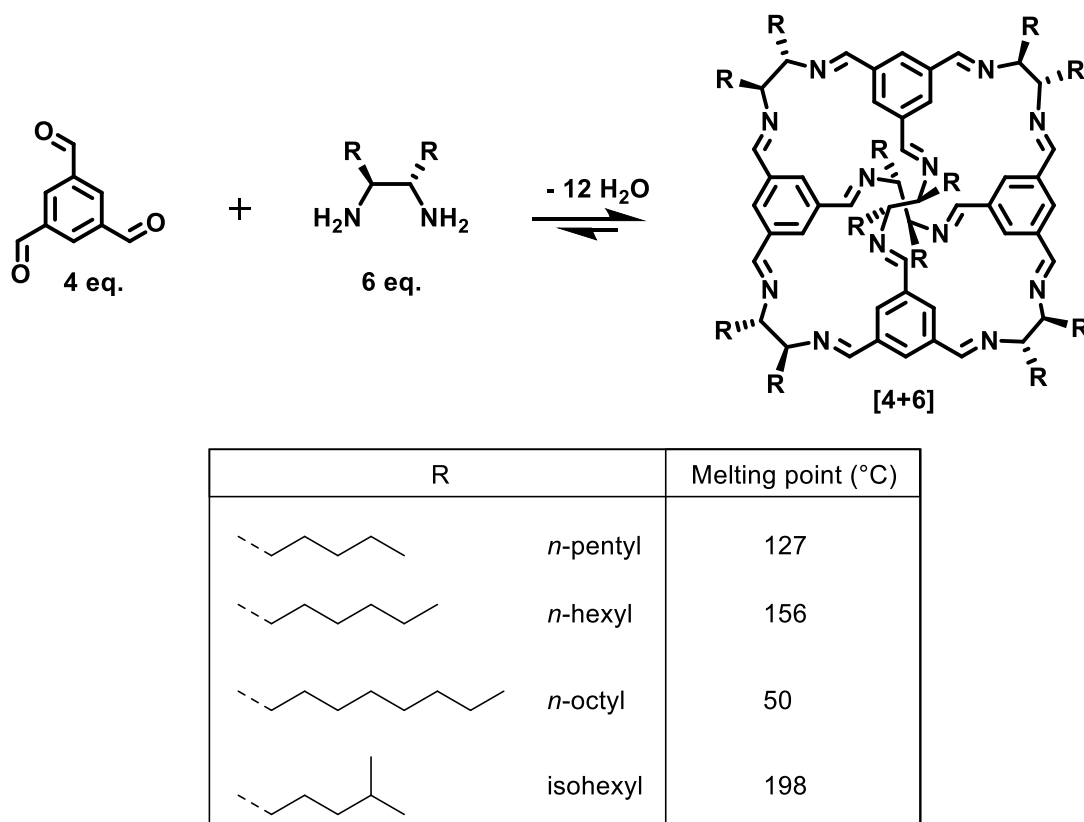


**Figure 1.16** Alkylated cages reported by Giri *et al.* showing how differing length of alkyl functionality effects the melting point of cages. Reproduced with permissions from ref (25).

There have been several reports of researchers trying to achieve a ‘true’ type 1 PL, though very few have succeeded, as most of these attempts have produced materials that require elevated temperatures, which results in a loss of porosity. However, the first successful example of a type 1 permanently microporous liquid was demonstrated by Ma *et al.* who designed a family of metal-organic cages (MOCs), where a longer chain example produced a liquid at room temperature (Figure 1.17).<sup>81</sup> To create these cages, they combined poly(ethylene glycol) (PEG) groups with a terminal imidazolium triflimide, with zinc (ii) triflimide, creating a MOC ionic liquid, where they say remains porous as the triflimide ( $\text{NTf}_2^-$ ) counter ion is too large to bind inside the cage. In this study, positron annihilation lifetime spectroscopy (PALS) was used to confirm that the pore remains empty, which has previously been used to explore the cavity of POC based PLs.<sup>8</sup> This technique works by using the lifetime of positions generated within a material, and their travel time before being annihilating corresponds with the average pore size of the material. In this study they also explore the pore size with  $^1\text{H}$  NMR spectroscopy studies with the addition of branched

alcohols, which have a binding preference over that of *n*-alkyl alcohols, which they believe is due to a better matching shape of the cavity towards the branched alcohols.

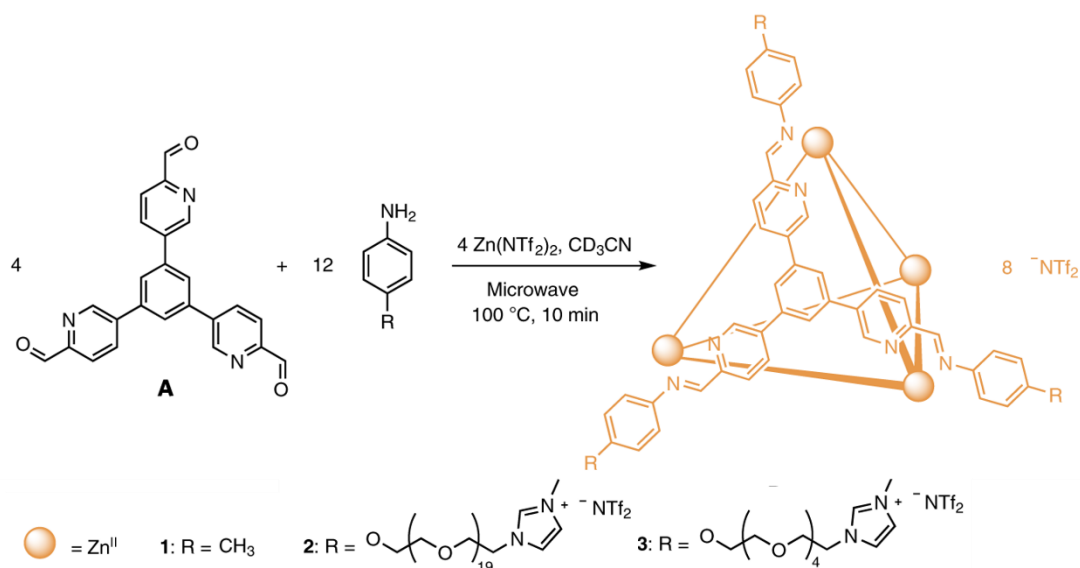


**Figure 1.17** Synthesis of the MOCs for room temperature type 1 porous ionic liquids. Reproduced with permissions from (81).

### 1.4.2 Type 2 Porous Liquids

In subsequent years, following the initial studies relating to POC-based type 1 porous liquids, type 2 porous liquids were reported. These first porous liquids were published by Cooper, James, and co-workers, where highly soluble porous organic cages were dissolved in a variety of bulky, size-excluded solvents.<sup>8,82</sup> One of the reported systems was based on an imine cage decorated with crown-ether functionality, making it highly soluble in 15-crown-5, which was bulky enough for it to not fit through the windows, leaving the cavity empty (Figure 1.18, a). The permanent porosity in the liquid was confirmed using positron annihilation lifetime spectroscopy (PALS) – PALS has the ability to probe the electron density distribution within a material, which can then be correlated to the average pore diameter. The solid cage, 15-crown-5, and the PL, were then compared using this technique to confirm that the pores were still empty in the porous liquid.

However, the synthesis of the crown-ether functionalised cage was not scalable due to its six-step synthesis, including the use of explosive azide intermediates, resulting in a poor overall yield (3.1-6.5%). Therefore, an alternative strategy was employed – the use of a scrambled cage mixture was introduced, formed from a mixture of vicinal diamines with TFB to form a mixture of Tri<sup>4</sup>Di<sup>6</sup> cages, which have similar cavity dimensions to that of the crown-ether cage.<sup>29</sup> The formation of a scrambled cage mixture has previously been reported to increase solubility in organic solvents,



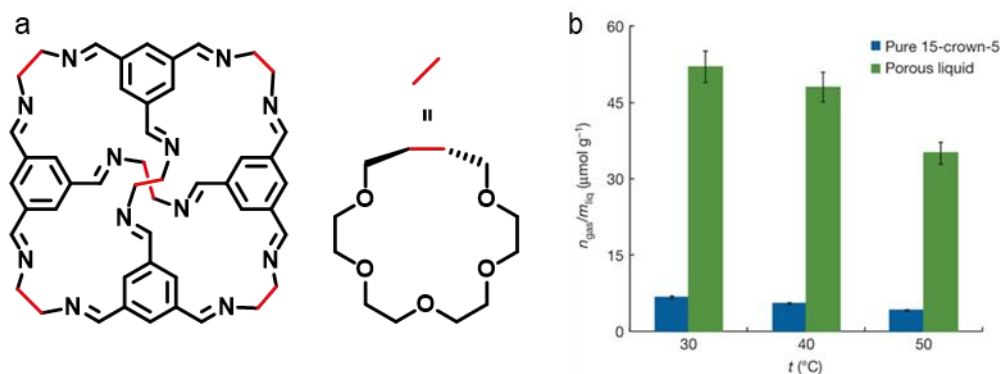


**Figure 1.18** a) Structure of the Tri<sup>4</sup>Di<sup>6</sup> crown-ether cage b) Dissolution of methane in the porous liquid and pure 15-crown-5. Reproduced with permissions from ref (82).

particularly when compared to the ‘parent’ cages formed using one of the same diamines.<sup>29</sup> They propose this works due to a mixture of exterior functionality disrupting crystal packing, lowering the crystal lattice energy, and therefore increasing the solubility. Two diamines were used in equal parts: *R,R*-CHDA, which is used to make **CC3**, and 1,2-diamino-2-methylpropane, which is used to make **CC13**. This resulted in a statistical mixture of **CC3:CC13** being formed (Figure 1.19). The solubility of this was then investigated by Greenaway *et al.*, where perchloropropene (PCP) was shown to dissolve a large quantity of cage, in excess of 230 mg of cage per mL of solvent.<sup>82</sup> This solubility was higher than either of the parent cages, **CC3** and **CC13**. The synthesis of the scrambled cage can also be carried out in a single step with much higher yields and produces a much less viscous porous liquid compared to that of the crown-ether system.

Several experiments were performed to determine if the cavities remained empty whilst dissolved in the solution. The first involved determining the gas uptake – methane uptake in both the neat solution (PCP) and the porous liquid were measured, and it was found there was a significant increase in uptake in the PL over that of the neat liquid alone. This trend was also observed with nitrogen, carbon dioxide, and xenon. Furthermore, <sup>1</sup>H NMR spectroscopic studies were performed on the neat solvent and porous liquid while loaded with methane. In neat PCP, methane was observed at -0.24 ppm, whereas in the porous liquid, a shift upfield to -2.80 ppm was observed. This upfield shift is caused by the shielding effects from methane being inside the cage and supports the hypothesis that methane is entering the internal cavity of the cage, as opposed to being absorbed into the solvent. Gas evolution studies also demonstrated the ability of the porous liquid to exhibit guest selectivity. Xenon was loaded into the porous liquid, and whilst the addition of a smaller solvent

(CHCl<sub>3</sub>) led to the spontaneous release of gas, the addition of a larger guest (1-*t*-butyl-3,5-dimethylbenzene) did not, confirming it was size-excluded from the cavity.

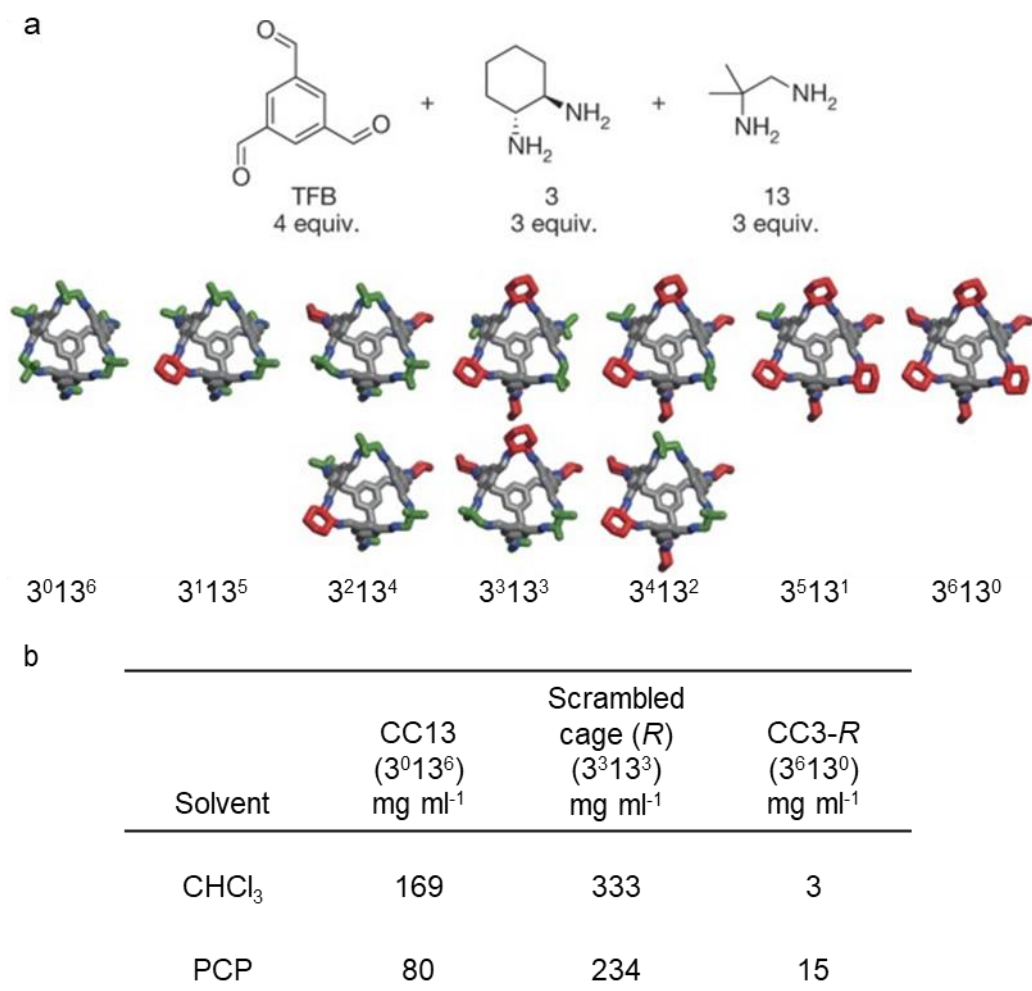


**Figure 1.19** a) Reaction of 1,3,5-triformylbenzene (TFB) with two diamines: (1*R*,2*R*)-cyclohexanediamine (used to form **CC3-*R***) and 1,2-diamino-2-methylpropane (used to form **CC13**), to form a statistical mixture of cages – scrambled **3<sup>3</sup>:13<sup>3</sup>-*R*** cage; b) Solubility testing of **CC3-*R***, **CC13**, and scrambled **3<sup>3</sup>:13<sup>3</sup>-*R*** cage, in perchloropropene (PCP) and chloroform. Reproduced with permissions from (82).

Another example of a type 2 PL was reported by Deng *et al.* who report the preparation of a type 2 PL from MOCs (Figure 1.20).<sup>83</sup> Here they use a previously reported MOC, known as MOP-18,<sup>84</sup> which is decorated with long alkyl chains (C<sub>12</sub>) dissolved in 15-crown-5. While the authors say that the cage has good solubility when heating the sample to 60 °C (up to 40 wt%), they also go on to comment that at room temperature they are only able to dissolve 5 wt% of MOP-15 into 15-crown-5. To explore the porosity, they utilised CO<sub>2</sub> as a probe gas and found that the 5 wt% had a modest increase in CO<sub>2</sub> solubility, increasing 5.9 mg g<sup>-1</sup> up to 6.9 mg g<sup>-1</sup>, an increase of 17%.

To further explain why the liquid does not enter the pores of the MOC, they performed MD simulations, and found that there was a large energy barrier of  $238 \text{ kJ mol}^{-1}$  that would have to be overcome for the 15-crown-5 to enter the MOC.

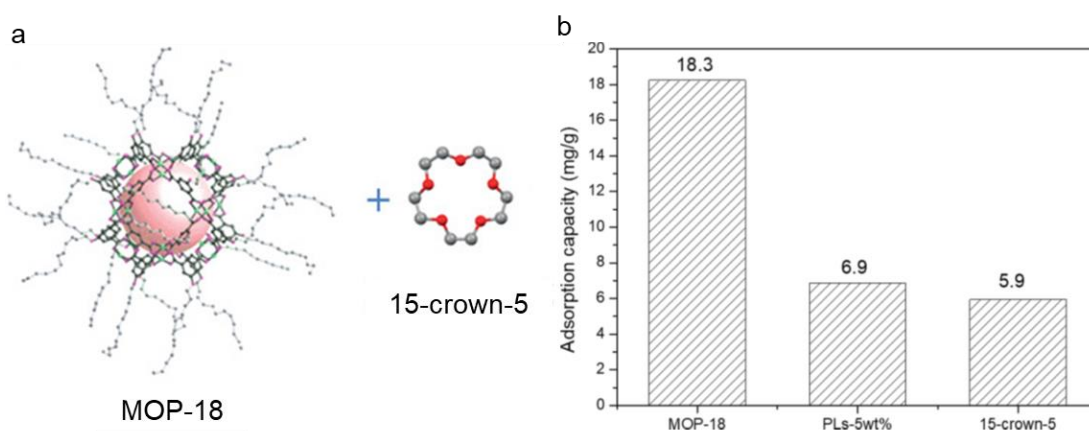


**Figure 1.20** a) the combination of MOC, MOP-18, and 15-crown-5 used to form a porous liquid. b) Gravimetric CO<sub>2</sub> solubility in MOP-18, 5 wt% PL, and 15-crown-5. Reproduced with permissions from (83).

### 1.4.3 Type 3 Porous Liquids

One of the earliest reports of a type 3 porous liquid was by Liu *et al.* in 2014 (Figure 1.21).<sup>73</sup> Their work was published prior to the first reported PL and was instead referred to as a hybrid adsorption-adsorption method. However, it does fit the criteria of a type 3 porous liquid. To create this porous liquid, a zeolitic imidazolate framework (ZIF), ZIF-8, was dispersed in ethylene glycol, and a mixture of ethylene glycol and 2-methylimidazole (MIm). Different solvent combinations were attempted but similar issues to previous porous liquid attempts were encountered, where solvents would fill the empty cavities. To probe the porosity of the liquid, a mixture of CO<sub>2</sub>, along with other gases, was introduced to observe selectivity. With the ZIF-8/glycol porous liquid, a large increase in CO<sub>2</sub> selectivity was observed, compared to neat solid ZIF-8, with a selectivity preference of CO<sub>2</sub>/H<sub>2</sub>, CO<sub>2</sub>/N<sub>2</sub>, and CO<sub>2</sub>/CH<sub>4</sub>. Furthermore, they note that selectivity was maintained through continued recycling. The addition of MIm into the porous liquid resulted in a significantly higher selectivity ratio of 951 for CO<sub>2</sub>/H<sub>2</sub>, 394 for CO<sub>2</sub>/N<sub>2</sub>, and 114 for CO<sub>2</sub>/CH<sub>4</sub>, respectively.

Another recent example reported by Shan *et al.* incorporated ionic liquids into type 3 porous liquids.<sup>85</sup> Ionic liquids are well known and are continually being investigated due to their ability to capture and store CO<sub>2</sub>.<sup>86,87</sup> Ionic liquids can be tailored to be sterically bulky, as well as having several additional benefits, such as low/no vapour pressure and being capable of dissolving organic/inorganic materials. This work

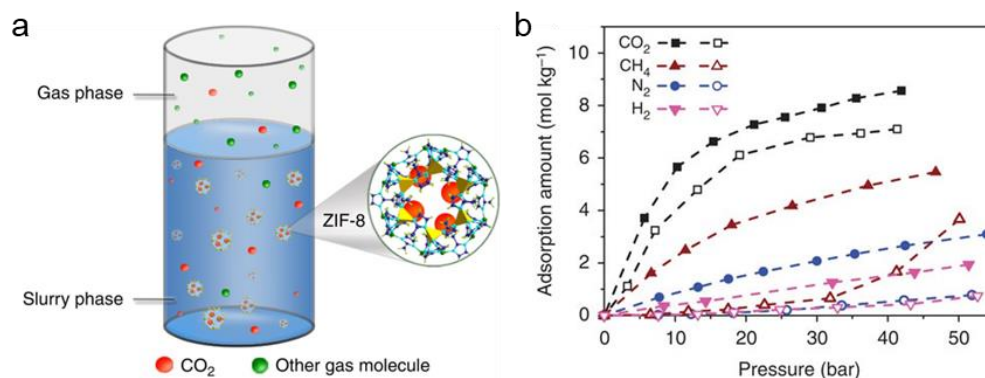


**Figure 1.21** a) Schematic of the type 3 PL produced from ZIF-8 and glycol solution; b) Adsorption isotherms of ZIF-8 (open symbols) and ZIF-8 PL (15 wt%) (closed symbols) with a variety of gases. Reproduced with permissions from (73).

utilised ZIF-8 dispersed in an ionic liquid, [DBU-PEG] [NTf<sub>2</sub>], with the main aim being to increase the CO<sub>2</sub> storage capacity. Porous liquids were prepared in various concentrations, ranging from 3.2 wt% up to a loading of 30.0 wt%, determined by thermogravimetric analysis (TGA). CO<sub>2</sub> sorption measurements were then carried out from 0 to 10 bar, and increased CO<sub>2</sub> uptakes for higher calculated loadings of ZIF-8 in the porous liquid were observed. Theoretical CO<sub>2</sub> adsorption capacities were also calculated, and the experimental values were all within 75% of the calculated uptake. Interestingly, experimental isotherms all exhibited broad desorption hysteresis, which the authors account to the adsorbed CO<sub>2</sub> in the porous liquid not being released immediately upon a decrease in pressure.

Since the first example of a type 3 PL, they are now arguably the most studied PL systems of the four.<sup>88</sup> This is likely due to the difficulty that can arise from trying to prepare type 1 systems, which there are very few examples of creating a neat liquid which can maintain its pores. There is also added complexity of type 2 systems, where a porous material has to be combined with a size-excluded solvent which must dissolve enough of the porous material to make a detectable change over that of the neat liquid, whereas type 3 systems do not have the solubility concerns and will need to be combined with a size-excluded solvent. This gives type 3 systems far more liquid options, though there are some limitations, such as the vapour pressure of the liquid, which has led to many commercially available options being utilised, such as organic oils and ionic liquids, rather than standard laboratory solvents.<sup>89</sup>

With this in mind, a recent study by Cahir *et al.* has shown the creation of over 90 PLs by combining 17 different MOFs with 16 different types of non-ionic liquids, such as silicone oils, triglyceride oils, and polyethylene glycols.<sup>90</sup> Many of these PL samples showed increased CO<sub>2</sub> and CH<sub>4</sub> capacity over that of the neat liquid, though porous

samples combined with PEG liquids displayed little to no improvement. This study also shows the difficulty in selecting liquids to combine with porous materials, as one would expect that if a solvent is size-excluded from a material, then a second material with a smaller aperture should also maintain an empty pore. This is not the case in this study. For example two MOFs in this study, HKUST-1 and ZIF-8 show enhanced CO<sub>2</sub> and CH<sub>4</sub> solubility with a majority of the oils, where the aperture for these MOFs are reported as 10 Å<sup>91</sup> and 3.4 Å,<sup>92</sup> respectively. Whereas, materials with pore apertures less than 10 Å show no improvement, which includes UiO-66 and ZIF-67, which have pore apertures of 6 Å<sup>93</sup> and 3.35 Å,<sup>94</sup> respectively. While the authors suggest that this occurs because of steric effects, there must be additional factors that are not yet known when developing PLs.

A similar study was also performed by Kai *et al.*, though rather than MOFs, they incorporated POCs with a combination of oils and ionic liquids (Figure 1.22).<sup>95</sup> Generally they displayed an increase of CO<sub>2</sub> solubility over the range of liquids attempted in the study, where silicone oil and ionic liquid, 1-butylpyridinium bis(trifluoromethanesulfonyl)imide ([BPy][NTf<sub>2</sub>]), produced CO<sub>2</sub> solubilities greater than two times that of the neat liquid. Interestingly, they also note how small changes of the liquid, for example, the movement of a methyl group in the ionic liquids tested, can result in a PL which has double the CO<sub>2</sub> solubility and the other produces very little increase. Interestingly, these ionic liquids were also used in a PL study in this thesis (Chapter 3) and found the opposite activity of the ionic liquids tested, hence there are factors that influence PLs that are still unknown due to the field being relatively new.

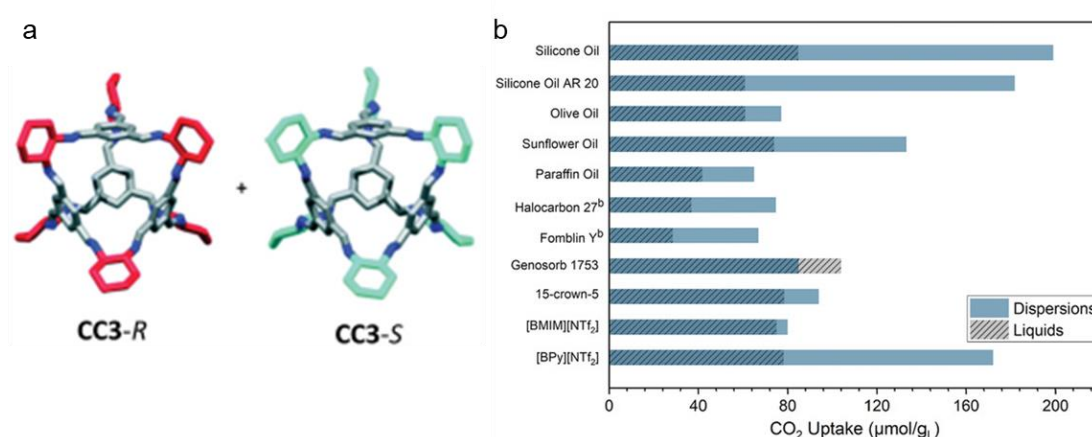


**Figure 1.22** a) Combination of **CC3-R** and **CC3-S** used in the formation of the PLs; b) Comparison of the CO<sub>2</sub> solubilities of the neat liquids versus the 12.5 wt% dispersion with the **CC3-R/CC3-S** mixture. Reproduced with permissions from (95).

#### 1.4.4 Type 4 Porous Liquids

Given the very recent expansion of the initially proposed types of PLs (1-3), to include another type of liquid known as type 4,<sup>75</sup> there are very few examples which fall into this category, though, like the previously mentioned PLs there may be older examples that fit this new definition. This new expanded definition of PLs is due to the transient nature of the pores and being a melting framework rather than a liquid created from discrete molecules or particles, meaning these type of system did not fit into the type 1-3 PL types.<sup>89</sup> The first report of this type of system was by Gaillac *et al.* who demonstrated the formation of a liquid zeolite, ZIF-4, which is composed of  $\text{Zn}(\text{Im})_4$  and tetrahedra linked by Zn-N coordination bonds (Figure 1.23).<sup>59</sup> Upon heating the material they note that there are minor changes in the material, where some of the coordination bonds break and undergo rapid interchange of metal-ligand coordination partners. This leads to an increase in accessible porosity, up to 95%, compared with the 74% which is accessible in the solid form, making this material coincide with the definition of a type 4 PL. As a side note, this material has also been previously shown to form glasses from melt-quenching,<sup>96</sup> which is discussed further in Chapter 4.

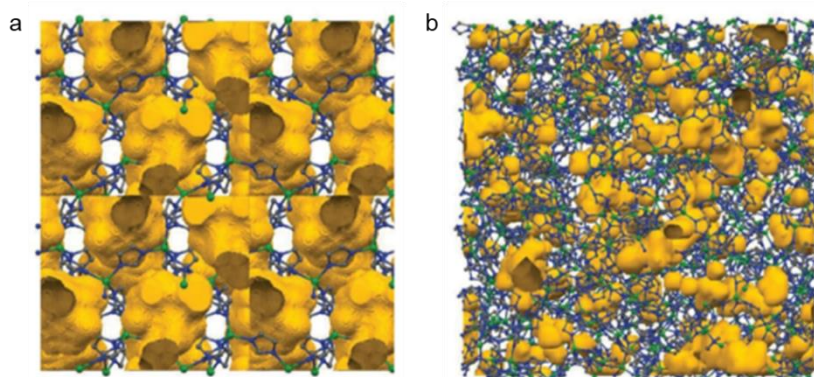


**Figure 1.23** a) Free volume in crystalline ZIF-4 obtained from the crystal structure; b) free volume in melt-quenched glass gained from modelling synchrotron and neutron total scattering data. Reproduced with permissions from (59).

#### 1.5 Photochromism

For some of the projects in this thesis, the aim was to incorporate stimuli-responsive components into POCs and PLs, creating the possibility of having dynamic systems capable of undergoing a change when exposed to an external stimulus. While there are many different types of stimuli-responsive molecules, which include temperature, pH, magnetic fields, and light, the decision was made to investigate components that respond to light, or photochromic molecules, due to the sensitivity of POCs to pH and temperature changes.

Photochromic molecules are widely used within the modern world with many people utilising their applications daily. These materials exist in various ways, including glass lenses, which are initially clear, that begin to turn dark after exposure to sunlight, as well as storage media, which allows rewritable features by employing two binary states of “0” and “1”.<sup>97</sup>

Photochromism is derived from the Greek words ‘photo’, meaning light, and ‘chroma’, meaning colour. Photochromism is defined as a reversible phototransformation of a chemical species between two forms which is exhibited by certain functional groups (Figure 1.24).<sup>98</sup> Switching from one isomer to another can cause a shift in the electronics between one another. Changes can be seen in the absorbance, causing the  $\lambda_{\max}$  to undergo a hypsochromic or bathochromic shift, refractive indices, dielectric constant and/or geometric structure.<sup>99</sup> Using light as a stimulus is particularly attractive as the response can be very quick and can be used at long distances due to the speed at which light travels. Light is also one of the most economical methods of inducing a change to a material, when compared to conventional methods such as heating or electrostatic stimulation. It is an unlimited energy source, and there are a range of light sources available with variable intensities, such as LEDs and xenon

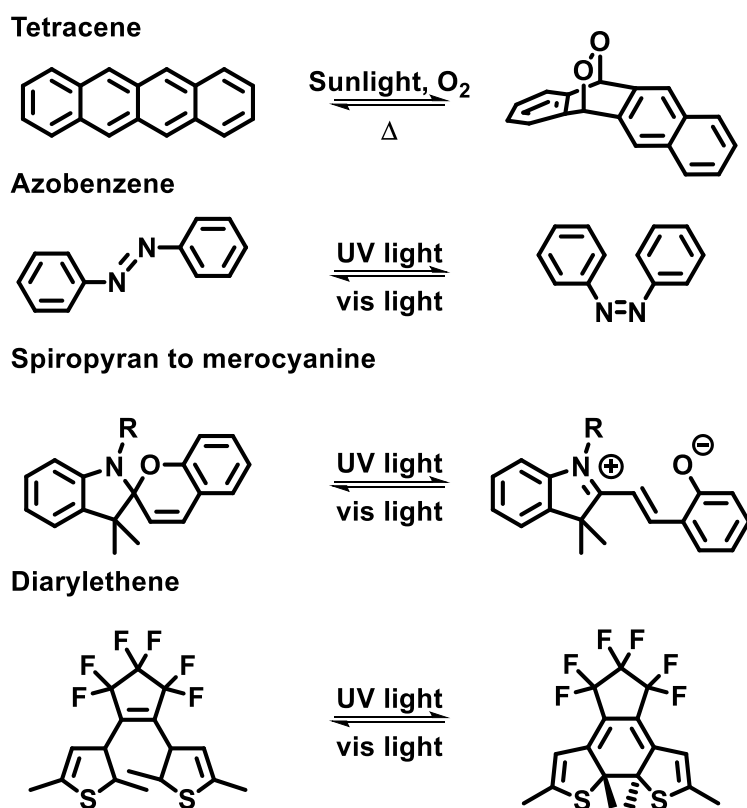


**Figure 1.24** Examples of photochromic reactions of tetracene, azobenzene, spiropyran and diarylethene.

lamps. One of the earliest references of photochromic behaviour dates back to approximately 356 BC, in the era of Alexander the Great. It is said that head warriors would wear photochromic bracelets so that they could coordinate their attacks when the colour of their bracelets would change.<sup>100</sup> One of the earliest reported materials capable of photochromic behaviour was by Fritsch in 1867.<sup>97</sup> In this report, they note how tetracene, which starts as an orange colour, becomes colourless when exposed to light and air after undergoing a photochemical [4+2]-cycloaddition with molecular oxygen (Figure 1.24, top). The initial colour can then be recovered if the sample is left in the dark.

Understanding the basic principle of photochromism can be described by using a model containing two molecular species, A and B, where A is the most stable isomer. This model assumes that these are the only species involved, where in some cases, like tetracene, other species may be involved.<sup>97</sup> The ease of converting one species to the other, and the stability of each species, depends on a potential barrier ( $\Delta E$ , Figure 1.25, a). Depending on the size of this barrier there are two possible scenarios. In the first, if the energy barrier is low, B can spontaneously revert to A, and can also be reverted by introducing thermal energy into the system. This is referred to as a *T-type* system. In the second, if the energy barrier is high, a bistable system is created and can only be reverted by photons ( $\lambda_B$ ). This is referred to as a *P-type* system.

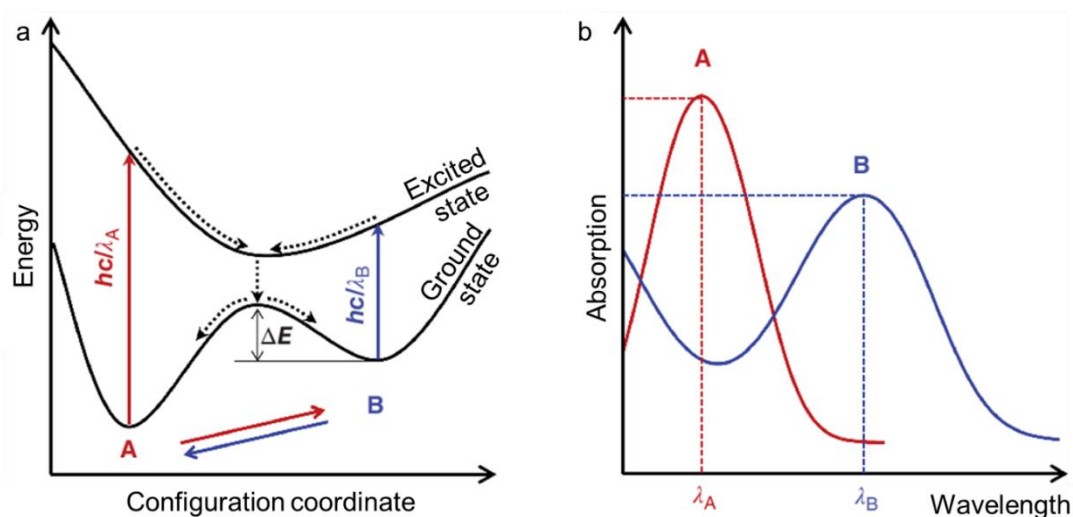


**Figure 1.25** Example of photoisomerisation between two molecules A and B: a) Potential energy diagram; b) related schematic absorption spectra. Reproduced with permissions from ref (97).

The absorption spectra of these systems have characteristic absorption bands which can determine the wavelength of light that is required to induce a transformation



(Figure 1.25, b). Typically, A will absorb in the UV region ( $\lambda_A$ ). When a photon is absorbed at the  $\lambda_A$ , A is excited from the ground state to the excited state, and yields B with a probability of  $\Phi_{A \rightarrow B}$  (where  $\Phi$  is the quantum yield, defined as the ratio of emitted photons versus photons absorbed by the system). The opposite is also true for B for reverting to A.

## 1.6 Photoresponsive Materials

Stimuli-responsive materials exist in our everyday lives, from the memory storage in phones, to the glasses on our faces. These types of materials also play an important role in nature and within our biological make-up which allows our bodies to function, from our eyes responding to light, or receptors on cell surfaces allowing our bodies to regulate themselves. Understanding and developing these materials not only broadens our knowledge of the subject but can also lead to new methods of drug and gene delivery.<sup>101,102</sup>

There has been an increase in popularity and research into incorporating stimuli-responsive behaviour into functional materials, moving away from static to more complex and dynamic systems. More recently, stimuli-responsive materials have gathered a lot more attention from a wider audience due to the 2016 Nobel Prize award in chemistry, which was presented to Sauvage, Stoddart and Feringa for their work towards molecular machines which ties together the core principles of supramolecular chemistry, stimuli-responsive materials, and fundamental science.<sup>103</sup> This prize collates the efforts of the design and synthesis of catenanes, which are mechanically interlocked molecules. These were reported by Sauvage in 1983.<sup>104</sup> Catenanes were later utilised by Stoddart to develop rotaxanes.<sup>105</sup> Again, these are mechanically interlocked molecules in which a macrocycle is threaded onto a thin molecular axis, like a dumbbell.<sup>105</sup> This concept was later developed into a molecular shuttle, where the macrocycle can move back and forth along the axle through electrochemical oxidation/reduction or pH-changes, which was reported by Stoddart and Sauvage in 1994.<sup>106,107</sup> Finally, molecular motors were developed in 1999 by Feringa.<sup>108</sup> In this publication they report the use of UV-light combined with heat, which causes an 'overcrowded' alkene to isomerise, producing a unidirectional rotation through cycles of light irradiation and thermal relaxation.

Since these milestone publications, many groups have set out to create a plethora of materials that are capable of undergoing stimuli-responsive transformations, including materials such as macrocycles, MOFs, and COFs. To date there is a continually growing number of publications relating to photoresponsive variants of

these materials, with applications including photocatalysis,<sup>109</sup> photochromic and thermochromic materials,<sup>110,111</sup> luminescent sensors for small molecules,<sup>112</sup> ion sensors,<sup>113</sup> selective gas uptake and release,<sup>114</sup> and gas separations.<sup>115</sup>

### 1.7 Incorporation of Photoresponsive Moieties

Photoresponsive moieties can be integrated into porous materials through several approaches.<sup>116</sup> The first method involves the addition of a photoresponsive guest molecule (Figure 1.26, a). In most cases of this approach, a known material is loaded with a photoactive guest, causing physical property changes in the host material which are imposed by the structural change of the guest.

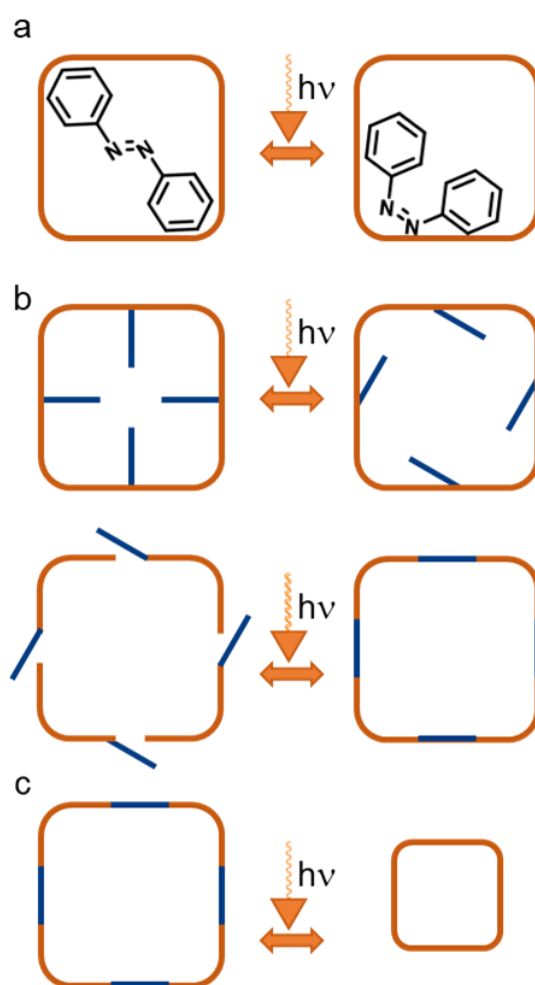


**Figure 1.26** Representation of the different methods of integration of a photoresponsive moiety into porous materials: a) loading with a photoactive guest; b) decorating with photoresponsive groups; c) inclusion of photoresponsive groups into the scaffold itself.

An excellent demonstration of this method in action was reported by Yanai *et al.*, who successfully loaded *trans*-azobenzene into the pores of a MOF,  $[\text{Zn}_2(\text{terephthalate})_2(\text{triethylenediamine})]_n$  (Figure 1.27).<sup>117</sup> On doing this, they were

able to determine that one azobenzene was present per unit cell. This causes the framework to change from a tetragonal structure when empty, to a distorted orthorhombic structure after the *trans*-azobenzene has been introduced. They were able to achieve almost two thirds isomerisation of *trans* → *cis*, which also caused a structure change back to the original tetragonal structure. Along with the structural changes that the azobenzene induced, very interesting gas sorption results were observed. When the azobenzene is in the *trans*-configuration, there is very little nitrogen uptake at 77 K. However, when the azobenzene is isomerised, an 8.3-fold increase was observed, demonstrating that N<sub>2</sub> was unable to fit in the pores with *trans*-azobenzene, but can fit on photoisomerisation.

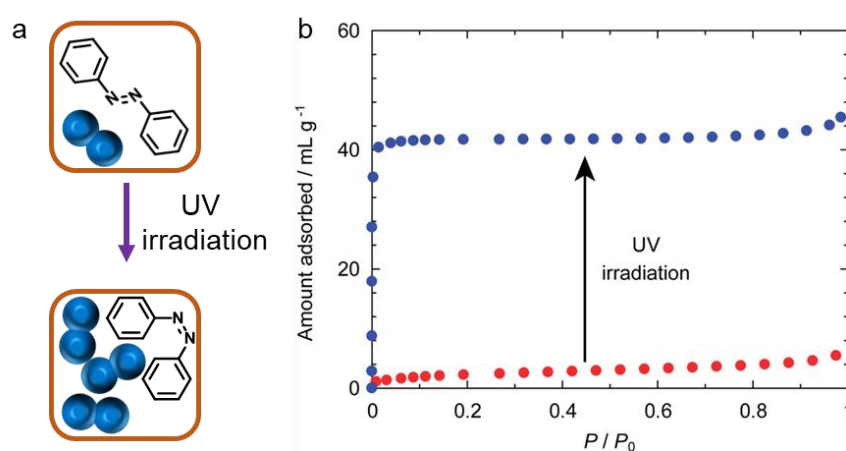


**Figure 1.27** a) Schematic of the concept of guest-to-host structural transition, where exposure to UV irradiation results in photoisomerisation and increases the amount of accessible pore volume; b) Adsorption isotherm of N<sub>2</sub> (77 K) of the MOF loaded with azobenzene before and after UV irradiation. Reproduced with permissions from ref (117).

In similar work, Lyndon *et al.* report the incorporation of diarylethene into a porous aromatic framework, PAF-1 (Figure 1.28).<sup>118</sup> PAF-1 is produced via a cross-coupling reaction of 1,5-cyclooctadiene with 2,2'-bipyridyl, and is one of the most porous PAF materials with BET surface areas of up to 5600 m<sup>2</sup> g<sup>-1</sup>, as well as exhibiting high thermal stability. Here, they show how diarylethene can be combined with PAF-1, which has an uptake that can range from 1 to 50 wt%, with a trade-off between total CO<sub>2</sub> uptake from steric competition and photodynamic release of CO<sub>2</sub>. On loading with CO<sub>2</sub>, they observe an almost instantaneous release on exposing the material to UV light, where desorption capacities increase by 65% from 5 to 50 wt% at 1 bar within 4 minutes of irradiation.

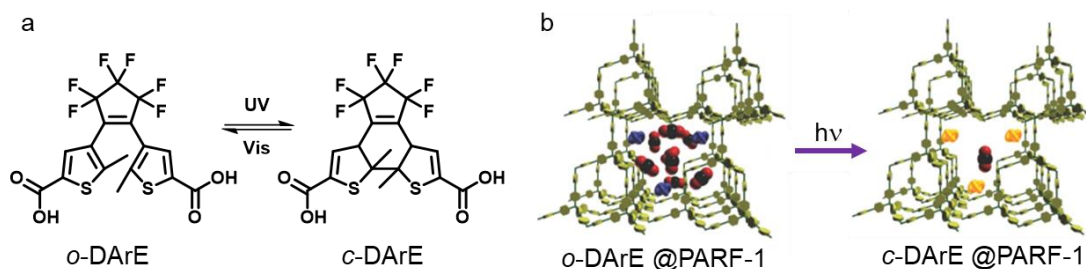


**Figure 1.28** MOF capable of photoswitching as a response to light, where a) structure of the open (*o*-DArE) and closed (*c*-DArE) diarylethene dye; b) MOF loaded with *o*-DArE which is capable of adsorbing CO<sub>2</sub> which is then released when exposed to UV light forming the *c*-DArE. Reproduced with permissions from ref (118).

Another alternative has been demonstrated by Lakmali *et al.*, where they incorporated a spiropyran, specifically spiroindolinobenzopyran, into a MOF, Zn-MOF-74 [Zn<sub>2</sub>(2,5-dihydroxyterephthalic acid)]<sub>n</sub> (Figure 1.29).<sup>119</sup> Spiroindolinobenzopyran in its solid form does not exhibit photo or thermochromism. However, once spiroindolinobenzopyran is loaded into MOF-74 by refluxing the mixture, a yellow/orange material is produced, due to a change in the absorption spectra, where the  $\lambda_{\text{max}}$  becomes more blue shifted. Once the material is heated to 80 °C, a colour change is observed from the yellow/orange to red crystals, indicating a change in the material has occurred and a change to the  $\lambda_{\text{max}}$  has occurred. These red crystals are then stable for several months when left in dark ambient conditions and can be converted back by UV irradiation.

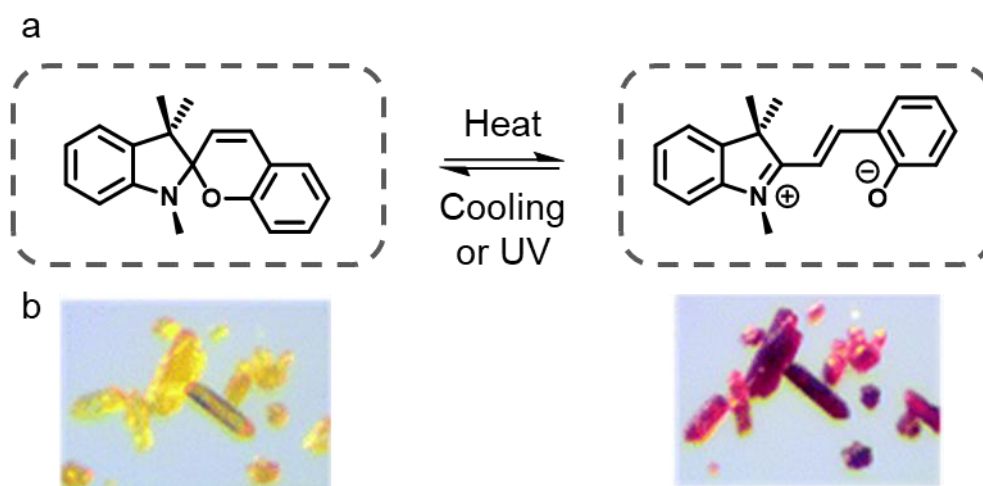


**Figure 1.29** a) Isomerisation of spiroindolinobenzopyran to merocyanine within Zn-MOF-74; b) Observed colour change of the corresponding loaded MOF crystals when heated and cooled or irradiated. Reproduced with permissions from ref (119).

Another method of incorporating a photoresponsive moiety is by decorating the material with photoresponsive groups, or by addition of photoresponsive auxiliary groups (Figure 1.26, b). This strategy utilises functional groups that are not key in the structure of the material, but rather bound in or out of the material. An example of this would be the pore being emptied and filled (or opened and closed), resulting in an increase and decrease in pore volume, or windows being opened and closed, either trapping or preventing molecules from exiting or entering the cavity. In both cases there should be minimal effect on the overall structure.

There are many examples of how researchers have incorporated these photoresponsive moieties as auxiliary groups. One such example was demonstrated by Brown *et al.*, which involves expanding and shrinking the pore size of a MOF (Figure 1.30).<sup>120</sup> They report the synthesis of a terphenyl linker with an auxiliary azobenzene group off of the centre ring, which when incorporated into the MOF, aligns into the pore of the framework. Unfortunately, they do not report any gas sorption analysis, other than the surface area. However, they do study the photoisomerisation effects using a dye, where propidium iodine is loaded into the material, and under ambient conditions no dye is released, but on exposure to UV light the dye is detected.

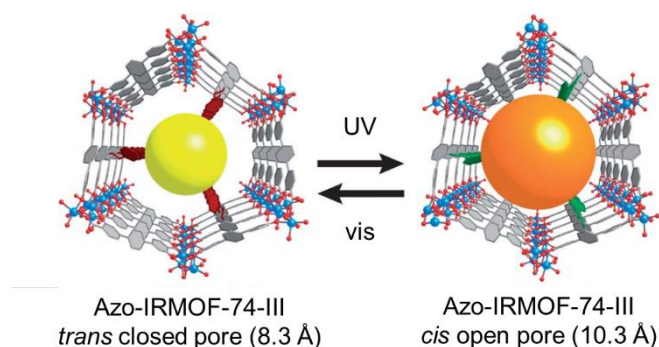


**Figure 1.30** Observed change in pore volume when the MOF is converted from its *trans* closed form to its *cis* open form. Reproduced with permissions from ref (120).

Park *et al.* described a similar MOF the year prior in 2012, but utilised the smaller linker terephthalic acid, rather than the terphenyl, again with an azobenzene attached to the side of the linker (Figure 1.31).<sup>121</sup> In this study, the produced MOF (PCN-123) had a significantly smaller pore size, allowing it to be used for small guest molecules, such as CO<sub>2</sub>. Prior to exposure, the material was capable of adsorbing 22.9 cm<sup>3</sup>g<sup>-1</sup> of CO<sub>2</sub> at 1 bar, which was successfully reduced to 16.8 cm<sup>3</sup>g<sup>-1</sup> after 1 hour of exposure to UV light, corresponding to a decrease of 26%. This is also shown by further irradiation experiments which resulted in a total decrease of ~54%, which corresponds to 10.5 cm<sup>3</sup>g<sup>-1</sup> of CO<sub>2</sub> after exposing the sample to UV light for an

additional 5 hours. The average pore size distribution also gives an insight into the change within the material, where the as-prepared material has a smaller average pore size of 10 Å, and after UV treatment this increases to 11 Å.

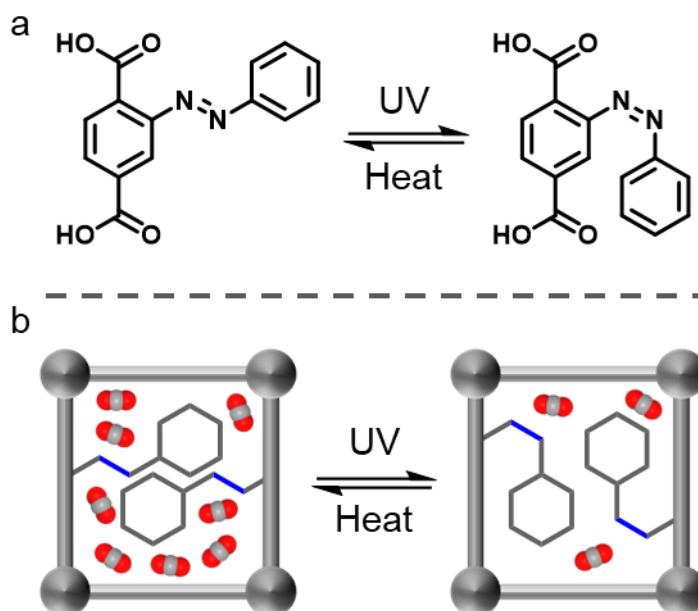


**Figure 1.31** a) Photoisomerisation of 2-(phenyldiazenyl)terephthalate ligand used to produce PCN-123; b) Diagram illustrating the change in CO<sub>2</sub> capacity upon photoisomerisation.<sup>121</sup>

Finally, the last method that can be utilised to incorporate photoresponsive components into materials, is by adding functionality directly into the molecular structure itself (Figure 1.26, c), for example, through the incorporation of photoresponsive linkers into a MOF.

An example of this was reported by Chen *et al.*, wherein they report the synthesis of a triply interpenetrated MOF.<sup>122</sup> In this work they showed the synthesis of a mixed-linker MOF using 4,4'-azobenzene dicarboxylate and bis(4-pyridyl)ethylene, which proved to be successful in gas sorption and showed selectivity for H<sub>2</sub>/CO and CO<sub>2</sub>/CH<sub>4</sub>. However, after producing a framework made from two known and well-studied responsive ligands, they performed no further studies to investigate the photoresponsive behaviour. Fast forward several years and the full potential was discovered by Lyndon *et al.*, where they studied the photoresponsive activity, and utilise this and its effects for gas sorption.<sup>114</sup> In this instance, the MOF creates a pillared structure, which when exposed to UV light causes the framework to compress, almost as if it's being squeezed. This creates a desirable effect and makes the material very responsive to light stimulation. This was demonstrated through a variety of dynamic and static experiments where a decrease of 42% can be seen for

CO<sub>2</sub> uptake under static irradiation, and instantaneous release under dynamic conditions, where a decrease of 64% is measured.

## 1.8 Thesis Summary

While this introduction is broad, reviewing the literature has showed that many materials orbit around trying to introduce free space into molecules and materials, as pores or cavities. Research in these areas has been ground-breaking, with many reports of designing materials and proving that they can be a reality. The recent successes in commercialisation with some of these materials is a promising sign that these can go beyond the fume hood and can become part of our everyday lives.

Chapter 2, *Synthesis of Azobenzene-Derived Organic Cages* - Since the discovery of organic cages, the focus has primarily been developing new cages building off previously reported architecture, creating different sizes and topologies. In this chapter, computational modelling is combined with laboratory experimentation to develop cages that are capable of undergoing a structural change, as a response to light by incorporating photochromic molecules into the scaffold of the cage.

Chapter 3, *Photoresponsive Type III Porous Liquids*, presents the development of creating a new PL by incorporating a photoresponsive porous material as one of the components to make the PL. Until now, PLs have used similar release mechanisms to remove gas from within the material which includes temperature and pressure swings, sonication or chemical displacement. This chapter aims to explore the possibility of a new release mechanism, focusing on light as a trigger to remove gas from the PL.

Chapter 4, *Melt-Quenched Porous Organic Cage Glasses*, focuses on investigating the possibility of melting POCs to become type 1 PLs, which so far, have only been achievable by using MOCs. While some melting cages have been reported, there have been no further investigations into the liquid state of these materials.

## 1.9 References

- 1 J. R. Holst, A. Trewin and A. I. Cooper, *Nat. Chem.*, 2010, **2**, 915–920.
- 2 S. Kitagawa, *Angew. Chemie Int. Ed.*, 2015, **54**, 10686–10687.
- 3 S. L. James, *Chem. Soc. Rev.*, 2003, **32**, 276–288.
- 4 J. P. Sculley, J.-R. Li, J. Park, W. Lu and H.-C. J. Zhou, *Sustain. Technol. Syst. Policies*, 2012, **2012**, 16.
- 5 A. P. Côté, A. I. Benin, N. W. Ockwig, M. O’Keeffe, A. J. Matzger and O. M. Yaghi, *Science.*, 2005, **310**, 5751, 1166–1170.
- 6 T. Tozawa, J. T. A. A. Jones, S. I. Swamy, S. Jiang, D. J. Adams, S. Shakespeare, R. Clowes, D. Bradshaw, T. Hasell, S. Y. Chong, C. Tang, S. Thompson, J. Parker, A. Trewin, J. Bacsa, A. M. Z. Z. Slawin, A. Steiner and A. I. Cooper, *Nat. Mater.*, 2009, **8**, 973–978.
- 7 M. A. Little and A. I. Cooper, *Adv. Funct. Mater.*, 2020, **30**, 1909842.
- 8 N. Giri, M. G. Del Pópolo, G. Melaugh, R. L. Greenaway, K. Rätzke, T. Koschine, L. Pison, M. F. C. Gomes, A. I. Cooper and S. L. James, *Nature*, 2015, **527**, 216–220.
- 9 K. S. W. Sing, D. H. Everett, R. A. W. Haul, L. Moscou, R. A. Pierotti, J. Rouquerol and T. Siemieniowska, *Pure Appl. Chem.*, 1985, **57**, 603–619.
- 10 B. D. Zdravkov, J. J. Čermák, M. Šefara and J. Janků, *Cent. Eur. J. Chem.*, 2007, **5**, 385–395.
- 11 F. Çeçen and Ö. Aktaş, in *Activated Carbon for Water and Wastewater Treatment*, Wiley-VCH Verlag GmbH & Co. KGaA, Weinheim, Germany, 2011, pp. 1–11.
- 12 S. J. Allen, L. Whitten and G. Mckay, *Dev. Chem. Eng. Miner. Process.*, 2008, **6**, 231–261.
- 13 A. E. Ogungbenro, D. V. Quang, K. A. Al-Ali, L. F. Vega and M. R. M. Abu-Zahra, *J. Environ. Chem. Eng.*, 2018, **6**, 4245–4252.
- 14 M. B. Ahmed, M. A. Hasan Johir, J. L. Zhou, H. H. Ngo, L. D. Nghiem, C. Richardson, M. A. Moni and M. R. Bryant, *J. Clean. Prod.*, 2019, **225**, 405–413.
- 15 S. Wong, N. Ngadi, I. M. Inuwa and O. Hassan, *J. Clean. Prod.*, 2018, **175**,



361–375.

- 16 F. Rodríguez-Reinoso, *Carbon N. Y.*, 1998, **36**, 159–175.
- 17 W. M. T. M. Reimerink, *Stud. Surf. Sci. Catal.*, 1999, **120 A**, 751–769.
- 18 A. G. Slater and A. I. Cooper, *Science*, 2015, **348**, 6238, aaa8075.
- 19 M. E. Davis, *Nature*, 2002, **417**, 813–821.
- 20 H. Furukawa, Y. B. Go, N. Ko, Y. K. Park, F. J. Uribe-Romo, J. Kim, M. O’Keeffe and O. M. Yaghi, *Inorg. Chem.*, 2011, **50**, 9147–9152.
- 21 S. Yuan, L. Zou, J. S. Qin, J. Li, L. Huang, L. Feng, X. Wang, M. Bosch, A. Alsalmé, T. Cagin and H. C. Zhou, *Nat. Commun.*, 2017, **8**, 1–10.
- 22 K. E. Jelfs and A. I. Cooper, *Curr. Opin. Solid State Mater. Sci.*, 2013, **17**, 19–30.
- 23 G. Zhang and M. Mastalerz, *Chem. Soc. Rev.*, 2014, **43**, 1934–1947.
- 24 M. J. Bojdys, M. E. Briggs, J. T. A. Jones, D. J. Adams, S. Y. Chong, M. Schmidtman and A. I. Cooper, *J. Am. Chem. Soc.*, 2011, **133**, 16566–16571.
- 25 N. Giri, C. E. Davidson, G. Melaugh, M. G. Del Pópolo, J. T. A. Jones, T. Hasell, A. I. Cooper, P. N. Horton, M. B. Hursthouse and S. L. James, *Chem. Sci.*, 2012, **3**, 2153–2157.
- 26 G. Melaugh, N. Giri, C. E. Davidson, S. L. James and M. G. Del Pópolo, *Phys. Chem. Chem. Phys.*, 2014, **16**, 9422–9431.
- 27 J. T. A. Jones, T. Hasell, X. Wu, J. Bacsá, K. E. Jelfs, M. Schmidtman, S. Y. Chong, D. J. Adams, A. Trewin, F. Schiffman, F. Cora, B. Slater, A. Steiner, G. M. Day and A. I. Cooper, *Nature*, 2011, **474**, 367–371.
- 28 T. Hasell, S. Y. Chong, K. E. Jelfs, D. J. Adams and A. I. Cooper, *J. Am. Chem. Soc.*, 2012, **134**, 588–598.
- 29 S. Jiang, J. T. A. Jones, T. Hasell, C. E. Blythe, D. J. Adams, A. Trewin and A. I. Cooper, *Nat. Commun.*, 2011, **2**, 1–7.
- 30 M. Eddaoudi, J. Kim, N. Rosi, D. Vodak, J. Wachter, M. O’Keeffe and O. M. Yaghi, *Science*, 2002, **295**, 469–472.
- 31 A. E. Baumann, D. A. Burns, B. Liu and V. S. Thoi, *Commun. Chem.*, 2019, **2**, 1–14.

- 32 D. Kim, X. Liu and M. S. Lah, *Inorg. Chem. Front.*, 2015, **2**, 336–360.
- 33 R. L. Greenaway, V. Santolini, M. J. Bennison, B. M. Alston, C. J. Pugh, M. A. Little, M. Miklitz, E. G. B. Eden-Rump, R. Clowes, A. Shakil, H. J. Cuthbertson, H. Armstrong, M. E. Briggs, K. E. Jelfs and A. I. Cooper, *Nat. Commun.*, 2018, **9**, 1–11.
- 34 V. Santolini, M. Miklitz, E. Berardo and K. E. Jelfs, *Nanoscale*, 2017, **9**, 5280–5298.
- 35 K. E. Jelfs, X. Wu, M. Schmidtman, J. T. A. Jones, J. E. Warren, D. J. Adams and A. I. Cooper, *Angew. Chemie Int. Ed.*, 2011, **50**, 10653–10656.
- 36 M. Mastalerz, *Acc. Chem. Res.*, 2018, **51**, 2411–2422.
- 37 M. E. Briggs, K. E. Jelfs, S. Y. Chong, C. Lester, M. Schmidtman, D. J. Adams and A. I. Cooper, *Cryst. Growth Des.*, 2013, **13**, 4993–5000.
- 38 T. Hasell and A. I. Cooper, *Nat. Rev. Mater.*, 2016, **1**, 16053.
- 39 A. G. Slater, M. A. Little, A. Pulido, S. Y. Chong, D. Holden, L. Chen, C. Morgan, X. Wu, G. Cheng, R. Clowes, M. E. Briggs, T. Hasell, K. E. Jelfs, G. M. Day and A. I. Cooper, *Nat. Chem.*, 2017, **9**, 17–25.
- 40 D. Chakraborty and P. S. Mukherjee, *Chem. Commun.*, 2022, **58**, 5558–5573.
- 41 J. L. Culshaw, G. Cheng, M. Schmidtman, T. Hasell, M. Liu, D. J. Adams and A. I. Cooper, *J. Am. Chem. Soc.*, 2013, **135**, 10007–10010.
- 42 S. I. Swamy, J. Bacsá, J. T. A. Jones, K. C. Stylianou, A. Steiner, L. K. Ritchie, T. Hasell, J. A. Gould, A. Laybourn, Y. Z. Khimyak, D. J. Adams, M. J. Rosseinsky and A. I. Cooper, *J. Am. Chem. Soc.*, 2010, **132**, 12773–12775.
- 43 M. Liu, M. A. Little, K. E. Jelfs, J. T. A. Jones, M. Schmidtman, S. Y. Chong, T. Hasell and A. I. Cooper, *J. Am. Chem. Soc.*, 2014, **136**, 7583–7586.
- 44 M. A. Mohamed, K. ichi Yamada and K. Tomioka, *Tetrahedron Lett.*, 2009, **50**, 3436–3438.
- 45 A. S. Bhat, S. M. Elbert, W. S. Zhang, F. Rominger, M. Dieckmann, R. R. Schröder and M. Mastalerz, *Angew. Chemie Int. Ed.*, 2019, **58**, 8819–8823.
- 46 M. W. Schneider, I. M. Oppel, H. Ott, L. G. Lechner, H. J. S. Hauswald, R. Stoll and M. Mastalerz, *Eur. J. Chem.*, 2012, **18**, 836–847.

- 47 M. Mastalerz, M. W. Schneider, I. M. Oppel and O. Presly, *Angew. Chemie - Int. Ed.*, 2011, **50**, 1046–1051.
- 48 H. Ding, Y. Yang, B. Li, F. Pan, G. Zhu, M. Zeller, D. Yuan and C. Wang, *Chem. Commun.*, 2015, **51**, 1976–1979.
- 49 Y. Jin, B. A. Voss, A. Jin, H. Long, R. D. Noble and W. Zhang, *J. Am. Chem. Soc.*, 2011, **133**, 6650–6658.
- 50 M. Liu, L. Zhang, M. A. Little, V. Kapil, M. Ceriotti, S. Yang, L. Ding, D. L. Holden, R. Balderas-Xicohténcatl, D. He, R. Clowes, S. Y. Chong, G. Schütz, L. Chen, M. Hirscher and A. I. Cooper, *Science*, 2019, **366**, 6465, 613–620.
- 51 C. M. Simon, R. Mercado, S. K. Schnell, B. Smit and M. Haranczyk, *Chem. Mater.*, 2015, **27**, 4459–4475.
- 52 L. Chen, P. S. Reiss, S. Y. Chong, D. Holden, K. E. Jelfs, T. Hasell, M. A. Little, A. Kewley, M. E. Briggs, A. Stephenson, K. M. Thomas, J. A. Armstrong, J. Bell, J. Busto, R. Noel, J. Liu, D. M. Strachan, P. K. Thallapally and A. I. Cooper, *Nat. Mater.*, 2014, **13**, 954–960.
- 53 J. H. Zhang, S. M. Xie, L. Chen, B. J. Wang, P. G. He and L. M. Yuan, *Anal. Chem.*, 2015, **87**, 7817–7824.
- 54 K. Acharyya and P. S. Mukherjee, *Chem. Commun.*, 2014, **50**, 15788–15791.
- 55 N. Stock and S. Biswas, *Chem. Rev.*, 2012, **112**, 933–969.
- 56 M. E. Briggs and A. I. Cooper, *Chem. Mater.*, 2017, **29**, 149–157.
- 57 B. D. Egleston, M. C. Brand, F. Greenwell, M. E. Briggs, S. L. James, A. I. Cooper, D. E. Crawford and R. L. Greenaway, *Chem. Sci.*, 2020, **11**, 6582–6589.
- 58 M. E. Briggs, A. G. Slater, N. Lunt, S. Jiang, M. A. Little, R. L. Greenaway, T. Hasell, C. Battilocchio, S. V. Ley and A. I. Cooper, *Chem. Commun.*, 2015, **51**, 17390–17393.
- 59 R. Gaillac, P. Pullumbi, K. A. Beyer, K. Chapman, D. A. Keen, T. D. Bennett and F. X. Coudert, *Nat. Mater.*, 2017, **16**, 1149–1155.
- 60 T. D. Bennett, Y. Yue, P. Li, A. Qiao, H. Tao, N. G. Greaves, T. Richards, G. I. Lampronti, S. A. T. Redfern, F. Blanc, O. K. Farha, J. T. Hupp, A. K. Cheetham and D. A. Keen, *J. Am. Chem. Soc.*, 2016, **138**, 3484–3492.

- 61 H. Yin, Y. Z. Chua, B. Yang, C. Schick, W. J. Harrison, P. M. Budd, M. Böhning and A. Schönhals, *J. Phys. Chem. Lett.*, 2018, **9**, 2003–2008.
- 62 F. W. Knobloch and W. H. Rauscher, *J. Polym. Sci.*, 1959, **38**, 261–262.
- 63 H. Li, M. Eddaoudi, M. O’Keeffe and O. M. Yaghi, *Nature*, 1999, **402**, 276–279.
- 64 S. Kitagawa, R. Kitaura and S. I. Noro, *Angew. Chemie Int. Ed.*, 2004, **43**, 2334–2375.
- 65 J. Liu, P. K. Thallapally, B. P. Mc Grail, D. R. Brown and J. Liu, *Chem. Soc. Rev.*, 2012, **41**, 2308–2322.
- 66 J. H. Cavka, S. Jakobsen, U. Olsbye, N. Guillou, C. Lamberti, S. Bordiga and K. P. Lillerud, *J. Am. Chem. Soc.*, 2008, **130**, 13850–13851.
- 67 S. M. Moosavi, A. Nandy, K. M. Jablonka, D. Ongari, J. P. Janet, P. G. Boyd, Y. Lee, B. Smit and H. J. Kulik, *Nat. Commun.*, 2020, **11**, 4068.
- 68 P. Rocío-Bautista, I. Taima-Mancera, J. Pasán and V. Pino, *Sep. 2019, Vol. 6, Page 33*, 2019, **6**, 33.
- 69 S. Bagi, S. Yuan, S. Rojas-Buzo, Y. Shao-Horn and Y. Román-Leshkov, *Green Chem.*, 2021, **23**, 9982–9991.
- 70 D. Crawford, J. Casaban, R. Haydon, N. Giri, T. McNally and S. L. James, *Chem. Sci.*, 2015, **6**, 1645–1649.
- 71 H. Furukawa, K. E. Cordova, M. O’Keeffe and O. M. Yaghi, *Science*, 2013, **341**, 6149, 123044.
- 72 S. Yuan, L. Feng, K. Wang, J. Pang, M. Bosch, C. Lollar, Y. Sun, J. Qin, X. Yang, P. Zhang, Q. Wang, L. Zou, Y. Zhang, L. Zhang, Y. Fang, J. Li, H.-C. Zhou, S. Yuan, L. Feng, K. Wang, J. Pang, M. Bosch, C. Lollar, Y. Sun, J. Qin, X. Yang, P. Zhang, Q. Wang, L. Zou, Y. Zhang, L. Zhang, Y. Fang, J. Li and H. Zhou, *Adv. Mater.*, 2018, **30**, 1704303.
- 73 H. Liu, B. Liu, L. C. Lin, G. Chen, Y. Wu, J. Wang, X. Gao, Y. Lv, Y. Pan, X. X. Zhang, X. X. Zhang, L. Yang, C. Sun, B. Smit and W. Wang, *Nat. Commun.*, 2014, **5**, 1–7.
- 74 N. O’Reilly, N. Giri and S. L. James, *Eur. J. Chem.*, 2007, **13**, 3020–3025.
- 75 T. D. Bennett, F. X. Coudert, S. L. James and A. I. Cooper, *Nat. Mater.*, 2021, **20**, 1179–1187.

- 76 J. Zhang, S.-H. Chai, Z.-A. Qiao, S. M. Mahurin, J. Chen, Y. Fang, S. Wan, K. Nelson, P. Zhang and S. Dai, *Angew. Chemie*, 2015, **127**, 946–950.
- 77 B. Lai, J. Cahir, M. Y. Tsang, J. Jacquemin, D. Rooney, B. Murrer and S. L. James, *ACS Appl. Mater. Interfaces*, 2021, **13**, 932–936.
- 78 B. D. Egleston, K. V. Luzyanin, M. C. Brand, R. Clowes, M. E. Briggs, R. L. Greenaway and A. I. Cooper, *Angew. Chemie Int. Ed.*, 2020, **59**, 7362–7366.
- 79 A. B. Bourlinos, R. Herrera, N. Chalkias, D. D. Jiang, Q. Zhang, L. A. Archer and E. P. Giannelis, *Adv. Mater.*, 2005, **17**, 234–237.
- 80 N. J. Fernandes, T. J. Wallin, R. A. Vaia, H. Koerner and E. P. Giannelis, *Chem. Mater.*, 2014, **26**, 84–96.
- 81 L. Ma, C. J. E. Haynes, A. B. Grommet, A. Walczak, C. C. Parkins, C. M. Doherty, L. Longley, A. Tron, A. R. Stefankiewicz, T. D. Bennett and J. R. Nitschke, *Nat. Chem.*, 2020, **12**, 270–275.
- 82 R. L. Greenaway, D. Holden, E. G. B. Eden, A. Stephenson, C. W. Yong, M. J. Bennison, T. Hasell, M. E. Briggs, S. L. James and A. I. Cooper, *Chem. Sci.*, 2017, **8**, 2640–2651.
- 83 Z. Deng, W. Ying, K. Gong, Y.-J. Zeng, Y. Yan, X. Peng, Z. Deng, W. Ying, X. Peng, Y. Zeng, K. Gong and Y. Yan, *Small*, 2020, **16**, 1907016.
- 84 H. Furukawa, J. Kim, K. E. Plass and O. M. Yaghi, *J. Am. Chem. Soc.*, 2006, **128**, 8398–8399.
- 85 W. Shan, P. F. Fulvio, L. Kong, J. A. Schott, C. L. Do-Thanh, T. Tian, X. Hu, S. M. Mahurin, H. Xing and S. Dai, *ACS Appl. Mater. Interfaces*, 2018, **10**, 32–36.
- 86 M. Aghaie, N. Rezaei and S. Zendejboudi, *Renew. Sustain. Energy Rev.*, 2018, **96**, 502–525.
- 87 S. K. Shukla, S. G. Khokarale, T. Q. Bui and J. P. T. Mikkola, *Front. Mater.*, 2019, **6**, 42.
- 88 H. Mahdavi, S. J. D. Smith, X. Mulet and M. R. Hill, *Mater. Horizons*, 2022, **9**, 1577–1601.
- 89 B. D. Egleston, A. Mroz, K. E. Jelfs and R. L. Greenaway, *Chem. Sci.*, 2022, **13**, 5042–5054.
- 90 J. Cahir, M. Y. Tsang, B. Lai, D. Hughes, M. A. Alam, J. Jacquemin, D. Rooney

- and S. L. James, *Chem. Sci.*, 2020, **11**, 2077–2084.
- 91 C. H. Hendon and A. Walsh, *Chem. Sci.*, 2015, **6**, 3674–3683.
- 92 K. S. Park, Z. Ni, A. P. Côté, J. Y. Choi, R. Huang, F. J. Uribe-Romo, H. K. Chae, M. O’Keeffe and O. M. Yaghi, *Proc. Natl. Acad. Sci. U. S. A.*, 2006, **103**, 10186–10191.
- 93 J. Winarta, B. Shan, S. M. McIntyre, L. Ye, C. Wang, J. Liu and B. Mu, *Cryst. Growth Des.*, 2020, **20**, 1347–1362.
- 94 P. Krokidas, M. Castier and I. G. Economou, *J. Phys. Chem. C*, 2017, **121**, 17999–18011.
- 95 A. Kai, B. D. Egleston, A. Tarzia, R. Clowes, M. E. Briggs, K. E. Jelfs, A. I. Cooper and R. L. Greenaway, *Adv. Funct. Mater.*, 2021, **31**, 2106116.
- 96 T. D. Bennett, J. C. Tan, Y. Yue, E. Baxter, C. Ducati, N. J. Terrill, H. H. M. Yeung, Z. Zhou, W. Chen, S. Henke, A. K. Cheetham and G. N. Greaves, *Nat. Commun.*, 2015, **6**, 1–7.
- 97 H. Tian and J. Zhang, *Photochromic materials: Preparation, properties and applications*, 2016.
- 98 M. Irie, *Chem. Rev.*, 2000, **100**, 1683–1684.
- 99 N. Tamai and H. Miyasaka, *Chem. Rev.*, 2000, **100**, 1875–1890.
- 100 D. Nunes, A. Pimentel, L. Santos, P. Barquinha, L. Pereira, E. Fortunato and R. Martins, *Metal oxide nanostructures: Synthesis, properties and applications*, Elsevier, 2018.
- 101 E. R. Ruskowitz and C. A. Deforest, *Nat. Rev. Mater.*, 2018, **3**, 1–17.
- 102 Y. Zhou, H. Ye, Y. Chen, R. Zhu and L. Yin, *Biomacromolecules*, 2018, **19**, 1840–1857.
- 103 The 2016 Nobel Prize in Chemistry - Press release, <https://www.nobelprize.org/prizes/chemistry/2016/press-release/>, (accessed 19 November 2021).
- 104 C. O. Dietrich-Buchecker, J. P. Sauvage and J. P. Kintzinger, *Tetrahedron Lett.*, 1983, **24**, 5095–5098.
- 105 P. L. Anelli, N. Spencer and J. Fraser Stoddart, *J. Am. Chem. Soc.*, 1991, **113**,

5131–5133.

- 106 R. A. Bissell, E. Córdova, A. E. Kaifer and J. F. Stoddart, *Nature*, 1994, **369**, 133–137.
- 107 A. Livoreil, C. O. Dietrich-Buchecker and J. P. Sauvage, *J. Am. Chem. Soc.*, 1994, **116**, 9399–9400.
- 108 N. Koumura, R. W. J. Zijlstra, R. A. Van Delden, N. Harada and B. L. Feringa, *Nature*, 1999, **401**, 152–155.
- 109 P. Wu, M. Jiang, Y. Li, Y. Liu and J. Wang, *J. Mater. Chem. A*, 2017, **5**, 7833–7838.
- 110 S. Zhang, S. Zhang, N. Yin, Z. Huang, W. Xu, K. Yue, X. Li and D. Li, *ACS Appl. Mater. Interfaces*, 2021, **13**, 6430–6441.
- 111 L. Tom and M. R. P. Kurup, *J. Mater. Chem. C*, 2020, **8**, 2525–2532.
- 112 É. Whelan, F. W. Steuber, T. Gunnlaugsson and W. Schmitt, *Coord. Chem. Rev.*, 2021, **437**, 213757.
- 113 S. A. A. Razavi and A. Morsali, *Coord. Chem. Rev.*, 2020, **415**, 213299.
- 114 R. Lyndon, K. Konstas, B. P. Ladewig, P. D. Southon, P. C. J. Kepert and M. R. Hill, *Angew. Chemie Int. Ed.*, 2013, **52**, 3695–3698.
- 115 Z. Wang, A. Knebel, S. Grosjean, D. Wagner, S. Bräse, C. Wöll, J. Caro and L. Heinke, *Nat. Commun.*, 2016, **7**, 1–7.
- 116 C. L. Jones, A. J. Tansell and T. L. Easun, *J. Mater. Chem. A*, 2016, **4**, 6714–6723.
- 117 N. Yanai, T. Uemura, M. Inoue, R. Matsuda, T. Fukushima, M. Tsujimoto, S. Isoda and S. Kitagawa, *J. Am. Chem. Soc.*, 2012, **134**, 4501–4504.
- 118 R. Lyndon, K. Konstas, R. A. Evans, D. J. Keddie, M. R. Hill and B. P. Ladewig, *Adv. Funct. Mater.*, 2015, **25**, 4405–4411.
- 119 U. G. R. Lakmali and C. V. Hettiarachchi, *CrystEngComm*, 2015, **17**, 8607–8611.
- 120 J. W. Brown, B. L. Henderson, M. D. Kiesz, A. C. Whalley, W. Morris, S. Grunder, H. Deng, H. Furukawa, J. I. Zink, J. F. Stoddart and O. M. Yaghi, *Chem. Sci.*, 2013, **4**, 2858–2864.

- 121 J. Park, D. Yuan, K. T. Pham, J. R. Li, A. Yakovenko and H. C. Zhou, *J. Am. Chem. Soc.*, 2012, **134**, 99–102.
- 122 B. Chen, S. Ma, E. J. Hurtado, E. B. Lobkovsky and H. C. Zhou, *Inorg. Chem.*, 2007, **46**, 8490–8492.



## **Chapter 2**

# **Synthesis of Azobenzene-Derived Organic Cages**

## 2.1 Preface

Porous organic cages have only been reported within the past 14 years, and have since gathered a wide range of interest, with applications in molecular sensing, catalysis, molecular separations, gas storage and gas separations. Whilst research continues to find applications, the rate of discovery for new cages remains low, especially when compared to materials such as metal-organic frameworks. The design of new cages typically relies on a trial-and-error approach, with small incremental changes to known precursors leading to a relatively small pool of materials.

More recently, the design of organic cages has combined computational prediction with experimental methods to expand into a wider range of precursors, leading to a rapid acceleration in the rate at which cages are discovered. In this chapter, a new variety of azobenzene-derived organic cages have been explored with the aid of computational prediction, with the aim of producing organic cages that are capable of undergoing a structural change as a result of photoisomerisation.

The work within this chapter has been compiled and is being prepared for publication (M. C. Brand, J. T. Pegg, J. L. Greenfield, M. A. Little, N. Rankin, M. J. Fuchter, A. I. Cooper, K. E. Jelfs and R. L. Greenaway, *Photoresponsive Organic Cages – Computationally Driven Discovery of Azobenzene-Derived Organic Cages*).

Synthesis, characterisation, and analysis was carried out by M. Brand. Development of the photoreactor for NMR photoisomerisation was carried out by M. Brand and N. Rankin. Photoisomerisation studies were carried out by M. Brand and J. Greenfield using equipment in the laboratory of M. Fuchter. Computational studies were carried out by J. Pegg and K. Jelfs. X-ray crystallography was carried out by M. Little. Project guidance was provided by R. Greenaway and A. Cooper.

## 2.2 Discovery of Organic Cages

Organic cages can be synthesised using a variety of methods, typically involving reversible chemistries such as boronic ester formation and imine condensations, which allows for error-correction, enabling cages to self-assemble as the thermodynamic product.<sup>1</sup> Based on this, in principle, self-assembled organic cages should be fairly easy to synthesise. However, selecting the correct precursors to give the correct topology and geometry is the first problem to overcome, followed by a continuous battle of cage formation versus polymerisation, unwanted side-products, partial cage formation, and in some cases, catenation.<sup>2</sup> While widely investigated, the difficulties that are encountered during organic cage synthesis has resulted in a fairly slow rate of discovery, in comparison to materials such as MOFs (Figure 2.1). New cages are often based off known precursors with small incremental chemical modifications creating a small pool of materials, for example, 1,3,5-triformylbenzene has been used as a precursor in over 10 cages,<sup>3</sup> with new topologies being encountered at an even slower rate.<sup>4</sup> This results in the discovery of organic cages being a time-consuming, trial-and-error process, while selecting precursors and carefully tuning reaction conditions to favour the desired product, which may or may not be possible to even synthesise.

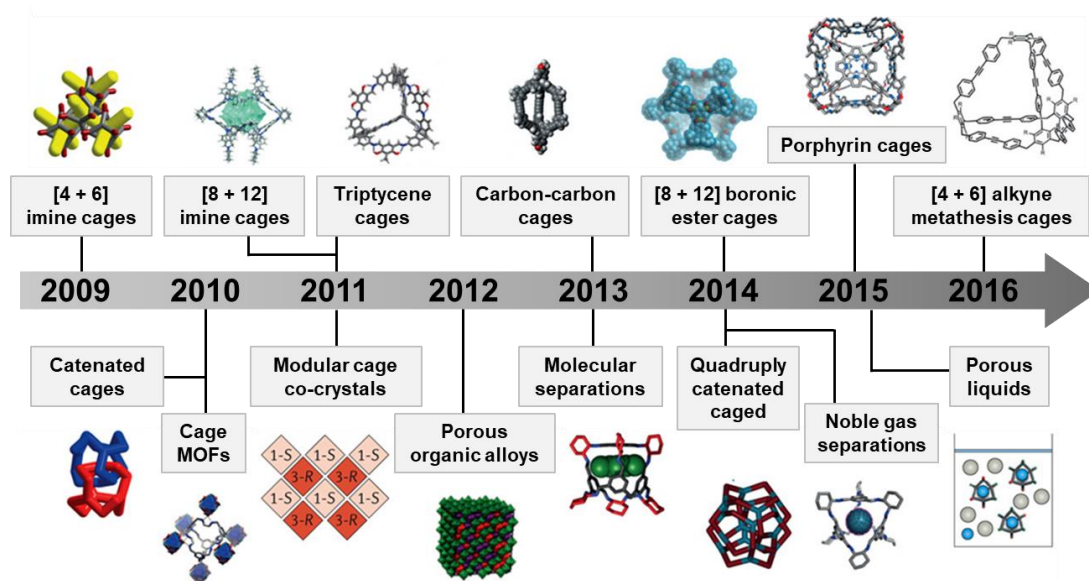


**Figure 2.1** A timeline of porous organic cages. Reproduced with permissions from ref (1).

One of the more recent advances in the development of organic cages has been the implementation of computational chemistry. Computational modelling can remove, or at least streamline, several of the experimental bottlenecks that can occur during the screening of these materials, the first being the time spent on the development of precursors that will yield a target POC. More extravagant precursors can be

expensive or may require complicated low-yielding, multi-step syntheses, which can be very time consuming.<sup>5</sup> The next step is testing and screening the precursors, which may result in wasted time and reagents if the desired cage reaction does not take place, if the target topology is not formed, or if a shape-persistent cage is not formed, and which may not be recoverable.

The use of computation aims to remove some of these factors from the experimental aspects of organic cage development.<sup>6</sup> By compiling a wide range of precursors that contain desirable functionality to create a precursor library,<sup>7</sup> suitable building blocks can then be selected that are synthetically viable and within the parameters of the final target cage. These precursors can be screened with a variety of other precursors to create energy-minimised models of potential organic cages. With the organic cages assembled, it is possible to then determine whether they are sterically feasible and shape-persistent in their lowest energy configuration, and what topology is most likely to form from a specific set of precursors. These steps provide a good indication of whether the reaction is worth pursuing experimentally, potentially saving time and costs.

A successful example of this hybrid experimental-computational workflow is by Greenaway *et al.*, who demonstrated the marriage of high-throughput methodologies and computational screening.<sup>8</sup> In this study, they build on previous work within the Cooper group, which predominantly focuses on the synthesis and applications of imine based organic cages, where an average of three new cage molecules are published each year, and there is approximately one new cage topology every three years. Here, they utilise the power of computational modelling with robotic automation and high-throughput characterisation techniques. Three triamines and 26 aldehydes were combined for a total of 78 combinations, which were all computationally screened, and the relative energies of each potential topology calculated for comparison (Figure 2.2). In total, 32 cages were synthesised, along with an additional 16 cages which were formed alongside unwanted side-products or contained unreacted starting material. This outcome demonstrates the power of cage prediction, which can provide extremely useful information regarding the lowest energy conformation, allowing the design to be adjusted to increase the likelihood of a successful reaction. It also shows a good success rate at predicting the lowest energy topology. However, there were also results which suggested that this protocol is not completely accurate and that there is a degree of unpredictability during the cage synthesis. In this chapter, a similar hybrid workflow was also used in the discovery of

azobenzene-derived organic cages, with back-and-forth experimentation outlined in Figure 2.3.

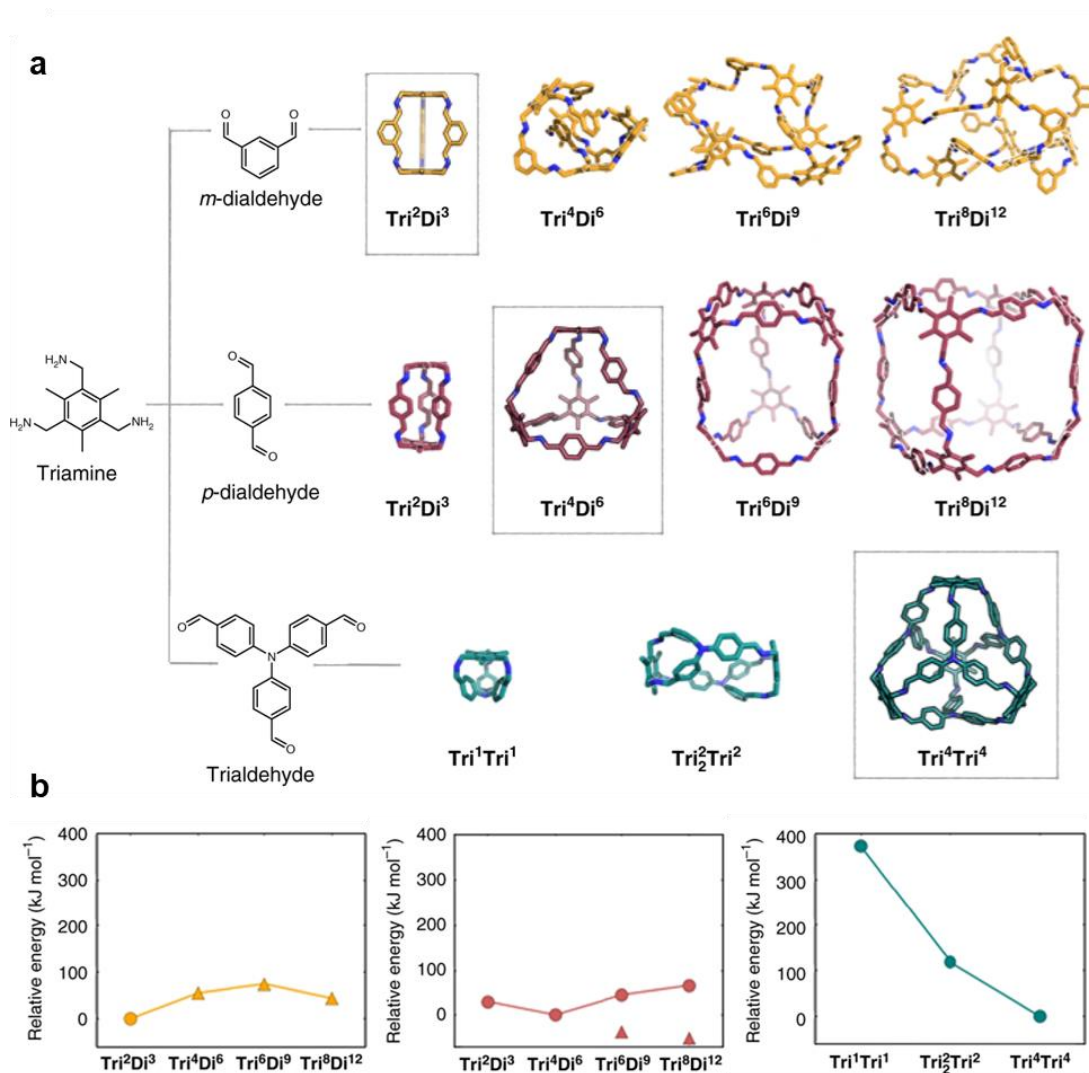


**Figure 2.2** a) Computationally assembled structures obtained by combining a tritopic amine (2,4,6-trimethylbenzene-1,3,5-triyl)trimethanamine), with ditopic aldehydes, isophthalaldehyde and terephthalaldehyde, and a tritopic aldehyde, tris(4-formylphenyl)amine; b) Relative internal energy plots versus the topology for the corresponding combinations. Reproduced with permissions from ref (8).

## 2.3 Azobenzene-Derived Organic Cages

### 2.3.1 Designing an Azobenzene-Derived Organic Cage

As mentioned previously, organic cages have been well studied for their applications in gas adsorption,<sup>9</sup> gas separations,<sup>10</sup> and chiral separations.<sup>11</sup> They have also been in the spotlight for their host-guest chemistry, such as when used as molecular sensors.<sup>12,13</sup> These applications have been largely focused on the intrinsic properties of these cages, rather than changes that occur due to a structural change of the cage

itself. Here, we try to design and synthesise a stimuli-responsive organic cage, based on imine chemistries, directly focusing on light-responsive or photochromic molecules as part of the cage structure, with the aim of ultimately creating an organic cage capable of a structural change on being irradiated with light.

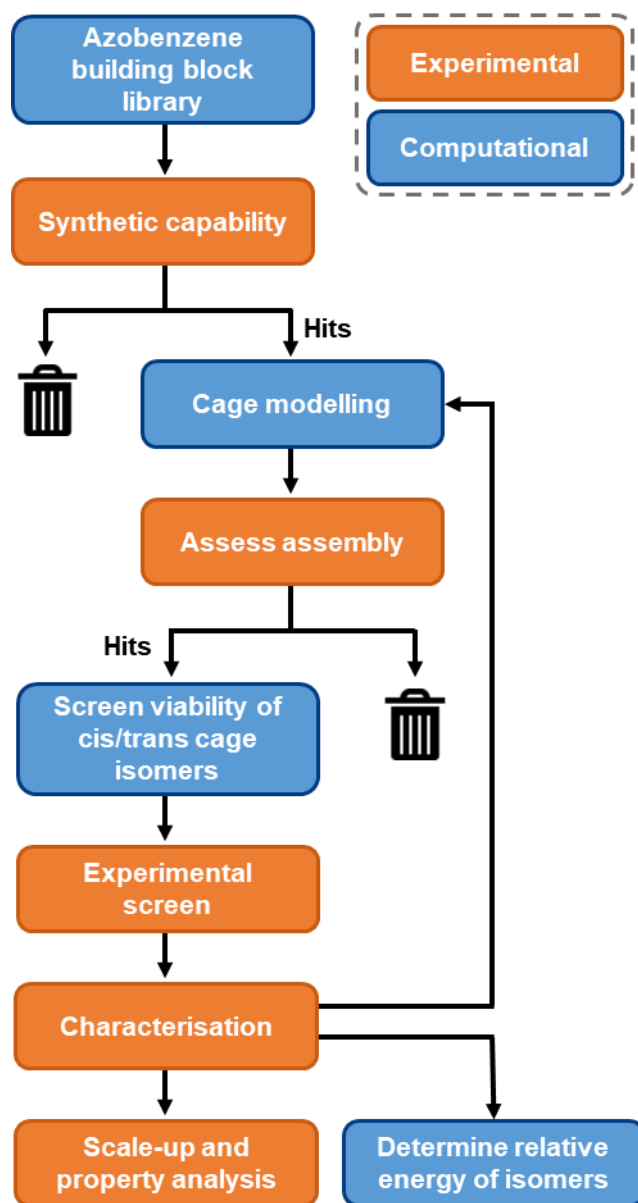


**Figure 2.3** Workflow for the discovery of azobenzene-derived organic cages, utilising the marriage of computational efforts with experimental guidance and modelling reiteration. Computational stages are shown in blue and experimental stages are shown in orange.

To begin, a decision had to be made on what type of photochromic molecule to try and incorporate within the cage structure. Of the few mentioned in 1.5, azobenzene derivatives were selected as the best option. Firstly, azobenzene-derived molecules are well studied with a variety of synthetic routes reported, providing many options to

create a wide range of precursors identified by a computational screen.<sup>14</sup> Secondly, the geometry and aromaticity of azobenzene also provides a good starting point with its similarities to previously reported organic cages, with aldehyde variants such as 1,1'-biphenyl and (*E*)-1,2-diphenylethene derived organic cages.<sup>15,16</sup> Comparatively, the Cooper group have previously found that aliphatic aldehyde variants have been far less successful in the synthesis of organic cages, arising from the increased degree of flexibility creating non-shape persistent cages, making them susceptible to collapse. Finally, azobenzene also exhibits a geometric change upon isomerisation, which should be capable of creating a significant structural change if it were successfully incorporated into a cage molecule.

A library of azobenzene-derived aldehydes as potential precursors was then compiled, performed by our computational collaborators. To create this library, Reaxys was searched for azobenzene-containing multi-topic and symmetrical aldehydes. This did not yield many results, and therefore, new molecules were also generated through the addition of diazene (N=N) functionality into previously reported aromatic cage precursors. For example, if a known precursor contained an alkyne, it would be swapped for a diazene, or if it contained biphenyl functionality, a diazene could be inserted in between the aromatic rings.

The azobenzene library was then pre-screened to select feasible precursors (*i.e.*, synthetically viable) before any cage modelling took place. As this collaborative effort was designed to try and simplify cage design and synthesis, any suggested molecules that would be particularly difficult or costly to synthesise, or required more than 5 synthetic steps to produce, were discarded. Finally, any molecules that contained incompatible or competing functional groups were also removed to prevent any undesired side reactions from occurring during the cage synthesis. This included precursors such as those with multiple diazene groups, to prevent the formation of both homo and hetero products severely reducing the yield of the desired product, hence the precursors that were selected focused on a singular diazene group. Additionally, precursors with both diazene and aniline functionality were also disregarded, this was to prevent any reaction of the aniline with nitroso intermediates and to avoid the use of anilines which have been far less successful than aliphatic amines in forming organic cages, and hence the focus primarily remained on trying to find suitable aldehydes with diazene functionality. Finally, any precursors with competing functional groups, such as additional aldehydes, ketones, amines, or nitro groups were removed from the pool of precursors to prevent unnecessary side reactions in addition to the cage reaction.

Using the azobenzene-derived aldehyde precursors that were accepted from the library, cage models were then built with a range of tritopic and ditopic amines that have previously been used for organic cage formation, using the *supramolecular toolkit (stk)*.<sup>17</sup> This is a Python framework developed by our collaborators for general supramolecular assembly that is able to produce models of complex supramolecular molecules such as cages, linear polymers, and COFs. To build molecular models in *stk*, the SMILES of building blocks are added into the script, and the functions then ensure these building blocks are correctly placed and connected to produce an idealised structure of a specified topology. This rapidly generates an initial structure which most likely does not represent the minimum on the potential energy surface (PES). Third party tools are then implemented, where *stk* is able to export this data into a format that is compatible with MacroModel for molecular dynamic simulations using the OPLS3 force field,<sup>18</sup> which has been shown to produce accurate representations of cages.<sup>8</sup> These simulations were performed at high temperature (750 K) for a total time of 200 ps with a timestep of 1 fs and structure samples taken every 4 ps, with each of these structures being geometry optimised. During these simulations the diazene bond angle was fixed to ensure they maintain either a *cis* or *trans* conformation. Of the samples taken, only the lowest energy conformation was used for further structural analysis.

### 2.3.2 Screening of Modelled Organic Cages

For the initial cage assemblies only the *trans* isomers were modelled, as they were going to be synthesised under dark conditions, where the *trans* isomer is the most stable isomer, rather than under constant irradiation to keep the azobenzene in their *cis* configuration. There are a few key aspects that need to be considered as to whether the predicted cage would be likely to form experimentally, mainly the strain of specific bonds and the overall strain of the cage.

The first signature bond to inspect is the imine bond. Imine bonds in cages typically exist in a planar configuration with the connecting aromatic ring, with previous cages showing little to no variation away from this configuration (Figure 2.4). Ideally this bond angle should be as close to 0° as possible to ensure the cage is the more favourable product, however some previous reported cages have found this imine bond to have a twist out of plane up to 10°. Many of the energy minimised models contained highly twisted imine bonds, with angles ranging up to 50°, which would be energetically unfavourable and therefore would be very unlikely to form cage.



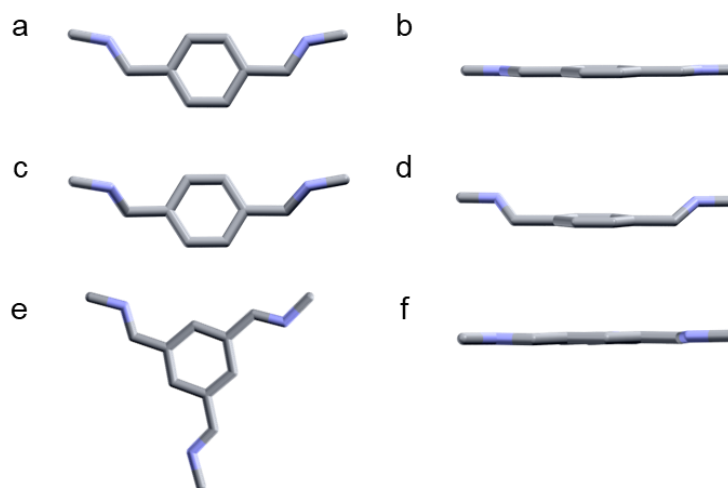


**Figure 2.4** Visual representations of imine bonds and an imine bond from a **CC3-R** crystal structure: a) an ideal configuration of an imine bond, created and energy minimised in CrystalMaker; b) as seen from the side; c) imine bonds with an unfavourable angle; d) as seen from the side; e) favourable planar imine bonds observed in the crystal structure of **CC3-R**; f) a side-on view. Some atoms and functional groups are removed for clarity.

In addition, the overall strain of the cage needs to be considered. In an ideal situation, the configuration of the components in the cage should be as close as possible to their precursors in their lowest energy conformation. For example, in a terphenyl molecule, the aromatic rings should all lay in the same plane (with the central ring being offset from the other two), and if a terphenyl segment was used as part of the scaffold in a cage it should also lie in a similar configuration, rather than sitting in a strained crescent configuration (Figure 2.5). This would result in an unfavourable strained conformation, and therefore cage formation is unlikely, with alternative reactions, such as polymerisation, being more favourable. Finally, it is also necessary to assess the cages for shape-persistence, hence any cages that are visibly collapsed will likely prove problematic upon trying to isolate the material.

Once the assembled cage models were evaluated and categorised as being experimentally viable or not, the structural suitability of the isomers had to be assessed. Any models that were carried through the first stages of the screen were subsequently modelled with the precursors locked in the *cis* conformation. In this case, all azobenzene-derived aldehyde precursors that were capable of undergoing photoisomerisation were modelled in the *cis* configuration, *i.e.*, if a  $\text{Tet}^2\text{Di}^4$  cage, comprised of two azobenzene derivatives, was successful in prior screening in the *trans* configuration, then all three units would be modelled as the *cis* isomer (Figure 2.6). As with the previous cages, these models were also subjected to the same

scrutiny in the hope that reasonable structures of fully isomerised cages would increase the probability of producing a cage that was capable of photoisomerisation.

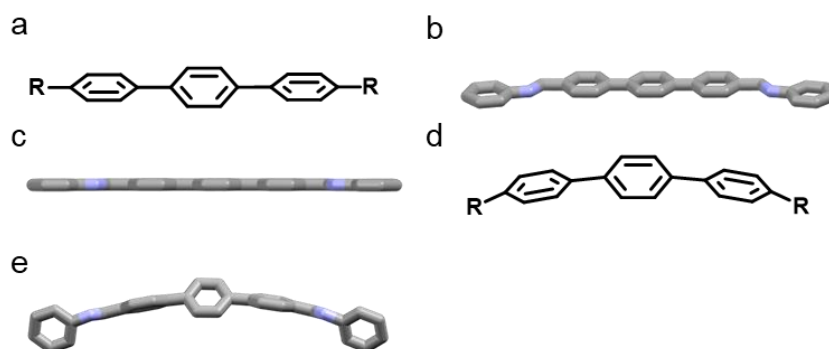


**Figure 2.5** Visual representations of a terphenyl cage segment: a) terphenyl in a linear planar configuration; b) an ideal configuration of the terphenyl segment, created and energy minimised in CrystalMaker; c) as seen from the side; d) terphenyl in a strained crescent configuration; e) side-on view of a strained terphenyl segment from an energy minimised cage model. Some atoms and functional groups are removed for clarity.

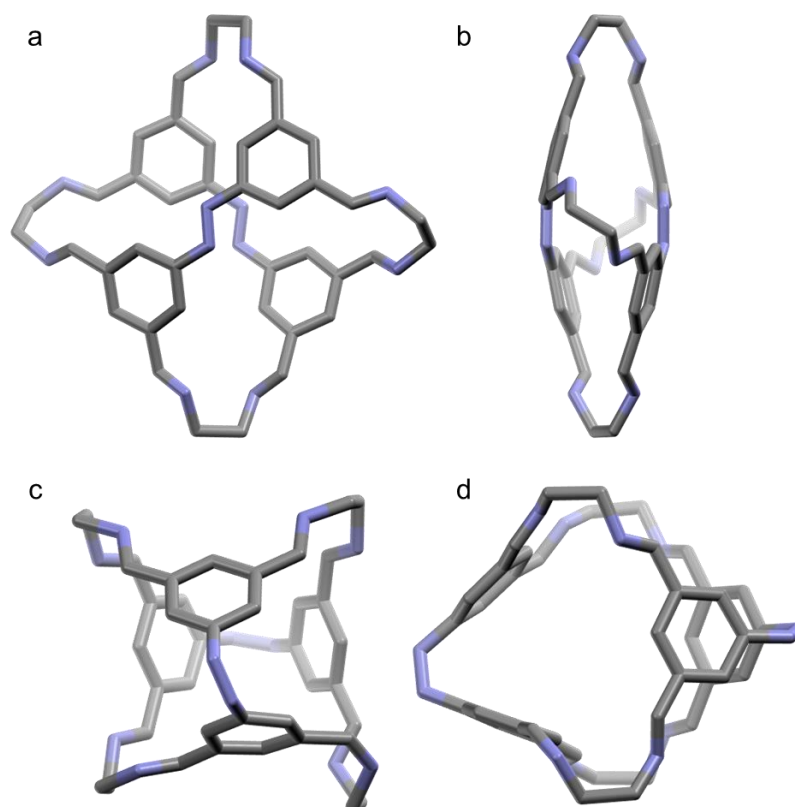


**Figure 2.6** A modelled Tet<sup>2</sup>Di<sup>4</sup> imine cage based on two equivalents of a tetraaldehyde azobenzene precursor, and four equivalents of ethane-1,2-diamine: a) front on view of the cage in the *trans* configuration; b) as (a) rotated 90° about the y-axis; c) front on view of the cage in the *cis* configuration; d) as (c) rotated 90° about the y-axis.

After inspecting all the proposed precursors and cage models, three synthetically viable precursors were selected for experimental screening (Figure 2.7). Two precursors are based on dynamic cage photoisomerisation, by incorporating them as part of the cage scaffold, with a tetraaldehyde azobenzene (**1**) and a dialdehyde azobenzene (**2**) selected. Another precursor was also selected based on static photoisomerisation, formed by functionalisation of a terphenyl cage precursor with an azobenzene arm located on the centre ring (**3**).

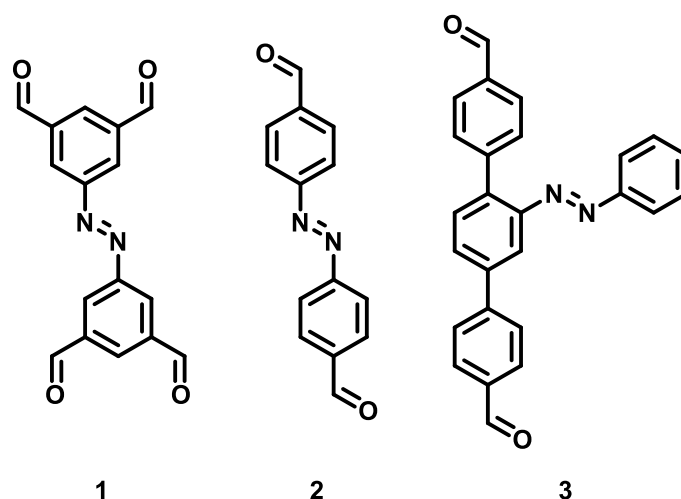
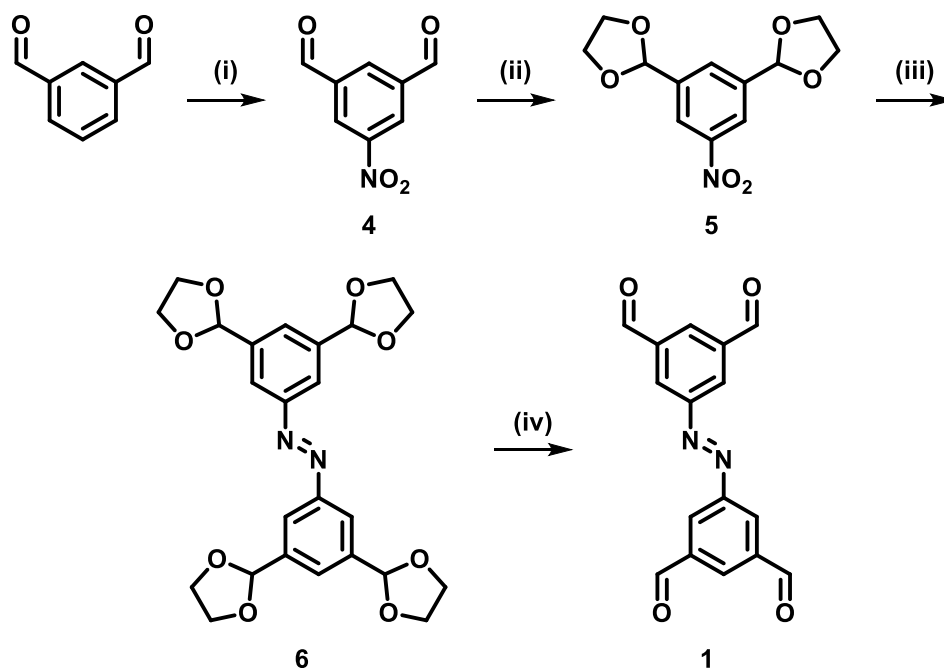


**Figure 2.7** Azobenzene-derived cage precursors identified through the computational screen and selected for experimental investigation.

### 2.3.3 Synthesis of Azobenzene-Derived Precursors

The synthesis of azobenzenes from nitrobenzenes was reported by Khan *et al.*, where they describe the use of sodium hydroxide and zinc in an ethanol/water mixture at 100 °C.<sup>19</sup> To begin the synthesis of the tetraaldehyde azobenzene **1** (Scheme 2.1), 5-nitroisophthalaldehyde therefore had to be synthesised so the nitro functional group could be used in a subsequent reduction to form the corresponding azobenzene. This was achieved by an electrophilic aromatic substitution reaction using nitric and sulfuric acid with isophthalaldehyde, to form 5-nitroisophthalaldehyde **4**. 5-Nitroisophthalaldehyde was then protected using ethylene glycol to form the respective acetal **5**. Protected nitrobenzenes were used to prevent a Cannizzaro reaction, which occurs under strong alkaline conditions when the starting material contains an aldehyde without an  $\alpha$ -proton, producing the corresponding carboxylic acid and alcohol.<sup>20</sup> The nitro-diacetal **5**, was then combined with sodium hydroxide, zinc and distilled ethanol and was refluxed for 20 hours, which after purification, yielded the protected azobenzene **6** in a 41% yield. The acetal deprotection was then

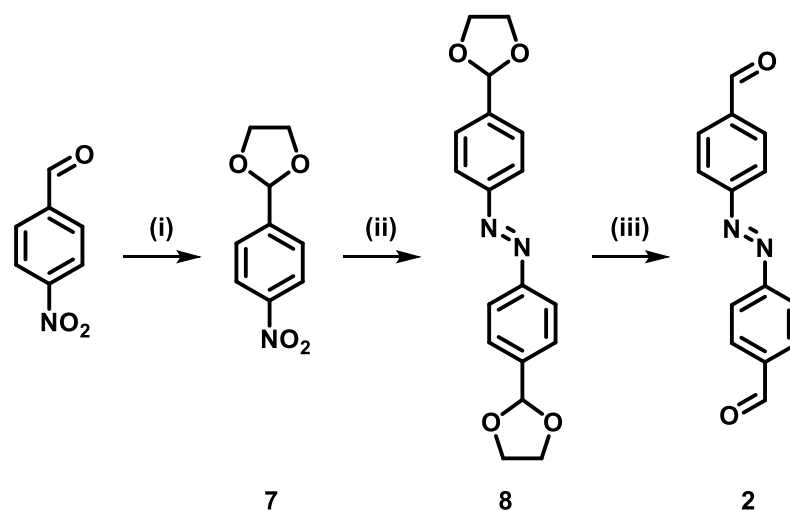
achieved by adding a 1:1 mixture of acetone/water and heating to 60 °C, yielding the desired tetraaldehyde azobenzene **1**.



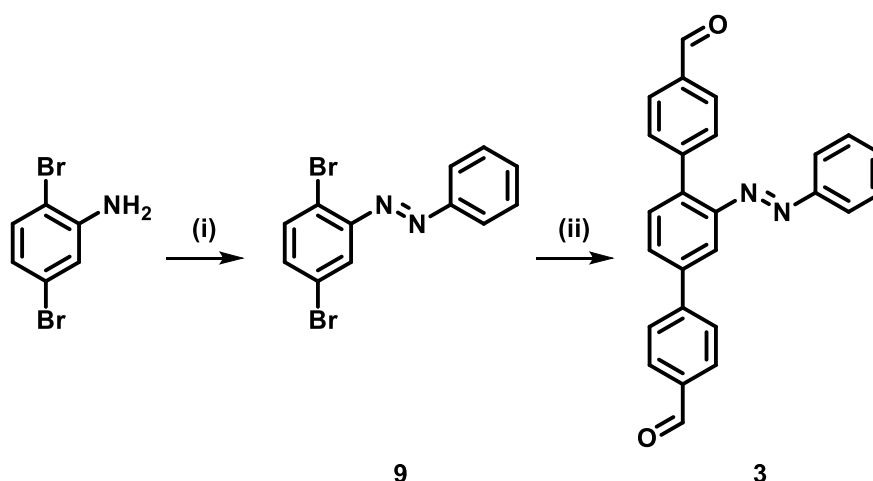
**Scheme 2.1** Reaction scheme for the synthesis of 5,5'-(diazene-1,2-diyl)diisophthalaldehyde, **1**. Reaction conditions: (i) HNO<sub>3</sub>, H<sub>2</sub>SO<sub>4</sub>, 0 °C for 2 h, then 50 °C for 1 h, 87%; (ii) Ethylene glycol, TsOH, toluene, reflux, 16 h, 92%; (iii) NaOH, Zn, EtOH/H<sub>2</sub>O, 100 °C, 20 h, 41%; (iv) Acetone/water mixture, TsOH, 60 °C, 18 h, 81%.

After finding a reliable synthetic route to the tetraaldehyde azobenzene derivative, a similar method was used to produce the dialdehyde azobenzene **2** (Scheme 2.2). Nitration was not necessary for this route as 4-nitrobenzaldehyde was commercially available. 4-Nitrobenzaldehyde was then protected using ethylene glycol, reduced with the sodium hydroxide, zinc and distilled ethanol mixture, and finally deprotected using acetone/water to yield the dialdehyde azobenzene **2**.

For the synthesis of the azobenzene-functionalised terphenyl dialdehyde **3** (Scheme 2.3), a different synthetic approach had to be taken, as the other two were symmetric azobenzenes in a homo-nitro reduction. In this case, the Mills coupling was implemented, which is a coupling reaction between aryl nitroso derivatives and amines,<sup>21</sup> hence two starting materials could be used rather than creating a mixture via the other methodology. Azobenzene functionality was incorporated through the addition of nitrosobenzene to 2,5-dibromoaniline in acetic acid to yield **9**. The resulting product was then used in a Suzuki cross-coupling reaction with (4-formylphenyl)boronic acid producing the desired product **3**.



**Scheme 2.2** Reaction scheme for the synthesis of 4,4'-(diazene-1,2-diyl)dibenzaldehyde, **2**. Reaction conditions: (i) Ethylene glycol, TsOH, toluene, reflux, 16 h, 96%; (ii) NaOH, Zn, EtOH/H<sub>2</sub>O, 100 °C, 20 h, 56%; (iii) Acetone/water mixture, TsOH, 60 °C, 18 h, >99%.



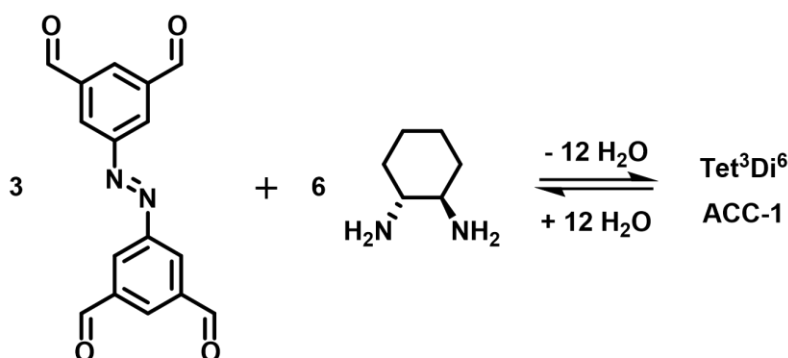
**Scheme 2.3** Reaction scheme for the synthesis of 2'-(phenyldiazenyl)-[1,1':4',1''-terphenyl]-4,4''-dicarbaldehyde **3**. Reaction conditions: (i) Nitrosobenzene, AcOH, 60 °C, 16 h, 20%; (ii) (4-Formylphenyl)boronic acid, Pd(PPh<sub>3</sub>)<sub>4</sub>, K<sub>2</sub>CO<sub>3</sub>, THF, reflux, 24 h, >99%.

### 2.3.4 Screening and Synthesis of Azobenzene-Derived Cages

After successfully synthesising all three precursors identified from the computational screen, the project moved towards cage synthesis. To begin the screening study, *R,R*-CHDA was selected as the diamine to combine with the tetraaldehyde azobenzene **1** (Table 2.1). This was due to *R,R*-CHDA being effective in the synthesis of previously reported cages, notably those reported as a reticular series of cages, **TCC1** and **TCC2**, which focuses on tetraaldehyde precursors which are structurally similar to the azobenzene variant in this study.<sup>4</sup> Reactions were conducted in deuterated solvents, which included CD<sub>2</sub>Cl<sub>2</sub>, CDCl<sub>3</sub>, and a 1:1 mixture of

CDCl<sub>3</sub>/CD<sub>3</sub>OD, for the ease of directly monitoring reactions by <sup>1</sup>H NMR spectroscopy without having to attempt to isolate reaction mixtures. Very dilute concentrations of less than 1 mg/mL were employed to prevent the formation of undesired side-products and to prevent premature precipitation of reaction intermediates prior to the desired cage forming.

**Table 2.1** Preliminary cage synthesis screen: varying the reaction conditions by changing the concentration and solvent for the reaction of (*E*)-5,5'-(diazene-1,2-diyl)diisophthalaldehyde **1** with (1*R*,2*R*)-cyclohexanediamine, to form the corresponding azobenzene-based covalent cage (**ACC-1**).



Entry	Concentration (mg/mL)	Solvent	Precipitate	Aldehyde SM in NMR	HRMS
1	0.25	CD <sub>2</sub> Cl <sub>2</sub>	✗	✗	✓
2	0.5	CD <sub>2</sub> Cl <sub>2</sub>	✗	✗	✓
3	0.5	CDCl <sub>3</sub>	✗	✗	✓
4	1.0	CDCl <sub>3</sub>	✗	✗	✓
5	0.5	CDCl <sub>3</sub> /CD <sub>3</sub> OD	✗	✗	✓
6	0.001	CDCl <sub>3</sub> /CD <sub>3</sub> OD	✗	✗	✓

The progress of the reaction was primarily monitored by <sup>1</sup>H NMR spectroscopy to identify whether the aldehyde signal of the starting material (SM) was still present in the reaction mixture, and whether the presence of new imine signals were apparent. Reactions were left to stir for seven days at room temperature and were performed in the absence of any additives or catalysts. After seven days, any precipitate was noted and removed by filtration from the reaction mixture, which is often indicative of the formation of undesired oligomeric or polymeric materials, where the filtrate was used

for further analysis. High-resolution mass spectroscopy (HRMS) was also utilised to identify if any cages, and in particular what topology, had formed over the course of the experiment.

For all conditions attempted, no precipitate was formed over the course of the reaction, indicating little to no polymer had been formed. In the case of DCM and chloroform, the reagents didn't dissolve immediately, as was observed in the 1:1 chloroform/methanol solvent system, although the solution became clear after several hours of stirring. Furthermore, no starting material was visible in the  $^1\text{H}$  NMR spectra which was identifiable by the disappearance of the aldehyde signal (10.25 ppm), and clean cage formation was apparent with the addition of an imine signal. The HRMS also indicated that in all cases a  $\text{Tet}^3\text{Di}^6$  cage had formed with a corresponding  $[\text{M}+\text{H}]^+$  mass ion with an  $m/z$  of 1351.7 (HRMS values in Table 2.2).

**Table 2.2** HRMS mass ions for  $[\text{M}+\text{H}]^+$  and  $[\text{M}+2\text{H}]^{2+}$  species for the reaction of 5,5'-(diazene-1,2-diyl)diisophthalaldehyde **1** with (1*R*,2*R*)-diaminocyclohexane, where the calculated  $[\text{M}+\text{H}]^+$  and  $[\text{M}+2\text{H}]^{2+}$  for  $\text{C}_{84}\text{H}_{90}\text{N}_{18}$  is 1351.7669 and 676.3871, respectively.

Entry	$[\text{M}+\text{H}]^+$	$[\text{M}+2\text{H}]^{2+}$
1	1351.7754	676.3931
2	1351.7822	676.3969
3	1351.7767	676.3954
4	1351.7763	676.3938
5	1351.7769	-
6	1351.7747	676.3937

After confirming that **ACC-1** could be formed over a wide range of conditions, it was decided to continue using  $\text{CDCl}_3$  in any further syntheses, as it was significantly cheaper than  $\text{CD}_2\text{Cl}_2$ , at the higher concentration of 1 mg/mL. Unfortunately, there were difficulties in isolating the material from solution. Once the reaction had gone to completion, the solvent was removed, and the residue re-dissolved in chloroform and filtered to remove any insoluble material. After removing the solvent again, the residual material was dissolved in chloroform-*d* for analysis. On doing so, a significant decrease in peak intensity was observed in the  $^1\text{H}$  NMR spectrum, where only small signals could be observed from the baseline, with very few corresponding to the

original cage signals seen in the initial reaction mixture. This was initially thought to be due to the instability of the cage, leading to decomposition upon isolation, which is a known inherent issue of organic cages.<sup>22-24</sup> Fortunately, in later experiments when investigating the photoisomerisation properties (discussed in 2.3.5) of the material, these were prepared as mixtures in dichloromethane (DCM) rather than chloroform due to the acidity of chloroform (from the generation of hydrochloric acid by oxidative decomposition of chloroform<sup>25</sup>). A study by Gibson *et al.*, showed that irradiation of an azobenzene compound in deuterated chloroform showed no presence of the *cis*-isomer by <sup>1</sup>H NMR spectroscopy, demonstrating a severely reduced half-life of the *cis*-isomer.<sup>25</sup> Photoisomerisation was observed by <sup>1</sup>H NMR spectroscopy after potassium carbonate had been added to the chloroform, confirming that the presence of acid severely decreased the half-life of the *cis*-isomer. Further NMR studies also confirmed the effect of acid by the addition of hydrochloric acid (2 M) to an azobenzene sample which reduced the half-life from 20 days to 5 minutes. After preparing the cage samples in deuterated DCM, the <sup>1</sup>H NMR spectrum (in CD<sub>2</sub>Cl<sub>2</sub>) of the cage material was almost identical to that observed in the initial experiments, and a work-up which included an acetonitrile solvent swap yielded the pure cage **ACC-1** (Figure 2.8). While the sample readily dissolved in chloroform and provided the expected spectrum of the cage, on standing, a layer of precipitate became apparent overnight. This precipitate was collected by filtration and attempts at dissolving the material proved unsuccessful, confirming that chloroform was causing decomposition of the cage.

To explore the possibility of producing further cages, including one with greater conformational flexibility, a small substrate screen was carried out with an additional six diamines, which included both aliphatic and aromatic species (Table 2.3) using the reaction conditions identified from the initial screen. In most cases, precipitate was formed over the course of 7 days, with the exception of 1,2-diamino-2-methylpropane (DA4), indicating the formation of insoluble oligomers and polymer. Samples were then analysed by <sup>1</sup>H NMR spectroscopy, where all samples other than propane-1,2-diamine (DA3) were found to have no aldehyde signals in the spectra, which suggests that any remaining material that had not formed insoluble oligomers had been used in some reaction, whether that is forming cage or other imine condensations.



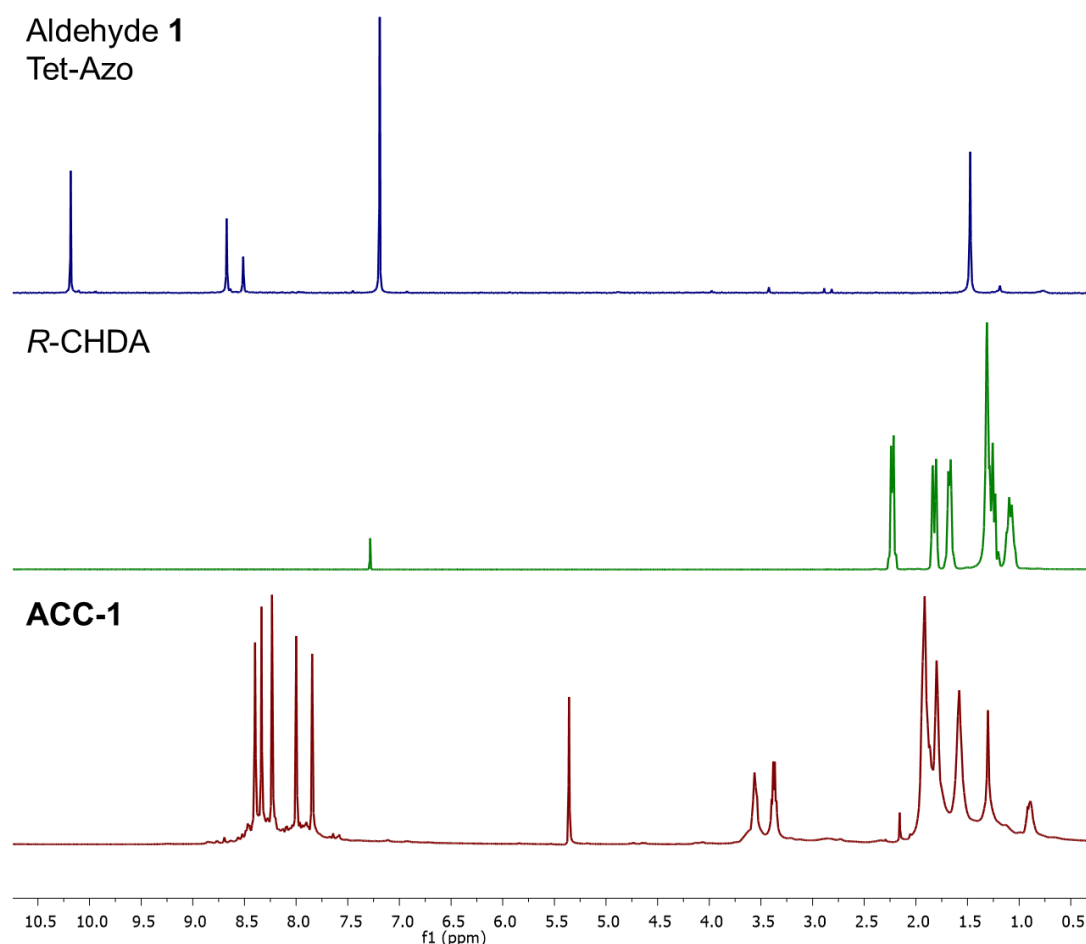
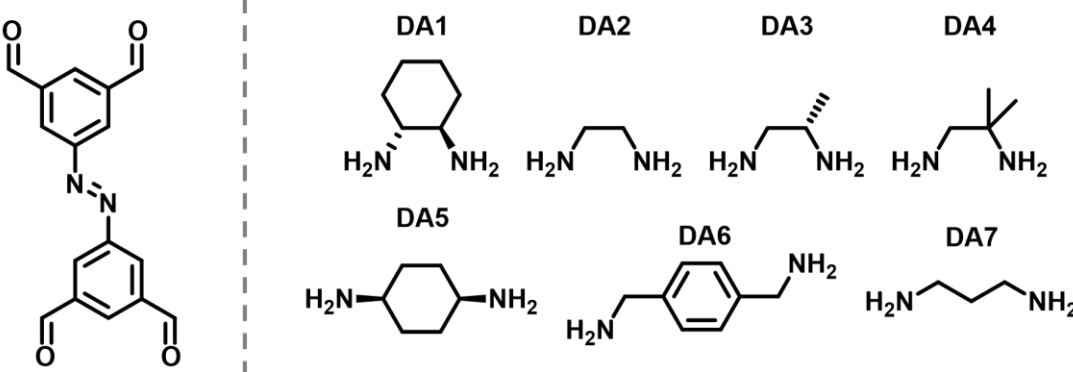


**Figure 2.8** Stacked  $^1\text{H}$  NMR spectra of **ACC-1** and its precursors, where tetraaldehyde **1** (top, blue,  $\text{CDCl}_3$ ), *R*-CHDA (middle, green,  $\text{CDCl}_3$ ), and **ACC-1** (bottom, red,  $\text{CD}_2\text{Cl}_2$ ).

The reaction mixtures were then analysed by HRMS, although for the *para*-substituted amines, cyclohexane-1,4-diamine (DA5) and 1,4-phenylenedimethanamine (DA6), no mass ions corresponding to cage species could be identified. The smaller diamines (DA1 – DA4) however, were all found to contain mass ions that indicated the formation of  $\text{Tet}^3\text{Di}^6$  cages, which were larger than the initial computational studies which were modelled as  $\text{Tet}^2\text{Di}^4$  cages. This data was fed back to our computational collaborators so the cages could be remodelled as the  $\text{Tet}^3\text{Di}^6$  species, along with their isomerised variants. The last diamine in this screen, propane-1,3-diamine (DA7), was identified as forming a  $\text{Tet}^2\text{Di}^4$  cage. This screen identified that DA4 might be a suitable candidate for a more flexible cage if that from DA1 failed to demonstrate any photoisomerisation. Given DA1 produced the  $^1\text{H}$  NMR spectrum with the least amount of additional peaks while the mass spectrum also produced far fewer additional mass ions it was selected for further testing, including the photophysical properties and single-crystal X-ray diffraction (scXRD).

**Table 2.3** A selection of diamines (DA 1-7) used in the synthetic screen for cage formation with 5,5'-(diazene-1,2-diyl)diisophthalaldehyde **1**, with their corresponding HRMS and size of cage formed. <sup>1</sup>No Trace of [M+H]<sup>+</sup>, [M+2H]<sup>2+</sup> or [M+3H]<sup>3+</sup> for Tet<sup>3</sup>Di<sup>6</sup> or Tet<sup>2</sup>Di<sup>4</sup> cage species.



Diamine	Precipitate	Aldehyde SM in NMR	HRMS		Cage formed
			Calc.	Found	
DA1	x	x	1351.7669	1351.7775	Tet <sup>3</sup> Di <sup>6</sup>
DA2	✓	x	1027.4852	1027.4839	Tet <sup>3</sup> Di <sup>6</sup>
DA3	✓	✓	1111.5791	1111.5745	Tet <sup>3</sup> Di <sup>6</sup>
DA4	x	x	1195.6730	1195.6615	Tet <sup>3</sup> Di <sup>6</sup>
DA5	✓	x	1519.9547	None <sup>1</sup>	No trace
DA6	✓	x	1453.4382	None <sup>1</sup>	No trace
DA7	✓	x	741.3885	741.3832	Tet <sup>2</sup> Di <sup>4</sup>

A solution of **ACC-1** was prepared from DA1 and tetraaldehyde **1**, and after 7 days, the solution was diluted in DCM, where 1 mL samples was taken to grow single crystals. Vial-in-vial slow diffusion was used, and the samples were combined with the following anti-solvents: methanol, ethanol, isopropanol, acetone, THF, ethyl acetate, acetonitrile, diethyl ether, hexane, and pentane. Single crystals of **ACC-1** were successfully grown from ethanol, and a structure was successfully identified using single-crystal X-ray diffraction, further confirming the formation of a Tet<sup>3</sup>Di<sup>6</sup> cage (Figure 2.9). **ACC-1** was found to be in a rhombic space group *R*32, and packs in stacks in a window-to-window configuration and offset azo-to-azo with the CHDA overlapping between stacks. Interestingly, the azobenzene contains a twist in the crystal structure, which can be seen from the top-down view (Figure 2.9, b), as

opposed to being planar like that of azobenzene in its natural state.<sup>14</sup> This twisting also exists in other organic cages containing similar linear tetraaldehyde precursors, namely the **TCC** series introduced earlier.<sup>4</sup> On scaling up the cage synthesis and isolating the bulk material, powder X-ray diffraction (PXRD) indicated the formation of amorphous material, which remained amorphous upon activation after being kept in a vacuum oven at 80 °C for 15 hours (Figure 2.10). Neither of the powder patterns (before or after activation) displayed any reflections that corresponded to those generated from the simulated pattern from the scXRD data.

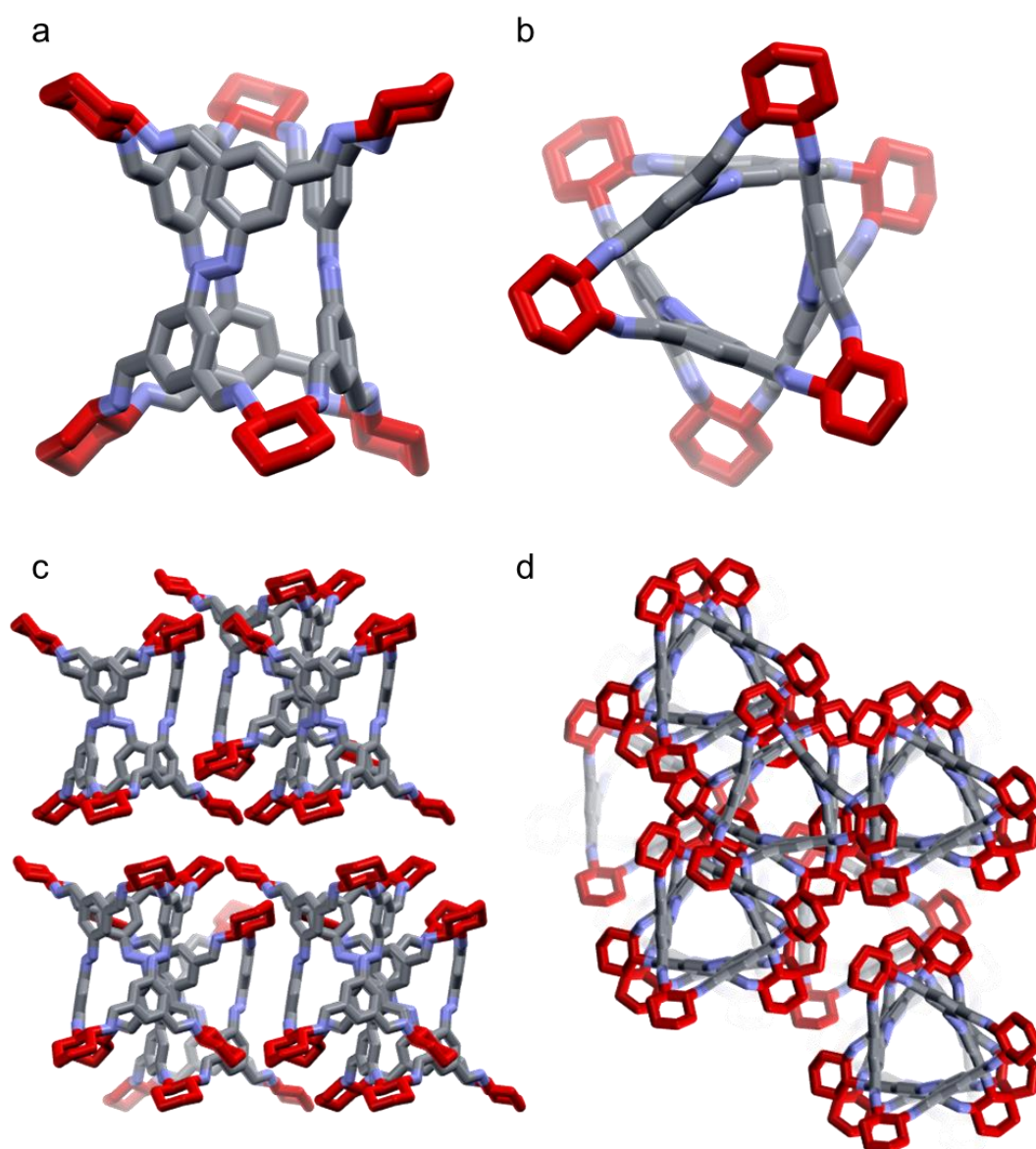


**Figure 2.9** Single-crystal structures of azobenzene derived cage **ACC-1**, where CHDA is highlighted in red: a) Side-on view; b) top-down view; c) side-on view of the offset azo-to-azo packing between stacks; d) top-down view of window-to-window stacks. Hydrogen atoms have been removed for clarity.

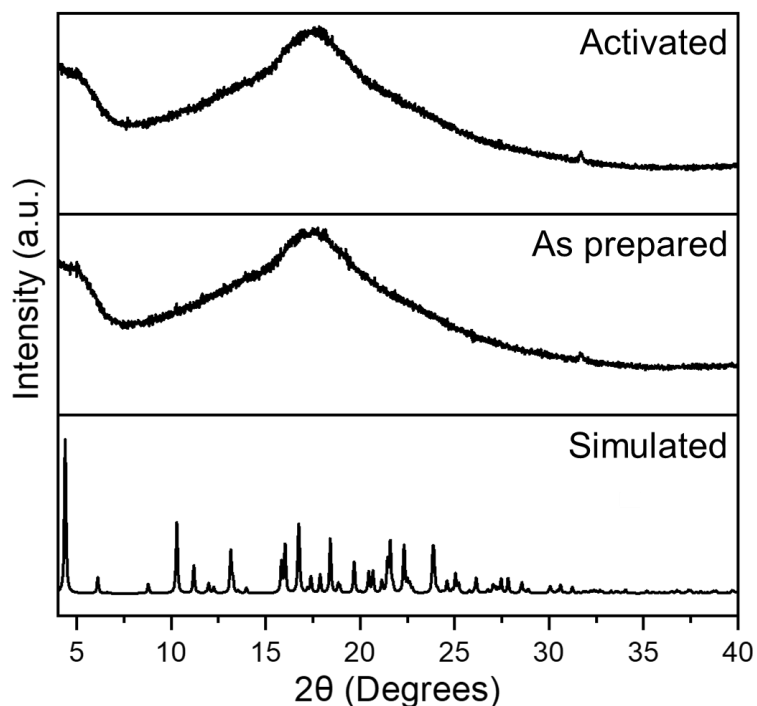
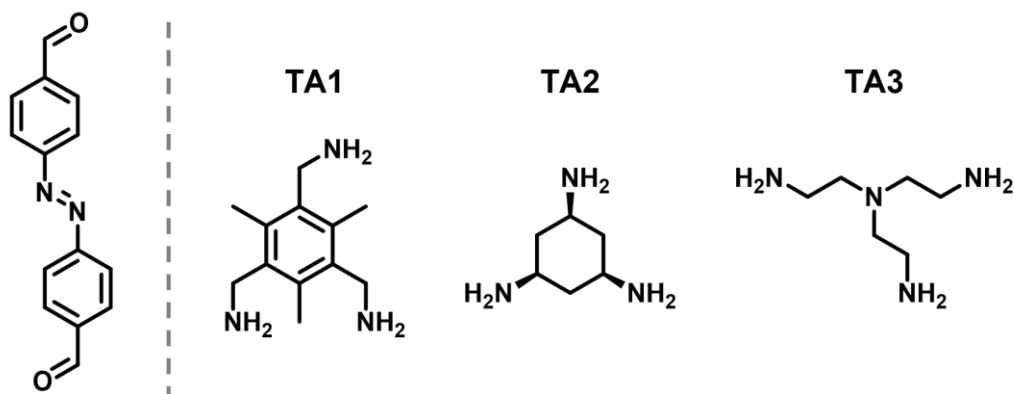


**Figure 2.10** PXR D patterns of **ACC-1**, with patterns from the activated sample which was heated in a vacuum oven at 80 °C for 15 hours, top, as prepared from the solvent swap with acetonitrile, middle, and simulated powder pattern from the scXRD data, bottom.

A smaller screen was performed on dialdehyde azobenzene **2** with three different triamines (Table 2.4), which was based off a similar linear dialdehyde that was successfully found to form organic cages in a high-throughput screen.<sup>26</sup> Reactions were performed under the same conditions as previously described for **ACC-1**, in CDCl<sub>3</sub> at a concentration of 1 mg/mL. In all cases, HRMS found mass ions that corresponded to Tri<sup>2</sup>Di<sup>3</sup> cages. However, the three reactions all proceeded differently. The reactions with (2,4,6-trimethylbenzene-1,3,5-triyl)trimethanamine (TA1) and (1*S*,3*S*,5*S*)-cyclohexane-1,3,5-triamine (TA2) had a significant amount of starting material remaining in the <sup>1</sup>H NMR spectra after 7 days, and were therefore heated to 50 °C for an additional 3 days. After additional heating no starting material could be identified with TA1, unlike TA2, which still contained starting material in the spectrum. Additionally, TA1 formed a significant amount of precipitate over the course of the reaction. The final triamine in the screen, tris(2-aminoethyl)amine (TREN, TA3), showed complete consumption of all aldehyde starting material and the formation of a single cage species, and also required no heating for the reaction to proceed. Of all three triamines screened, TA3 gave the cleanest conversion with dialdehyde **2**, and could be readily isolated by a hexane solvent swap and filtration to yield pure cage, named **ACC-2** (Figure 2.11).

**Table 2.4** Triamines (TA 1-3) used in the synthetic screen for cage formation with 4,4'-(diazene-1,2-diyl)dibenzaldehyde, **2**, with their corresponding HRMS and size of cage formed.



Diamine	Precipitate	Aldehyde		HRMS		Cage formed
		SM in NMR	Calc.	Found		
TA1	✓	✗	1021.5137	1021.5194	Tri <sup>2</sup> Di <sup>3</sup>	
TA2	✗	✓	865.4198	865.4280	Tri <sup>2</sup> Di <sup>3</sup>	
TA3	✗	✗	899.4729	899.4787	Tri <sup>2</sup> Di <sup>3</sup>	

On performing a more detailed literature search, a 1992 report by Vögtle reports the synthesis of this cage, along with the reduced variant.<sup>27</sup> This was missed in an initial literature search as an English version was unavailable. However, while the authors report the synthesis of the cage, they do not investigate any photophysical properties of the material. Unfortunately, during the Covid-19 pandemic, another report was published which focused on the imine version of this Tri<sup>2</sup>Di<sup>3</sup> cage and its ability to separate xylene.<sup>28</sup> Two other reports were also released within the same period which investigated the reduced variant of the Tri<sup>2</sup>Di<sup>3</sup> cage, and both investigated the photoisomerisation of the reduced variant.<sup>29,30</sup> However, no photophysical behaviours have been reported for this imine cage.

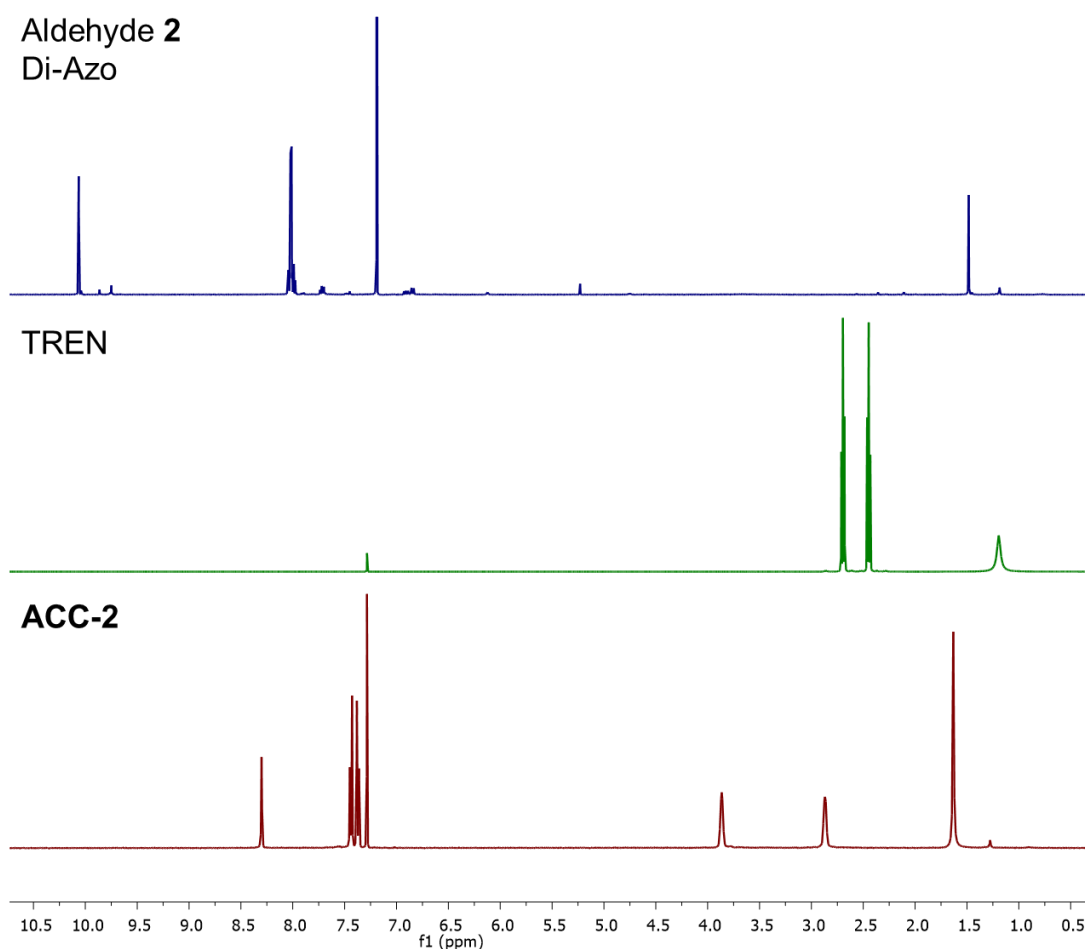


**Figure 2.11** Stacked <sup>1</sup>H NMR spectra of **ACC-2** and its precursors, where dialdehyde **2** (top, blue, CDCl<sub>3</sub>), TREN (middle, green, CDCl<sub>3</sub>), and **ACC-2** (bottom, red, CDCl<sub>3</sub>).

Therefore, from the small screen with dialdehyde azobenzene **2**, the cage **ACC-2** formed from the reaction with TREN (TA3) was selected for further experiments, including photoisomerisation studies. Single crystals were grown using vial-in-vial diffusion, using the same approach as in the case of **ACC-1**. Single crystals were successfully grown from ethanol, where the corresponding structure confirmed the formation of a Tri<sup>2</sup>Di<sup>3</sup> cage (Figure 2.12). **ACC-2** was found to pack in a rhombic space group *R3c*, in stacks with TREN-to-TREN faces, and offset window-to-window packing between stacks. As observed with **ACC-1**, some degree of twisting can be observed in the azobenzene when looking top-down at the crystal structure (Figure 2.12, b). On scaling up the reaction, PXRD analysis showed the formation of a crystalline material, with little to no change of the powder pattern after activation of the material after 15 hours in a vacuum oven at 80 °C (Figure 2.13). The PXRD patterns of the bulk material also show similar reflections to the simulated powder pattern from the scXRD data, albeit slightly shifted to a lower angle.

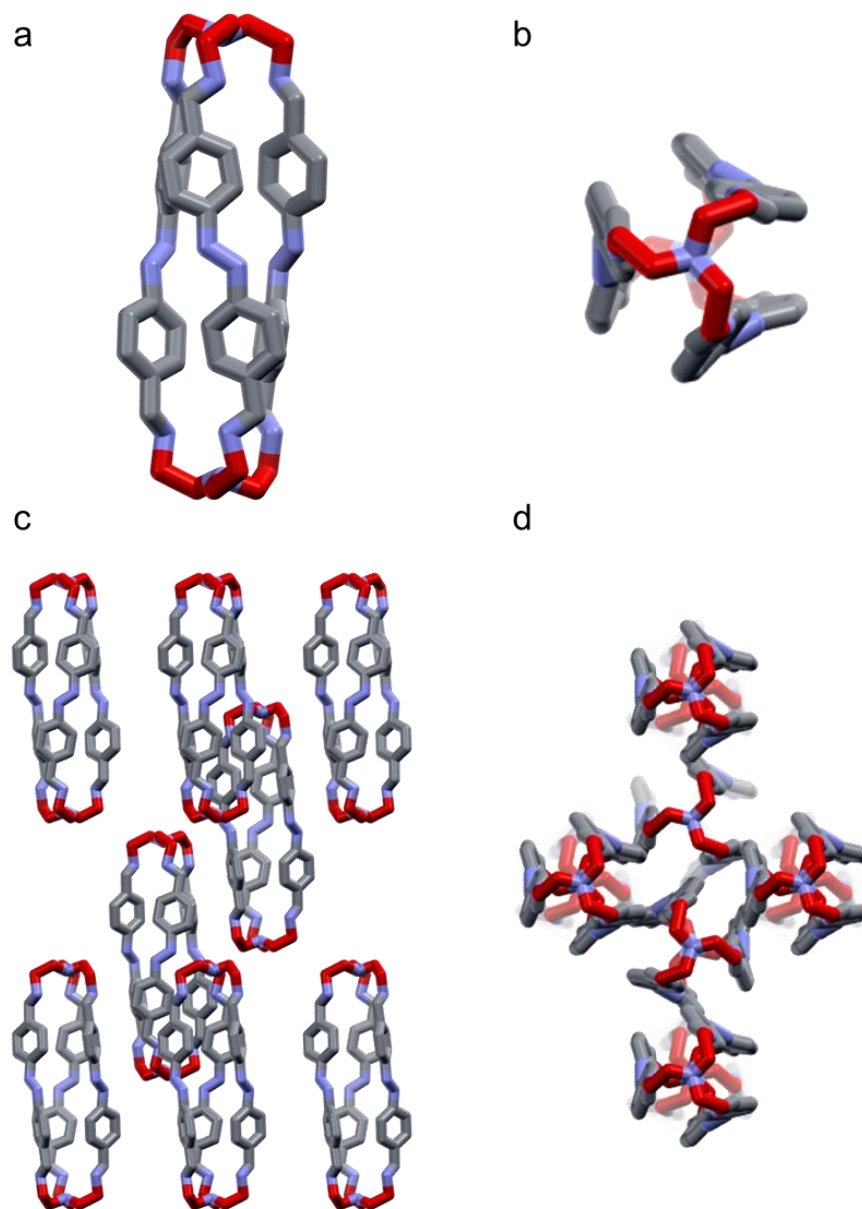


**Figure 2.12** Single-crystal structures of azobenzene-derived cage **ACC-2**, where TREN is highlighted in red: a) Side-on view; b) top-down view; c) side-on view of the staggered window-to-window packing between stacks; d) top-down view of the stacks. Hydrogen atoms have been removed for clarity.

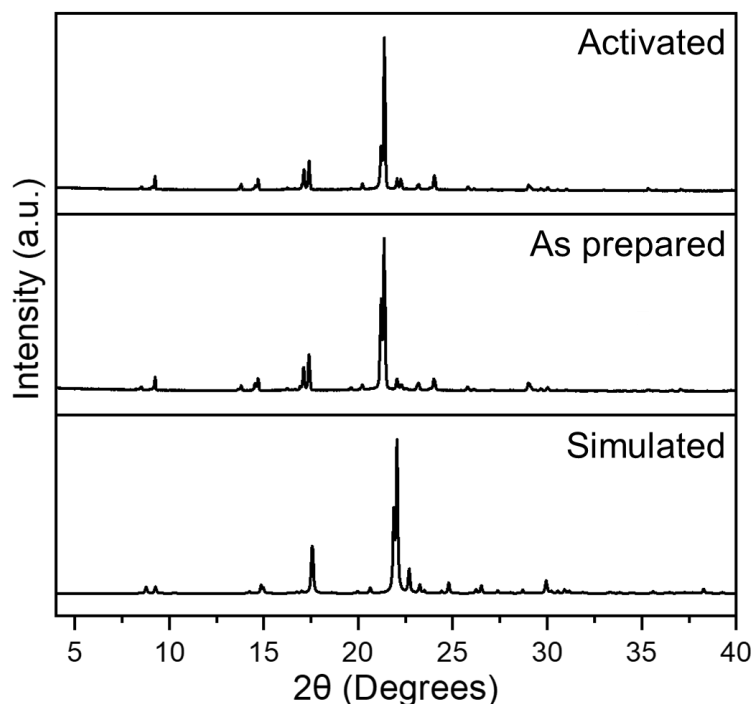
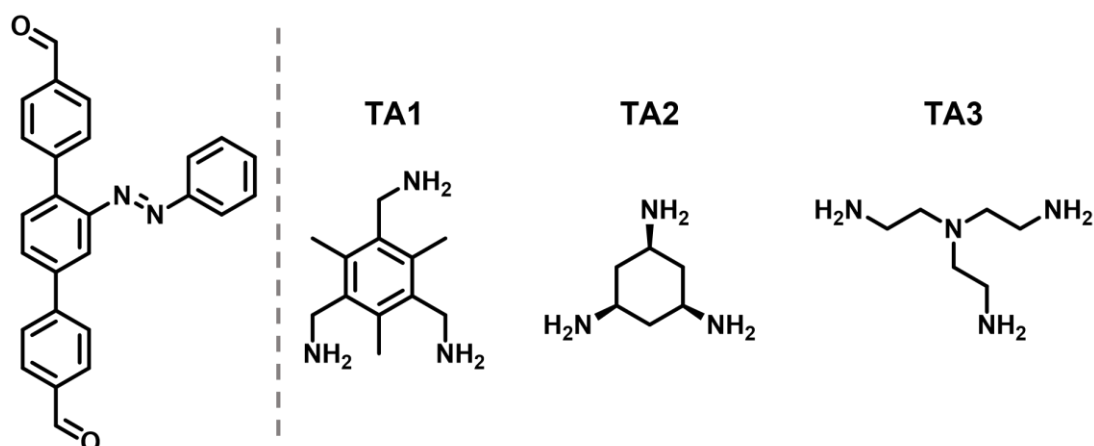


**Figure 2.13** PXR D patterns of **ACC-2**, with patterns from the activated sample which was heated in a vacuum oven at 80 °C for 15 hours, top, as prepared from the solvent swap with hexane, middle, and simulated powder pattern from the scXRD data, bottom.

Finally, another small screen was performed on the azo-arm dialdehyde **3** with the same three triamines used in the screen for dialdehyde **2** (Table 2.5) For the most part, the results of this screen almost mimicked those observed in the screen of dialdehyde **2**. Both TA1 and TA2 produced large amounts of insoluble precipitate over the course of the reaction and were heated to 50 °C after the initial 7 days at room temperature, due to residual starting material being present in the  $^1\text{H}$  NMR spectra. After heating the sample for an additional 3 days, TA1 continued to display peaks that corresponded with starting material, whereas no starting material remained in the reaction with TA2. In both cases, HRMS showed mass ions that confirmed  $\text{Tri}^2\text{Di}^3$  cages had been formed. TA3 performed just as well with the azo-arm dialdehyde **3** as it did with dialdehyde **2**, with no precipitate forming over the course of the reaction at room temperature, and the disappearance of all the corresponding aldehyde peaks in the  $^1\text{H}$  NMR spectrum (Figure 2.14). HRMS also showed mass ions that matched the calculated  $\text{Tri}^2\text{Di}^3$  cage as the  $[\text{M}+\text{H}]^+$  ion.



**Table 2.5** A selection of triamines (TA1-3) used in the synthetic screen for cage formation with 2'-(phenyldiazenyl)-[1,1':4',1''-terphenyl]-4,4''-dicarbalddehyde, **3**, with their corresponding HRMS and size of cage formed.



Diamine	Precipitate	Aldehyde	HRMS		Cage formed
		SM in NMR	Calc.	Found	
TA1	✓	✗	1478.7046	1478.7256	Tri <sup>2</sup> Di <sup>3</sup>
TA2	✓	✓	1322.6107	1322.6208	Tri <sup>2</sup> Di <sup>3</sup>
TA3	✗	✗	1356.6637	1356.6744	Tri <sup>2</sup> Di <sup>3</sup>

However, there would be many possible cage isomers that could be formed with this azo-arm dialdehyde, due to the precursor being non-symmetrical, for example, it could give rise to different combinations of up/up/up or up/up/down, in terms of the orientation of the arm within the cage. In addition, there is the further possibility of the azobenzene laying within or outside the cage, which gives rise to another four possibilities as in/in/in, in/in/out, in/out/out, or out/out/out. While the likelihood of having more than one occupying the cage cavity is low, given the size of the cavity diameter should be similar to that of **ACC-2**, in theory this could be a possibility, especially if they were combined with up/down orientations. As there is a wide range of possibilities, it was difficult to determine whether the cages could be isolated because of the increased complexity of the <sup>1</sup>H NMR spectrum of the isolated material. Attempts were also made to prepare single crystals of the material using vial-in-vial diffusion, using the same range of anti-solvents as the other two cages. This proved unsuccessful, which is likely attributed to the wide range of possible cage isomers, leaving the cages unable to pack efficiently, preventing the formation of crystals.

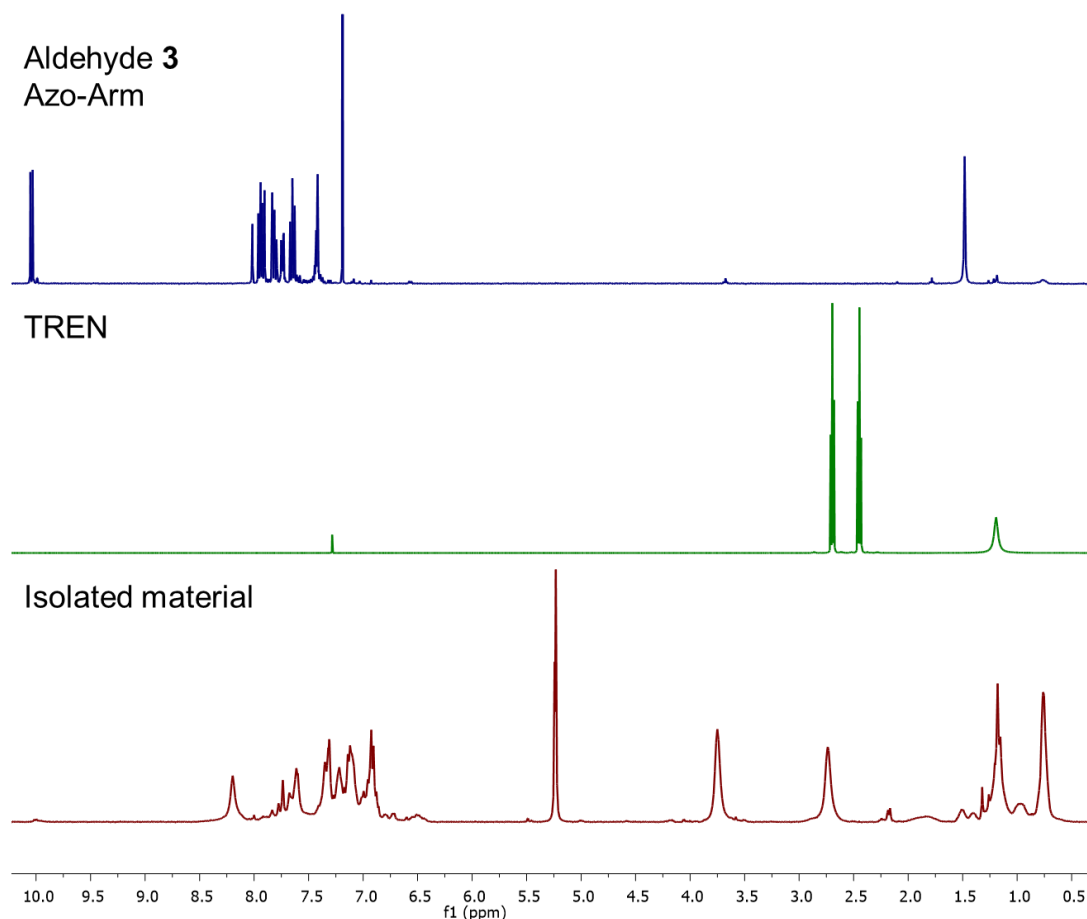


**Figure 2.14** Stacked  $^1\text{H}$  NMR spectra of the isolated mixture from dialdehyde **3** reaction and its precursors, where dialdehyde **3** (top, blue), TREN (middle, green), and isolated mixture (bottom, red).

Due to the added complexity of this azo-arm cage and the low likelihood of a single cage being formed, it was decided that further studies would concentrate on the cages that could be isolated as single species, that is **ACC-1** and **ACC-2**, rather than a mixture of cages which would likely have varying photophysical properties depending on the position of the azo-arm within the cage, leading to ambiguous results. Hence, further studies in this chapter will focus solely on the cages where the photoresponsive group has been incorporated into the scaffold of the cage rather than being decorated with photoresponsive groups. Future studies investigating the effects of the separated azo-arm material would be very interesting and could possibly be achieved through preparative HPLC, like that of the dynamic covalent scrambled cages.<sup>31</sup>

### 2.3.5 Photophysical Properties of Azobenzene-Derived Organic Cages

The photophysical properties of photochromic molecules can be determined through a variety of UV-vis experiments, which can provide information about several key factors of a photodynamic system, the first being the photostationary state (PSS). This is the steady state reached by irradiation of light in a system in equilibrium, that is, the maximum amount of photoisomerisation of a given system for a specific photon flux. Secondly, the thermal isomerisation half-life can be measured, which describes the time taken for 50% of the molecules to isomerise back to their thermodynamically stable form. Finally, the quantum yield ( $\Phi$ ) of photoisomerisation can then be established, which describes the efficiency of the photoisomerisation and can be determined by monitoring the change in concentration after irradiating the sample with a specific photon flux.

To determine the PSS of a photoreversible system  $A \xrightleftharpoons{h\nu} B$ , UV-vis can be used where a sample must be prepared in a non-absorbing solvent (such as DCM). Measurements must be performed on the thermodynamically stable form (pure A, a sample prepared in the dark, assumed to be 100% *trans*), and experiments performed under irradiation to the point of photoequilibration with two different wavelengths of light. These values obtained through UV-vis experiments can then be used in a series of calculations described by Fischer.<sup>32</sup>

In an example of a theoretical compound, X, the PSS ( $\alpha$ ) can be determined from UV-vis data of the pre-irradiated sample, along with irradiation of the sample at two wavelengths until no further change is observed through longer irradiation times, which can provide information of 365 nm ( $\alpha_1$ ) and 405 nm ( $\alpha_2$ ). From this data, one can extract the ratio of the absorbances from the two different wavelengths at a point, where this ratio is denoted  $\eta$ , and is expressed as Eq. (1). This ratio then describes the relationship between the PSSs at both wavelengths of light, as Eq. (2). The difference in absorbance when exposed to each wavelength is denoted as  $\Delta$ , and the absorbance at each wavelength is D. This change in absorbance can then be used to describe the relationship between the pure A, and the PSS attained by irradiation at the same wavelength, allowing the PSS to be determined through Eq. (3) as  $\alpha_2$ , which can then be utilised in Eq. (2) to determine  $\alpha_1$ . Finally, after determining these values from the experimental data, they can then be used to determine a spectrum of pure B by using Eq. (4).

$$\eta = \frac{(Abs_{\lambda 1} - Abs_{dark})}{(Abs_{\lambda 2} - Abs_{dark})} \quad \text{Eq. (1)}$$

$$\alpha_1 = \eta \alpha_2 \quad \text{Eq. (2)}$$

$$\alpha_2 = \frac{\left(\frac{\Delta_1}{D_1} - \frac{\Delta_2}{D_2}\right)}{1 + \frac{\Delta_1}{D_1} - \eta \left(1 + \frac{\Delta_2}{D_2}\right)} \quad \text{Eq. (3)}$$

$$D_B = D_A + \frac{\Delta}{\alpha} \quad \text{Eq. (4)}$$

In this theoretical compound, which is assumed to be a photoreversible system as  $A \xrightleftharpoons{h\nu} B$ , absorption occurs within the region of 250 nm – 425 nm. This sample can be irradiated with 405 nm light until no further changes can be observed in the spectrum, which is the PSS of 405 nm and the change in concentration associated with the PSS is proportional to the quantum yield, photon flux and the fraction of photons absorbed by A. The same experiment can then be conducted with a second wavelength, such as 365 nm. A visual demonstration of this can be seen in Figure 2.15, with the values listed at each selected wavelength in Table 2.6. Using Eq. (1) – (3), the values obtained from the UV-vis spectra from the PSS using 405 nm light results in 45% conversion of A to B, whereas the PSS using 365 nm light can convert 59% of A to B.

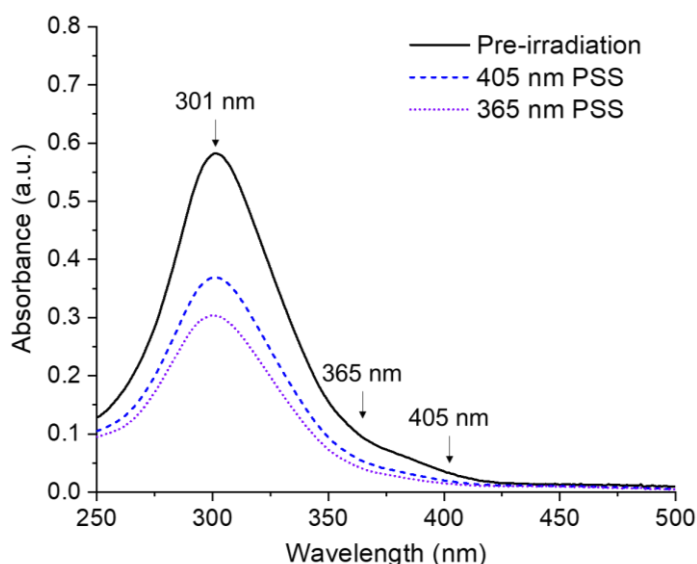


**Figure 2.15** Theoretical absorption spectra of a theoretical compound X, where pre-irradiation is a solid black line, photostationary state attained by irradiation at 405 nm is a dashed blue line, and photostationary state attained by irradiation at 365 nm is a dotted purple line.

**Table 2.6** Top - Absorption values of theoretical compound X, as pure A (dark) and the photostationary state achieved by irradiation at 365 nm and 405 nm. Bottom – Calculated values using Eq. (1) – (3) to determine the percentage of photoisomerised molecules, B.

Selected $\lambda$ (nm)	Abs. in dark (a.u.)	Abs. at 365 nm after reaching the PSS with 365 nm light (a.u.)	Abs. at 405 nm after reaching the PSS with 405 nm light (a.u.)
301	0.582	0.367	0.303
365	0.094	0.053	0.040
405	0.030	0.017	0.013
$\eta$	1.306		
$\Delta_1/D_1$	-0.571		
$\Delta_2/D_2$	-0.428		
$\alpha_2$	0.45	45% converted to B	
$\alpha_1$	0.59	59% converted to B	

As the structures of **ACC-1** and **ACC-2** had been confirmed as having Tet<sup>3</sup>Di<sup>6</sup> and Tri<sup>2</sup>Di<sup>3</sup> topologies, which were identified through a combination of <sup>1</sup>H NMR, HRMS, and scXRD analysis, these structures were then provided to our computational collaborators to determine the relative energies of each isomeric form of the cages. While these models do not offer information about the energy of the transition state, they do provide a good estimate of whether photoisomerisation could occur on comparison of the relative energies to a known system. Given each of these cages contains three separate azobenzenes, a comparison molecule also comprised of three azobenzene units is most applicable. Therefore, as a comparison for the relative energies, a multi-azobenzene macrocycle designed and synthesised by Heindl *et al.* was selected, which was able to achieve 73% photoisomerisation of a trisazo-macrocycle from (*EEE*) to (*ZZZ*) on irradiation with 365 nm light (Figure 2.16).<sup>33</sup> In this study, density functional theory (DFT) studies were also performed for each isomer, which suggests that there is a 106 kJ mol<sup>-1</sup> relative energy difference from (*EEE*) to (*ZZZ*), with over double the relative energies for the transition state for each consecutive isomerisation. They also note that the intermediate isomers, (*EEZ*) and

(*EZZ*) have similar relative energies, which they believe is due to the difference in ring strain of each isomer.

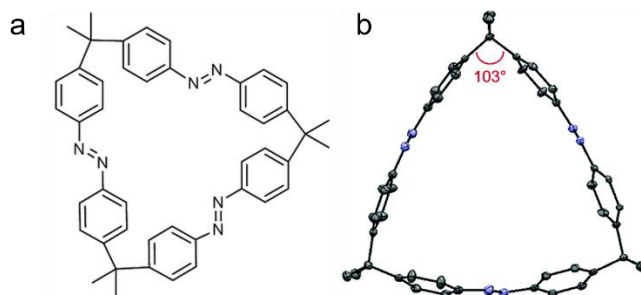


**Figure 2.16** a) Structure of the trisazo-macrocycle; b) scXRD structure of the trisazo-macrocycle.<sup>33</sup>

In both cases, for **ACC-1** (Figure 2.17 a) and **ACC-2** (Figure 2.18, b), the relative energies of the cages with all three azobenzenes in their *cis*-configuration (*ZZZ*) was the highest, and those with the azobenzenes in their *trans*-configuration (*EEE*) was the lowest. Though, unlike the comparison macrocycle, the intermediates in each of these cages increased in relative energy. Both cages in their *cis*-configuration also exhibited significantly higher relative energies than that of the trisazo-macrocycle, where the relative energy for the fully *cis*-configuration of **ACC-1** is over double that of the macrocycle at  $260 \text{ kJ mol}^{-1}$ , and the fully *cis*-configuration of **ACC-2** is  $170 \text{ kJ mol}^{-1}$  higher than the fully *trans*-configuration.

As both **ACC-1** and **ACC-2** are 3-dimensional cages, they possess an internal cavity. Unlike that of smaller macrocycles, the cavity diameter can also be determined for the modelled cages of each isomer, which was achieved by using pywindow, an open-source code for the determination of cavity size, the number of windows and diameter of windows for porous molecules.<sup>34</sup> **ACC-1** has a larger internal cavity than **ACC-2** in all cases, but the internal cavity diameters of the two cages behave rather differently on switching. When in a fully *trans*-configuration (*EEE*), **ACC-1** has an internal cavity diameter of  $4.4 \text{ \AA}$ , which increases to  $6.4 \text{ \AA}$  when fully isomerised into the *cis*-configuration (*ZZZ*), and the intermediate *EEZ* and *EZZ* forms have a similar cavity size of  $5.5$  and  $5.4 \text{ \AA}$ , respectively (Figure 2.17, a). **ACC-2**, however, suffers from a complete loss of its internal cavity when it is predominantly in its *cis*-configuration, although there is an initial small increase in cavity diameter when going from *EEE* to *EEZ* of  $2.2$  to  $2.4 \text{ \AA}$  (Figure 2.17, b).

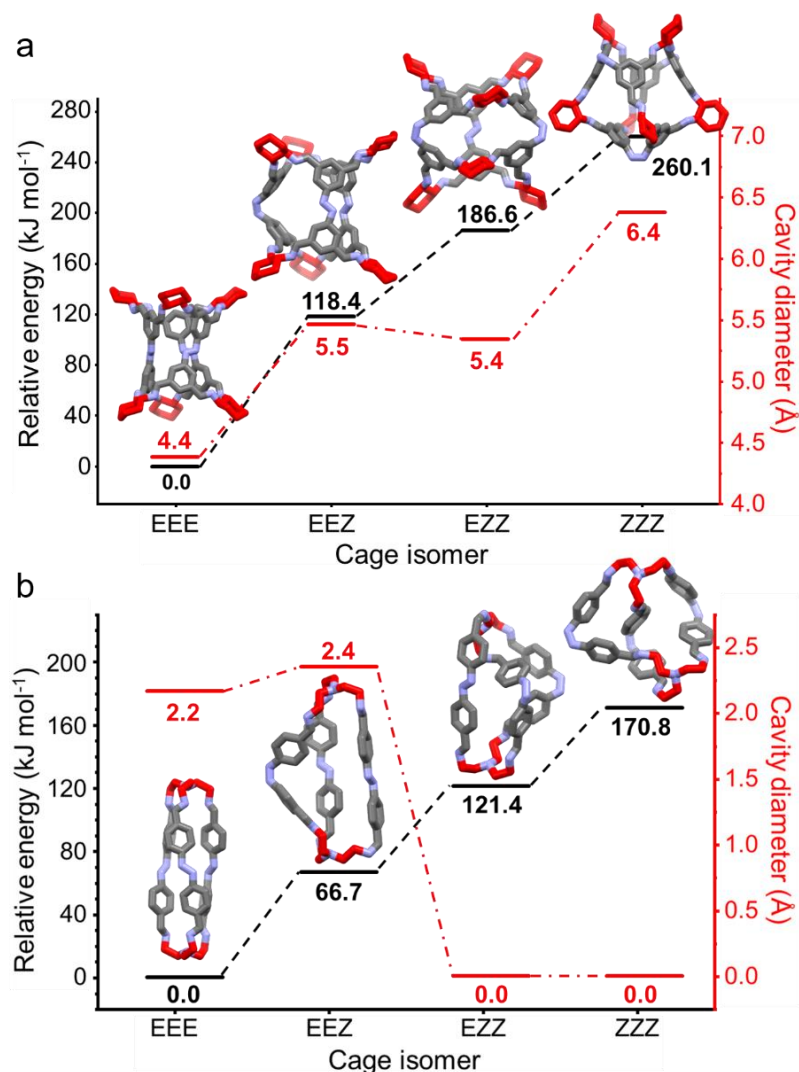


**Figure 2.17** Relative energy (kJ mol<sup>-1</sup>) of azobenzene-derived cages for each isomeric state, *EEE*, *EEZ*, *EZZ*, *ZZZ*, in black, and the corresponding intrinsic cavity diameters (Å) from DFT simulations at the PBE/TZVP-D3 level, where: a) **ACC-1**; b) **ACC-2**.

To explore the degree of photoisomerisation within these cages, samples were prepared in DCM to prevent the acidity of chloroform from forming azonium ions (protonated azobenzene), which is known to have a significantly reduced half-life.<sup>25</sup> Samples were prepared at known concentrations, and are noted as concentration per azobenzene unit rather than concentration of cage, which will be used in further experiments to determine the thermal isomerisation half-life and quantum yield. The PSS was explored using several wavelengths of light to determine the maximum amount of photoisomerisation that could be achieved through continuous exposure with the corresponding wavelength, until no further change was observed in the UV-vis spectra.

Both cages performed very well in terms of their photoisomerisation, where a significant change can be observed in the UV-vis spectra, even before values are determined using Fischer calculations (Figure 2.18). Surprisingly, the cage with the higher relative energy, **ACC-1**, achieved a higher amount of photoisomerisation from *trans* → *cis* than **ACC-2**, which was also unexpected as it was thought **ACC-2** would be more flexible and have more degrees of freedom with the amine component being TREN rather than CHDA. Using the Fischer calculations with the corresponding values from the UV-vis measurements (Tables 2.7-2.8), **ACC-1** was able to achieve 78% photoisomerisation using 340 nm and 73% using 365 nm, which is slightly lower than what pure *trans*-azobenzene is able to achieve (~90%), and is slightly higher than the trisazo-macrocyle.<sup>33,35</sup> **ACC-2** was able to achieve 62% photoisomerisation using 365 nm, which is significantly lower than the reduced Tri<sup>2</sup>Di<sup>3</sup> variant which is reported to have achieved 87% photoisomerisation.<sup>30</sup> This lower photoisomerisation is likely due to the added rigidity of the imine bonds compared to the reduced variant which will contain more flexible secondary amines, creating a lower energy transition state and a less strained cage upon isomerisation.

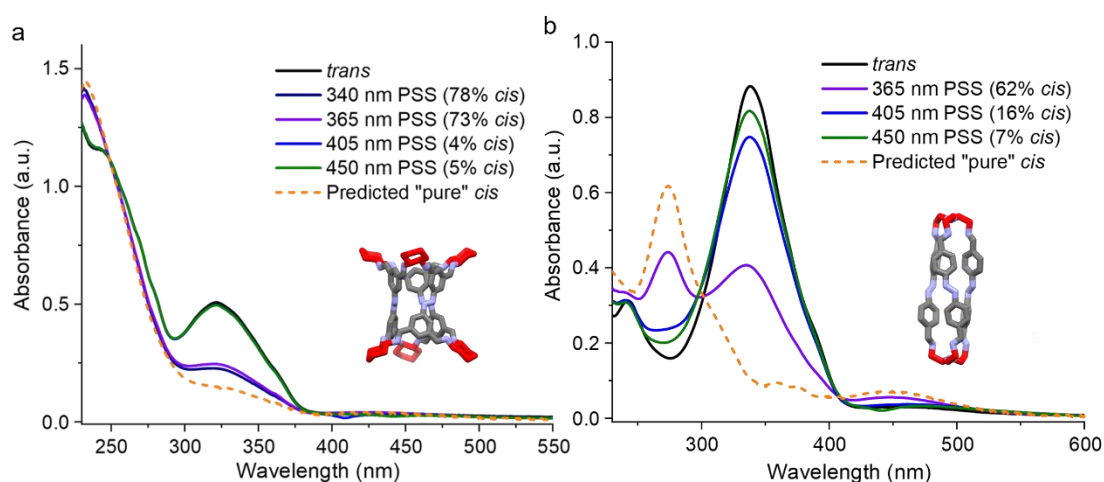


**Figure 2.18** The UV-vis spectra of azobenzene-derived cages measured at 20 °C in CH<sub>2</sub>Cl<sub>2</sub>, where: a) **ACC-1** with ca. 20 μM with respect to the azobenzene units; b) **ACC-2** with ca. 30 μM with respect to the azobenzene units. The percentage of the *cis* isomer present at the PSS of each irradiation wavelengths, and the “pure” *cis* spectrum.



**Table 2.7** Top - Absorption values of **ACC-1** from UV-vis experiments, under dark conditions and irradiated with 340 nm and 365 nm light. Bottom – Calculated values for the PSS using 340 nm and 365 nm light.

Selected $\lambda$ (nm)	Abs. in dark (a.u.)	Abs. at 340 nm after reaching the PSS with 340 nm light (a.u.)	Abs. at 365 nm after reaching the PSS with 365 nm light (a.u.)
365	0.188	0.095	0.104
340	0.413	0.186	0.202
322	0.507	0.227	0.245
$\alpha_2$	0.78	78% Z at 340 nm	
$\alpha_1$	0.73	73% Z at 365 nm	

**Table 2.8** Top - Absorption values of **ACC-2** from UV-vis experiments, under dark conditions and irradiated with 365 nm and 450 nm light. Bottom – Calculated values for the PSS using 340 nm and 450 nm light.

Selected $\lambda$ (nm)	Abs. in dark (a.u.)	Abs. at 365 nm after reaching the PSS with 365 nm light (a.u.)	Abs. at 450 nm after reaching the PSS with 450 nm light (a.u.)
450	0.029	0.055	0.035
365	0.515	0.251	0.514
338	0.884	0.405	0.828
$\alpha_2$	0.07	7% Z at 450 nm	
$\alpha_1$	0.62	62% Z at 365 nm	

One of the other photophysical properties of materials that can be determined through a series of UV-vis experiments is the thermal isomerisation half-life, where azobenzene derivatives can range from picoseconds to more than 1,000 days.<sup>36</sup> For an azobenzene photoreversible system which contains two possible isomers,  $A \xrightleftharpoons{h\nu} B$ , the *cis* to *trans* isomerisation follows first-order kinetics, Eq. (5), where  $k$  is the rate constant.<sup>37</sup> Given the *trans* isomer (A) of azobenzene is the more thermodynamically stable isomer, when switched to the *cis* isomer (B), it will gradually convert back to A

over time. This gradual switching back to the thermodynamically stable isomer can be monitored over time by taking the sample to the PSS by irradiation at a specific wavelength and then recording spectra at regular intervals with the sample in the absence of light. From the data recorded at these intervals, the relative concentrations can be determined which can then be plotted as  $\ln[B]$  versus time, Eq. (6), which should produce a straight line with a negative gradient, following first-order kinetics. The resulting gradient will be equal to the rate constant at that specific temperature.

If the UV-vis spectrometer allows for temperature control of the sample, a series of rate constants can be determined at different temperatures, which can then be utilised in the Eyring equation, Eq. (7), where  $T$  is the absolute temperature in Kelvin,  $R$  is the molar gas constant ( $8.314 \times 10 \text{ J mol}^{-1} \text{ K}^{-1}$ ),  $h$  is Planck's constant ( $6.626 \times 10^{-34} \text{ Js}$ ), and  $k_B$  is Boltzmann's constant ( $1.381 \times 10^{-23} \text{ J K}^{-1}$ ). If the data is plotted as  $\ln(k/T)$  from the previous rate constant experiments, versus  $1/T$ , a straight line should be produced with a negative gradient equal to  $\Delta H/R$ , which allows the enthalpy ( $\Delta H$ ) to be determined. Finally, with these values calculated, the Gibbs free energy can be determined using Eq. (8).

$$\text{Rate} = k[B] \quad \text{Eq. (5)}$$

$$\ln[B] = -kt + \ln [B]_0 \quad \text{Eq. (6)}$$

$$\ln \frac{k}{T} = \frac{-\Delta H}{R} \frac{1}{T} + \ln \frac{k_B}{h} + \frac{\Delta S}{R} \quad \text{Eq. (7)}$$

$$\Delta G = \Delta H - T\Delta S \quad \text{Eq. (8)}$$

$$A = \epsilon cl \quad \text{Eq. (9)}$$

$$\frac{d[A]}{dt} = - \frac{\Phi_A I (1 - 10^{-Abs(t)})}{N_A V} \quad \text{Eq. (10)}$$

To determine the rate constants for **ACC-1** and **ACC-2**, UV-vis experiments were conducted at four different temperatures below the boiling point of DCM, ranging from 15 °C – 35 °C, with these measurements being conducted in a sealed cuvette to prevent solvent loss and changes in concentration (**ACC-1** - Figure 2.19, **ACC-2** - Figure 2.20). Samples were converted to the *cis*-rich PSS using 365 nm, and scans were taken over several hours to produce an accurate representation of the time taken to switch back to the more stable *trans*-configuration. As expected from the previously mentioned equations and the inherent properties of azobenzene, the concentration of the *cis*-isomer decreases over time, where all temperatures for both samples produced a straight line with a negative gradient (best fit line  $R^2 > 0.966$  for all samples). The calculated rate constants from the gradient also provides some insight into the stability of the *cis*-isomer, where **ACC-1** has lower rate constants at the same temperatures as **ACC-2**, demonstrating a slower conversion back to the *trans*-isomer (**ACC-1** - Table 2.9, **ACC-2** - Table 2.10). This seems rather unusual given the significantly higher relative energy for this cage, although the models used to determine the relative energy take place in the gas phase and do not account for the added stability of the solvent. Finally, the rate constants are also consistent with the increasing temperature, where the higher temperatures result in a higher rate constant – **ACC-1** ranges from  $4.06 \times 10^{-6} \text{ s}^{-1}$  to  $1.62 \times 10^{-5} \text{ s}^{-1}$  from 20 °C to 35 °C, whereas **ACC-2** ranges from  $4.64 \times 10^{-6}$  to  $3.71 \times 10^{-5} \text{ s}^{-1}$  over the same temperature range. The use of these rate constants also provides information relating to the thermal isomerisation half-life ( $\tau_{1/2}$ ), where at 20 °C, **ACC-1** has a  $\tau_{1/2}$  of 367 hours (15.3 days) and **ACC-2** has a  $\tau_{1/2}$  of 40 hours (1.7 days). While the data obtained for the thermal half-lives follows a linear fit and represents a first-order process, there is slight deviation away from the linear fit. The time scale of these experiments was also fairly short (less than 8 hours for each experiment) in comparison to the calculated half-lives of **ACC-1** and **ACC-2** which were determined to be 367 hours and 40 hours, where longer experiments may suggest that these systems might not follow first-order kinetics as these experiments suggest. Future experiments will utilise a longer experiment time to gather more data points to determine whether these systems follow first-order kinetics or another possibility would be to attempt the experiment at higher temperatures (in a higher boiling point solvent such as dichloroethane, though this could also lead to different photophysical properties) to reduce the experiment time and observe more of the thermal conversion to get a broader understanding of the system.

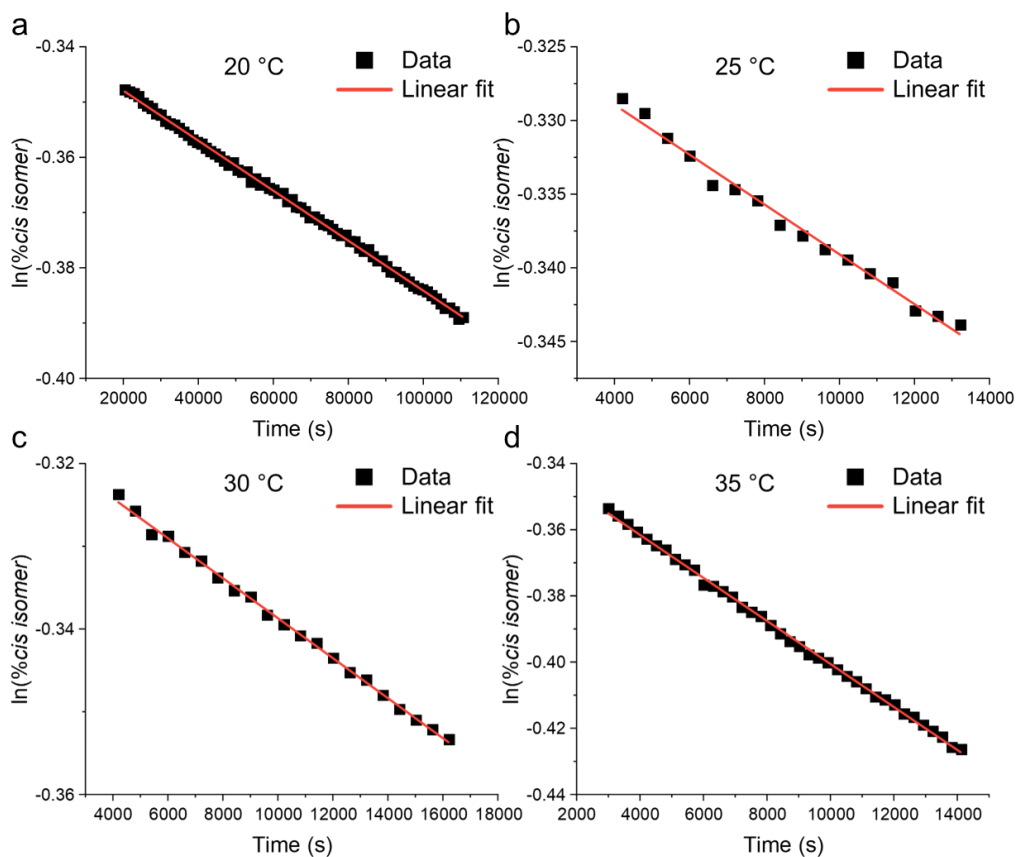


**Figure 2.19** The percentage of the *cis* isomer present in **ACC-1** over time for varying temperatures with the corresponding linear fit line, where: a) 20 °C / 293 K; b) 25 °C / 298 K; c) 30 °C / 303 K; d) 35 °C / 308 K. The percentage of the *cis* isomer was determined via UV-vis measurements.

**Table 2.9** Summary of rate constants,  $k$ , for **ACC-1** at the varying temperatures, with the R-squared value of the linear fit line from Figure 2.19.

Temperature (°C)	Rate constant $k$ (s <sup>-1</sup> )	R-squared of linear fit
20	$1.09 \times 10^{-6}$	0.998
25	$4.06 \times 10^{-6}$	0.985
30	$5.65 \times 10^{-6}$	0.998
35	$1.62 \times 10^{-5}$	0.999

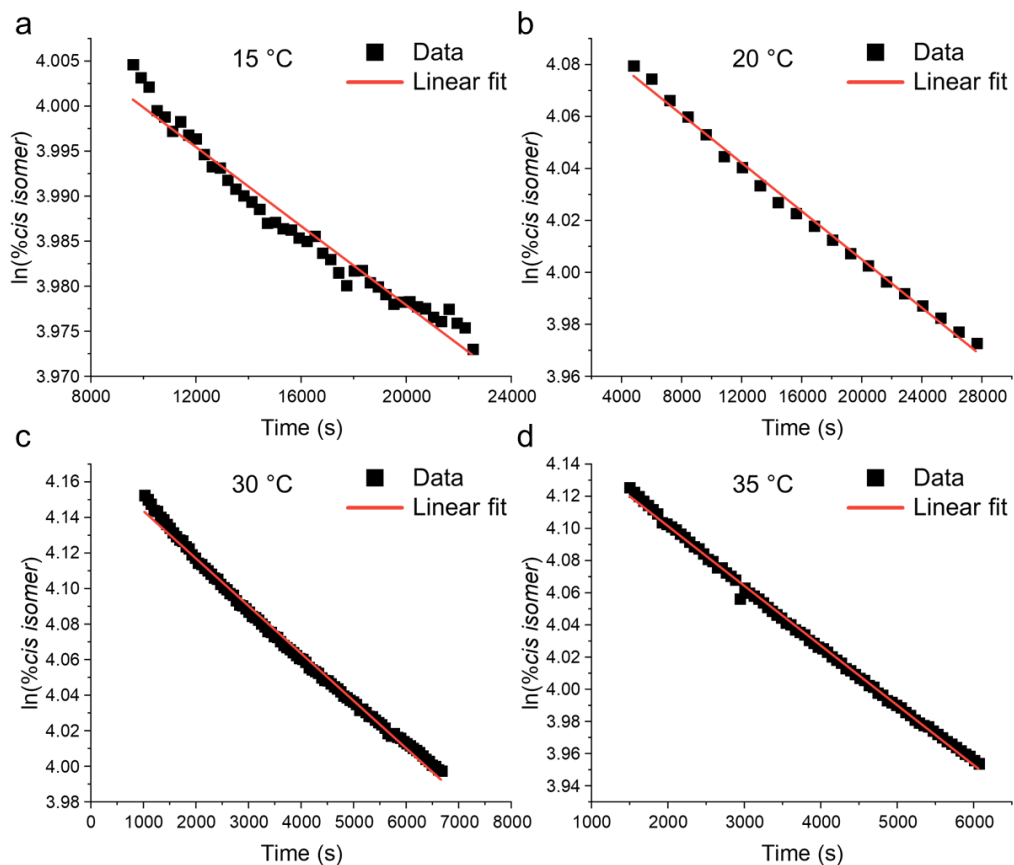


**Figure 2.20** The percentage of the *cis* isomer present in **ACC-2** over time for varying temperatures with the corresponding linear fit line, where: a) 15 °C / 288 K; b) 20 °C / 293 K; c) 30 °C / 303 K; d) 35 °C / 308 K. The percentage of the *cis* isomer was determined via UV-vis measurements.

**Table 2.10** Summary of rate constants,  $k$ , for **ACC-2** at the varying temperatures, with the R-squared value of the linear fit line from Figure 2.20.

Temperature (°C)	Rate constant $k$ (s <sup>-1</sup> )	R-squared of linear fit
15	$2.19 \times 10^{-6}$	0.966
20	$4.64 \times 10^{-6}$	0.994
30	$2.67 \times 10^{-5}$	0.994
35	$3.71 \times 10^{-5}$	0.998

After determining the rate constants, these values can then be plotted as  $\ln(k/T)$  versus  $1/T$  and used in the Eyring equation (Eq. (7)) (**ACC-1** - Figure 2.21, a, **ACC-2** - Figure 2.21, b). This data was plotted for both cages, and produces a linear trend with a negative gradient (best fit line  $R^2 > 0.96$  for both samples). Extrapolation of the data from the gradient of the best fit lines can produce the enthalpy, the intercept provides information relating to the entropy, and the Gibbs free energy can be calculated using the enthalpy and entropy values in Eq. (8) at a specific temperature. This produces the enthalpy, entropy, and Gibbs free energy (at 298 K) as 123 kJ mol<sup>-1</sup>, 55 J mol<sup>-1</sup>, and 107 kJ mol<sup>-1</sup> for **ACC-1**, and 108 kJ mol<sup>-1</sup>, 23 J mol<sup>-1</sup>, and 101.5 kJ mol<sup>-1</sup> for **ACC-2**, respectively (Table 2.11).

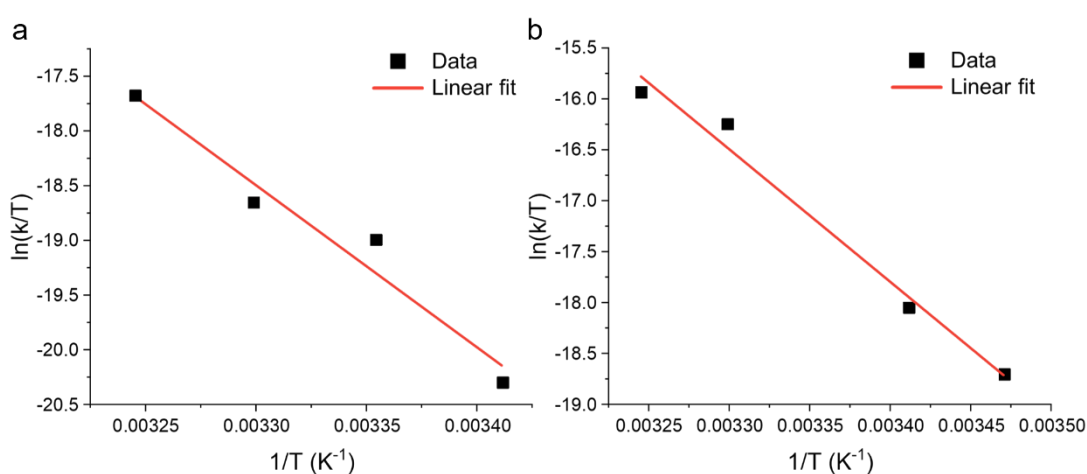


**Figure 2.21** The Eyring plots of azobenzene-derived cages, where: a) **ACC-1**, using the rate constants calculated in Figure 2.19 ( $R^2 = 0.96$ ); b) **ACC-2**, using the rate constants calculated in Figure 2.20 ( $R^2 = 0.98$ ).

**Table 2.11** Summary of values obtained from the Eyring plot's, Beer Lambert law, and Gibbs free energy equations at 298 K for **ACC-1** and **ACC-2**.

Sample	Extinction Coefficient ( $M^{-1} cm^{-1}$ ) at 365 nm		$\Delta H$ (kJ mol <sup>-1</sup> )	$\Delta S$ (J mol <sup>-1</sup> )	$\Delta G$ (kJ mol <sup>-1</sup> )
	<i>Trans</i>	<i>Cis</i>			
<b>ACC-1</b>	11100	4350	123	55	107
<b>ACC-2</b>	12010	1310	108	23	102

Finally, the quantum yields ( $\Phi$ ) for each cage can be established, that is, the ratio of molecules that are converted to the number of photons absorbed by the sample. To determine the quantum yields, experiments were conducted on the sample with methods described by Stranius and Börjesson.<sup>38</sup> The work by Stranius and Börjesson also has a computer programme which can be used to calculate the photon flux and the photoisomerisation quantum yield. To determine these values a light source needs to be used with a known output (as photon flux, number of photons per second), which can be determined through a chemical actinometer (such as a tris-phenanthroline iron (II) complex). With a known photon flux value and a combination of values determined from earlier experimental data, which includes the rate constant (thermal conversion from the *cis* to *trans* isomer), and the extinction coefficients for both the *cis* and *trans* isomers (Table 2.11, determined from the Beer Lambert law (Eq (9))), these values can be input into the programme. Using the light source with a known photon flux, a series UV-vis spectra can be taken after a period of irradiation which will be repeated until the PSS is reached for that wavelength, in the case of these experiments the samples were irradiated for 10 seconds with 365 nm light and a photon flux of  $1.845 \times 10^{16}$  photons per second, which was repeated until no further changes were observed in the UV-vis spectrum. From this data the absorbance at a single point and the irradiation time can then be compiled and added into the programme. Using the constants previously mentioned, the programme is then able to plot the change in absorbance can then be used to plot the experimental data and fits this data with a curve expressed by Eq (10) (Figure 2.22, a and c). With this information it is also able to plot the change in concentration of both components *trans* and *cis* with respect to time, showing the relative concentrations of each isomer. (Note – the concentration of the *cis*-isomer is lower than that determined in previous PSS experiments, which is due to a lower power LED, the specifics of both light sources are noted in the experimental section of this chapter). From the experimental data of the changing concentration with respect to time using a specific light source, the programme is then able to combine the three rates, the forward process (*trans*  $\rightarrow$  *cis*) based on the quantum yield, photon flux and portion of photons absorbed by the *trans* isomer, the thermal conversion to the more stable isomer (*cis*  $\rightarrow$  *trans*), and the backward process (*cis*  $\rightarrow$  *trans*), which is also based on the quantum yield, photon flux and portion of photons absorbed of *cis* isomer. This produces the quantum yields for the *trans*  $\rightarrow$  *cis* process as 0.092 and 0.031, for **ACC-1** and **ACC-2**, and *cis*  $\rightarrow$  *trans* as 0.215 and 0.248 **ACC-1** and **ACC-2**.

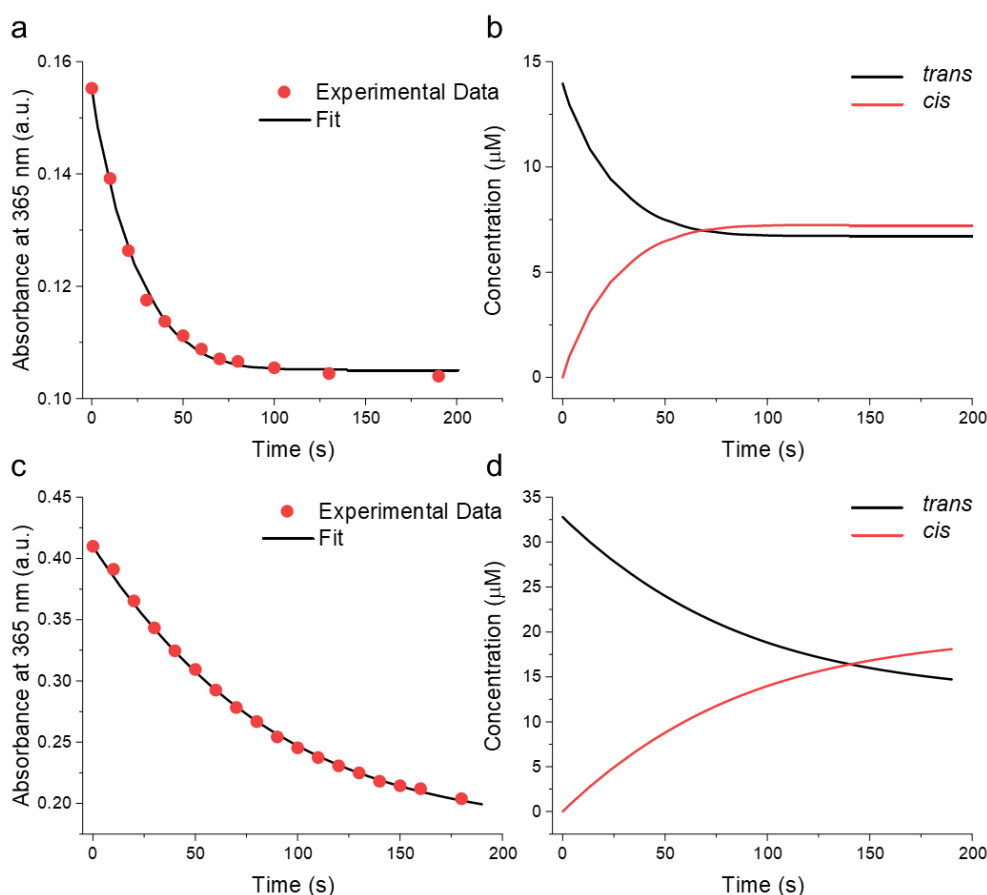


**Figure 2.22** a) Plot of the absorbance at 365 nm of **ACC-1** as a function of irradiation time with a 365 nm LED emitting  $1.845 \times 10^{16}$  photons per second; b) Plot of concentration of **ACC-1** as a function of irradiation time with 365 nm light; c) Plot of the absorbance at 365 nm of **ACC-2** as a function of irradiation time with a 365 nm LED emitting  $1.845 \times 10^{16}$  photons per second; d) Plot of concentration of **ACC-2** as a function of irradiation time with 365 nm light.

### 2.3.6 NMR Studies of Azobenzene-Derived Organic Cages

After determining the amount of photoisomerisation possible using a variety of UV-vis experiments, the question that emerged was whether this photoisomerisation could be observed using  $^1\text{H}$  NMR spectroscopy. While UV-vis provides a large amount of information about photochromic systems in a relatively short time, it lacks the structural information that  $^1\text{H}$  NMR can provide.<sup>39</sup> One of the additional benefits of UV-vis spectroscopy also relates to the sample concentration, as samples are required to be very dilute to prevent oversaturation of the experiment, and specifically with photoisomerisation, means there are fewer molecules absorbing the probe irradiation (*i.e.*, UV light), whereas  $^1\text{H}$  NMR spectroscopy requires a significantly higher sample concentration for the molecules to be observed in the spectra, requiring longer irradiation to observe the effects.



However, before looking at irradiated NMR samples, it makes sense to fully interpret and identify the signals observed from the 'pure' cage samples of **ACC-1** and **ACC-2**. To fully assign all of the peaks observed in the  $^1\text{H}$  and  $^{13}\text{C}$  NMR spectra, a combination of 1D ( $^1\text{H}$ ,  $^{13}\text{C}$ ) and 2D NMRs (COSY, NOESY, HSQC, and HMBC) were used. In both cases, there are a range of proton environments observed in the  $^1\text{H}$  NMR spectra (Figure 2.23, a and Figure 2.28, a), with peaks appearing in the aromatic region (7.0 ppm – 8.5 ppm), along with some mid-region peaks (2.5 ppm – 4 ppm), and several peaks in the lower regions (1.0 ppm – 2.0 ppm). For simplicity, the full characterisation of both cages will be discussed separately, with **ACC-1** first, and **ACC-2** being discussed later. Some spectra have been cut along the axis for clarity, indicated by a broken axis with two diagonal lines. Note – some of the synthesised precursors have some minor impurities which can be seen in the  $^1\text{H}$  NMR spectra in the experimental section of this chapter. In future work will repeat these experiments to ensure they are not present in the cage synthesis.

From the  $^1\text{H}$  NMR spectrum of **ACC-1**, the peaks in the aromatic region appear mostly sharp, but with wide broadening on the base of each peak apparent (Figure 2.23, a). This becomes more apparent later in the chapter, and is a result of partial cage isomerisation, which leads to a lower integration value, when compared to the CHDA-NC(H) protons, which are two distinct peaks occurring at 3.52 ppm and 3.34 ppm, and appear as 'quartets', rather than two doublets of triplets, like that of the reticular cage series reported by Slater *et al.*<sup>4</sup> Peak broadening can also be seen in this region, along with CHDA-C(H) protons, though peak integrations mostly align with those expected from this cage (integrations are normalised to 1 for simplicity, rather than 6). This also adds another degree of complexity in the 2D NMR spectra, as signals from the partially isomerised cages begin to show coupling in regions of interest. In the aromatic region there are 5 distinct proton environments, all with similar integrations, two imines, and three aromatic protons. Three proton environments are observed with equal integrations, rather than two (as 1H and 2H), which arises from the meta-substituted imines which exist in an 'up/down' configuration and can be observed in the scXRD structure (as shown in the structure Figure 2.23). Unfortunately, in the process of trying to isolate the cage using a solvent swap (screening hexane, ethanol, methonal, acetone, and heptane, before determining acetonitrile was a suitable anti-solvent), both H grease and Si grease were introduced into the system and proved difficult to remove.

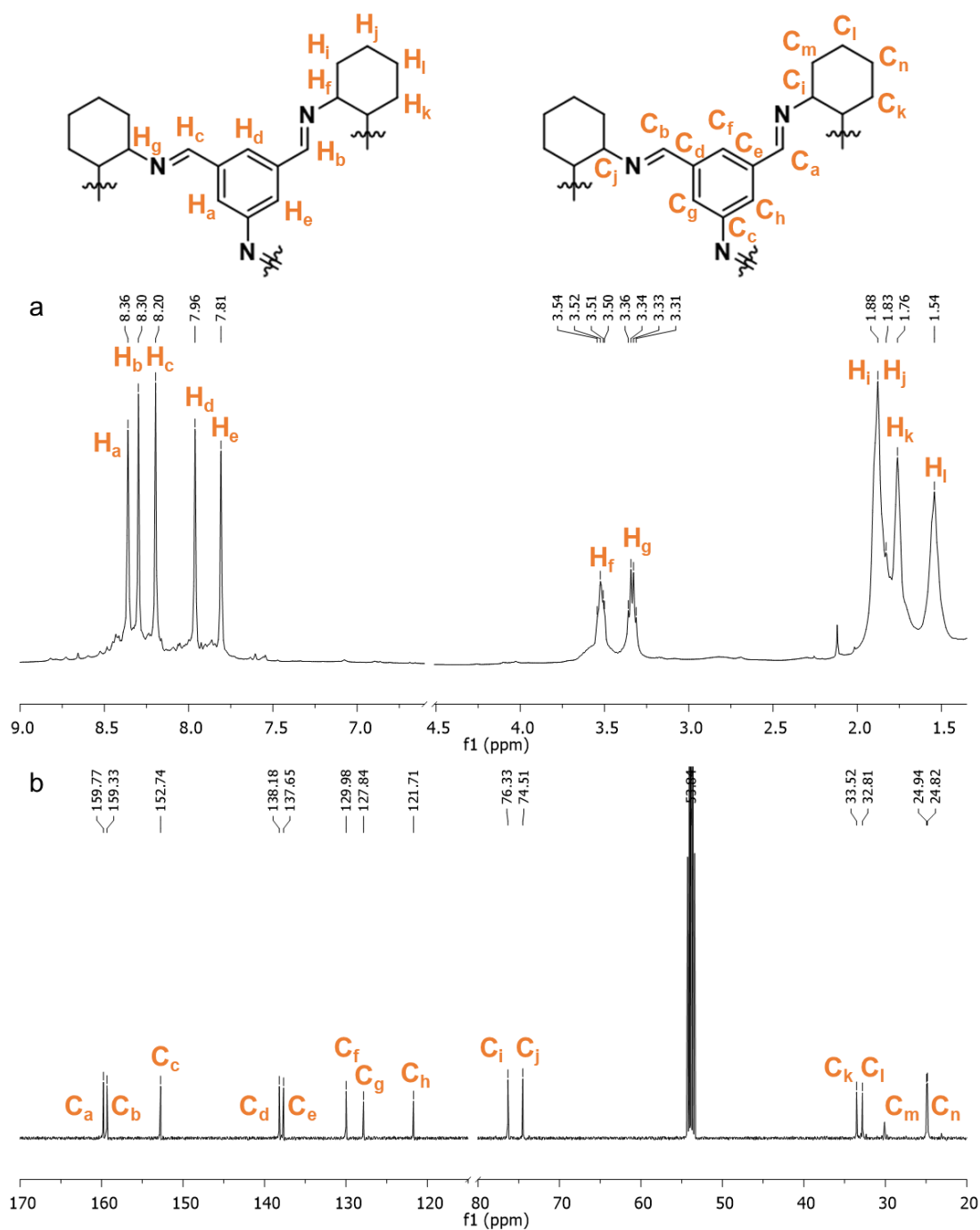


**Figure 2.23** Proton and carbon assignments of **ACC-1** from 1D and 2D NMR interpretation, where a) assigned  $^1\text{H}$  NMR spectrum in  $\text{CD}_2\text{Cl}_2$ ; b) assigned  $^{13}\text{C}$  NMR spectrum in  $\text{CD}_2\text{Cl}_2$ .

A 2D COSY spectrum of **ACC-1** (Figure 2.24) can be used to differentiate the imine protons from the aromatic protons, with  $^1\text{H}$ - $^1\text{H}$  couplings displayed between all three aromatic protons, allowing them to be identified at 8.36 ppm, 7.96 ppm, and 7.81 ppm. No coupling is observed between the aromatic protons and imine protons at 8.30 ppm and 8.20 ppm. Coupling is also observed between both CHDA-NC(H) protons, along with the higher CHDA-NC(H) (3.52 ppm) proton showing coupling to the higher

chemical shift CHDA protons at 1.88 ppm – 1.83 ppm (observed as overlapping peaks), and the lower CHDA-NC(H) (3.34 ppm) proton showing coupling to CHDA protons at 1.76 ppm.

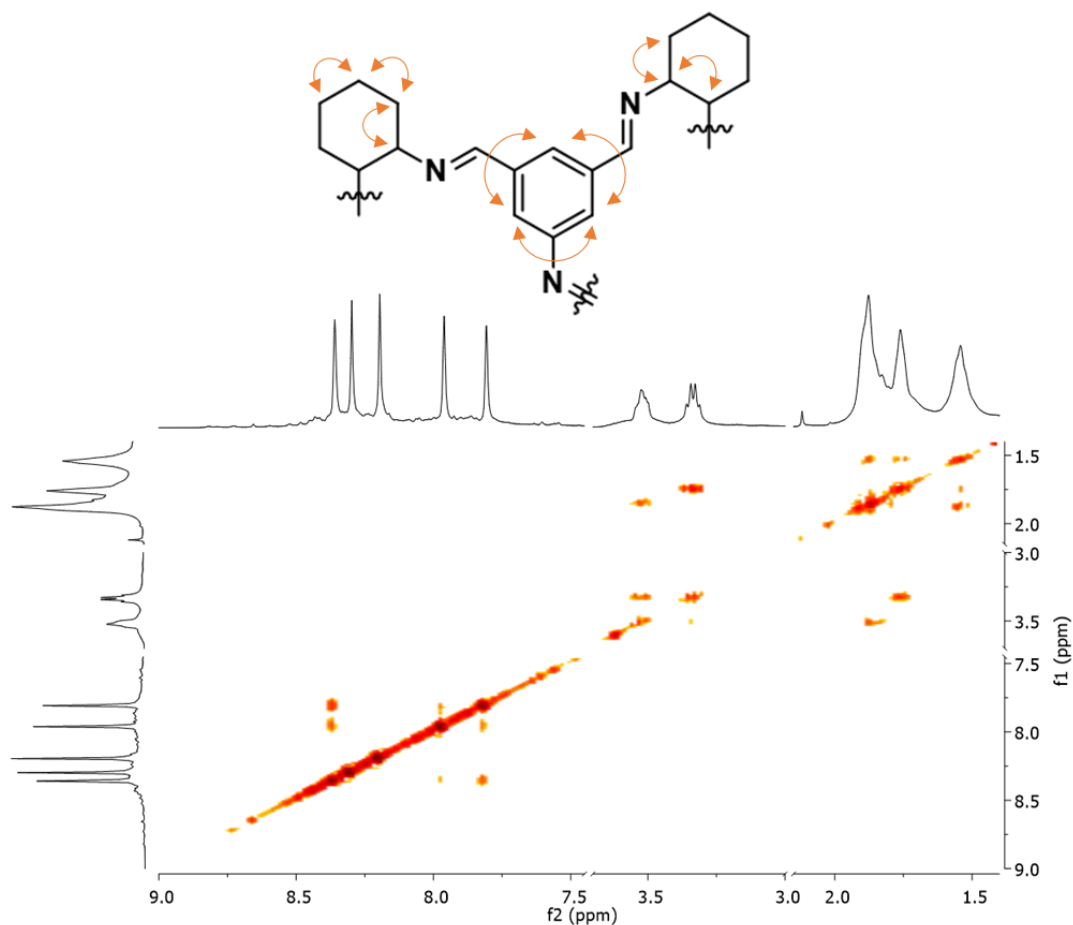


**Figure 2.24** 2D COSY NMR ( $^1\text{H} - ^1\text{H}$ ) spectrum of **ACC-1** in  $\text{CD}_2\text{Cl}_2$  with coupling interactions labelled as orange arrows.

A 2D NOESY spectrum of **ACC-1** (Figure 2.25) also provides a little more insight about several key interactions within the molecule, the first being the interaction between the imine at 8.30 ppm with both the aromatic proton at 7.81 ppm and CHDA-NC(H) proton at 3.52. The second interactions are between the second imine at 8.20 ppm with another aromatic proton at 7.96 ppm and the CHDA-NC(H) proton at 3.34 ppm. This indicates that one proton has no neighbouring imine proton, which can be identified as the proton at 8.36 ppm, marked with an asterisk (\*) in Figure 2.25. Finally, an interaction can also be seen between a set of CHDA protons at 1.88 ppm and 1.54 ppm.

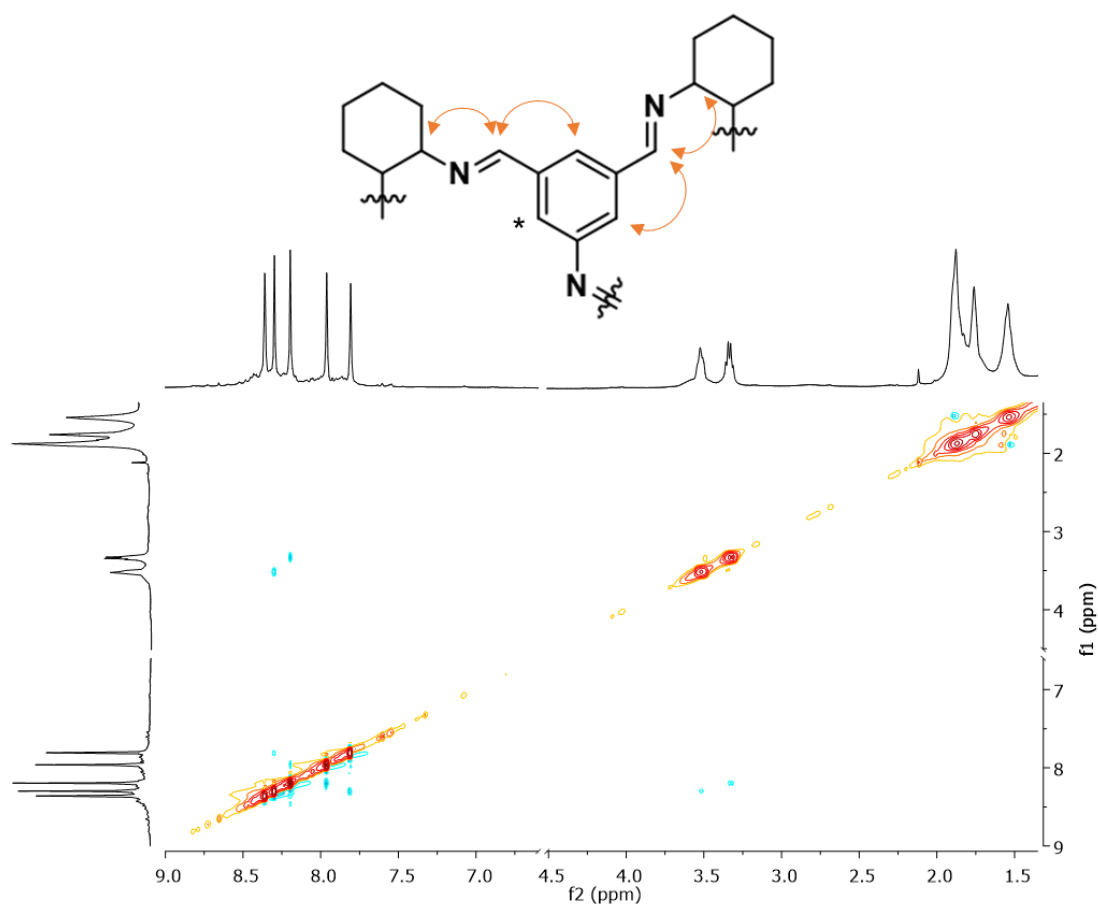


**Figure 2.25** 2D NOESY NMR ( $^1\text{H} - ^1\text{H}$ ) spectrum of **ACC-1** in  $\text{CD}_2\text{Cl}_2$  with coupling interactions labelled as orange arrows. The proton marked with an asterisk (\*) shows no imine interaction.

The  $^{13}\text{C}$  NMR spectrum also exhibits the expected number of peaks, with 14 observable carbon environments (Figure 2.23, b). However, given the close proximity of the signals, it does not provide additional information regarding which carbons correspond to which peak, whereas the 2D HSQC does provide some insight as to which peaks correspond to those with attached protons (Figure 2.26). Unfortunately, the experiment only had a range up to 157 ppm, which misses out both imine peaks. The HSQC further confirms the aromatic protons at 8.36 ppm, 7.96 ppm, and 7.81 ppm, which were identified in the COSY. It also confirms that the broad peak at 1.88 ppm – 1.83 ppm contains two separate protons with vastly different carbon environments, and two very similar carbon environments (24.94 ppm and 24.82 ppm) for the corresponding protons at 1.88 ppm and 1.54 ppm.

Finally, the HMBC (Figure 2.27) enables all of the puzzle pieces to be compiled to determine each signal in the  $^1\text{H}$  and  $^{13}\text{C}$  NMR spectra (Figure 2.23). From the proton identified in the NOESY (8.36 ppm, marked with an asterisk in Figure 2.25), the

HMBC shows coupling with the imine peak at 8.20 ppm, and the remaining two protons at 7.96 ppm, and 7.81 ppm. This confirms the imine at 8.20 ppm is that with the upward facing proton, leaving the downward facing proton as 8.30 ppm. Extrapolation of the NOESY then allows the assignment of the proton between both imines at 7.96 ppm, and the remaining proton between the imine and diazene at 7.81 ppm. HMBC and NOESY also shows coupling between the imine carbons to the CHDA-NC(H) protons, where the downward facing imine proton is coupling with the CHDA-NC(H) proton at 3.52 ppm, and the upward facing imine proton is coupling with the CHDA-NC(H) proton at 3.34. Finally, the COSY spectrum can be used to assign the remaining CHDA protons from both of the CHDA-NC(H) protons. The full proton assignment is shown in Figure 2.23, a. The full carbon assignment can then be determined from these proton assignments using the HSQC and HMBC, and full carbon assignment is shown in Figure 2.23, b.

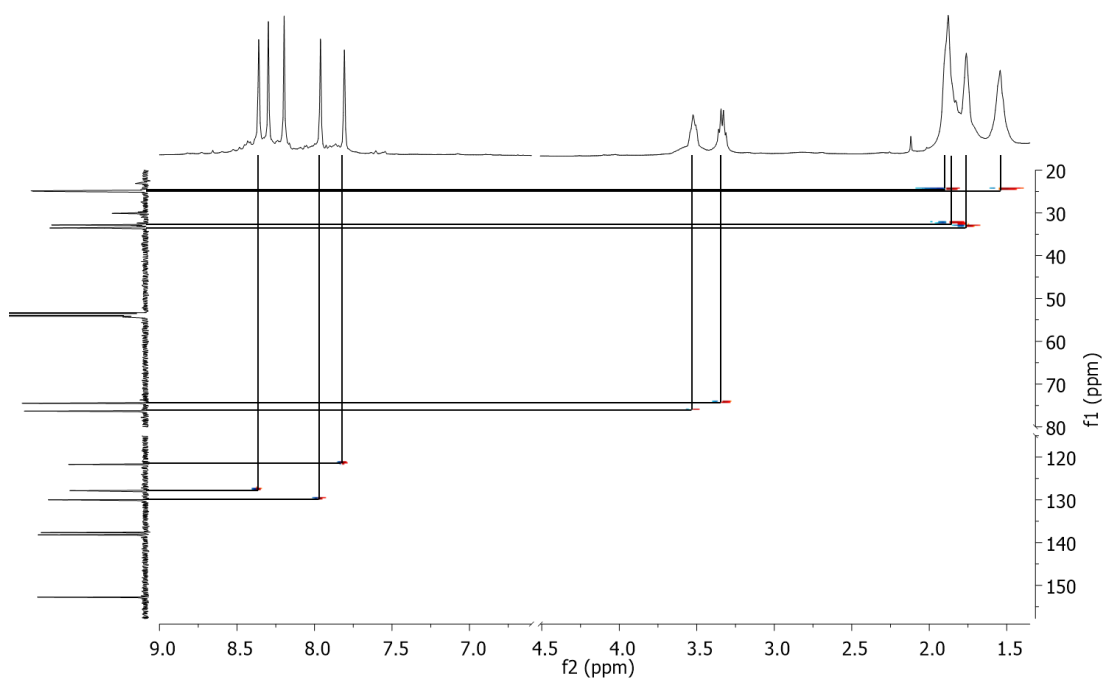


**Figure 2.26** 2D HSQC NMR ( $^1\text{H} - ^{13}\text{C}$ ) spectrum of **ACC-1** in  $\text{CD}_2\text{Cl}_2$  with the  $^1J_{\text{CH}}$  couplings displayed with a black line.

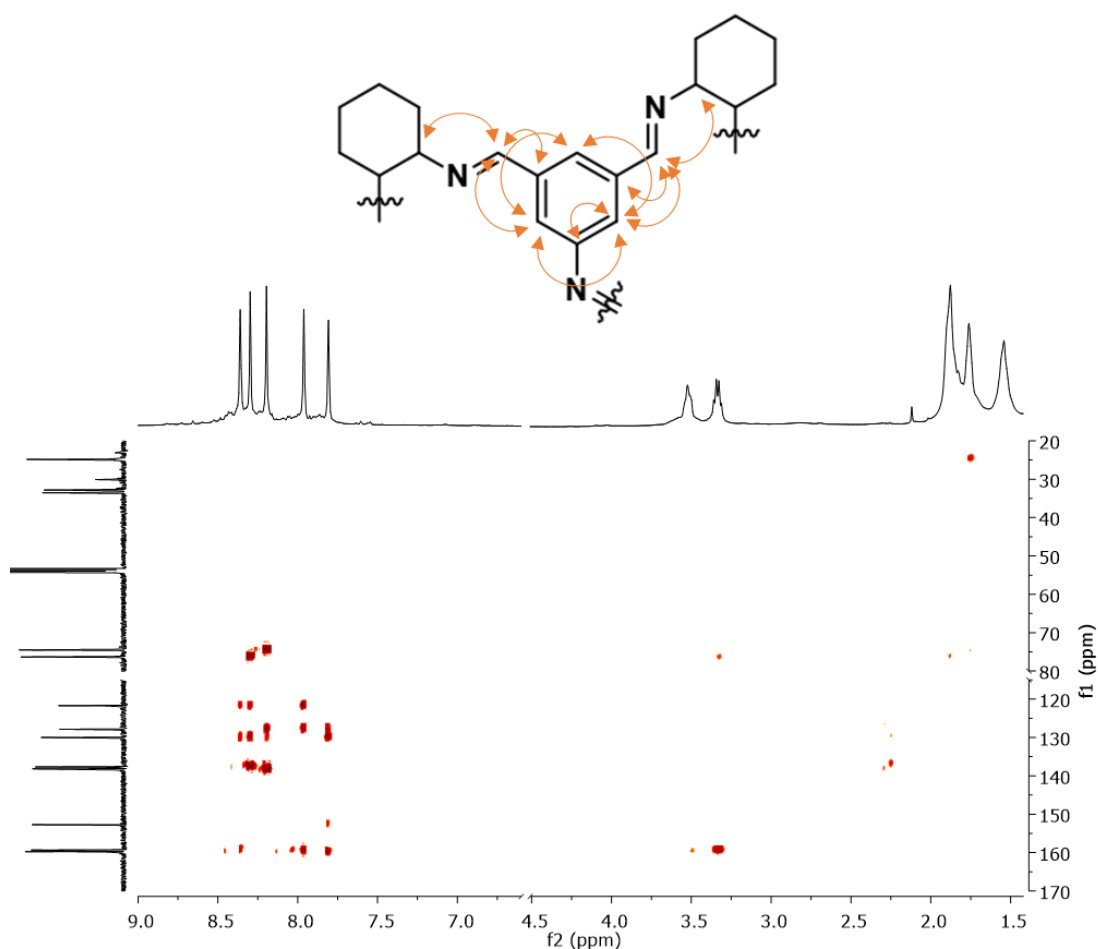


**Figure 2.27** 2D HMBC NMR ( $^1\text{H} - ^{13}\text{C}$ ) spectrum of **ACC-1** in  $\text{CD}_2\text{Cl}_2$  with key interactions labelled as orange arrows.

Fortunately, **ACC-2** provides much simpler  $^1\text{H}$  and  $^{13}\text{C}$  NMR spectra due to the para-substituted imine bonds, which creates a degree of symmetry producing more chemically equivalent protons (Figure 2.28, a). It was previously mentioned that these cages could not be isolated from chloroform, hence they are prepared from dichloromethane. However, **ACC-2** is poorly soluble in  $\text{CD}_2\text{Cl}_2$ , where only small peaks could be observed in the  $^1\text{H}$  NMR spectrum after sonication and gentle heating of the sample. However, it is soluble in  $\text{CDCl}_3$ , and produces all the expected number of peaks in both the  $^1\text{H}$  and  $^{13}\text{C}$  NMR spectra. Sample deterioration is noted with the production of insoluble material in the NMR tube upon collecting the samples the next morning (approximately 16 hours), but is slow enough to allow full characterisation in  $\text{CDCl}_3$ .

The  $^1\text{H}$  NMR spectrum shows five proton environments, with three peaks in the aromatic region, one imine and two aromatic protons, and two peaks in the 2.8 ppm – 3.9 ppm region, for both  $\text{CH}_2$  on TREN. The imine can be identified at 8.28 ppm through integrations (normalised to 1 for simplicity, rather than 6). A 2D COSY

spectrum of the material then shows coupling between the imine signal and one of the CH<sub>2</sub> protons, identifying the protons nearest to the imine at 3.84 ppm, which itself shows coupling with the CH<sub>2</sub> nearest the tertiary amine at 2.84 ppm (Figure 2.29, a). There is also coupling observed between both aromatic protons. A 2D NOESY spectrum of the material shows coupling between the imine and the lower chemical shift aromatic proton, which identifies the doublet at 7.35 ppm and the remaining aromatic protons nearest the diazene as 7.41 ppm (Figure 2.29, b).

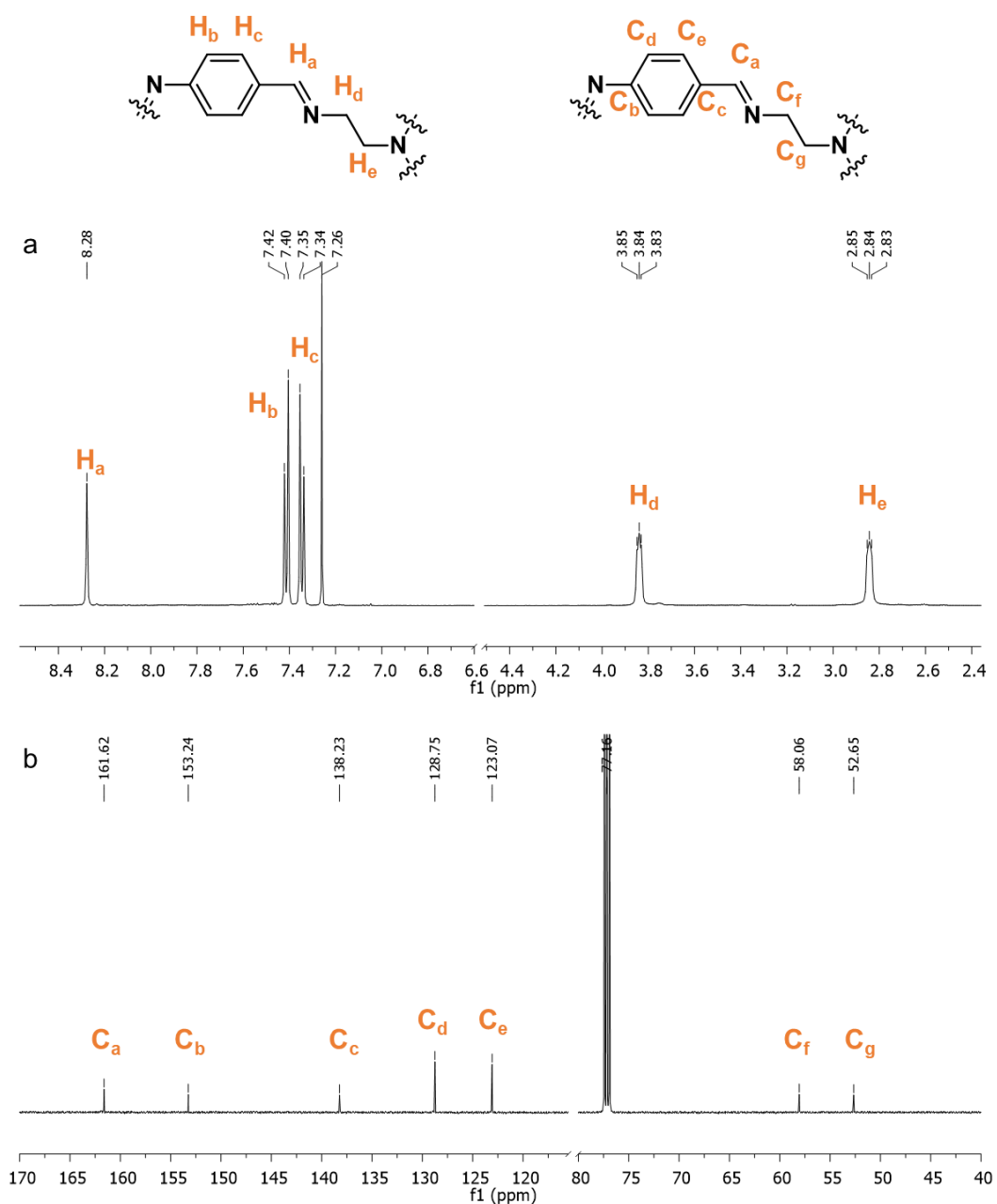


**Figure 2.28** Proton and carbon assignments of **ACC-2** from 1D and 2D NMR interpretation, where: a) assigned <sup>1</sup>H NMR spectrum in CDCl<sub>3</sub>; b) assigned <sup>13</sup>C NMR spectrum in CDCl<sub>3</sub>.

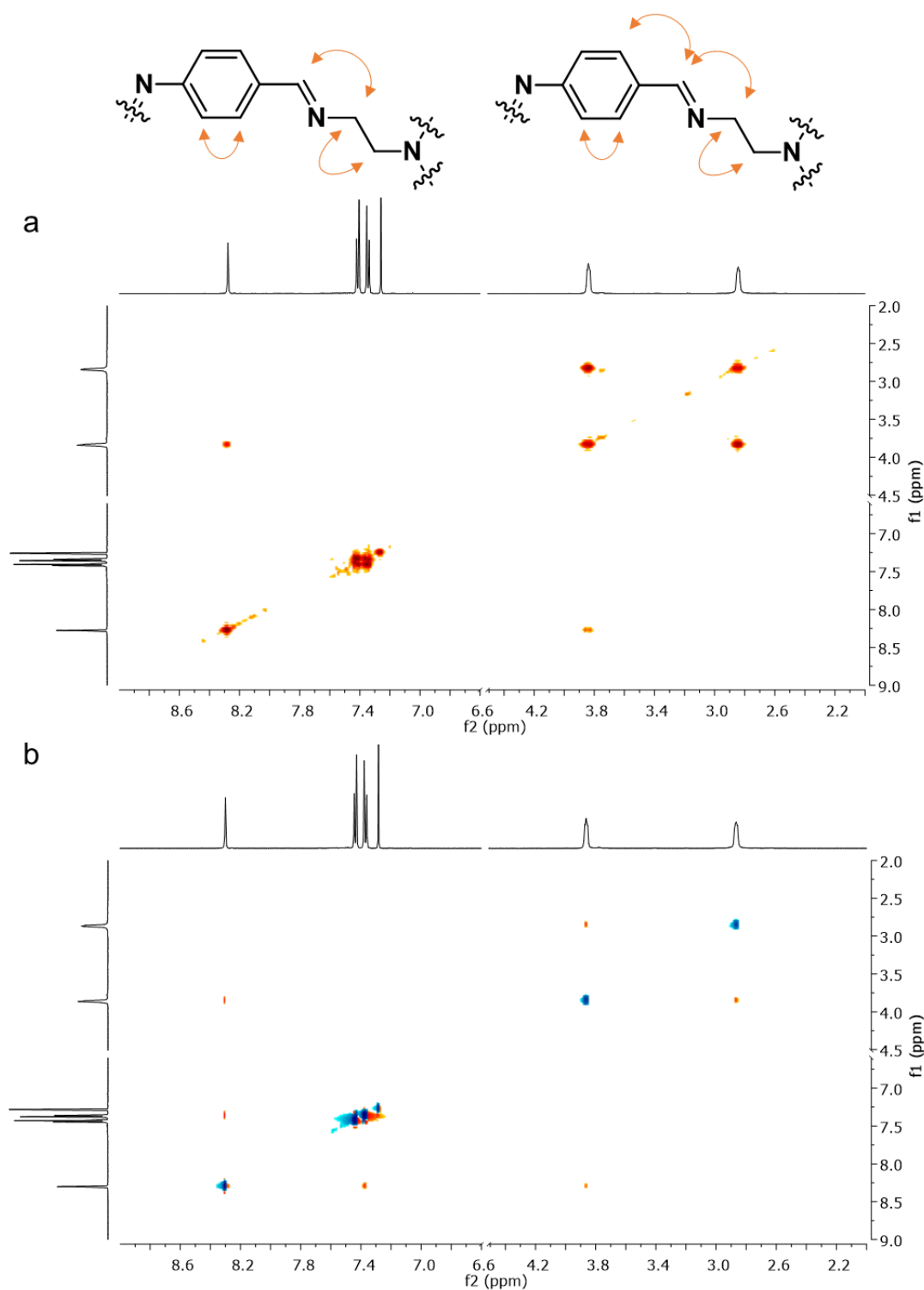


**Figure 2.29** Key couplings observed in the  $^1\text{H}$ – $^1\text{H}$  2D NMR spectra of **ACC-2**, where: a) 2D COSY NMR spectrum in  $\text{CDCl}_3$ ; b) 2D NOESY NMR spectrum in  $\text{CDCl}_3$ .

After the protons had been assigned, the carbon assignment could be achieved using the 2D HSQC NMR spectrum (Figure 2.30, a) to assign carbons based on the known protons, and any additional carbons could be assigned using the HMBC spectrum (Figure 2.30, b). The full proton and carbon assignment is shown in Figure 2.28.



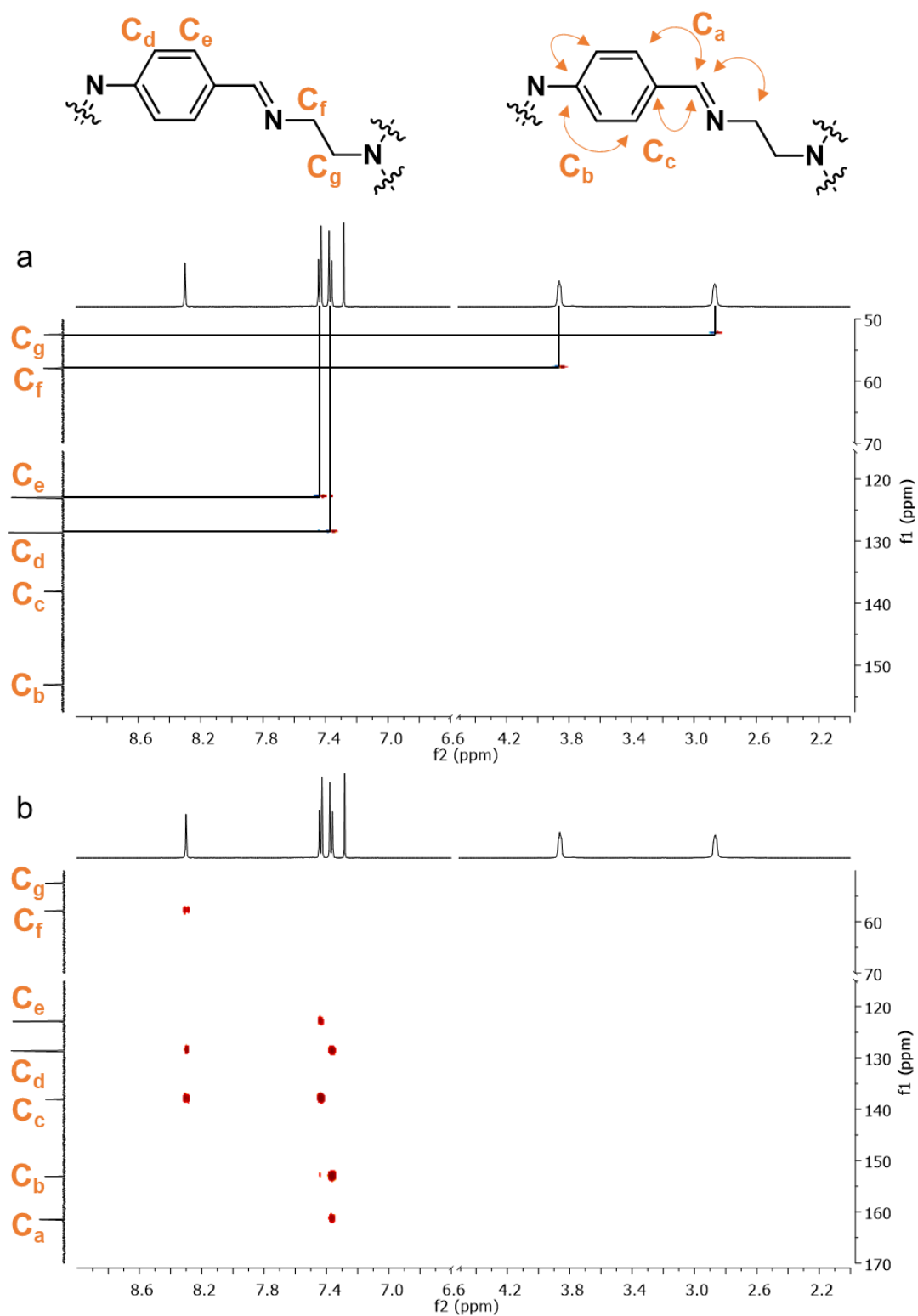


**Figure 2.30** Carbon NMR assignments of **ACC-2**, where: a) HSQC ( $^1\text{H} - ^{13}\text{C}$ ) spectrum of **ACC-2**; b) HMBC ( $^1\text{H} - ^{13}\text{C}$ ) spectrum of **ACC-2**.

Once fully assigned, the  $^1\text{H}$  NMR spectra of **ACC-1** and **ACC-2** were studied after irradiating the sample with 365 nm light (5,200 mW). The  $^1\text{H}$  NMR spectra shows a variety of new proton environments appearing after irradiation, which become more

apparent with longer irradiation times (Figures 2.31-2.32, where the cumulative irradiation times are shown with the corresponding spectrum). As mentioned earlier, the signals in the aromatic region of **ACC-1** displayed some broadening at the base of the peak. This becomes more apparent after irradiation, where new peaks begin to appear from the 'broadening', indicating that some of the initial material showed partial isomerisation under ambient conditions, which explains why the initial integrations of the aromatic peaks were lower than expected when compared to other peaks such as the CHDA-NC(H) protons. There is also an emergence of two new proton environments approximately 0.6 ppm and 1.1 ppm lower than the proton identified at 7.81 ppm. While there are quite dramatic differences in the aromatic region, there are far fewer distinct new peaks in the upfield regions where the CHDA peaks become broader and less defined.

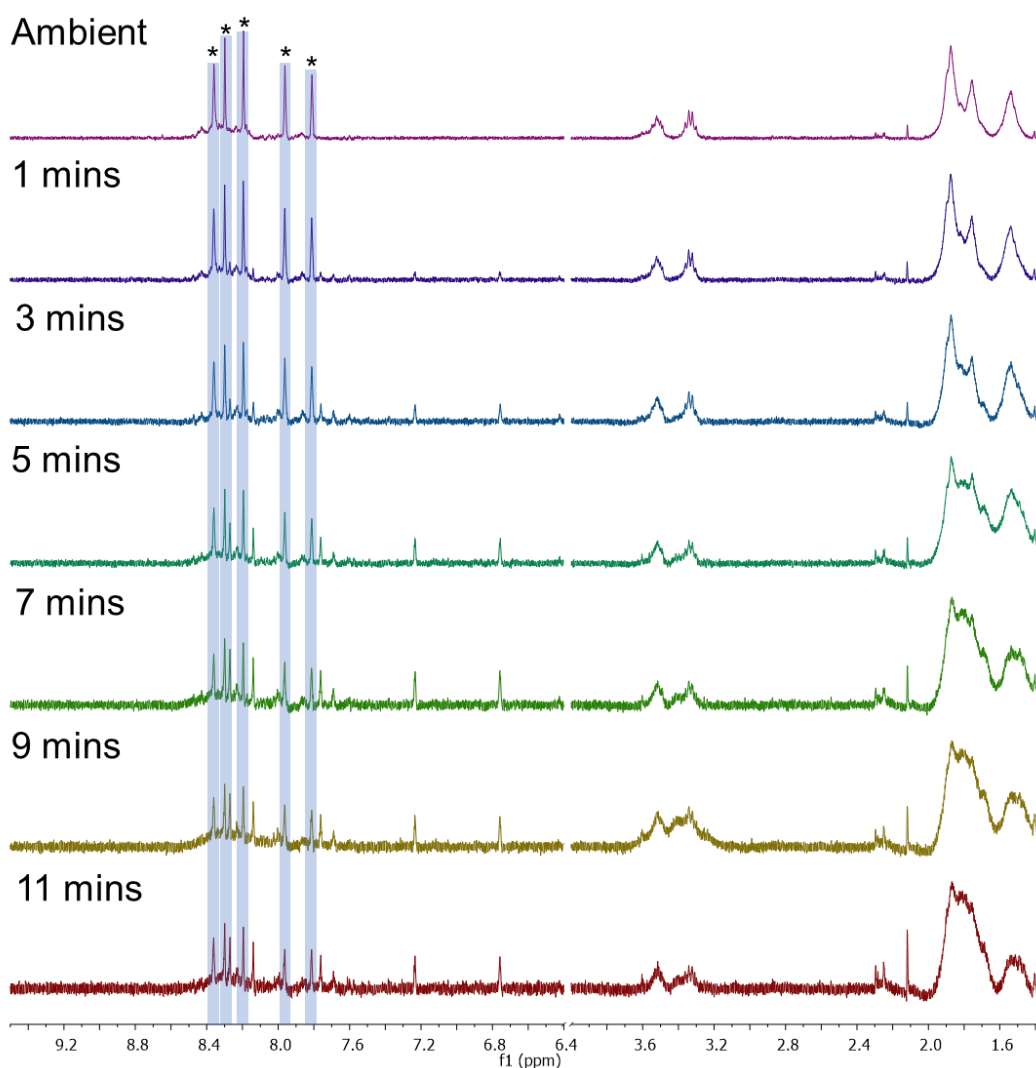


**Figure 2.31** Stacked <sup>1</sup>H NMR spectra in CD<sub>2</sub>Cl<sub>2</sub> of ambient and irradiated samples of **ACC-1**. Time shown is the cumulative irradiation time with 365 nm light. Peaks marked with an asterisk (\*) are used for calculations to determine an approximation of photoisomerisation.

With the same method applied to **ACC-2**, several new peaks also appear in the  $^1\text{H}$  NMR spectra upon irradiation (Figure 2.32), though continued exposure results in a reduced intensity of all cage peaks (Figure 2.33). While no precipitate becomes apparent after irradiation for longer periods (cumulative total irradiation time of 12 minutes), a thin layer of precipitate was observed on the internal walls of the NMR tube upon removing the sample, which proved difficult to remove with organic solvents. After a short period of exposure, there are several distinct new peaks in the aromatic region, one of which is partly visible in the ambient spectrum, at 7.53 ppm. There is also the appearance of a shoulder on the imine peak at 8.28 ppm, along with the appearance of a sharp peak at 8.00 ppm and a doublet at 6.75 ppm. There are also noticeable changes in the TREN region, with two triplets moving closer together at 3.61 ppm and 2.90 ppm.

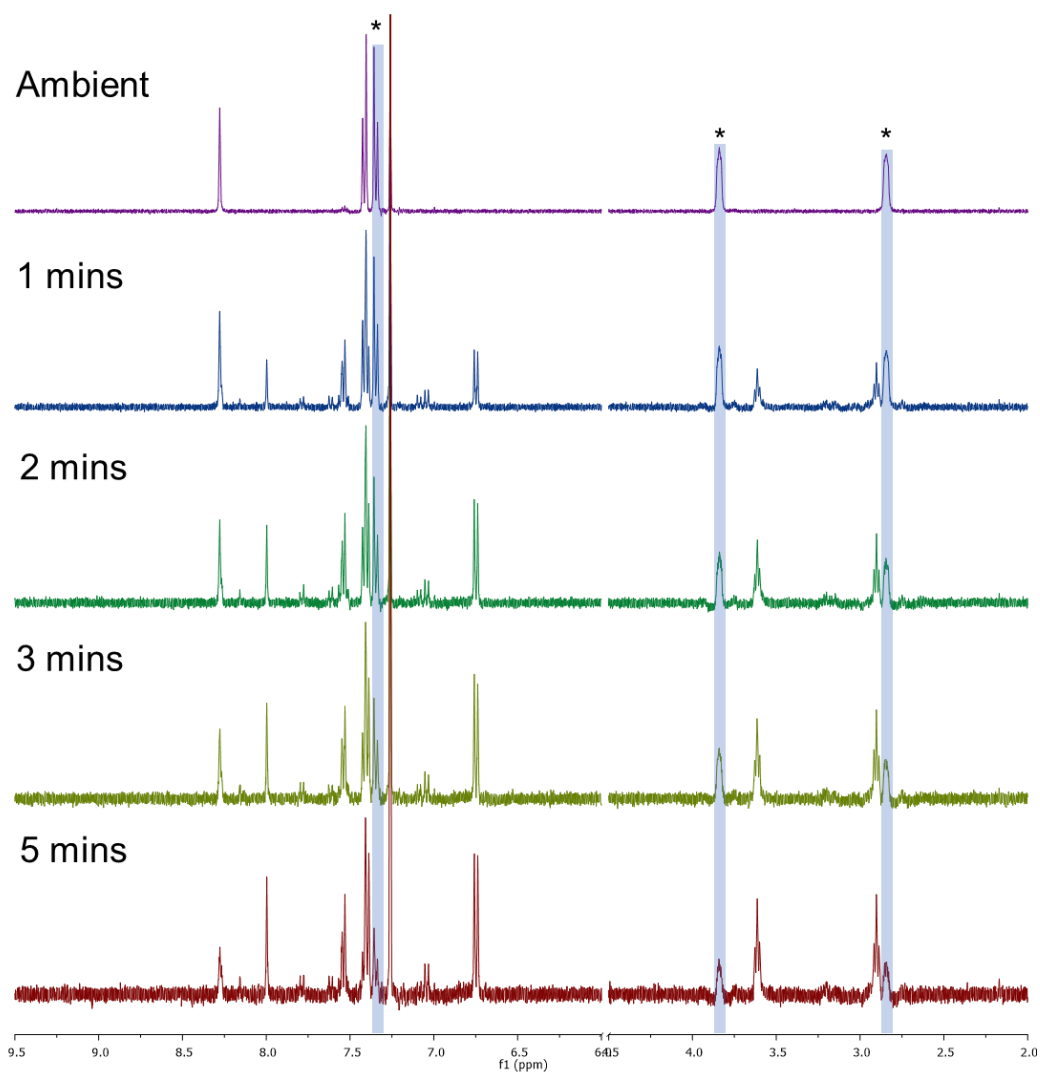


**Figure 2.32** Stacked  $^1\text{H}$  NMR spectra in  $\text{CDCl}_3$  of ambient and irradiated samples of **ACC-2**. Time shown is the cumulative irradiation time with 365 nm light. Peaks marked with an asterisk (\*) are used for calculations to determine an approximation of photoisomerisation.

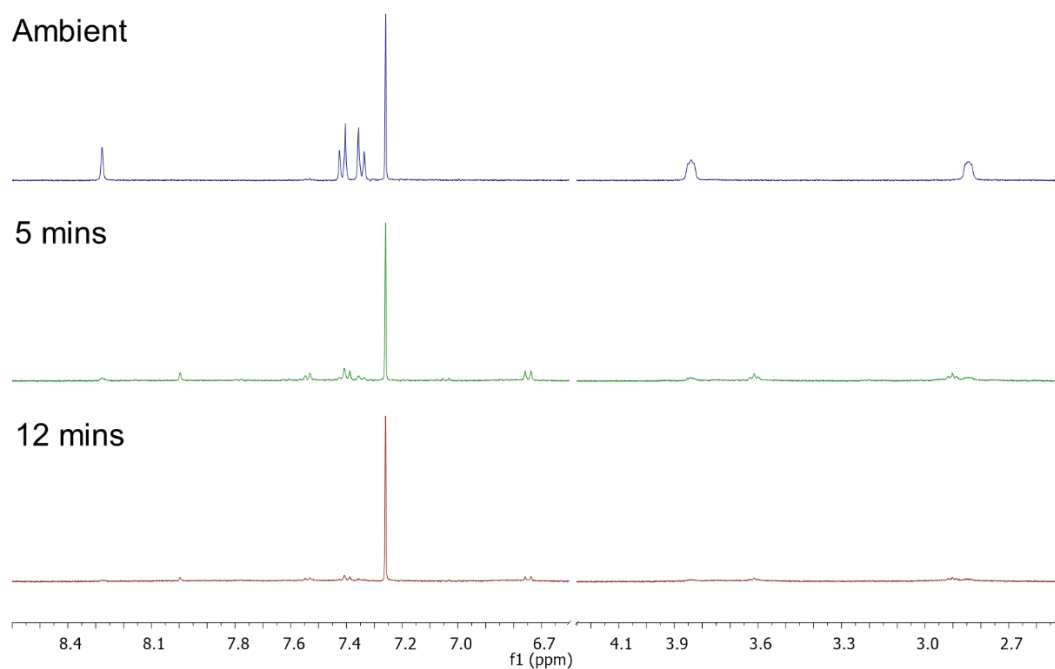


**Figure 2.33** Stacked  $^1\text{H}$  NMR spectra of **ACC-2** in  $\text{CDCl}_3$  with no irradiation (top), 5 minutes of cumulative irradiation (middle), and 12 minutes of cumulative irradiation (bottom).

For both **ACC-1** and **ACC-2**, while it remains fairly difficult to determine the exact quantity of each isomer (that is, *EEZ*, *EZZ*, and *ZZZ*) due to the cages containing three separate azobenzenes each capable of isomerisation, an approximation of the amount of photoisomerisation can be made by utilising the integrations of known peaks. Given the integration of an NMR signal corresponds to the number of nuclei associated with a peak, if an internal standard is used, then the change in integration of known peaks can produce an approximation of the amount of that species remaining in the solution.<sup>39</sup> Given there are some peak overlaps, proton environments were selected that showed no peaks appearing in the direct vicinity. Calculations are based on the assumption that the internal standard does not change throughout the experiments, where the integration of either  $\text{CD}_2\text{Cl}_2$  or  $\text{CDCl}_3$  is normalised to 1. To account for any overlapping peaks, several peaks from the *trans*-isomer were selected and an average was taken to reduce the effect of any new peaks that appear within the same region. For both cages, a significant decrease in integrations was observed across all of the ambient cage peaks, where a percentage decrease of 85% was seen for **ACC-1** (Table 2.12) and a decrease of 90% was seen for **ACC-2** (Table 2.13) which is an approximation of the amount of photoisomerisation. While these values are moderately higher than those determined using UV-vis spectroscopy, these values are an approximation based off of the solvent peaks, which are assumed to be unaffected by the UV irradiation. Another possible reason for the higher values is that a light source was used for with over double the power output (365 nm, 5.2

mW versus 2.4 mW) for the NMR studies, which may lead to more photoisomerisation if the power was insufficient (during the UV-vis studies) to overcome an energy barrier.

**Table 2.12** Summary of integrations at selected  $^1\text{H}$  NMR chemical shifts at different irradiation times for **ACC-1** with the solvent signal,  $\text{CD}_2\text{Cl}_2$ , normalised to 1 and the corresponding average and percentage decrease.

Cumulative irradiation time (minutes)	Integration at selected peaks from $^1\text{H}$ NMR spectrum					Average	Percentage decrease (%)
	8.36	8.3	8.19	7.96	7.81		
0	0.17	0.16	0.16	0.16	0.14	0.158	0
1	0.12	0.11	0.12	0.11	0.09	0.110	30
3	0.08	0.07	0.07	0.07	0.07	0.072	54
5	0.06	0.05	0.05	0.05	0.04	0.050	68
7	0.04	0.04	0.03	0.03	0.02	0.032	79
9	0.03	0.03	0.03	0.03	0.02	0.028	82
11	0.03	0.03	0.02	0.02	0.02	0.024	85

**Table 2.13** Summary of integrations at selected  $^1\text{H}$  NMR chemical shifts at different irradiation times for **ACC-2** with the solvent signal,  $\text{CDCl}_3$ , normalised to 1 and the corresponding average and percentage decrease.

Cumulative irradiation time (minutes)	Integration at selected peaks from $^1\text{H}$ NMR spectrum			Average	Percentage decrease (%)
	7.35	3.84	2.84		
0	0.87	0.86	0.86	0.863	0
1	0.42	0.40	0.40	0.407	53
2	0.26	0.21	0.20	0.223	74
3	0.19	0.18	0.19	0.187	78
5	0.10	0.08	0.08	0.087	90

## 2.4 Conclusions

In this chapter, two organic cages were identified through a computational screen, leading to the successful incorporation of three azobenzene-derived aldehydes into both cages. These aldehydes were based on creating a cage which was capable of undergoing a structural change upon irradiation, resulting in a change in shape with each consecutive isomerisation, as *EEE*, *EEZ*, *EZZ*, and *ZZZ*, which would also produce a change in cavity size. A computational study showed both cages increase in relative energies on isomerisation, where both cages in their *trans*-configuration would have the lowest relative energy, and the cages in their *cis*-configuration would have the highest relative energy. A computational study also showed that the larger cage in the study, **ACC-1**, would have an increasing cavity size upon total isomerisation (*EEE* to *ZZZ*) from 4.4 Å to 6.4 Å, and the smaller cage, **ACC-2**, would result in a complete collapse of the internal cavity from 2.2 Å to 0 Å.

Both cages were successfully isolated and fully characterised through 1D and 2D NMR studies, along with single crystal X-ray crystallography, where the structure and packing were established. Photoisomerisation NMR studies also showed a variety of new proton environments and the amount of photoisomerisation was determined to be 85% for **ACC-1** and 90% for **ACC-2**.

The photophysical properties of each cage were also investigated using a number of UV-vis experiments. These experiments were used in combination with reported literature on systems capable of photoisomerisation to determine the photophysical properties of the cages including the photostationary state, quantum yield, and the thermal isomerisation half-lives. Both cages were shown to be able of undergoing *trans* to *cis* photoisomerisation, where **ACC-1** demonstrated a photoisomerisation of 78% on irradiation at 365 nm with a thermal half-life of 367 hours, and **ACC-2** displayed a possible photoisomerisation of 62% on irradiation at 365 nm with a 40-hour thermal half-life.

## 2.5 Experimental

**Materials:** Chemicals were purchased from Sigma-Aldrich, Fluorochem or TCI UK and used as received. Solvents were reagent or HPLC grade purchased from Fisher Scientific or Sigma-Aldrich. All chemicals and solvents were used as received, unless otherwise specified.

**Synthesis:** Any reactions requiring anhydrous or inert conditions were performed in oven-dried or flame dried apparatus under an inert atmosphere of dry nitrogen, using anhydrous solvents introduced into the flask using disposable needles and syringes. All reactions were stirred magnetically using Teflon-coated stirring bars. Where heating was required, the reactions were warmed using a stirrer hotplate with heating blocks with the stated temperature being measured externally to the reaction flask with an attached probe. Removal of solvents was done using a rotary evaporator.

**TLC and column chromatography:** Reactions were monitored by thin layer chromatography (TLC). Spots were visualised either by an ultraviolet light, staining with potassium permanganate or staining with vanillin. Flash column chromatography was performed manually or using a Biotage Isolera with KP-Sil normal phase disposable columns.

**NMR spectra:**  $^1\text{H}$  and  $^{13}\text{C}$  Nuclear magnetic resonance (NMR) spectra were recorded using Bruker Avance III 400 (400 MHz) or Bruker DRX500 (500 MHz) spectrometers at ambient probe temperature. NMR data are presented as follows: chemical shift (expressed in ppm on a  $\delta$  scale), peak multiplicity (s = singlet, brs = broad singlet, d = doublet, t = triplet, q = quartet, m = multiplet), coupling constants ( $J$  / Hz) and integration. Chemical shifts are reported referenced to residual solvent where  $^1\text{H}$   $\text{CDCl}_3$  ( $\delta$  = 7.26 ppm),  $^1\text{H}$   $\text{CD}_2\text{Cl}_2$  ( $\delta$  = 5.32 ppm),  $^{13}\text{C}$   $\text{CDCl}_3$  ( $\delta$  = 77.16 ppm), and  $^{13}\text{C}$   $\text{CD}_2\text{Cl}_2$  ( $\delta$  = 53.84 ppm). For irradiated samples an external light source (Omicure S1000, fitted with a 365 nm filter) was used to irradiate the respective samples in quartz NMR tubes for the appropriate amount of time prior to running the experiment.

**HRMS:** Electrospray ionization mass spectrometry (ES-MS) was carried out using an Agilent Technologies 6530B accurate-mass QTOF Dual ESI mass spectrometer (MeOH + 0.1% formic acid, capillary voltage 4000 V, fragmentor 225 V) in positive-ion detection mode for cage samples. For all other compounds the departmental analytical services were used and were run using an Agilent Technologies QTOF 7200 or Agilent Technologies QTOF 6540.

**Melting points:** Obtained using Stuart SMP10 digital melting point apparatus and are reported uncorrected.

**IR spectra:** Infra-red (IR) spectra were recorded on a Bruker Alpha Platinum-ATR with measurements for oils and solids as neat samples.

**Single crystal X-ray Diffraction:** Single crystal X-ray data for **ACC-1** and **ACC-2**, crystallised from CHCl<sub>3</sub>/MeOH, were measured on a Rigaku MicroMax-007 HF rotating anode diffractometer (Mo-K $\alpha$  radiation,  $\lambda = 0.71073 \text{ \AA}$ , Kappa 4-circle goniometer, Rigaku Saturn724+ detector. Absorption corrections, using the multi-scan method, were performed with the program CrysAlisPro 1.171.40.45a. Structures were solved with SHELXT,<sup>40</sup> and refined by full-matrix least-squares on  $|F|^2$  by SHELXL,<sup>41</sup> interfaced through the program OLEX2.<sup>42</sup> H atom positions for the C-H groups were refined using the riding model.

**PXRD:** Powder X-ray diffraction data were collected in transmission mode on samples held on a metal 96-shallow well plate on a Panalytical X'Pert PRO MPD equipped with a high-throughput screening (HTS) XYZ stage, X-ray focusing mirror and PIXcel detector, using Ni-filtered Cu K $\alpha$  radiation. Data were measured over the range 4–50° in ~0.013° steps over 30 minutes.

**UV-Vis:** UV-vis absorption spectra of materials were obtained on a Cary 60 UV-vis spectrophotometer equipped with a temperature controller, Shimadzu UV-2550 UV-vis, or an Agilent 8453 UV-vis spectrophotometer operated at room temperature. Samples were measured in a UV Quartz cuvette with a path length of 10 mm. Solutions of the compounds were prepared in HPLC or higher-grade solvents.

**Photoswitching:** Samples were irradiated with a custom-built irradiation set up using 365 nm (3  $\times$  800 mW Nichia NCSU276A LEDs), 405 nm (3  $\times$  770 mW Nichia NCSU119C LEDs), and 450 nm (3  $\times$  900 mW NCSC219B-V1 LEDs) light sources, operated at 100% power. To verify that PSS at each wavelength was reached, the sample was irradiated until no change in the UV-vis spectrum was observed. For all compounds, the UV-vis measurements were taken immediately after irradiation.

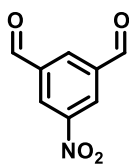
**Quantum Yield Measurements:** Ferrioxalate actinometry was used to determine the photon flux from a Nichia NCSU276A 365 nm LED (365 nm, 800 mW @ 100% power) operating at 5% power, fitted with a collimating lens, following a previously reported procedure.<sup>38</sup> The cuvette was placed 3.5 cm away from the light source. The photon flux of the 365 nm LED operating at 5% power for the setup was determined to be  $1.845 \times 10^{16}$  photons/s. The quantum yield of photoisomerization ( $\Phi$ ) for the switches



under 365 nm light was determined using a previously reported literature procedure and the calculation was performed using their provided software.<sup>38</sup>

**Thermal Isomerisation Kinetics** Thermal *Z-E* isomerisation kinetics were followed by UV-vis spectroscopy. The thermal isomerisation kinetics were measured over a range of temperatures allowing the creation of a Eyring plots to determine the thermodynamic parameters of the thermal isomerisation. The measurements were performed in an air-tight cuvette using CH<sub>2</sub>Cl<sub>2</sub> as the solvent. The samples were initially converted to the *cis*-rich PSS (using 365 nm light) and the absorbance was then recorded over time. The samples were left to equilibrate for a minimum of 10 minutes in the temperature-controlled cell holder. Between measurements the sample was kept inside the instrument at a constant temperature in the absence of ambient light.

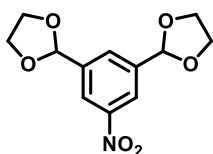
### 5-Nitroisophthalaldehyde (**4**)



Isophthalaldehyde (4.0 g, 30 mmol, 1.0 eq.) was dissolved in H<sub>2</sub>SO<sub>4</sub> (98%, 13 mL) and cooled to 0 °C in an ice bath. A mixture containing H<sub>2</sub>SO<sub>4</sub> (98%, 4 mL) and HNO<sub>3</sub> (65%, 8 mL) was added dropwise over the course of 2 hours. The resulting mixture was then heated to 50 °C for 1 hour. After cooling to room temperature, the mixture was then poured over ice. The precipitate was extracted with DCM (~150 mL) and washed with water (3 x 100 mL). The organic layer was isolated, dried (MgSO<sub>4</sub>), and the solvent was removed *in vacuo*. Purification *via* column chromatography (gradient petroleum ether/EtOAc 0-20%) afforded the desired product **4** as a colourless solid (4.6 g, 26 mmol, 87%).

**<sup>1</sup>H NMR** (400 MHz, CDCl<sub>3</sub>) δ 10.21 (s, 2H), 8.96 (d, *J* = 1.4 Hz, 2H), 8.72 (t, *J* = 1.4 Hz, 1H); **<sup>13</sup>C NMR** (101 MHz, CDCl<sub>3</sub>) δ 188.65, 149.63, 138.41, 134.71, 128.70; Data in accordance with literature values.<sup>43</sup>

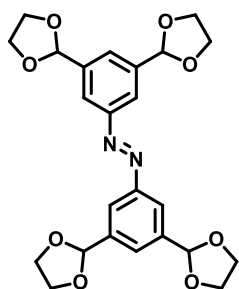
### 2,2'-(5-Nitro-1,3-phenylene)bis(1,3-dioxolane) (**5**)



5-Nitroisophthalaldehyde **4** (2.5 g, 14 mmol, 1.0 eq.), ethylene glycol (2.06 mL, 37 mmol, 2.6 eq.) and *p*-toluenesulfonic acid (0.4 g, 2 mmol, 0.14 eq.) were dissolved in toluene (50 mL). The reaction mixture was heated to reflux for 16 hours, fitted with a pre-filled Dean-Stark apparatus. After cooling to room temperature, the toluene was removed *in vacuo*. Water was added to the solid mixture, and the solid collected by filtration under vacuum and washed with additional water (200 mL). The resulting solid was left to dry under continuous air flow to afford the desired product **5** as a colourless solid (3.3 g, 12.9 mmol, 92%) and was used without further purification.

**MP** 57 - 60 °C; **IR** (ν<sub>max</sub>/cm<sup>-1</sup>) 2954, 2892, 1532, 1465, 1344, 1164, 1083, 967, 881, 725, 706, 655; **<sup>1</sup>H NMR** (400 MHz, CDCl<sub>3</sub>) δ 8.34 (d, *J* = 1.5 Hz, 2H), 7.91 (t, *J* = 1.5 Hz, 1H), 5.90 (s, 2H), 4.15 - 4.05 (m, 8H); **<sup>13</sup>C NMR** (101 MHz, CDCl<sub>3</sub>) δ 148.49, 140.85, 130.84, 122.29, 102.24, 65.63; **HRMS** (CI) calc. for C<sub>12</sub>H<sub>13</sub>NO<sub>6</sub> [M+H]<sup>+</sup> 268.0816, found 268.0820.

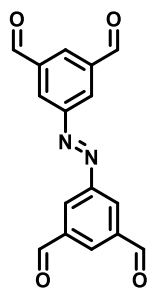
### (E)-1,2-Bis(3,5-di(1,3-dioxolan-2-yl)phenyl)diazene (6)



2,2'-(5-Nitro-1,3-phenylene)bis(1,3-dioxolane) **5** (0.99 g, 5.8 mmol, 1.0 eq.), sodium hydroxide (0.9 g, 23.2 mmol, 4.0 eq.), and zinc dust (0.7 g, 11.6 mmol, 2.0 eq.) was dissolved in distilled ethanol (25 mL) and water (12.5 mL). The reaction mixture was heated to 100 °C for 20 hours. The reaction mixture was diluted with water and neutralized with 1 M HCl. The crude mixture was filtered and washed with water. The filtrate was separated with chloroform (3 x100 mL), and the organic layers combined. The combined organic layers were dried (Na<sub>2</sub>SO<sub>4</sub>) and concentrated *in vacuo*. The crude product was purified by column chromatography (gradient petroleum ether/EtOAc 0-50%). This afforded the desired product **6** as an orange/brown solid (0.57 g, 1.2 mmol, 41%).

**MP** 155 - 157 °C; **IR** ( $\nu_{\max}/\text{cm}^{-1}$ ) 2886, 1369, 1165, 1007, 939, 882, 701; **<sup>1</sup>H NMR** (400 MHz, CDCl<sub>3</sub>)  $\delta$  8.06 (d,  $J = 1.5$  Hz, 4H), 7.73 (t,  $J = 1.5$  Hz, 2H), 5.95 (s, 4H), 4.19 – 4.13 (m, 8H), 4.10 – 4.06 (m, 8H); **<sup>13</sup>C NMR** (101 MHz, CDCl<sub>3</sub>)  $\delta$  152.77, 139.88, 127.25, 121.88, 103.22, 65.51; **HRMS** (ES<sup>+</sup>) calc. for C<sub>24</sub>H<sub>26</sub>N<sub>2</sub>O<sub>8</sub> [M+H]<sup>+</sup> 471.1762, found 471.1760.

### (E)-5,5'-(Diazene-1,2-diyl)diisophthalaldehyde (1)



(E)-1,2-Bis(3,5-di(1,3-dioxolan-2-yl)phenyl)diazene **6** (0.4 g, 1 mmol, 1.0 eq.) and *p*-toluenesulfonic acid (0.02 g, 0.1 mmol, 0.1 eq.) was dissolved in a 3:1 mix of acetone/water (20 mL). The reaction mixture was heated to 60 °C for 18 hours. After cooling to room temperature, the acetone was removed *in vacuo*. The mixture was filtered and washed with additional water (200 mL). The resulting solid was dried under vacuum to afford the desired product **1** as an orange solid (0.24 g, 0.84 mmol, 81%).

**MP** 239 - 240 °C; **IR** ( $\nu_{\max}/\text{cm}^{-1}$ ) 1694, 1597, 1381, 1127, 961, 894, 683, 648, 527; **<sup>1</sup>H NMR** (400 MHz, CDCl<sub>3</sub>)  $\delta$  10.25 (s, 4H), 8.74 (d,  $J = 1.5$  Hz, 4H), 8.58 (t,  $J = 1.5$  Hz, 2H); **<sup>13</sup>C NMR** (101 MHz, CDCl<sub>3</sub>)  $\delta$  190.28, 153.13, 138.36, 132.74, 128.81; **HRMS** (CI) calc. for C<sub>16</sub>H<sub>10</sub>N<sub>2</sub>O<sub>4</sub> [M+H]<sup>+</sup> 295.0713, found 295.0720.

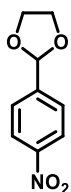
### Azobenzene Covalent Cage – 1 (ACC-1, Tet<sup>3</sup>Di<sup>6</sup> cage)

(*E*)-5,5'-(Diazene-1,2-diyl)diisophthalaldehyde (1) (0.12 g, 0.4 mmol, 1.0 eq.) and (1*R*,2*R*)-cyclohexanediamine ((*R,R*)-CHDA, 0.09 g, 0.8 mmol, 2.0 eq.) were dissolved in DCM (70 mL). The reaction mixture was stirred at room temperature for 7 days. The reaction mixture was filtered to remove insoluble precipitates before the addition of acetonitrile (~50 mL). The DCM was carefully removed *in vacuo* (no heat on rotary evaporator water bath), and the resulting precipitate was collected by filtration. The isolated solid was left to dry under continuous air flow to afford the desired product as an orange solid (0.16 g, 0.12 mmol, 88%)

**IR** ( $\nu_{\max}/\text{cm}^{-1}$ ): 2923, 2853, 1643, 1446, 1370, 1309, 1234, 1154, 1141, 1091, 1038, 975, 940, 886, 860, 845, 797, 749, 688, 665, 553, 535, 476, 443; **<sup>1</sup>H NMR** (500 MHz, CD<sub>2</sub>Cl<sub>2</sub>)  $\delta$  8.36 (s, 5H), 8.30 (s, 5H), 8.20 (s, 5H), 7.96 (s, 5H), 7.81 (s, 5H), 3.54 – 3.50 (m, 6H), 3.36 – 3.31 (m, 6H), 1.88 (brs, 24H), 1.83 (s, 6H), 1.76 (br s, 18H), 1.54 (brs, 18H); **<sup>13</sup>C NMR** (126 MHz, CD<sub>2</sub>Cl<sub>2</sub>)  $\delta$  159.77, 159.33, 152.74, 138.18, 137.65, 129.98, 127.84, 121.71, 76.33, 74.51, 33.52, 32.81, 24.94, 24.82; **HRMS** (ES+) calc. for **ACC-1** C<sub>84</sub>H<sub>90</sub>N<sub>18</sub> [M+H]<sup>+</sup> 1351.7669, found [M+H]<sup>+</sup> 1351.7664.

Note – <sup>1</sup>H NMR integration values are reported as observed rather than ‘true’ values, full characterisation can be found in **2.3.6**.

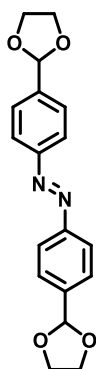
### 2-(4-Nitrophenyl)-1,3-dioxolane (7)



4-Nitrobenzaldehyde (5.2 g, 35 mmol, 1.0 eq.), ethylene glycol (2.06 mL, 37 mmol, 1.05 eq.), and *p*-toluenesulfonic acid (1.0 g, 5 mmol, 0.15 eq.) were dissolved in toluene (50 mL). The reaction mixture was heated at reflux for 16 hours, fitted with a pre-filled Dean-Stark apparatus. After cooling to room temperature, the toluene was removed *in vacuo*. Water was added to the solid mixture, and the solid collected by filtration under vacuum and washed with additional water (200 mL). The resulting solid was left to dry under continuous air flow to afford the desired product **7** as a yellow solid (6.6 g, 33.8 mmol, 96%) which was used without further purification.

**<sup>1</sup>H NMR** (400 MHz, CDCl<sub>3</sub>)  $\delta$  8.23 (d, *J* = 8.8 Hz, 2H), 7.65 (d, *J* = 8.5 Hz, 2H), 5.89 (s, 1H), 4.14 – 4.05 (m, 4H); **<sup>13</sup>C NMR** (101 MHz, CDCl<sub>3</sub>)  $\delta$  148.54, 145.08, 127.55, 123.71, 102.37, 65.61; Data in accordance with literature values.<sup>44</sup>

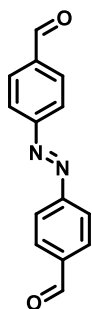
### (E)-1,2-Bis(4-(1,3-dioxolan-2-yl)phenyl)diazene (**8**)



2-(4-Nitrophenyl)-1,3-dioxolane **7** (1.0 g, 5 mmol, 1.0 eq.), sodium hydroxide (0.8 g, 20 mmol, 4.0 eq.), and zinc dust (0.6 g, 10 mmol, 2.0 eq.) was dissolved in distilled ethanol (25 mL) and water (12.5 mL). The reaction mixture was heated to 100 °C for 20 hours. The reaction mixture was diluted with water and neutralized with 1 M HCl. The crude mixture was filtered and washed with water. The filtrate was separated with chloroform (3 x100 mL), and the organic layers combined. The combined organic layers were dried ( $\text{Na}_2\text{SO}_4$ ) and concentrated *in vacuo*. The crude product was purified by column chromatography (gradient petroleum ether/EtOAc 0-40%), and the orange band collected. This afforded the desired product **8** as an orange solid (0.46 g, 1.4 mmol, 56%).

**MP** 146 - 148 °C; **IR** ( $\nu_{\text{max}}/\text{cm}^{-1}$ ) 2895, 2847, 1385, 1218, 1073, 1011, 975, 939, 834, 695, 594, 529; **<sup>1</sup>H NMR** (400 MHz,  $\text{CDCl}_3$ )  $\delta$  7.94 (d,  $J = 8.5$  Hz, 4H), 7.63 (d,  $J = 8.3$  Hz, 4H), 5.90 (s, 2H), 4.30 – 3.95 (m, 8H); **<sup>13</sup>C NMR** (101 MHz,  $\text{CDCl}_3$ )  $\delta$  153.23, 140.89, 127.42, 123.08, 103.38, 65.53; **HRMS** (ES+) calc. for  $\text{C}_{18}\text{H}_{18}\text{N}_2\text{O}_4$   $[\text{M}+\text{H}]^+$  327.1339, found 327.1347.

### (E)-4,4'-(Diazene-1,2-diyl)dibenzaldehyde (**1**)



(E)-1,2-Bis(4-(1,3-dioxolan-2-yl)phenyl)diazene **8** (0.15 g, 0.47 mmol, 1.0 eq.) and *p*-toluenesulfonic acid (0.008 g, 0.05 mmol, 0.1 eq.) was dissolved in an 3:1 mix of acetone/water (10 mL). The reaction mixture was heated to 50 °C for 18 hours. After cooling to room temperature, the acetone was removed *in vacuo*. The mixture was filtered and washed with additional water (100 mL). The resulting solid was dried under vacuum to afford the desired product **1** as an orange solid (0.11 g, 0.47 mmol, quant.).

**MP** 234 - 235 °C; **IR** ( $\nu_{\text{max}}/\text{cm}^{-1}$ ) 1734, 1607, 1476, 1433, 1340, 1225, 881, 798, 656, 560, 539; **<sup>1</sup>H NMR** (400 MHz,  $\text{CDCl}_3$ )  $\delta$  10.13 (s, 2H), 8.10 (d,  $J = 8.7$  Hz, 4H), 8.07 (d,  $J = 8.7$  Hz, 4H); **<sup>13</sup>C NMR** (101 MHz,  $\text{CDCl}_3$ )  $\delta$  191.49, 155.59, 138.07, 130.75, 123.73; **HRMS** (CI) calc for  $\text{C}_{14}\text{H}_{10}\text{N}_2\text{O}_2$   $[\text{M}+\text{H}]^+$  239.0815, found 239.0823.

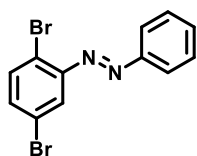
### Azobenzene Covalent Cage – 2 (ACC-2, Tri<sup>2</sup>Di<sup>3</sup> cage)

(*E*)-4,4'-(Diazene-1,2-diyl)dibenzaldehyde (**1**) (0.12 g, 0.50 mmol, 3.0 eq.) and tris(2-aminoethyl)amine (TREN) (36  $\mu$ L, 0.3 mmol, 2.0 eq.) were dissolved in DCM (70 mL). The reaction mixture was stirred at room temperature for 7 days. The reaction mixture was filtered to remove insoluble precipitates before the addition of hexane (~100 mL). The DCM was carefully removed *in vacuo* (no heat on rotary evaporator water bath), and the resulting precipitate was collected by filtration. The isolated solid was left to dry under continuous air flow to afford the desired product as a red solid (0.112 g, 0.13 mmol, 78%).

(Note – sample is highly soluble in chloroform, though formation of insoluble material occurs after some time. Sample is partly soluble in DCM.)

**IR** ( $\nu_{\max}/\text{cm}^{-1}$ ); 2962, 2869, 2832, 2787, 1641, 1573, 1367, 1337, 1291, 1239, 1209, 1149, 1074, 1037, 902, 842, 753, 552, 432; **<sup>1</sup>H NMR** (500 MHz, CDCl<sub>3</sub>)  $\delta$  8.28 (s, 6H), 7.41 (d,  $J$  = 8.4 Hz, 12H), 7.35 (d,  $J$  = 8.4 Hz, 12H), 3.84 (t,  $J$  = 4.4 Hz, 12H), 2.84 (t,  $J$  = 4.6 Hz, 12H); **<sup>13</sup>C NMR** (126 MHz, CDCl<sub>3</sub>)  $\delta$  161.62, 153.24, 138.23, 128.75, 123.07, 58.06, 52.65; **HRMS** (ES+) calc. for **ACC-2** C<sub>54</sub>H<sub>54</sub>N<sub>14</sub> [M+H]<sup>+</sup> 899.4729, found [M+H]<sup>+</sup> 899.1126.

### (*E*)-1-(2,5-Dibromophenyl)-2-phenyldiazene (**9**)

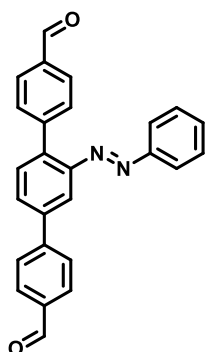


2,5-Dibromoaniline (1.31 g, 5.2 mmol, 1.0 eq.) and nitrosobenzene (0.54 g, 5 mmol, 1.0 eq.) was dissolved in glacial acetic acid (~20 mL). The reaction mixture was heated to 60 °C for 16 hours. After cooling to room temperature, the solvent was removed *in vacuo*. The

crude mixture was partitioned between water (50 mL) and chloroform (50 mL), and the organic layer separated. The aqueous layer was extracted with chloroform (3 x 50 mL) and the combined organic layers dried (Na<sub>2</sub>SO<sub>4</sub>) and concentrated *in vacuo*. Purification *via* column chromatography (gradient hexane/EtOAc 0-5%) afforded the desired product **9** as a red solid (0.33 g, 0.98 mmol, 20%).

**MP** 80 - 84 °C; **IR** ( $\nu_{\max}/\text{cm}^{-1}$ ) 1441, 1367, 1206, 1147, 1067, 1031, 931, 884, 849, 807, 768, 701, 680, 568, 539, 502, 445; **<sup>1</sup>H NMR** (400 MHz, CDCl<sub>3</sub>)  $\delta$  8.02 – 7.96 (m, 2H), 7.83 (d,  $J$  = 2.4 Hz, 1H), 7.62 (d,  $J$  = 8.5 Hz, 1H), 7.57 – 7.51 (m, 3H), 7.43 (dd,  $J$  = 8.5, 2.4 Hz, 1H); **<sup>13</sup>C NMR** (101 MHz, CDCl<sub>3</sub>)  $\delta$  152.50, 150.26, 135.00, 134.51, 132.26, 129.40, 124.55, 123.77, 122.15, 121.16; **HRMS** (CI) calc. for C<sub>12</sub>H<sub>8</sub>Br<sub>2</sub>N<sub>2</sub> [M+H]<sup>+</sup> 338.9127, found 338.9126.

**(E)-2'-(Phenyldiazenyl)-[1,1':4',1''-terphenyl]-4,4''-dicarbaldehyde (3)**



To an oven dried round bottomed flask equipped with a stirrer bar, was added (*E*)-1-(2,5-dibromophenyl)-2-phenyldiazene **9** (0.30 g, 0.88 mmol, 1.0 eq.) and (4-formylphenyl)boronic acid (0.31 g, 2.11 mmol, 2.4 eq.), before being evacuated and refilled with N<sub>2</sub> (x3). THF (50 mL) and 2M aqueous potassium carbonate (5.28 mL, 10.56, 12.0 eq.) were added, and the mixture degassed (N<sub>2</sub> bubbling, 30 mins), prior to the addition of Pd(PPh<sub>3</sub>)<sub>4</sub> (0.04 g, 0.04 mmol, 0.05 eq.). The reaction was brought to reflux and left for 24 hours. After cooling to room temperature, the THF was removed *in vacuo* before the remaining mixture was diluted with chloroform (50 mL) and washed with water (3 x 50 mL). The organic layer was isolated, dried (Na<sub>2</sub>SO<sub>4</sub>), and the solvent removed *in vacuo* to afford the desired product **3** as a brown solid (0.33 g, 0.88 mmol, >99%).

**MP** 172 - 174 °C; **IR** ( $\nu_{\max}/\text{cm}^{-1}$ ) 1692, 1601, 1300, 1209, 1169, 812, 774, 745, 686, 538, 493; **<sup>1</sup>H NMR** (400 MHz, CDCl<sub>3</sub>)  $\delta$  10.12 (s, 1H), 10.10 (s, 1H), 8.09 (d, *J* = 1.8 Hz, 1H), 8.04 – 7.97 (m, 4H), 7.91 – 7.85 (m, *J* = 8.0 Hz, 3H), 7.83 – 7.79 (m, 2H), 7.71 (t, *J* = 8.2 Hz, 3H), 7.50 (d, *J* = 1.8 Hz, 1H), 7.49 (d, *J* = 2.0 Hz, 2H); **<sup>13</sup>C NMR** (101 MHz, CDCl<sub>3</sub>)  $\delta$  192.27, 191.95, 152.78, 150.02, 146.00, 144.77, 140.67, 139.87, 135.82, 135.43, 131.73, 131.61, 131.53, 130.54, 129.66, 129.40, 129.25, 127.96, 123.53, 115.07; **HRMS** (CI) calc. for C<sub>26</sub>H<sub>18</sub>N<sub>2</sub>O<sub>2</sub> [M+H]<sup>+</sup> 391.1441, found 391.1448.

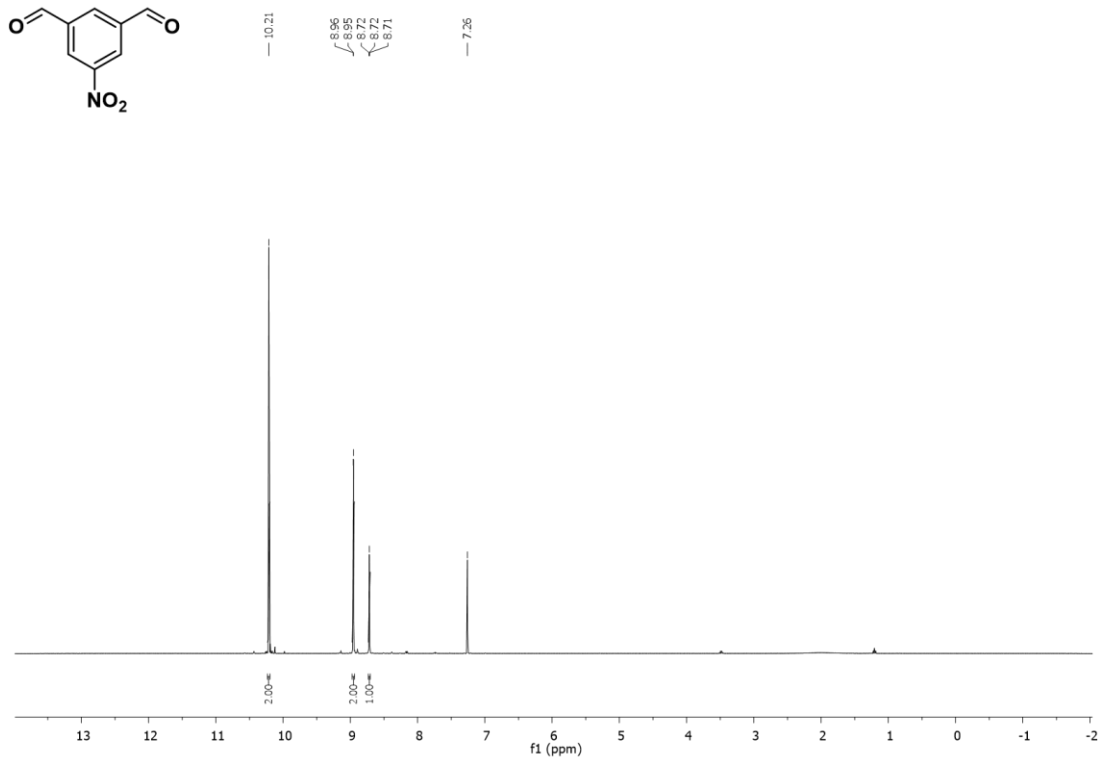


Figure 2.34 <sup>1</sup>H NMR spectrum of 4 in CDCl<sub>3</sub>

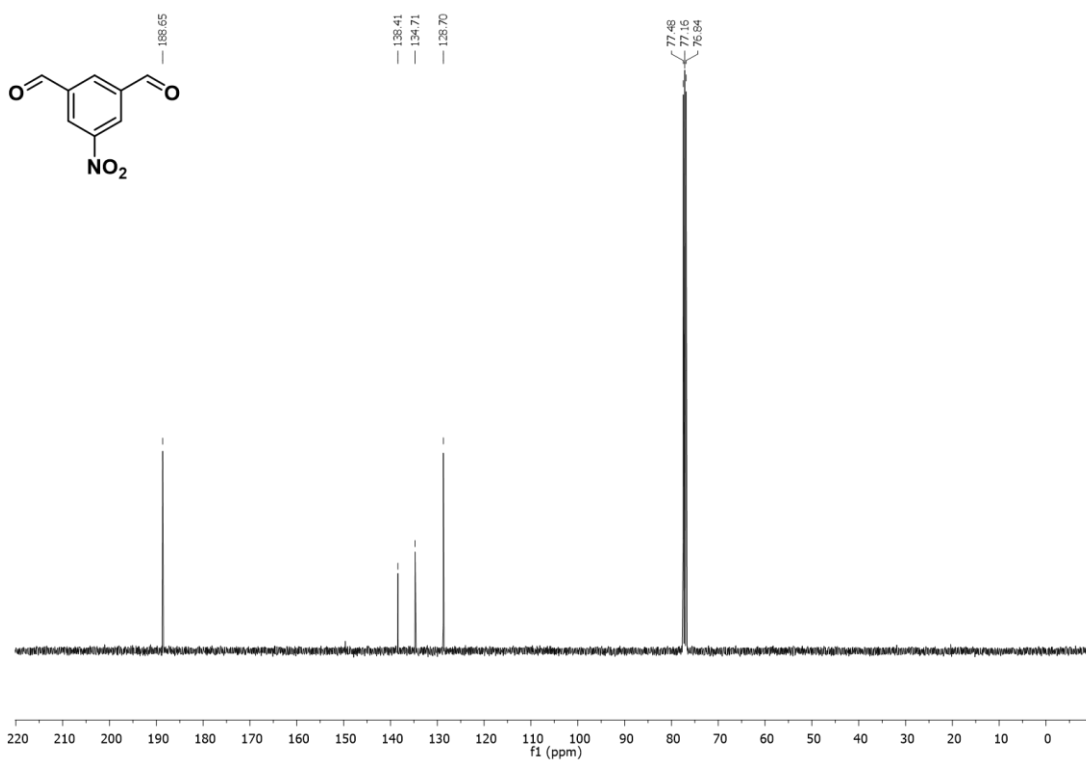


Figure 2.35 <sup>13</sup>C NMR spectrum of 4 in CDCl<sub>3</sub>



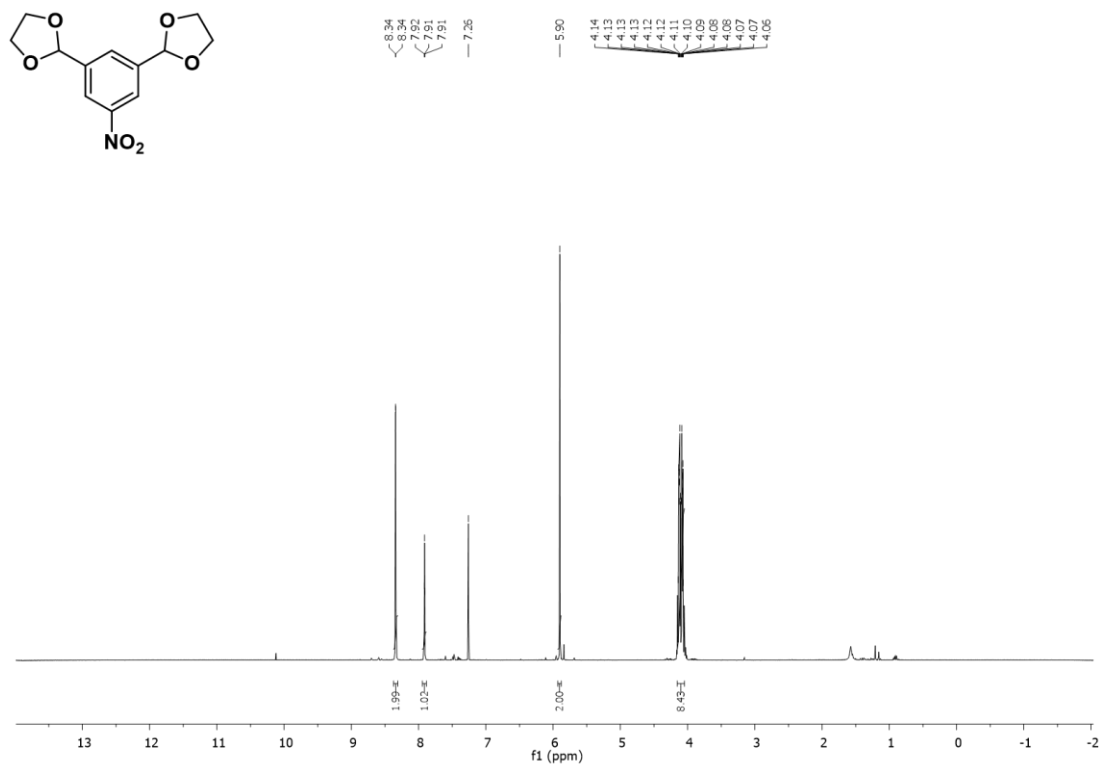


Figure 2.36 <sup>1</sup>H NMR spectrum of 5 in CDCl<sub>3</sub>

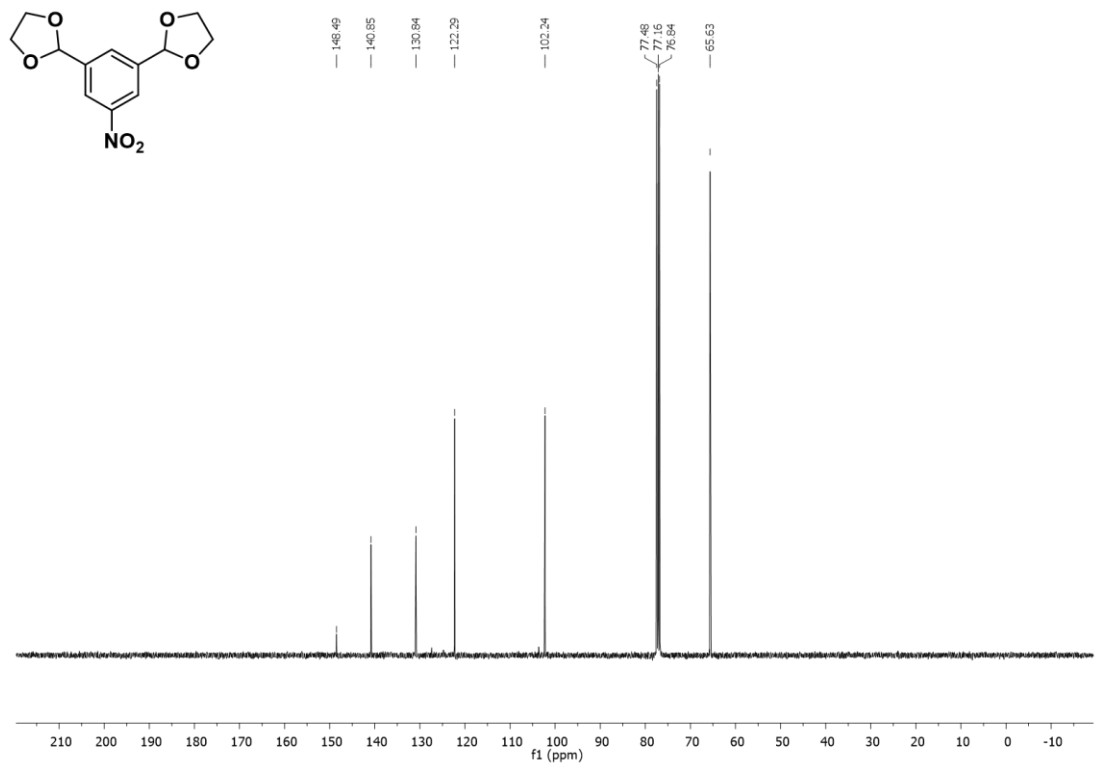


Figure 2.37 <sup>13</sup>C NMR spectrum of 5 in CDCl<sub>3</sub>

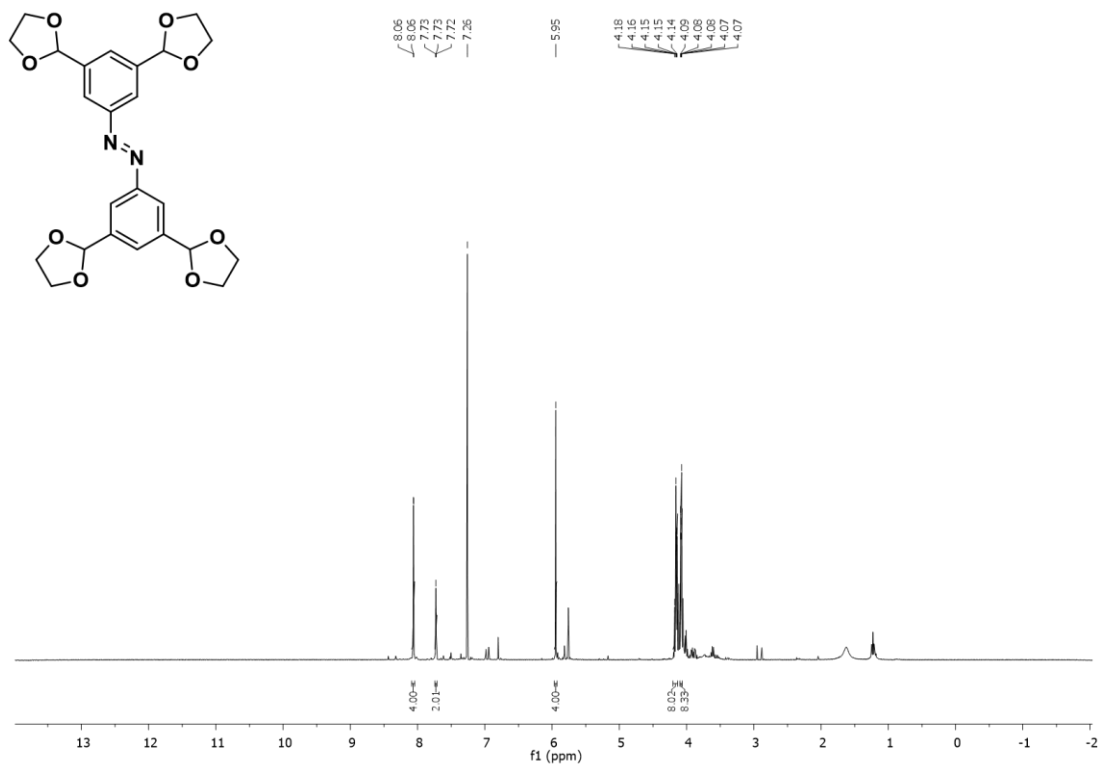


Figure 2.38  $^1\text{H}$  NMR spectrum of **6** in  $\text{CDCl}_3$

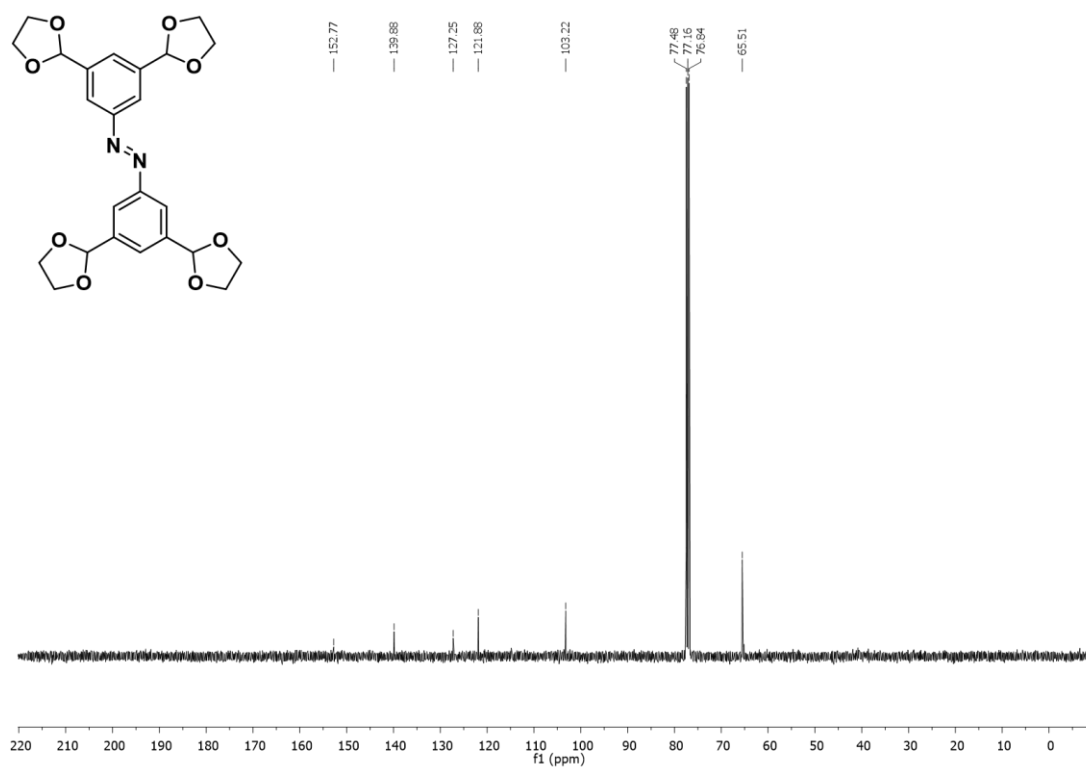


Figure 2.39  $^{13}\text{C}$  NMR spectrum of **6** in  $\text{CDCl}_3$

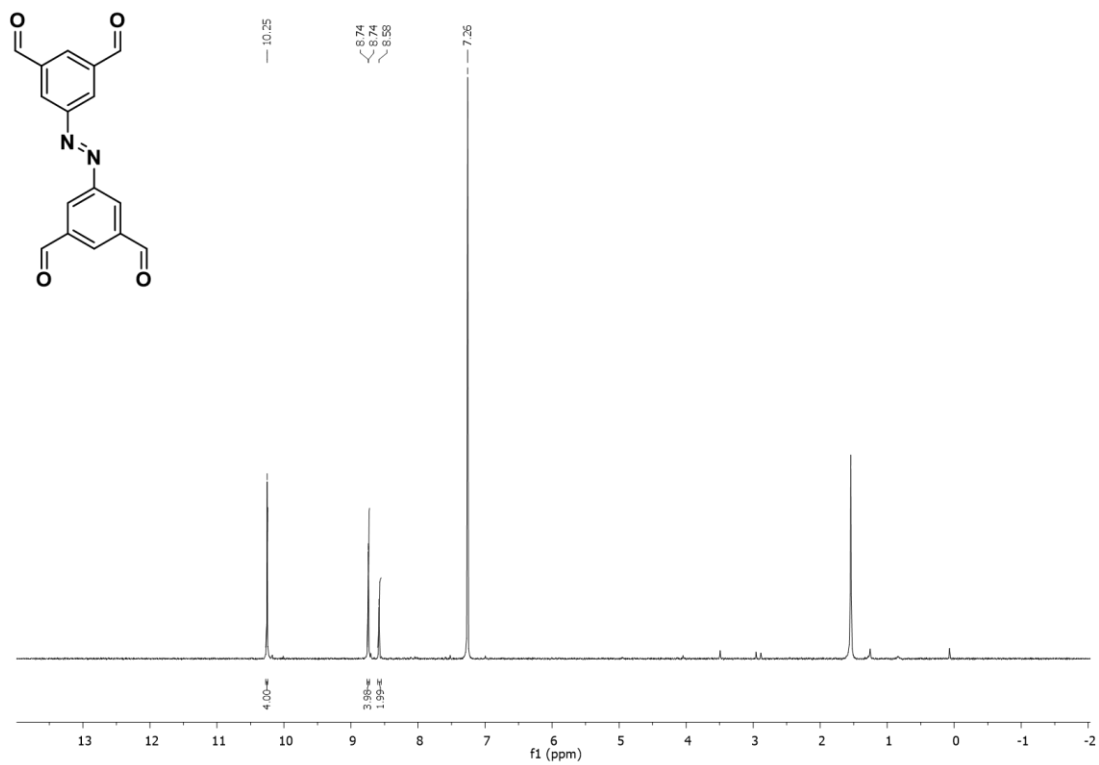


Figure 2.40  $^1\text{H}$  NMR spectrum of 1 in  $\text{CDCl}_3$

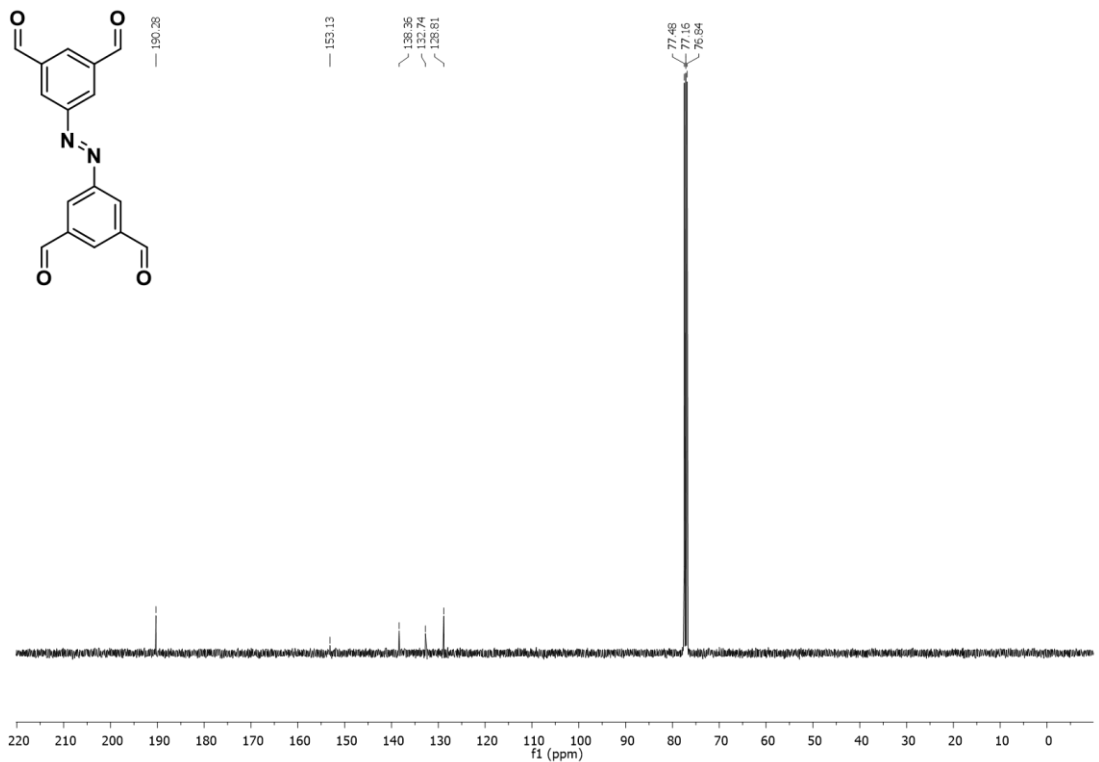
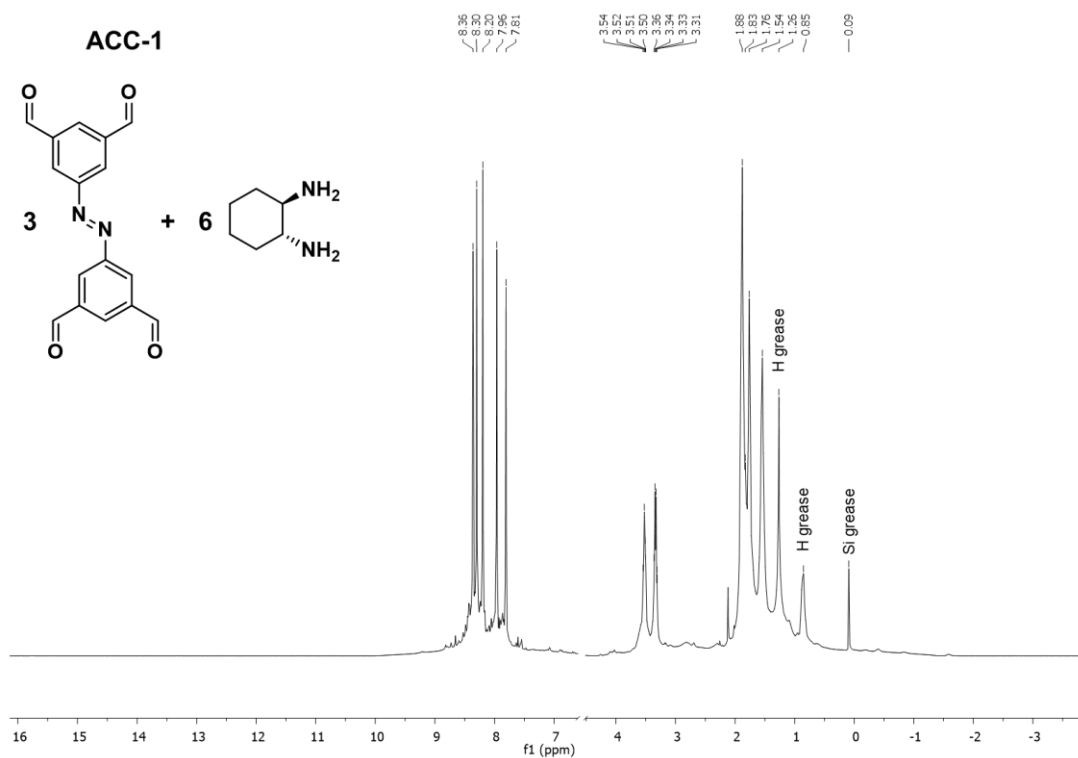
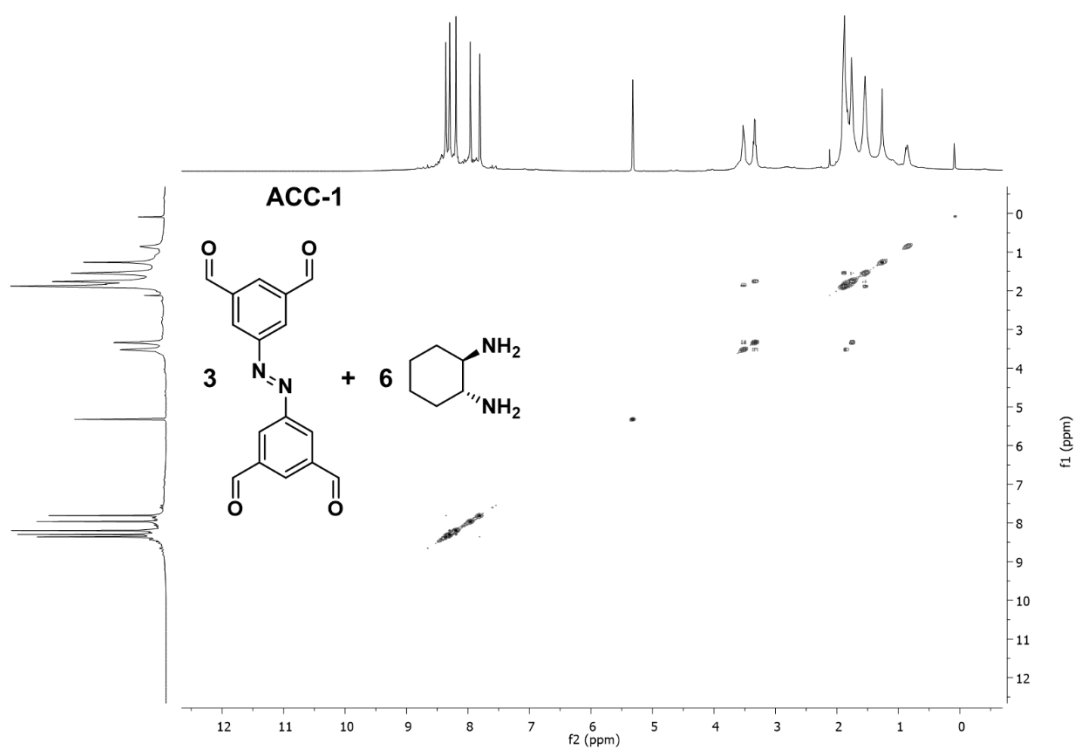


Figure 2.41  $^{13}\text{C}$  NMR spectrum of 1 in  $\text{CDCl}_3$



**Figure 2.42**  $^1\text{H}$  NMR spectrum of **ACC-1** in  $\text{CD}_2\text{Cl}_2$



**Figure 2.43** Correlation spectroscopy (COSY) NMR spectrum of **ACC-1** in  $\text{CD}_2\text{Cl}_2$

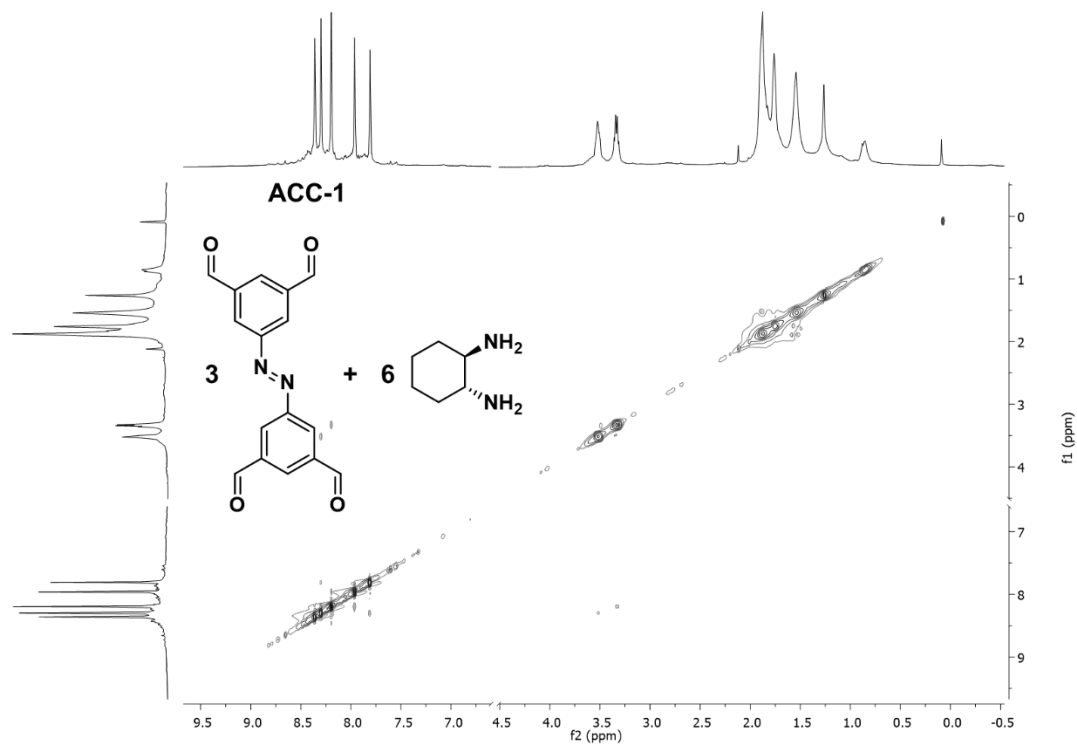


**Figure 2.44** Nuclear Overhauser Effect Spectroscopy (NOESY) NMR spectrum of **ACC-1** in  $\text{CD}_2\text{Cl}_2$

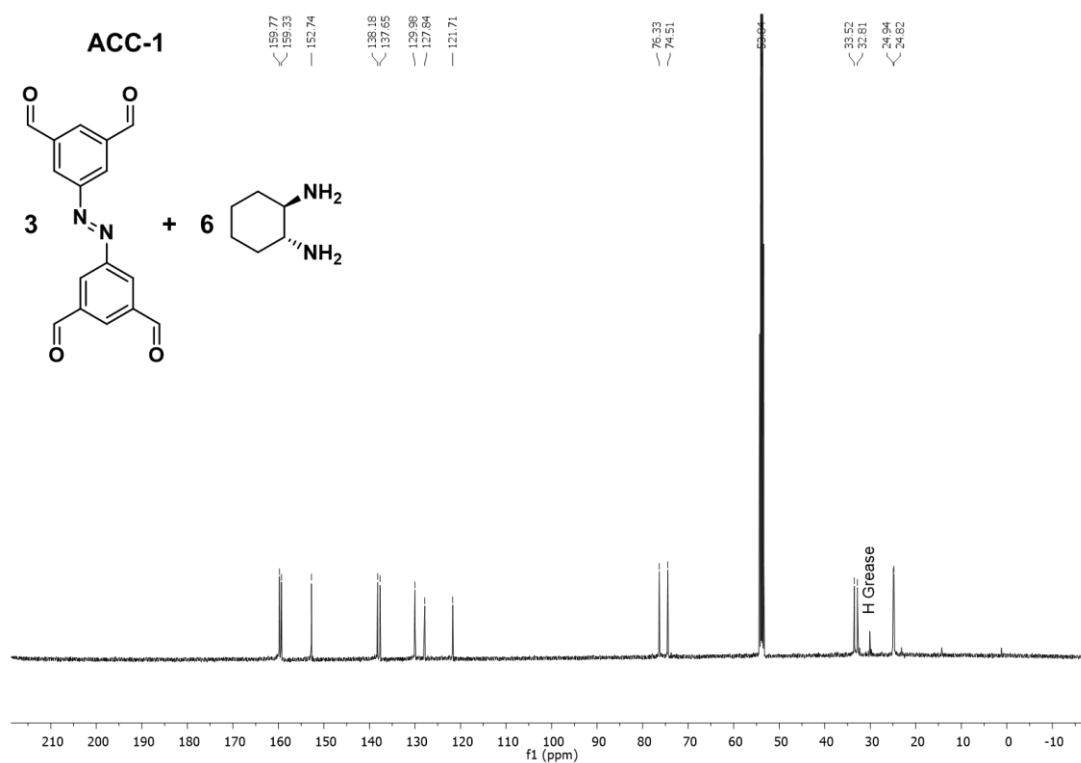


**Figure 2.45**  $^{13}\text{C}$  NMR spectrum of **ACC-1** in  $\text{CD}_2\text{Cl}_2$

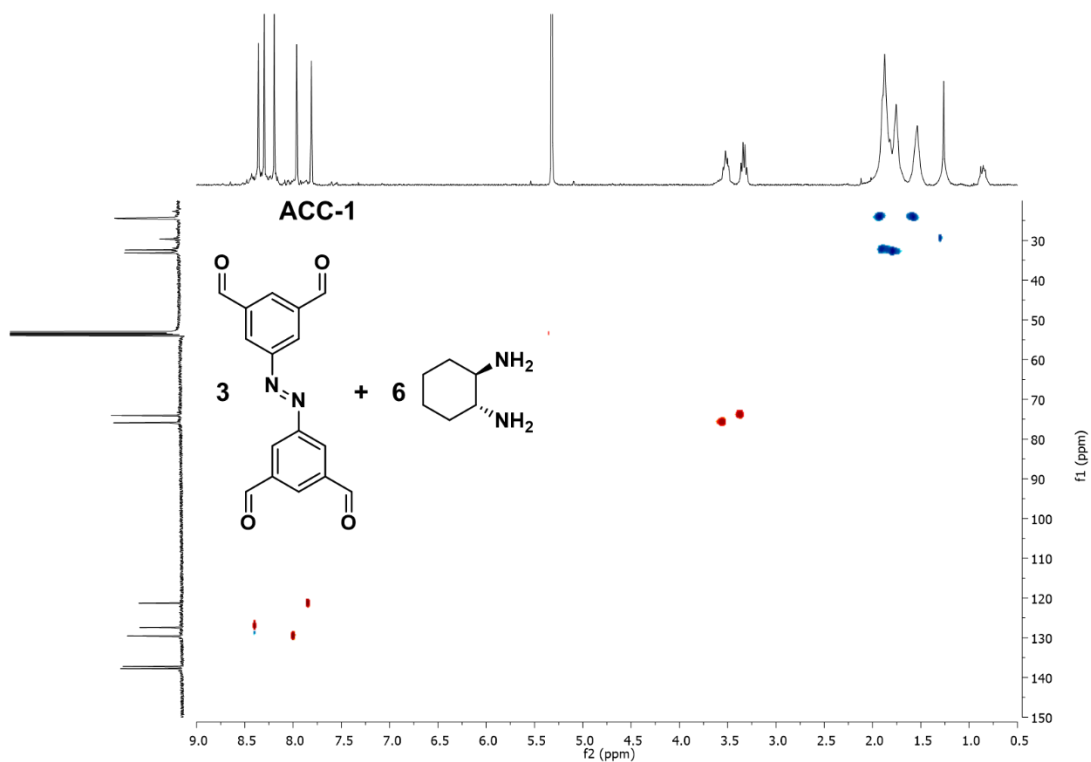


**Figure 2.46** Heteronuclear Single Quantum Coherence (HSQC) NMR spectrum of **ACC-1** in  $\text{CD}_2\text{Cl}_2$

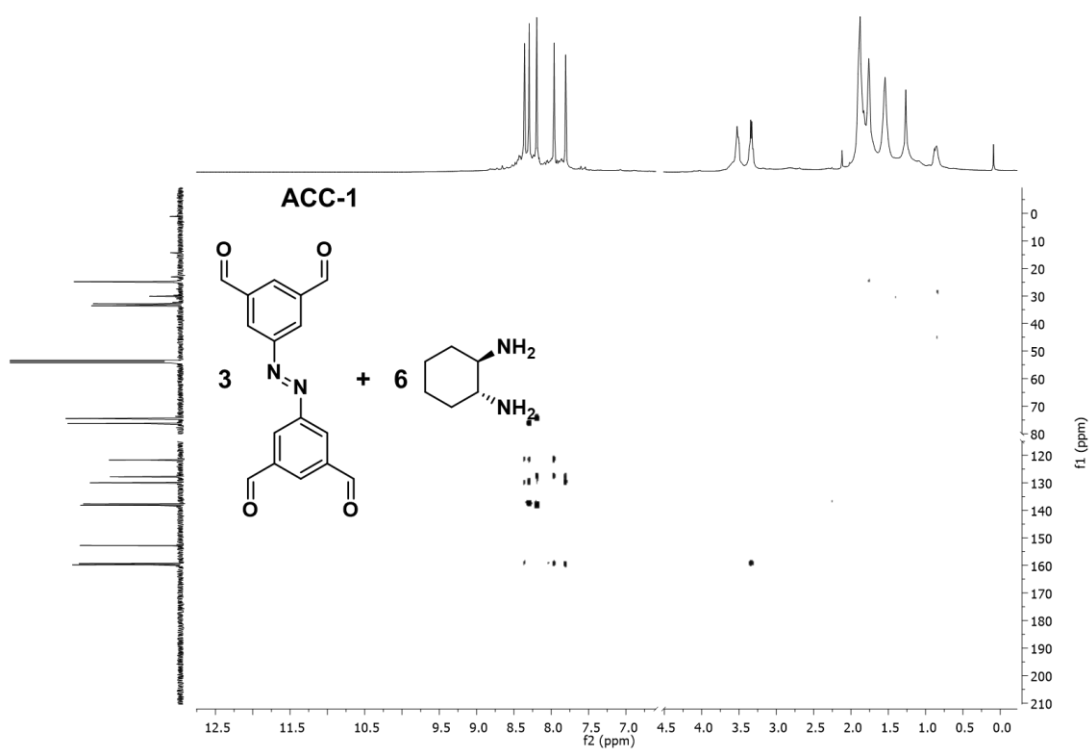


**Figure 2.47** Heteronuclear Multiple Bond Correlation (HMBC) NMR spectrum of **ACC-1** in  $\text{CD}_2\text{Cl}_2$

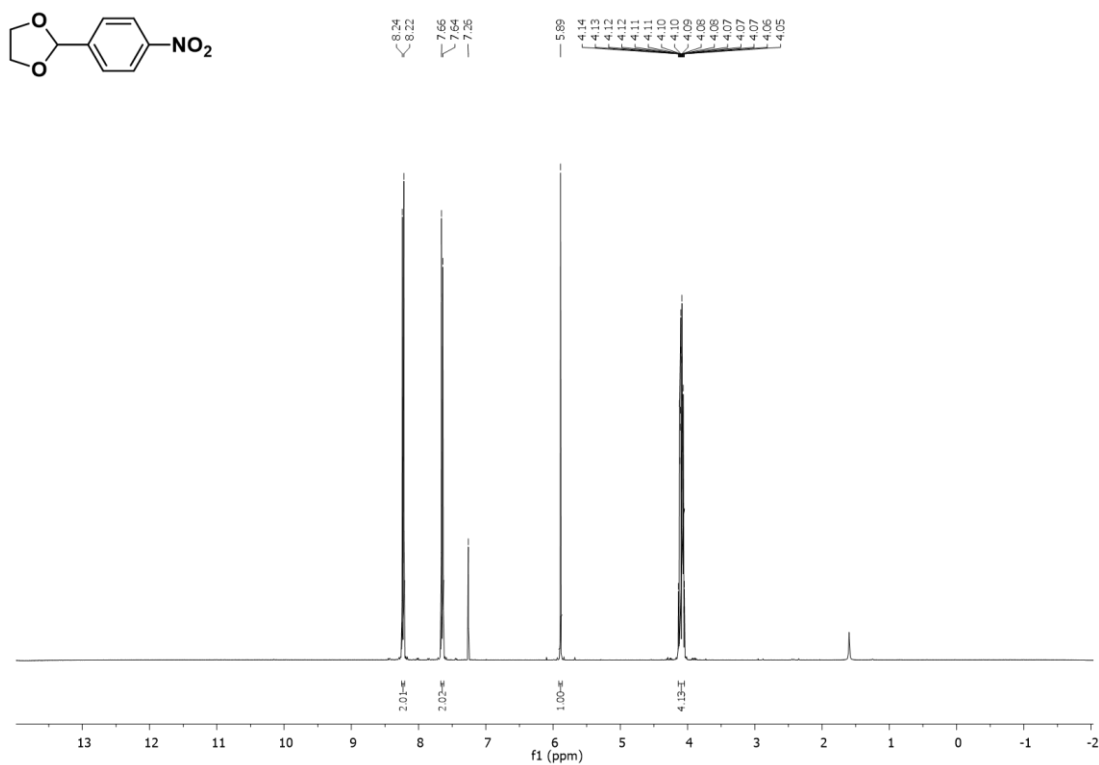


Figure 2.48 <sup>1</sup>H NMR spectrum of 7 in CDCl<sub>3</sub>

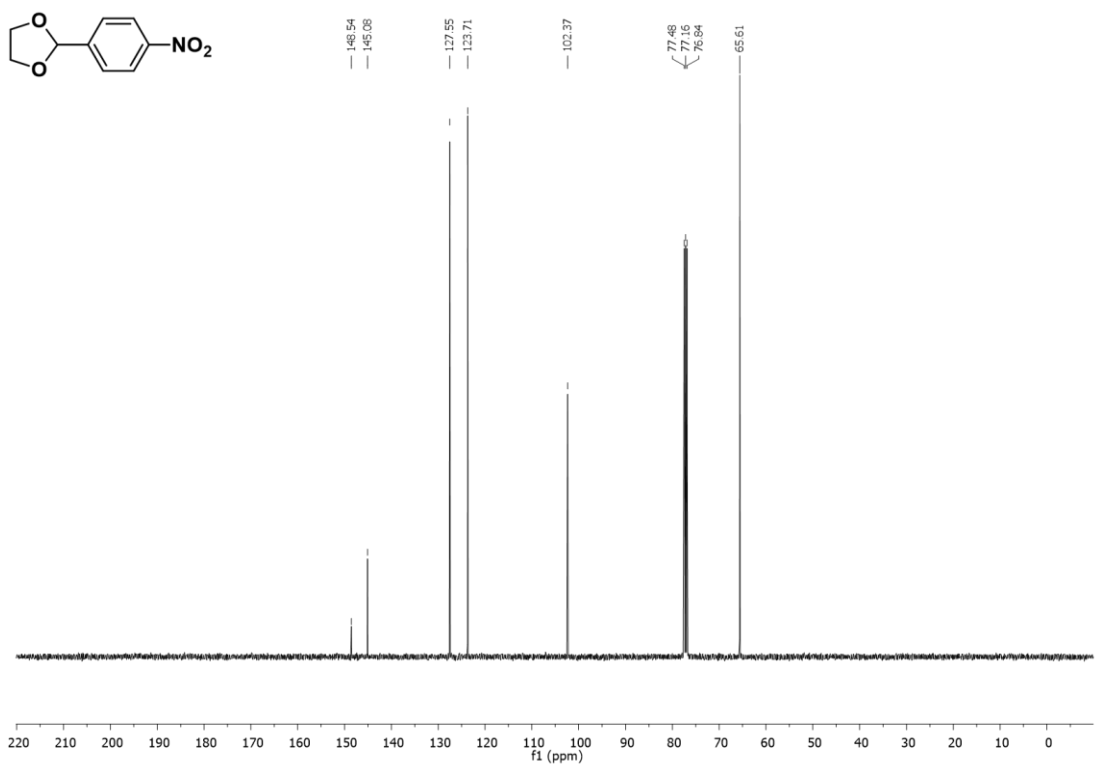


Figure 2.49 <sup>13</sup>C NMR spectrum of 7 in CDCl<sub>3</sub>

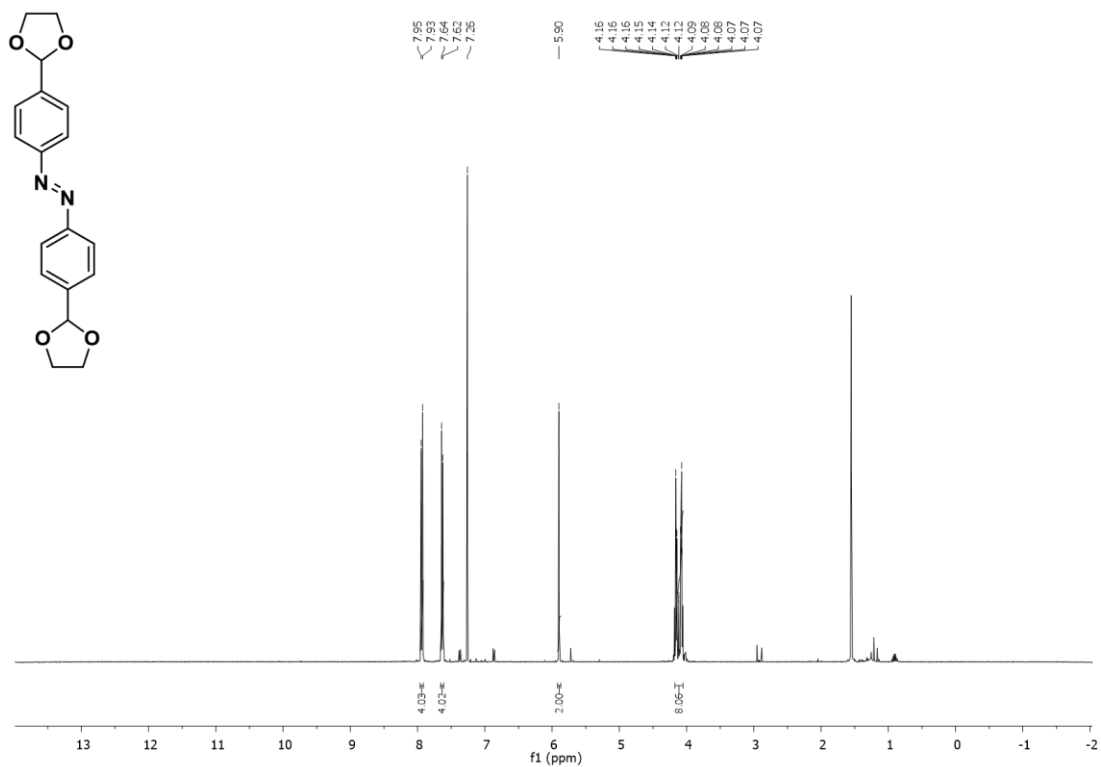


Figure 2.50 <sup>1</sup>H NMR spectrum of **8** in CDCl<sub>3</sub>

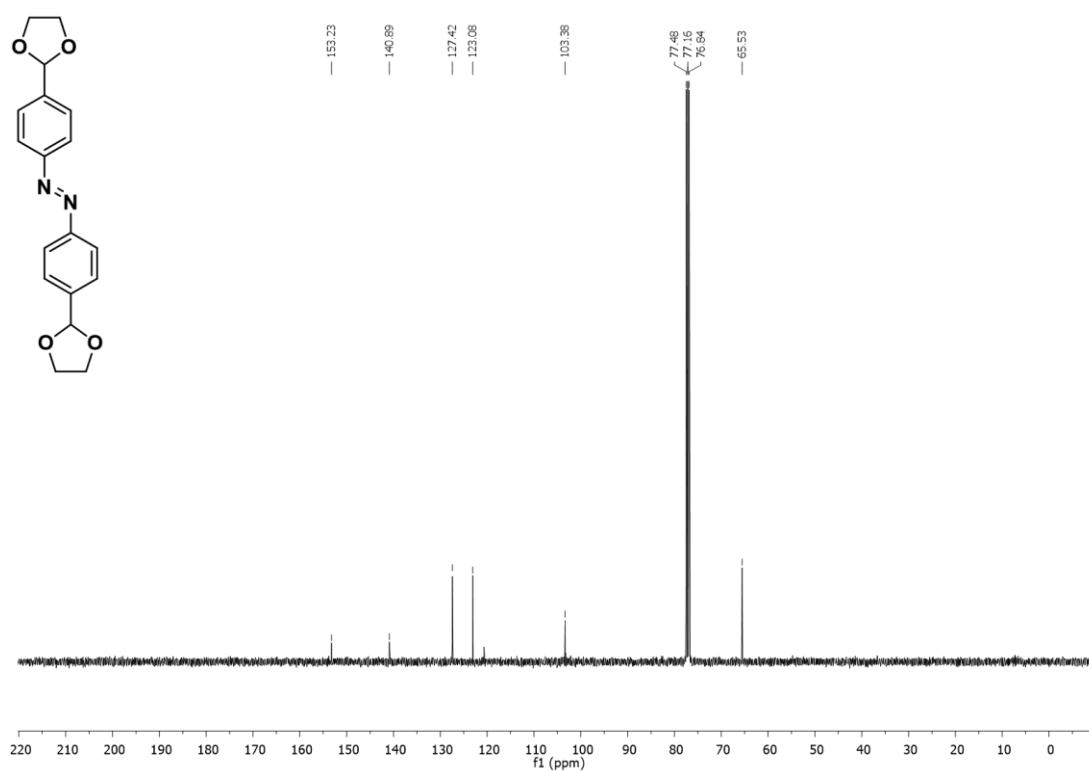


Figure 2.51 <sup>13</sup>C NMR spectrum of **8** in CDCl<sub>3</sub>



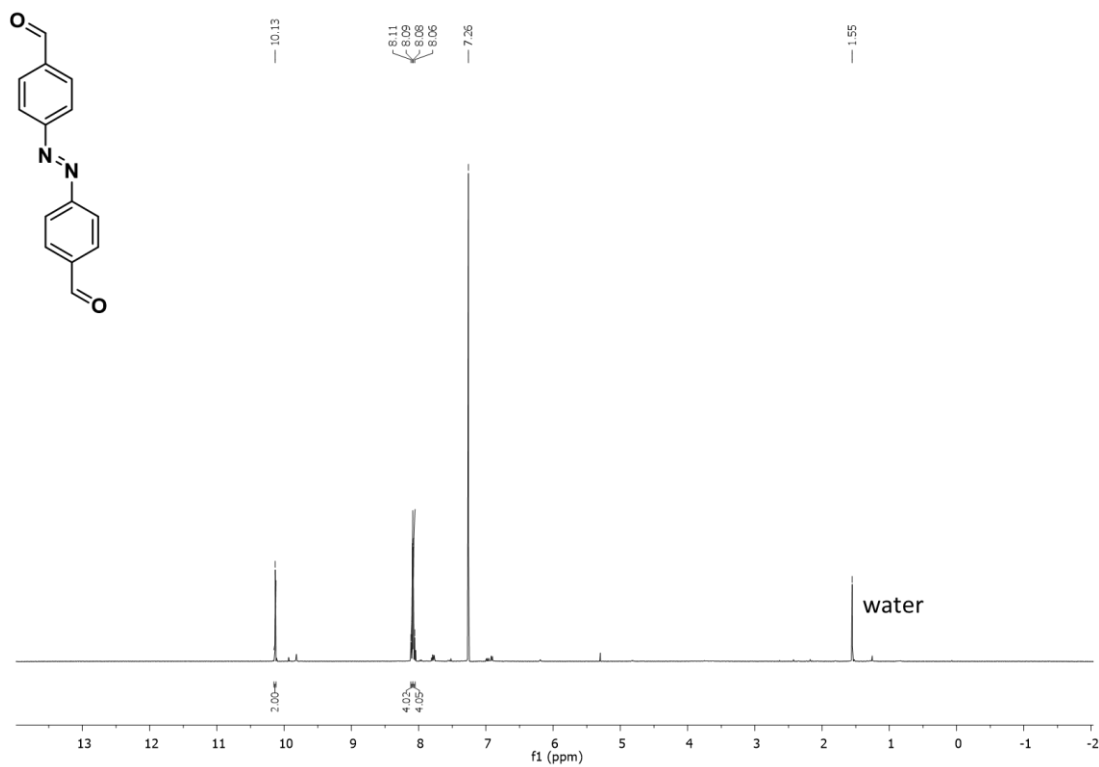


Figure 2.52 <sup>1</sup>H NMR spectrum of **2** in CDCl<sub>3</sub>

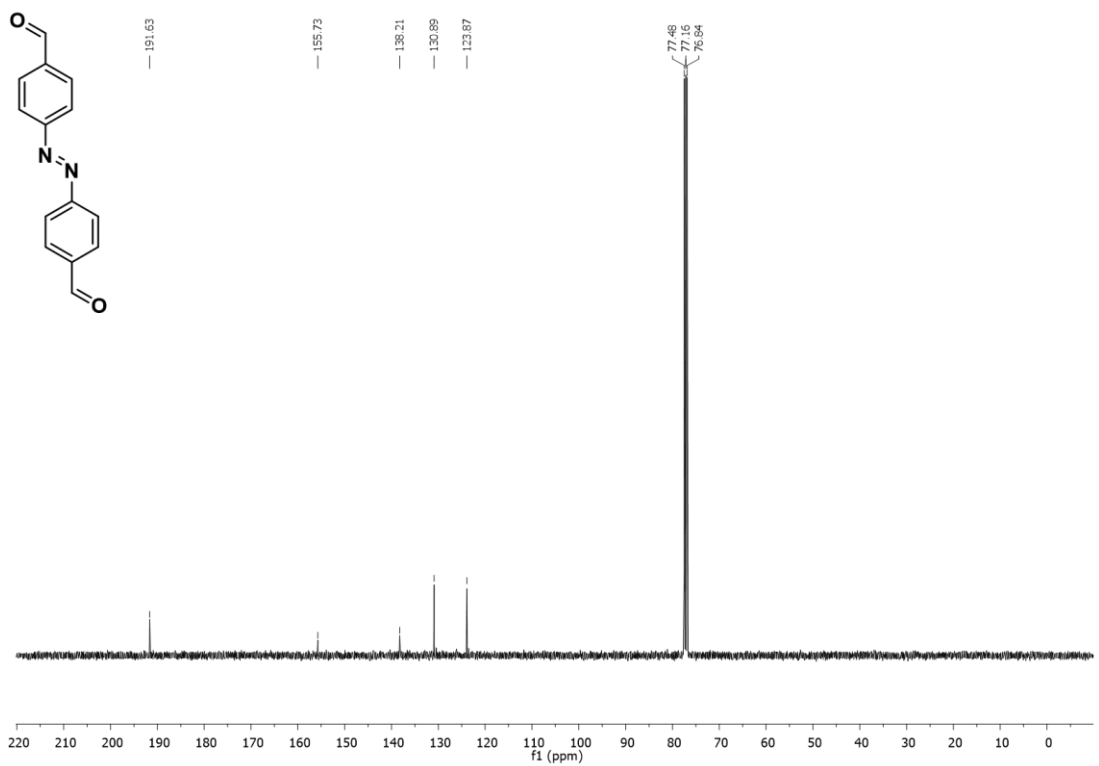
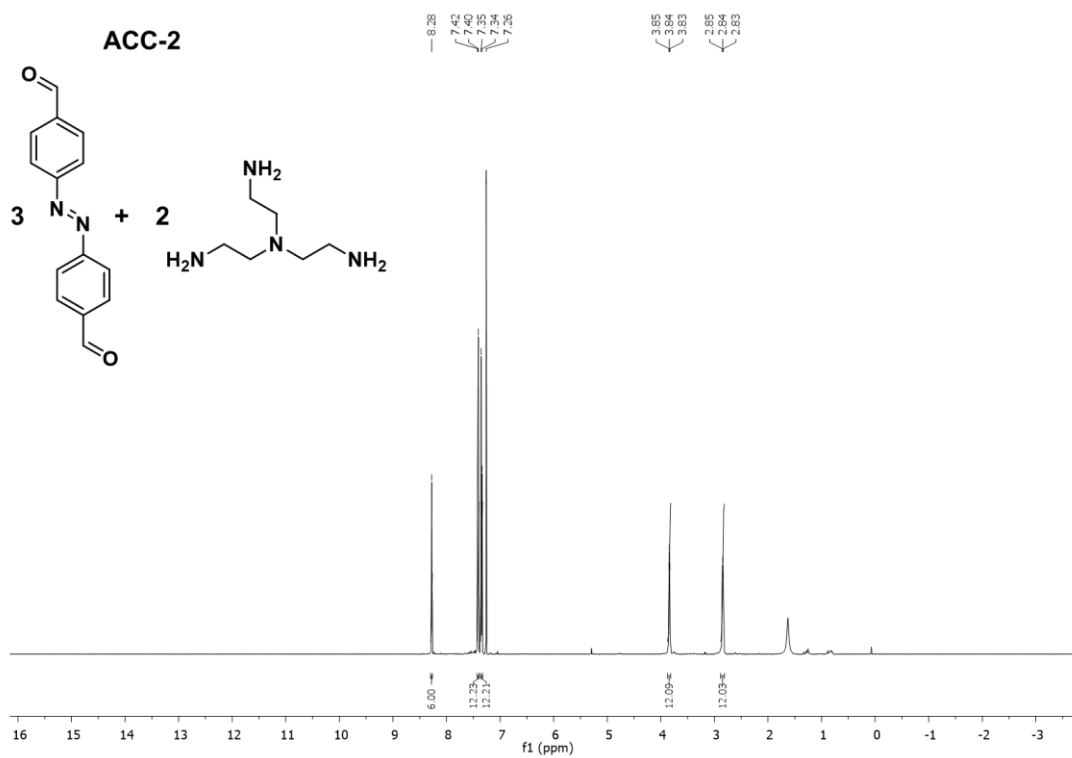
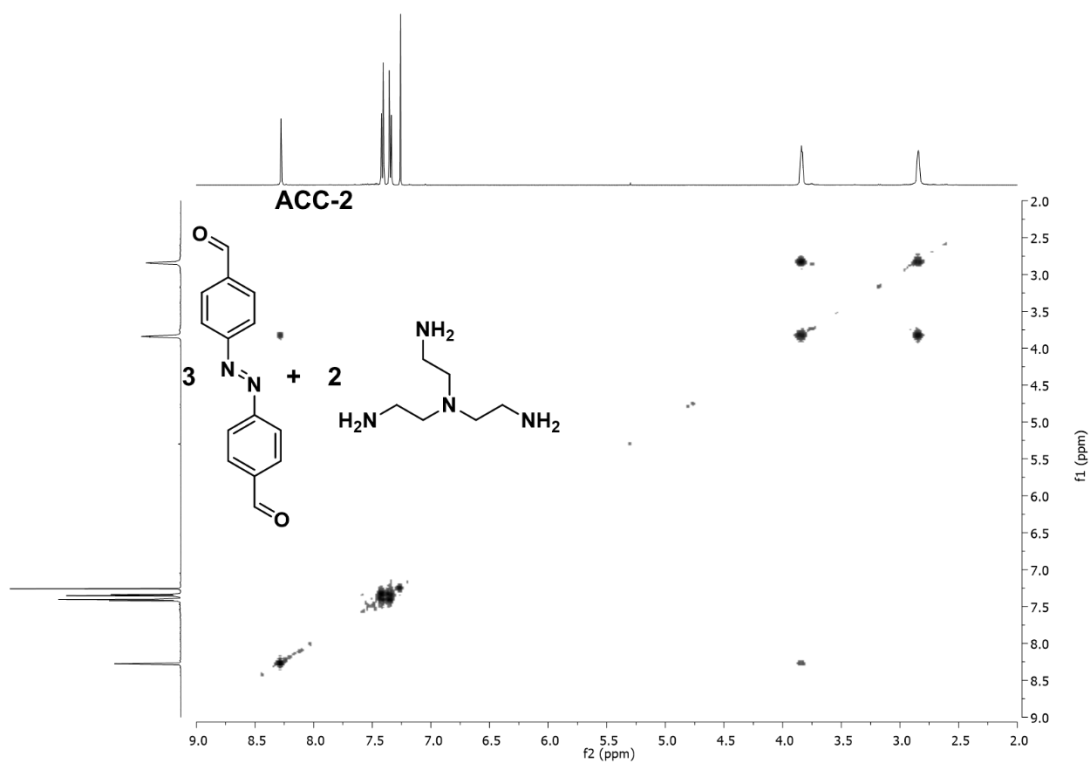


Figure 2.53 <sup>13</sup>C NMR spectrum of **2** in CDCl<sub>3</sub>



**Figure 2.54**  $^1\text{H}$  NMR spectrum of **ACC-2** in  $\text{CDCl}_3$



**Figure 2.55** Correlation spectroscopy (COSY) NMR spectrum of **ACC-2** in  $\text{CDCl}_3$

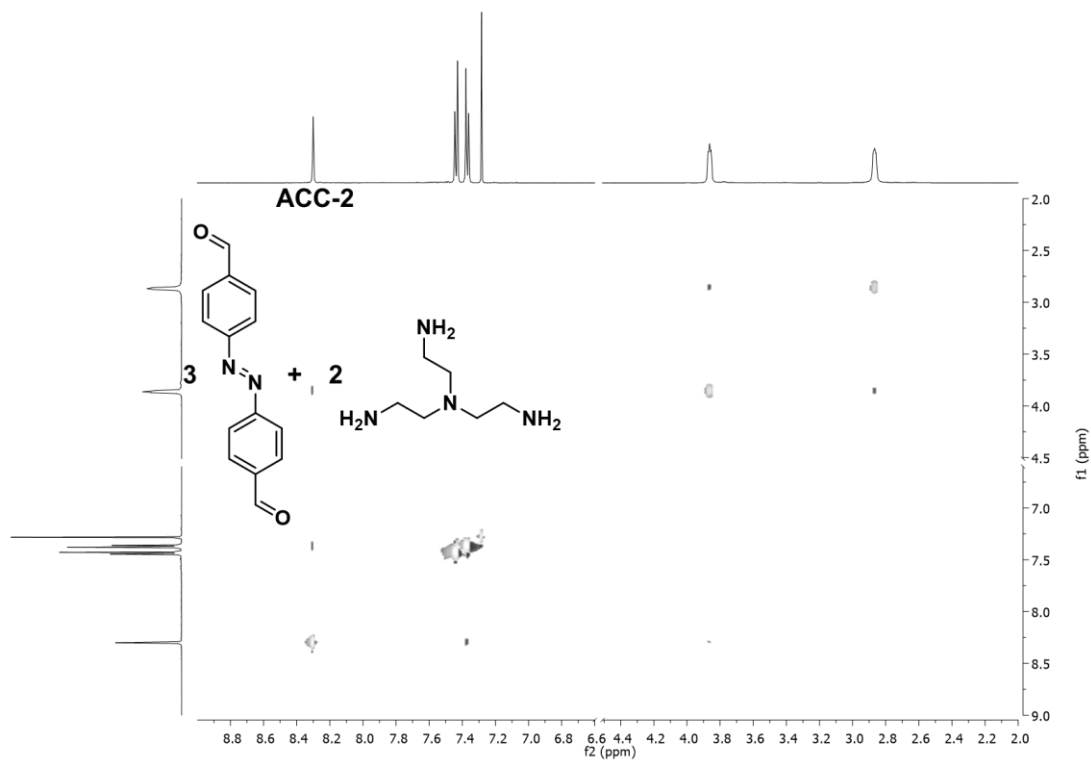


**Figure 2.56** Nuclear Overhauser Effect Spectroscopy (NOESY) NMR spectrum of **ACC-2** in CDCl<sub>3</sub>

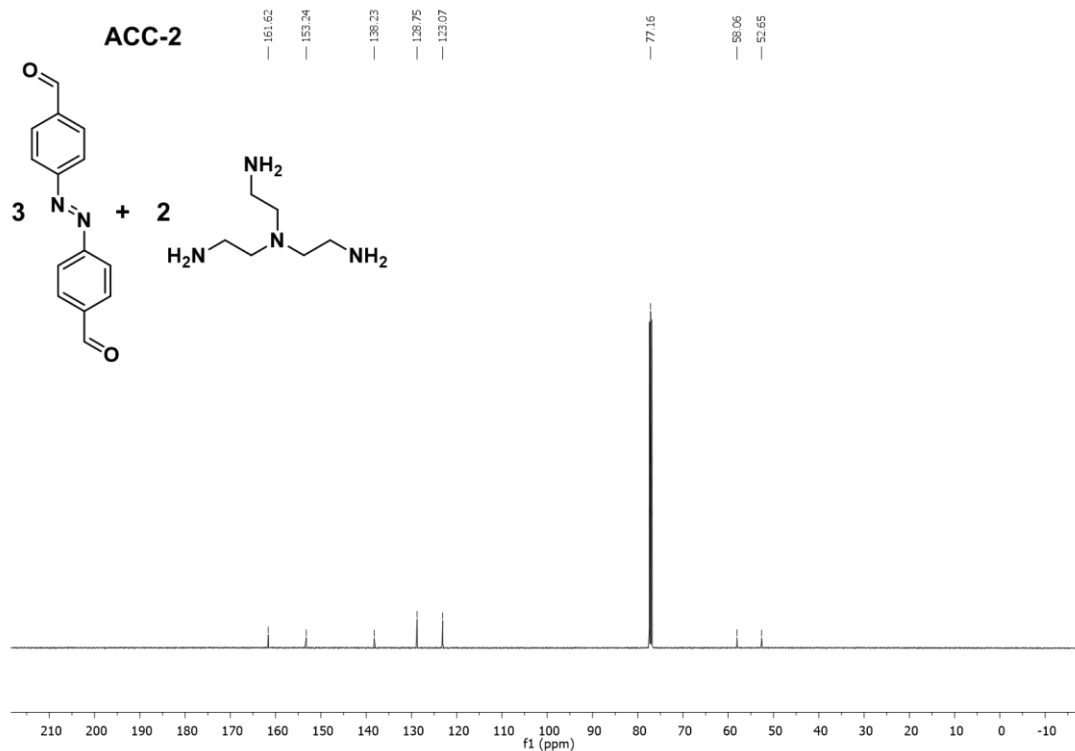


**Figure 2.57** <sup>13</sup>C NMR spectrum of **ACC-2** in CDCl<sub>3</sub>

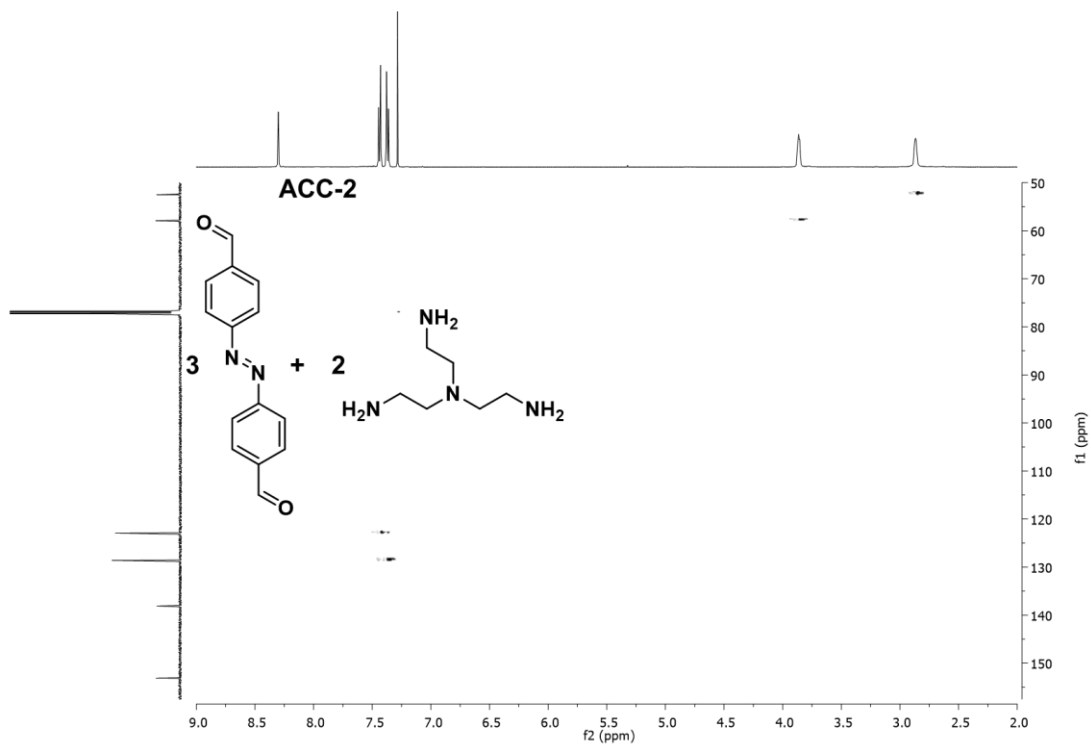


**Figure 2.58** Heteronuclear Single Quantum Coherence (HSQC) NMR spectrum of **ACC-2** in  $\text{CDCl}_3$

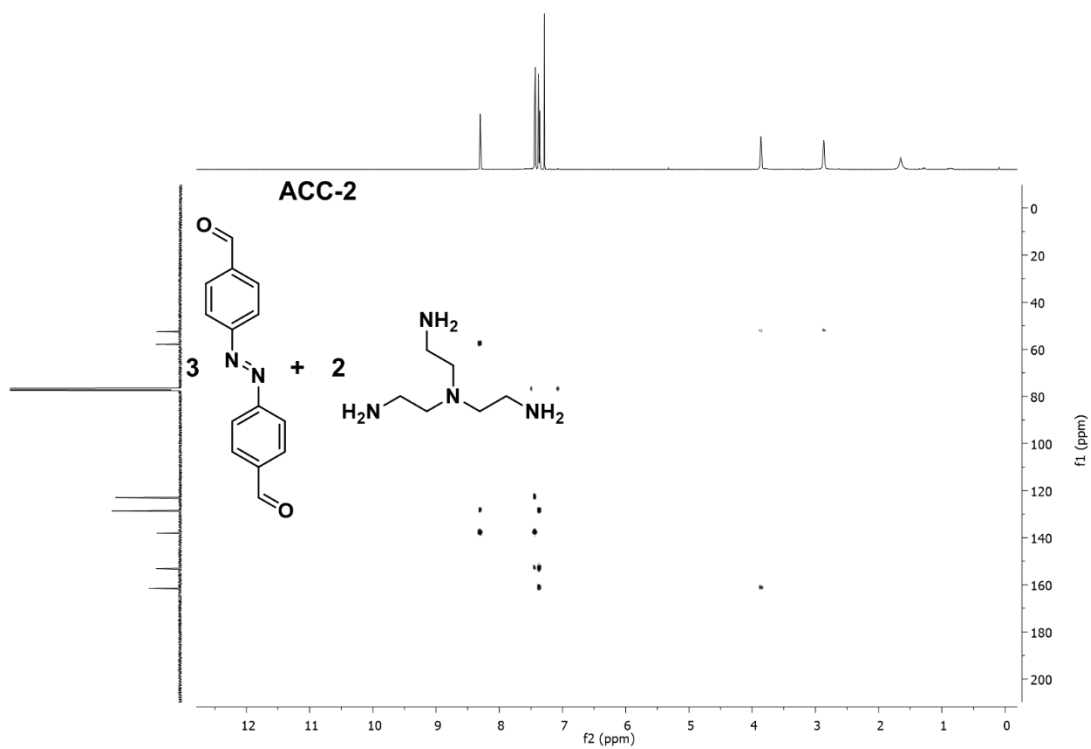


**Figure 2.59** Heteronuclear Multiple Bond Correlation (HMBC) NMR spectrum of **ACC-2** in  $\text{CDCl}_3$

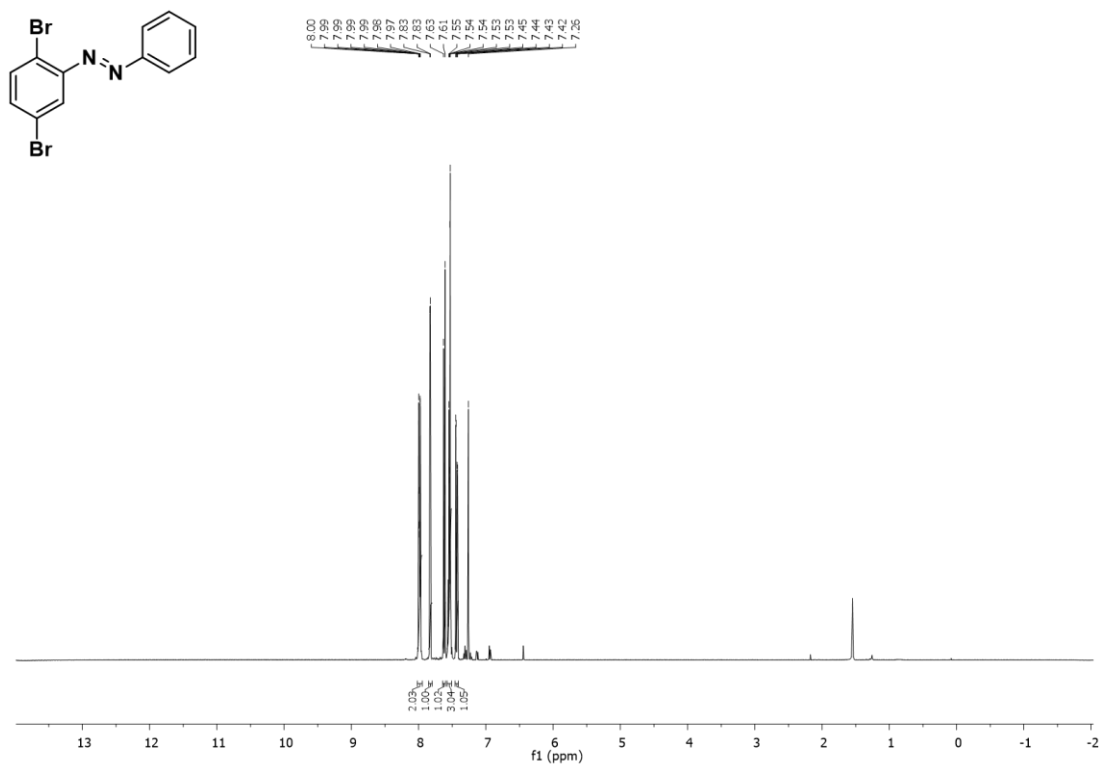


**Figure 2.60**  $^1\text{H}$  NMR spectrum of **9** in  $\text{CDCl}_3$

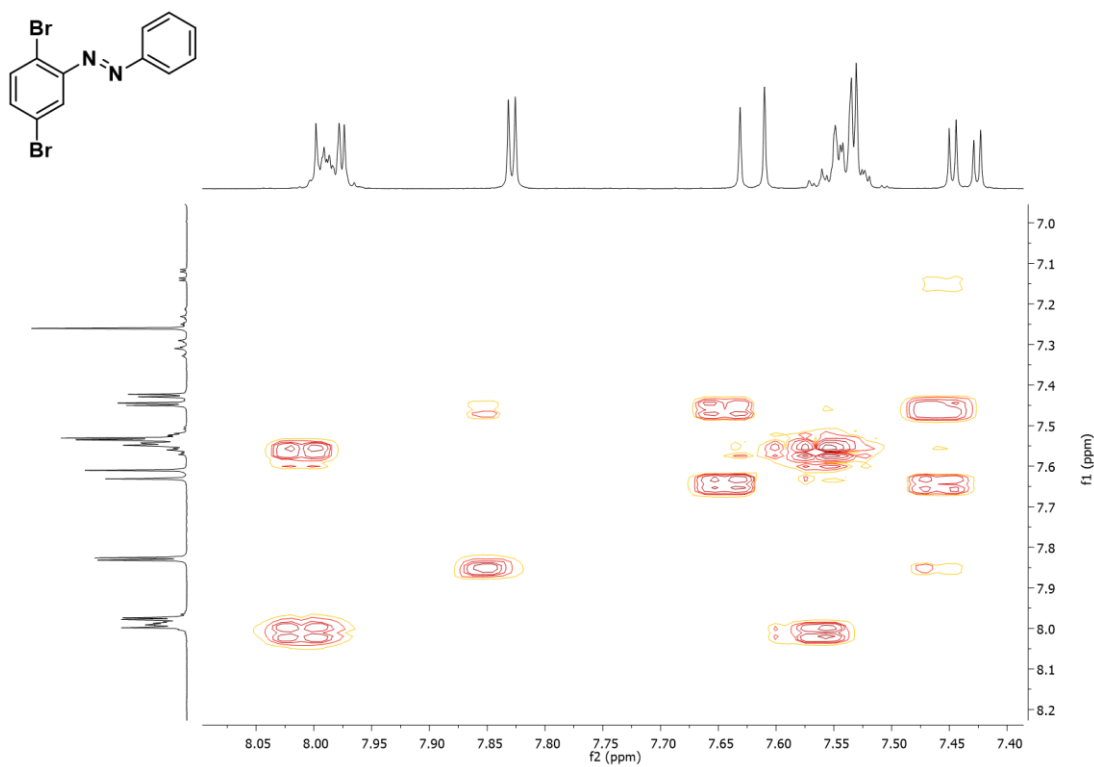


**Figure 2.61**  $^1\text{H}$  -  $^1\text{H}$  COSY NMR spectrum of **9** in  $\text{CDCl}_3$

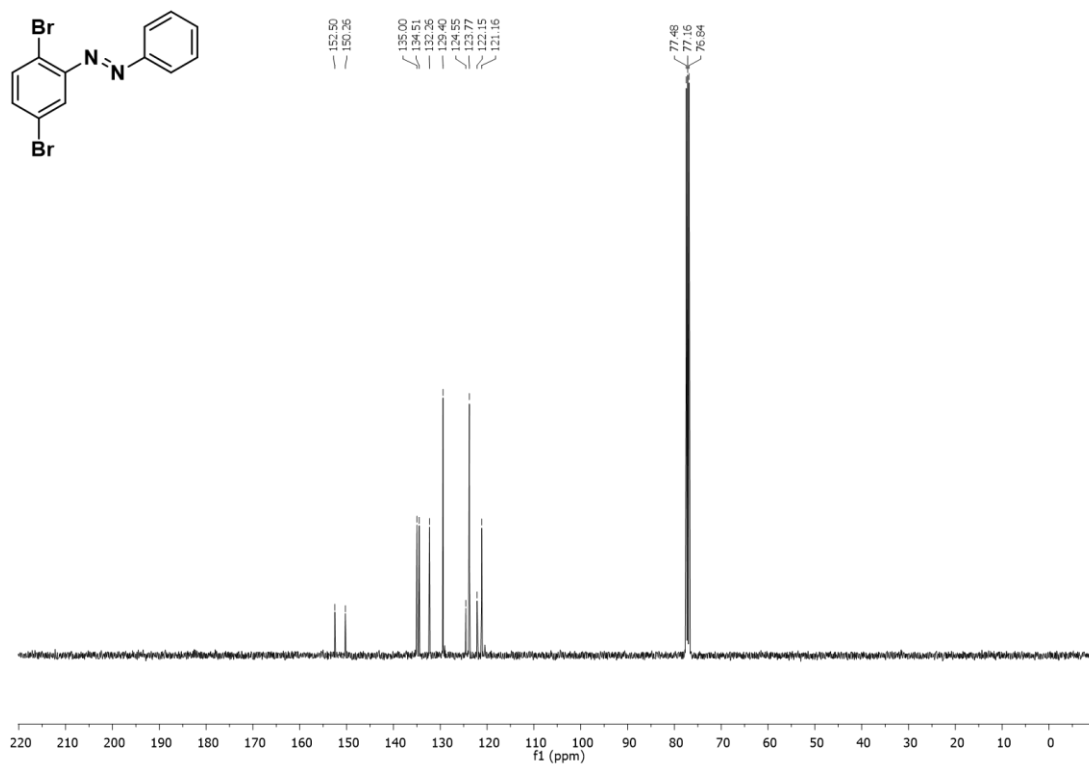


Figure 2.62  $^{13}\text{C}$  NMR spectrum of **9** in  $\text{CDCl}_3$

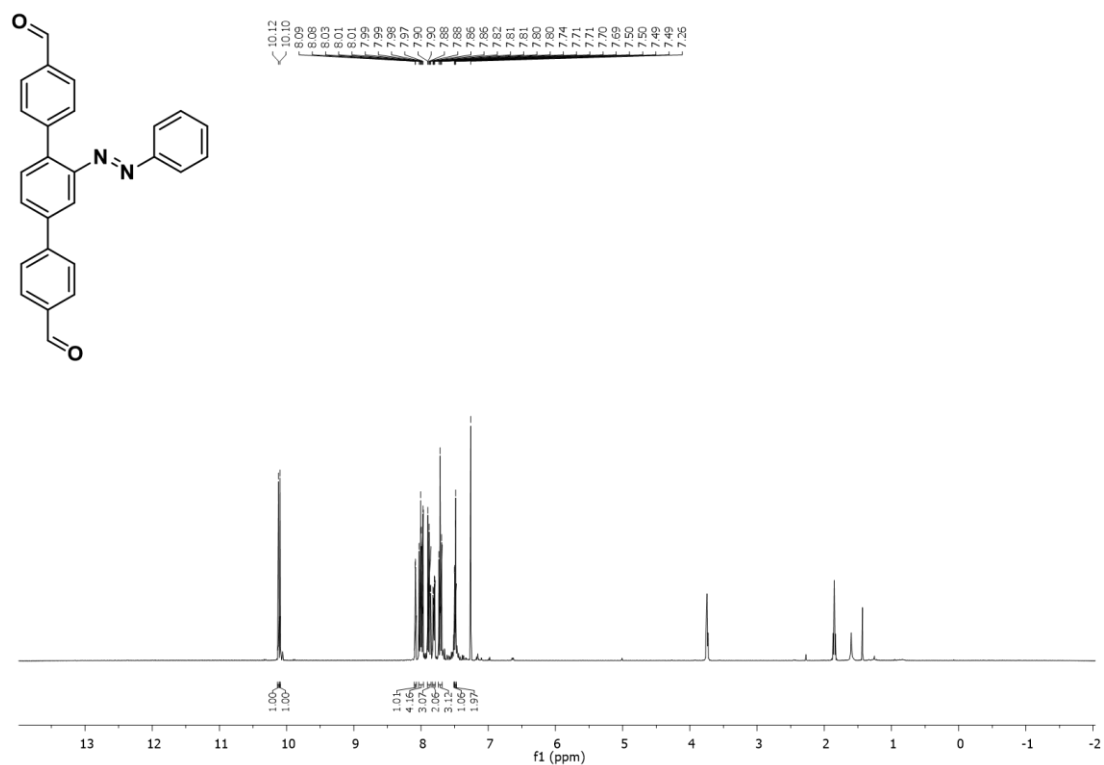


Figure 2.63  $^1\text{H}$  NMR spectrum of **3** in  $\text{CDCl}_3$

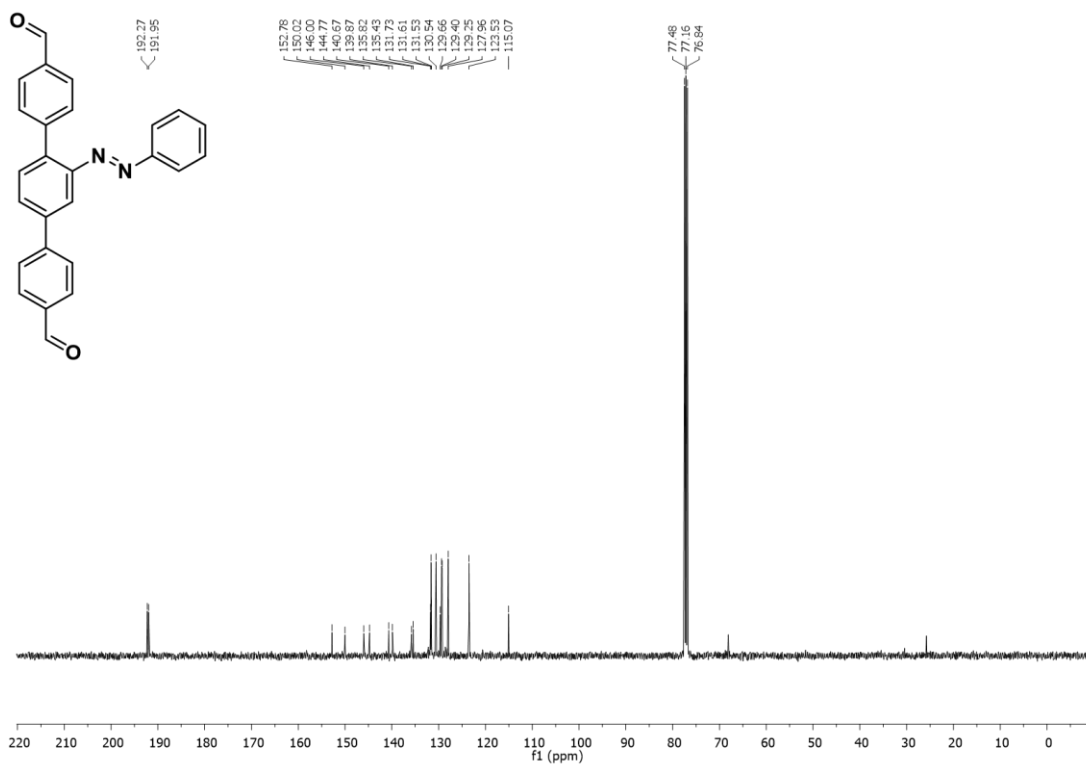
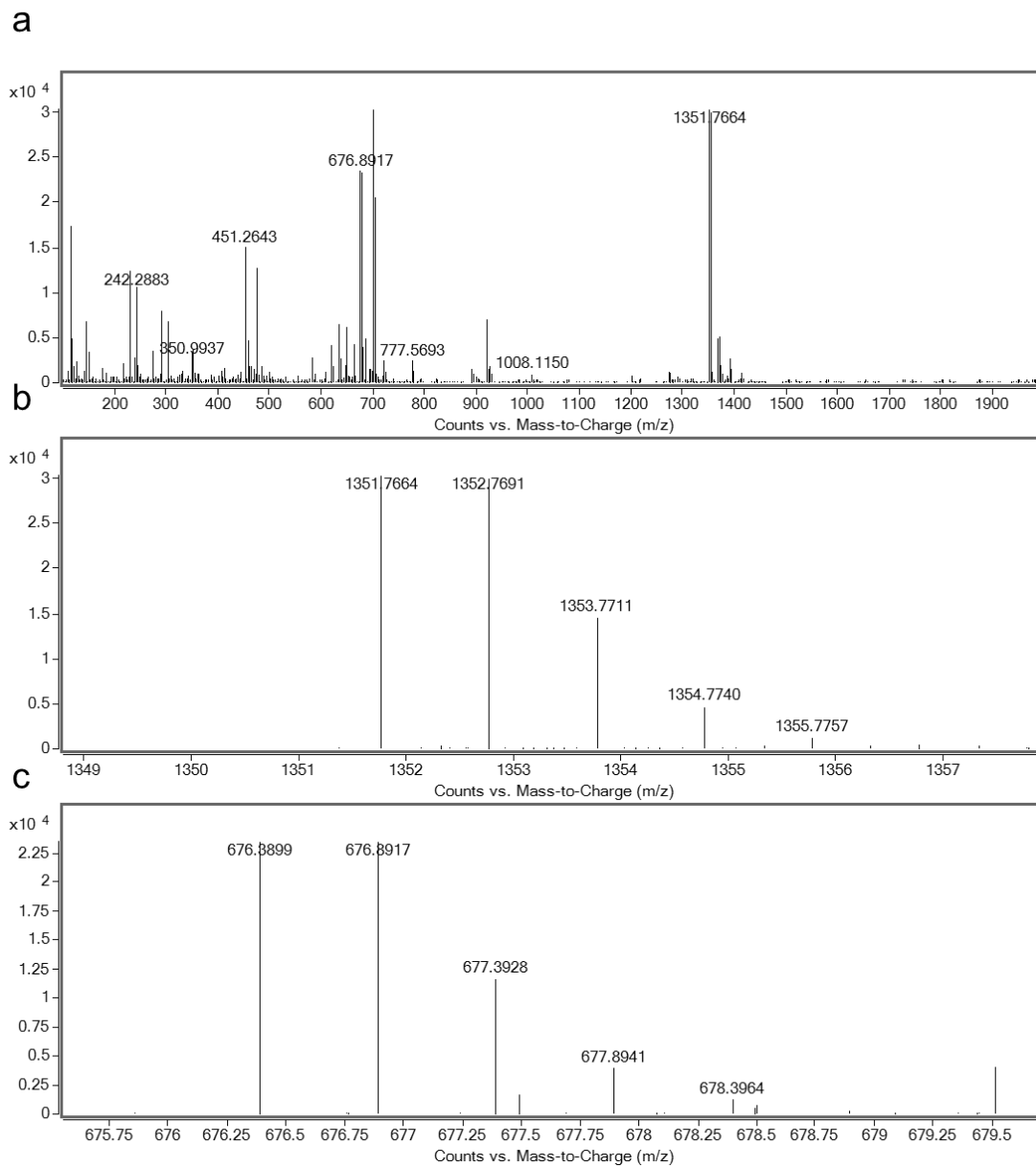
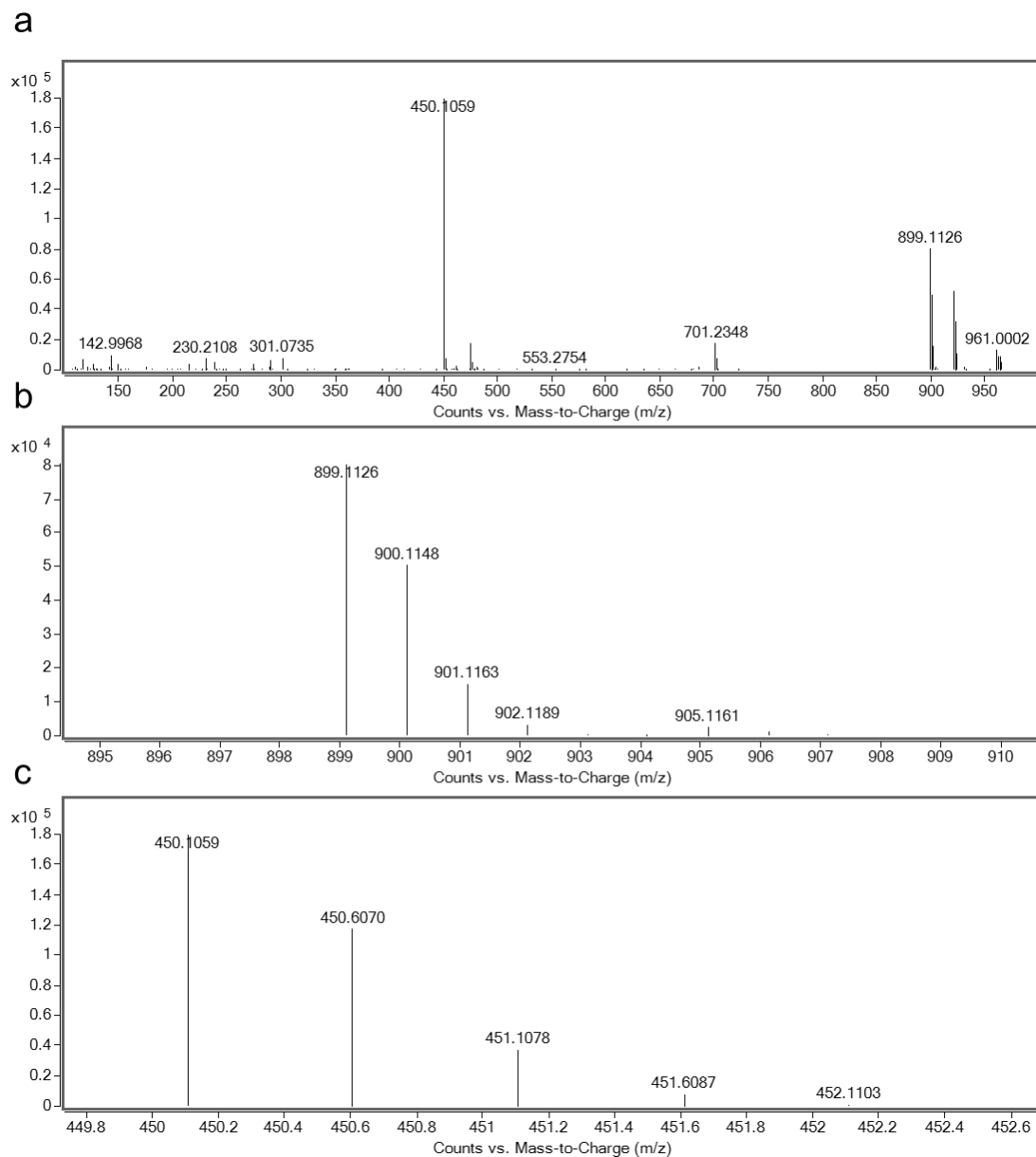


Figure 2.64 <sup>13</sup>C NMR spectrum of 3 in CDCl<sub>3</sub>



**Figure 2.65** High resolution mass spectrum of **ACC-1**, where a) full mass spectrum; b) [M+H]<sup>+</sup> ion; c) [M+2H]<sup>2+</sup> ion.





**Figure 2.66** High resolution mass spectrum of **ACC-2**, where a) full mass spectrum; b)  $[M+H]^+$  ion; c)  $[M+2H]^{2+}$  ion.

**Table 2.14** Single crystal refinement details for **ACC-1** and **ACC-2**.

Molecule	ACC-1	ACC-2
$\lambda$ [Å]	Mo-K $\alpha$	Mo-K $\alpha$
Collection Temperature	100 K	100 K
Formula	C <sub>84</sub> H <sub>90</sub> N <sub>18</sub> , 1.5(CH <sub>2</sub> Cl <sub>2</sub> ), 1.5(C <sub>2</sub> H <sub>6</sub> O)	C <sub>54</sub> H <sub>54</sub> N <sub>14</sub> , CH <sub>2</sub> Cl <sub>2</sub>
Mr [g mol <sup>-1</sup> ]	1548.22	984.03
Crystal Size [mm]	0.23 × 0.21 × 0.09	0.28 × 0.23 × 0.14
Crystal System	trigonal	trigonal
Space Group	R32	R $\bar{3}c$
a [Å]	16.9884(7)	12.4324(11)
b [Å]	16.9884(7)	12.4324(11)
c [Å]	59.610(4)	57.227(5)
$\alpha$ [°]	90	90
$\beta$ [°]	90	90
$\gamma$ [°]	120	120
V [Å <sup>3</sup> ]	14898.9(15)	7660.2(15)
Z	6	6
D <sub>calcd</sub> [g cm <sup>-3</sup> ]	1.035	1.275
$\mu$ [mm <sup>-1</sup> ]	0.142	0.086
F(000)	4932	3090
2 $\theta$ range [°]	3.088–41.626	4.042–43.986
Reflections collected	49104	14909
Independent reflections, R <sub>int</sub>	3478, 0.1531	1052, 0.0330
Obs. Data [ $I > 2\sigma(I)$ ]	3042	818
Data/restraints/ parameters	3478/12/345	1052/154/185
R <sub>1</sub> ( $I > 2\sigma(I)$ )	7.27%	5.98%
R <sub>1</sub> (all data)	8.58%	7.41%
wR <sub>2</sub> (all data)	17.17%	16.80%
Goodness-of-fit (or S) on F <sup>2</sup>	1.077	1.096
Largest difference peak and hole (or Dr <sub>max</sub> and Dr <sub>min</sub> ) [e Å <sup>-3</sup> ]	0.220 and -0.254	0.305 and -0.197

## 2.6 References

- 1 T. Hasell and A. I. Cooper, *Nat. Rev. Mater.*, 2016, **1**, 1–14.
- 2 T. Hasell, X. Wu, J. T. A. Jones, J. Bacsá, A. Steiner, T. Mitra, A. Trewin, D. J. Adams and A. I. Cooper, *Nat. Chem.*, 2010, **2**, 750–755.
- 3 J. H. Zhang, S. M. Xie, M. Zi and L. M. Yuan, *J. Sep. Sci.*, 2020, **43**, 134–149.
- 4 A. G. Slater, M. A. Little, A. Pulido, S. Y. Chong, D. Holden, L. Chen, C. Morgan, X. Wu, G. Cheng, R. Clowes, M. E. Briggs, T. Hasell, K. E. Jelfs, G. M. Day and A. I. Cooper, *Nat. Chem.*, 2016, **9**, 17–25.
- 5 R. L. Greenaway, K. E. Jelfs, R. L. Greenaway and K. E. Jelfs, *Adv. Mater.*, 2021, **33**, 2004831.
- 6 R. L. Greenaway and K. E. Jelfs, *Chempluschem*, 2020, **85**, 1813–1823.
- 7 S. Bennett, F. T. Szczypiński, L. Turcani, M. E. Briggs, R. L. Greenaway and K. E. Jelfs, *J. Chem. Inf. Model.*, 2021, **61**, 4342–4356.
- 8 R. L. Greenaway, V. Santolini, M. J. Bennison, B. M. Alston, C. J. Pugh, M. A. Little, M. Miklitz, E. G. B. Eden-Rump, R. Clowes, A. Shakil, H. J. Cuthbertson, H. Armstrong, M. E. Briggs, K. E. Jelfs and A. I. Cooper, *Nat. Commun.*, 2018, **9**, 1–11.
- 9 Y. Jin, Y. Zhu and W. Zhang, *CrystEngComm*, 2013, **15**, 1484–1499.
- 10 A. Kewley, A. Stephenson, L. Chen, M. E. Briggs, T. Hasell and A. I. Cooper, *Chem. Mater.*, 2015, **27**, 3207–3210.
- 11 L. Chen, P. S. Reiss, S. Y. Chong, D. Holden, K. E. Jelfs, T. Hasell, M. A. Little, A. Kewley, M. E. Briggs, A. Stephenson, K. M. Thomas, J. A. Armstrong, J. Bell, J. Busto, R. Noel, J. Liu, D. M. Strachan, P. K. Thallapally and A. I. Cooper, *Nat. Mater.*, 2014, **13**, 954–960.
- 12 T. Hasell, M. Schmidtman and A. I. Cooper, *J. Am. Chem. Soc.*, 2011, **133**, 14920–14923.
- 13 H. Ren, C. Liu, X. Ding, X. Fu, H. Wang and J. Jiang, *Chinese J. Chem.*, 2022, **40**, 385–391.
- 14 E. Merino, *Chem. Soc. Rev.*, 2011, **40**, 3835–3853.

- 15 G. Zhang and M. Mastalerz, *Chem. Soc. Rev.*, 2014, **43**, 1934–1947.
- 16 J. D. Evans, C. J. Sumby and C. J. Doonan, *Chem. Lett.*, 2015, **44**, 582–588.
- 17 L. Turcani, E. Berardo and K. E. Jelfs, *J. Comput. Chem.*, 2018, **39**, 1931–1942.
- 18 E. Harder, W. Damm, J. Maple, C. Wu, M. Reboul, J. Y. Xiang, L. Wang, D. Lupyan, M. K. Dahlgren, J. L. Knight, J. W. Kaus, D. S. Cerutti, G. Krilov, W. L. Jorgensen, R. Abel and R. A. Friesner, *J. Chem. Theory Comput.*, 2016, **12**, 281–296.
- 19 A. Khan and S. Hecht, *Eur. J. Chem.*, 2006, **12**, 4764–4774.
- 20 T. A. Geissman, *Org. React.*, 2011, **2**, 94–113.
- 21 M. H. Davey, V. Y. Lee, R. D. Miller and T. J. Marks, *J. Org. Chem.*, 1999, **64**, 4976–4979.
- 22 P. Skowronek, B. Warzajtis, U. Rychlewska and J. Gawroński, *Chem. Commun.*, 2013, **49**, 2524–2526.
- 23 K. E. Jelfs, X. Wu, M. Schmidtman, J. T. A. Jones, J. E. Warren, D. J. Adams and A. I. Cooper, *Angew. Chemie Int. Ed.*, 2011, **50**, 10653–10656.
- 24 M. E. Briggs, K. E. Jelfs, S. Y. Chong, C. Lester, M. Schmidtman, D. J. Adams and A. I. Cooper, *Cryst. Growth Des.*, 2013, **13**, 4993–5000.
- 25 R. S. L. Gibson, J. Calbo and M. J. Fuchter, *ChemPhotoChem*, 2019, **3**, 372–377.
- 26 R. L. Greenaway, V. Santolini, M. J. Bennison, B. M. Alston, C. J. Pugh, M. A. Little, M. Miklitz, E. G. B. Eden-Rump, R. Clowes, A. Shakil, H. J. Cuthbertson, H. Armstrong, M. E. Briggs, K. E. Jelfs and A. I. Cooper, *Nat. Commun.*, 2018, **9**, 1–11.
- 27 M. Bauer and F. Vögtle, *Chem. Ber.*, 1992, **125**, 1675–1686.
- 28 B. Moosa, L. O. Alimi, A. Shkurenko, A. Fakim, P. M. Bhatt, G. Zhang, M. Eddaoudi and N. M. Khashab, *Angew. Chemie - Int. Ed.*, 2020, **59**, 21367–21371.
- 29 A. S. Oshchepkov, S. S. R. Namashivaya, V. N. Khrustalev, F. Hampel, D. N.

- Laikov and E. A. Kataev, *J. Org. Chem.*, 2020, **85**, 9255–9263.
- 30 T. Yuan, Z. Q. Wang, X. Q. Gong and Q. Wang, *Tetrahedron Lett.*, 2020, **61**, 152626.
- 31 S. Jiang, J. T. A. Jones, T. Hasell, C. E. Blythe, D. J. Adams, A. Trewin and A. I. Cooper, *Nat. Commun.*, 2011, **2**, 1–7.
- 32 E. Fischer, *J. Phys. Chem.*, 1967, **71**, 3704–3706.
- 33 A. H. Heindl, J. Becker and H. A. Wegner, *Chem. Sci.*, 2019, **10**, 7418–7425.
- 34 M. Miklitz and K. E. Jelfs, *J. Chem. Inf. Model.*, 2018, **58**, 2387–2391.
- 35 H. M. D. Bandara and S. C. Burdette, *Chem. Soc. Rev.*, 2012, **41**, 1809–1825.
- 36 S. Crespi, N. A. Simeth and B. König, *Nat. Rev. Chem.*, 2019, **3**, 133–146.
- 37 Z. F. Liu, K. Morigaki, T. Enomoto, K. Hashimoto and A. Fujishima, *J. Phys. Chem.*, 1992, **96**, 1875–1880.
- 38 K. Stranius and K. Börjesson, *Sci. Rep.*, 2017, **7**, 1–9.
- 39 S. Delbaere and G. Vermeersch, *J. Photochem. Photobiol. C Photochem. Rev.*, 2008, **9**, 61–80.
- 40 G. M. Sheldrick and IUCr, *Acta Crystallogr. Sect. C Struct. Chem.*, 2015, **71**, 3–8.
- 41 G. M. Sheldrick and IUCr, *Acta Crystallogr. Sect. A Found. Crystallogr.*, 2015, **71**, 3–8.
- 42 O. V. Dolomanov, L. J. Bourhis, R. J. Gildea, J. A. K. Howard and H. Puschmann, *J. Appl. Crystallogr.*, 2009, **42**, 339–341.
- 43 X. H. Yu, C. C. Peng, X. X. Sun and W. H. Chen, *Eur. J. Med. Chem.*, 2018, **152**, 115–125.
- 44 N. R. Reddy, R. Kumar and S. Baskaran, *European J. Org. Chem.*, 2019, **2019**, 1548–1552.



## **Chapter 3**

### **Photoresponsive Type III Porous Liquids**

### 3.1 Preface

In this chapter, a new variation of a type III porous liquid (that is, a suspension of a porous material in a size-excluded solvent) is explored. Until now, almost all examples of porous liquids largely focused on the porosity of the material, with gas uptake being the primary point of study. While gas uptake remains at the heart of this study, we aim to investigate alternative mechanisms to release the gas from within the porous liquid. Currently there are only four methods implemented to release gas from a porous liquid: heating, sonication, chemical displacement, and pressure swings. Here, we explore a proof-of-concept and create the first photoresponsive type III porous liquid. To achieve this, we utilise a known metal-organic framework which is capable of dynamic photo-switching and changing the amount of gas adsorbed by irradiating the sample with UV light. In addition to the ability to change the CO<sub>2</sub> uptake by irradiation, we identify excellent CO<sub>2</sub>/CH<sub>4</sub> selectivity, which we believe demonstrates the highest selectivity observed in any porous liquid.

The work within this chapter has been prepared for publication and a pre-print is available (M. C. Brand, N. Rankin, A. I. Cooper, and R. L. Greenaway, *Shining a Light on Photoresponsive Type III Porous Liquids*, ChemRxiv, **2022**, DOI: 10.26434/chemrxiv-2022-mgwnm).

Synthesis, characterisation, gas sorption and analysis were carried out by M. Brand. Development of the photoreactor for porous liquids was carried out by M. Brand and N. Rankin. Project guidance was provided by R. Greenaway and A. Cooper.



### 3.2 Type III Porous Liquids

Type III porous liquids (PLs) are a class of PL produced from dispersing a microporous material in a size-excluded solvent.<sup>1</sup> While one of the earliest reports of a PL was in 2015, which is one of the most cited publications in the field,<sup>2</sup> another report published the year before describes a type III system which falls under the definition of a PL, though it was not described as one at that time and was referred to as a hybrid absorption–adsorption system.<sup>3</sup> There, the authors report the production of a slurry, composed of a MOF (zeolitic imidazolate framework-8, ZIF-8) dispersed in an imidazole-modified poly(ethylene glycol) (PEG), which was capable of selectively adsorbing CO<sub>2</sub> in its slurry form. Type III PLs are now arguably the most researched class of PL, which is likely due to the wide range of porous materials that can be incorporated, and the ever-growing list of size-excluded liquids. These materials can include MOFs, zeolites, POCs, and porous organic polymers (Figure 3.1).<sup>4</sup>

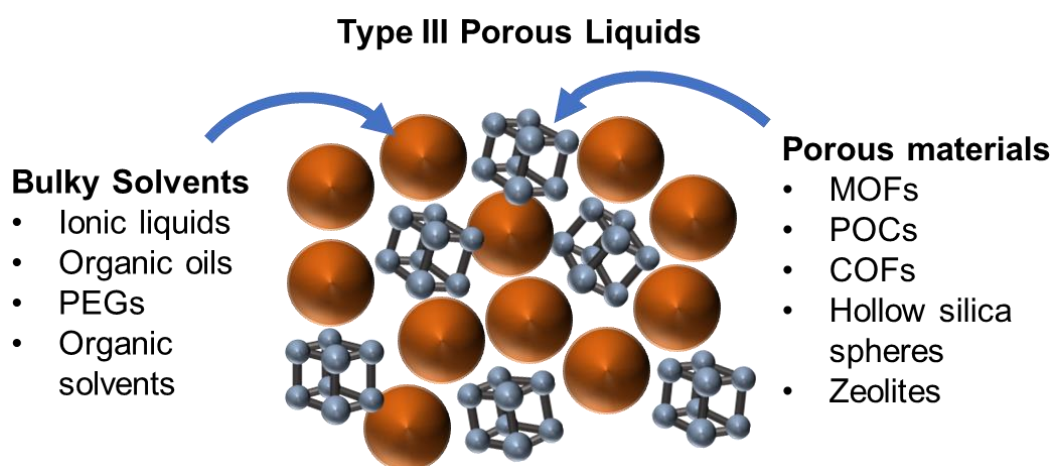


**Figure 3.1** Summary of materials used to prepare type III porous liquids.

While it may seem simple to select a porous material based on its properties in the solid state, these do not always directly translate over to the porous liquid. This has previously been shown by Egleston *et al.*, who demonstrated a vast difference in gas selectivity in a type II porous liquid versus in the solid state.<sup>5</sup> Xenon selectivity was completely lost when a POC with a smaller pore window was incorporated into the porous liquid, whereas changing the POC (and increasing the window size) allowed for xenon uptake in the same solvent, while both samples were confirmed to remain porous by CH<sub>4</sub> measurements. Although, in some cases, desirable features of the porous material in the solid state does directly translate to those incorporated into porous liquids. Such is the case for a silver zeolite which showed selectivity for ethane over ethene in the solid state.<sup>6</sup> This followed through to the porous liquid variant,

which also demonstrated selectivity for ethane over ethene, by utilising a variety of ionic liquids and oils to disperse the silver zeolite material.<sup>7</sup>

One of the other considerations that needs to be taken into account when designing a type III porous liquid, other than being size-excluded from the material, is the vapour pressure of the liquid. Having a liquid with a high vapour pressure can result in mass loss from the sample, which could lead to an increased concentration of the PL. This could cause an increase in the viscosity, reducing its ability to flow and possibly leading to sedimentation of the porous material from the liquid. It could also prevent the possibility of removing gaseous guest molecules using temperature and pressure swings because of the loss of solvent, making it difficult to justify industrial and scientific applications if the porous liquid cannot be regenerated. Porous liquids formed using high vapour pressure solvents can also cause issues with analytical procedures, such as gas sorption, which could cause damage to the instrumentation if the solvent condenses in the components of the apparatus.

To satisfy that consideration there are some excellent candidates with low vapour pressures, which include various oils and ionic liquids. They are good candidates due to their broad range of commercial availability, including some simplistic options like vegetable and olive oil. Ionic liquids are also an option which have the advantage of being synthetically modifiable, where they can be tailored towards, or against, certain types of gases, such as CO<sub>2</sub>. One of the earliest reports of a permanently microporous

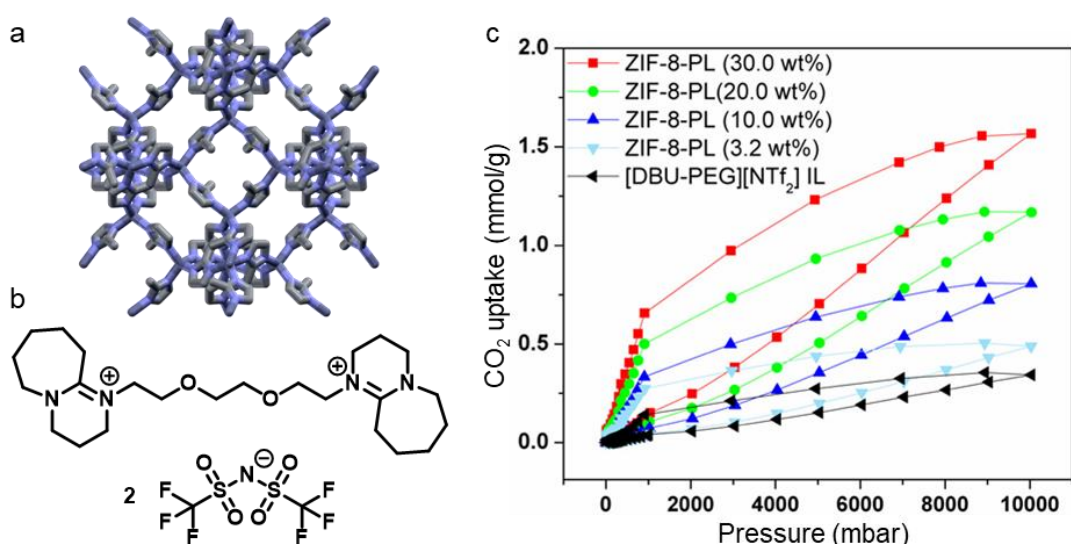


**Figure 3.2** a) Crystal structure of ZIF-8; b) structure of the ionic liquid [DBU-PEG][NTf<sub>2</sub>]; c) CO<sub>2</sub> isotherms of the neat ionic liquid and ZIF-8 porous liquid at various concentrations. Reproduced with permissions from ref (8).

dispersion as a type III PL was investigated by Shan *et al.*, which focused on producing a PL by using a bulky ionic liquid ([DBU-PEG][NTf<sub>2</sub>]), containing two capped ends, similar to that of rotaxanes, to prevent the solvent from entering the porous material.<sup>8</sup> Here they utilise a well-studied MOF, ZIF-8, in combination with the ionic liquid to form a stable dispersion with concentrations up to 30 wt%, which resulted in a CO<sub>2</sub> uptake approximately 5 times higher than that of the neat ionic liquid (Figure 3.2).

Organic oils are perhaps the most studied solvents in terms of developing new type III PLs, with a study from Cahir *et al.* reporting the creation of over 90 new PLs by the addition of 17 MOFs to 16 different types of oils.<sup>9</sup> This included a range of silicone and paraffin oils with differing viscosities, along with household triglyceride oils (olive oil, sunflower oil, sesame oil, and more). Of these PLs, they observed enhanced CO<sub>2</sub> and CH<sub>4</sub> uptake in many samples, whereas solvents based on PEG liquids were shown to have no increase in gas uptake in the PL versus the neat liquid. A similar study using organic oils was reported by Kai *et al.*, where they implemented POCs rather than MOFs as the porous material.<sup>10</sup> Here they describe an increase in CO<sub>2</sub> uptake in the corresponding PLs from all 7 oils in the study, where they found that some PLs (at a 12.5 wt% loading) were able to achieve two times the CO<sub>2</sub> uptake than the neat liquid. In addition to the measurements using organic oils, they also implemented ionic liquids as a solvent for type III PLs. Interestingly, while the ionic liquids they used were bulky, and they reported an uptake over double that of the neat liquid when a pyridinium-derived ionic liquid was used in the PL, another system produced from a slightly different ionic liquid containing a methylated imidazole and the same counterion showed negligible difference in uptake between the PL and neat liquid. This demonstrates the difficulty that comes with choosing solvents for the development of PLs, where previously reported size-excluded solvents may be specific to each system rather than being a general trend, and solvents which may appear sufficiently bulky can behave differently depending on the material.

### **3.3 Developing a Photoresponsive Porous Liquid**

#### **3.3.1 Choice of Material**

While it may seem trivial to combine porous material, A, with bulky solvent, B, to form a type III PL, C, designing a porous liquid is far more difficult in reality. While some solvents may be identified as sufficiently large to not block or enter porous materials, they may lead to unusual properties when combined with other materials, or even prevent porosity. As the field is relatively new, having only been discovered within the

past decade, there are still trends in developing these materials that remain widely unknown. While there are increasing numbers of researchers in this field, the research seems almost stagnant in terms of trying to discover new ways to utilise these materials. New publications are typically aimed at finding appropriate solvents and porous materials, and appear to be trying to find the holy grail of high gas uptake for a PL,<sup>11</sup> similar to the first decade of MOFs where a large emphasis was on trying to create the highest surface area,<sup>12,13</sup> rather than branching out to gather a wider understanding of the field.

One of the areas that has yet to receive much attention is the mechanism of gas release from PLs. To date, there are several methods used to release the gas from within the cavities of PLs, which include sonication,<sup>14</sup> chemical displacement,<sup>15</sup> temperature swings,<sup>10</sup> and pressure swings.<sup>8</sup> All of these have problems associated with them that could prevent their wide-scale applications in industry. Temperature and pressure swings are currently the most extensively used methods within industry, especially in terms of liquid-based sorbents such as amine gas scrubbers, which are required to regenerate the material for the purpose of recycling. While these methods are well studied, they still account for vast amounts of waste as they are very energetically demanding.<sup>16</sup> This also limits the possibilities of PLs in relation to solvent choice, due to the inherent problems mentioned regarding vapour pressures and solvent loss. In addition to solvent choice, considerations need to be made in terms of the porous materials used to ensure they withstand these conditions. For example, flue gas contains a large quantity of water which could cause an imine-derived POC-based PL to decompose, along with high temperatures, which could lead to a degree of instability of the material. This also makes the argument to develop a new system to remove gas from industrial processes difficult if there are no significant advantages over current processes, or if they do not produce a feasible return on investment. Chemical displacement uses small liquid guests to displace gas molecules within the pores of the material, causing the release of gas. This can lead to a mixture which is difficult to regenerate, making it hard to recycle, which realistically would not be considered for industrial applications. Finally, while sonication is possibly the least invasive of all four methods, it is not currently used within large-scale operations due to the technical limitations.<sup>17</sup>

One can look towards the possibility of an alternative low energy mechanism to release gas from a PL, one of those being photochromic or photoresponsive materials. While there are examples of photoresponsive liquids<sup>18–20</sup> and liquid crystals,<sup>21</sup> there are no reports of a photoresponsive PL. With this in mind, there are

very few options which can be used to incorporate a material into a photoresponsive PL. As the photoresponsive porous organic cages developed in Chapter 2 were not at a point where they could be utilised in either type II or type III PLs, and there were no other types of photoresponsive organic cages when this project was started, we looked towards MOFs for a suitable material to create a proof-of-concept photoresponsive type III PL. The MOF selected was originally reported by Chen *et al.*, who found a triple interpenetrated material, with a combination of 4,4'-azobenzenedicarboxylate (AzDC), *trans*-bis(4-pyridyl)ethylene (4,4'-BPE), and zinc nodes as  $\text{Zn}(\text{AzDC})(4,4'\text{-BPE})_{0.5}$  (**Figure 3.3**).<sup>22</sup> They reported a variety of gas sorption studies with some desirable gas selectivity such as  $\text{H}_2/\text{N}_2$ ,  $\text{H}_2/\text{CO}$ , and  $\text{CO}_2/\text{CH}_4$ . Unfortunately, while they successfully incorporated two molecules that are capable of isomerisation, there was no mention of trying to isomerise the material. This material was later studied by Lyndon *et al.*, who managed to successfully identify the dynamic photoswitching aspect that this material had to offer.<sup>23</sup> Here they demonstrated the material's ability to increase and decrease  $\text{CO}_2$  by irradiating it with UV light or leaving it under ambient conditions, demonstrating its ability to expand and contract depending on the wavelength it was exposed to. The material's selective behaviour towards  $\text{CO}_2$  over  $\text{CH}_4$ , in combination with its active photoresponsive nature, makes it an excellent candidate to try and incorporate into a PL.

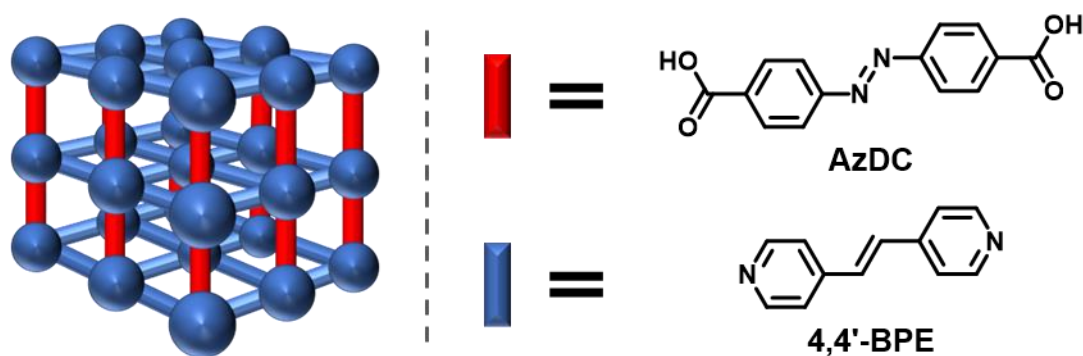


**Figure 3.3** Representative image of the photoswitching MOF,  $\text{Zn}(\text{AzDC})(4,4'\text{-BPE})_{0.5}$ , and its precursors *trans*-4,4'-azobenzenedicarboxylate (AzDC) and *trans*-bis(4-pyridyl)ethylene (4,4'-BPE).<sup>22</sup>

### 3.3.2 Designing a Photoreactor for Gas Sorption of Porous Liquids

Measuring the gas adsorption properties in PLs can be done in a variety of ways, with several methods similar to those that are performed for porous solids. There are examples of PLs being measured using gravimetric analysis (determined by changes in weight at each dosing),<sup>8</sup> volumetric analysis (determined by changes in pressure at each dosing),<sup>15</sup> and gas displacement measurements,<sup>14</sup> all of which are viable

methods to obtain gas uptake data. The Cooper group have been utilising a Quantachrome Nova 4200e for volumetric gas sorption analysis of PLs, which has been shown to be within error of other reports of gas solubility in liquids at room temperature.<sup>10</sup> One of the limitations of a liquid versus a solid material is the nature of diffusion. In a solid, gas has the capability to diffuse through the material which allows gas sorption analysis to be taken on static samples. Gas sorption of liquids can be limited by the diffusion of gas into the material, which can lead to a lower observed gas uptake or long equilibration times for saturation of the material. The observed accuracy can be greatly increased by adding stirring which allows for good mixing between the gas and liquid, enhancing the diffusion of the gas into the material. As the samples require constant stirring, a circulating water cooler cannot be used and therefore temperatures below room temperature cannot be achieved. Though, sample heating can take place using a heating block.

These factors needed to be taken into consideration when developing a reactor capable of irradiating a porous liquid sample. The first consideration was to create a reactor where the distance between the sample and the stirrer plate had to be small enough for the stirrer bar to still feel the effect, allowing the sample to stir. The maximum distance the sample can be from the stirrer plate is approximately 4 cm, which still provides adequate stirring of the sample. This leaves very few options for any type of active water cooling, like the setup used by Lyndon *et al.*, that uses an aluminium block submerged in water for measurements on their photoresponsive MOF, which can be performed without stirring.<sup>23</sup> Other types of photoresponsive porous materials with a longer half-life are able to be irradiated prior to the experiment, where the long half-life provides significant change for the duration of the experiment.<sup>24</sup> The material selected for this study has a short isomerisation half-life which leads to very dynamic uptakes, leading to fast differences in gas uptake when the sample is irradiated with UV light or in dark conditions. Hence, for this study, the sample needed to be under constant irradiation throughout the experiment.

To design reactors, additive manufacturing (3D printing) was implemented. 3D printing has become vastly more accessible over the past decade, with cheaper units available costing as little as £100. While cheaper units tend to be less reliable and can often need more maintenance than more expensive units, they are an excellent starting point as an introduction to 3D printing. 3D printing offers a wide range of versatility, and there are a large number of open access designs along with free tutorials available online. Free design software is also widely available, for example, Autodesk Fusion 360 was used to create the computer-aided designs for this project.

3D printing also offers a relatively short production time, which allows for fast prototypes to be developed compared to the timeframes for CNC machining of materials like aluminium.

The first iteration of the photoreactor combined a simple 3D printed box, to prevent external light from reaching the sample, and a low power LED (365 nm) fitted to an aluminium heat sink with a variable power supply (Figure 3.4, a). Preliminary experiments found that there was no change in CO<sub>2</sub> uptake, which was likely due to the significantly lower power output of the LED, which was only 1/20<sup>th</sup> of the power output of the initial report for this material. After measuring the internal temperature of the photoreactor, a negligible temperature increase was observed (>1 °C).

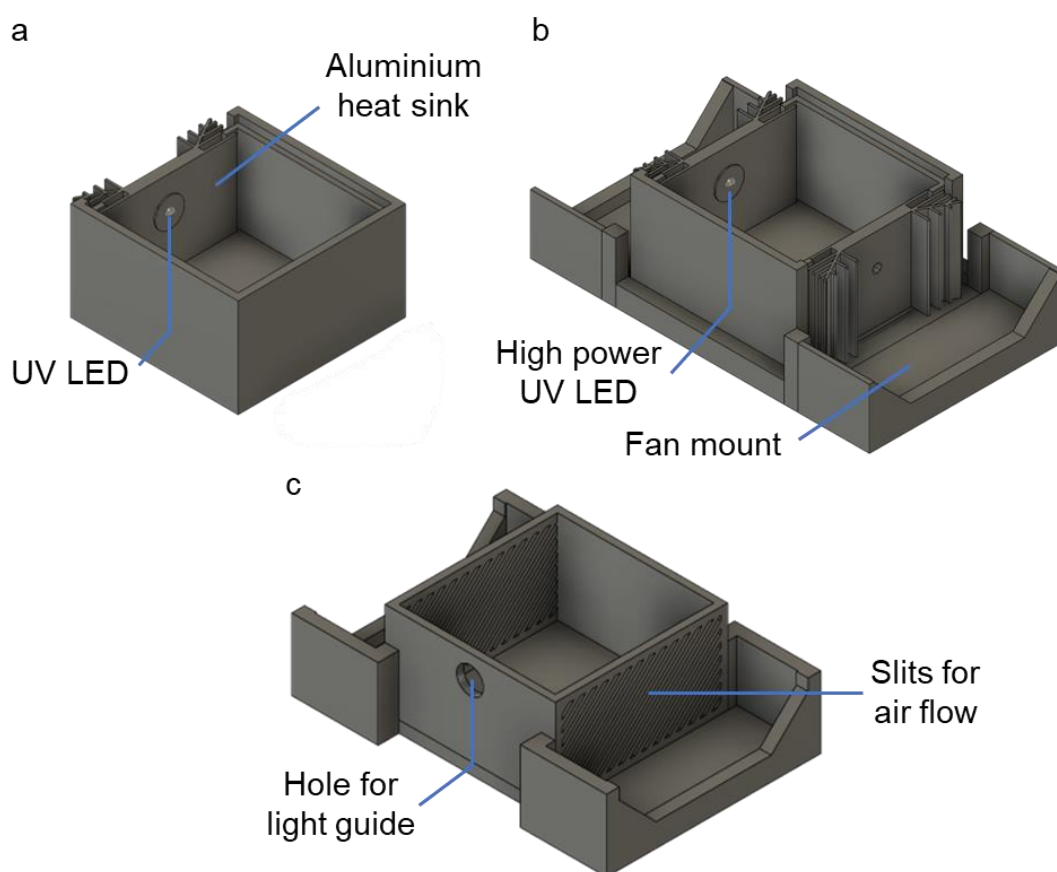


**Figure 3.4** Various 3D models of photoreactor design iterations, where a) version 1, simple box design with low power LED; b) version 2, two high power LEDs fitted with two external fans; c) version 3, slitted box design for airflow with side hole for external light source.

A higher power LED (3,800 mW, 365 nm) was then utilised to increase power output nearer to that previously reported for this material (5,200 mW). To increase the amount of exposure, the interior walls were covered in aluminium foil to reflect any UV light. After replacing the setup with this LED, a far greater change in CO<sub>2</sub> uptake

was observed at 1 bar measurements while irradiating, though still significantly less than the original report. Hence, a second LED was added to the setup on the opposite side of the photoreactor to increase sample exposure and provide a greater power output (Figure 3.4, b). A significant change in CO<sub>2</sub> uptake was observed, although on measuring the internal temperature there was a substantial increase in the region of 20 – 30 °C above ambient conditions, which would have contributed to the observed decrease in gas uptake. Two external fans were fitted to the rear side of the heatsink to increase airflow and dissipate heat generated by the LEDs. This noticeably decreased the internal temperature of the photoreactor, however, the temperature inside the box remained elevated. While this was promising, it would remain unsuitable to perform measurements under constant irradiation and ambient conditions due to the ~10 °C difference, causing a difference in gas uptake due to an increased temperature, rather than as a direct result of just the irradiation.

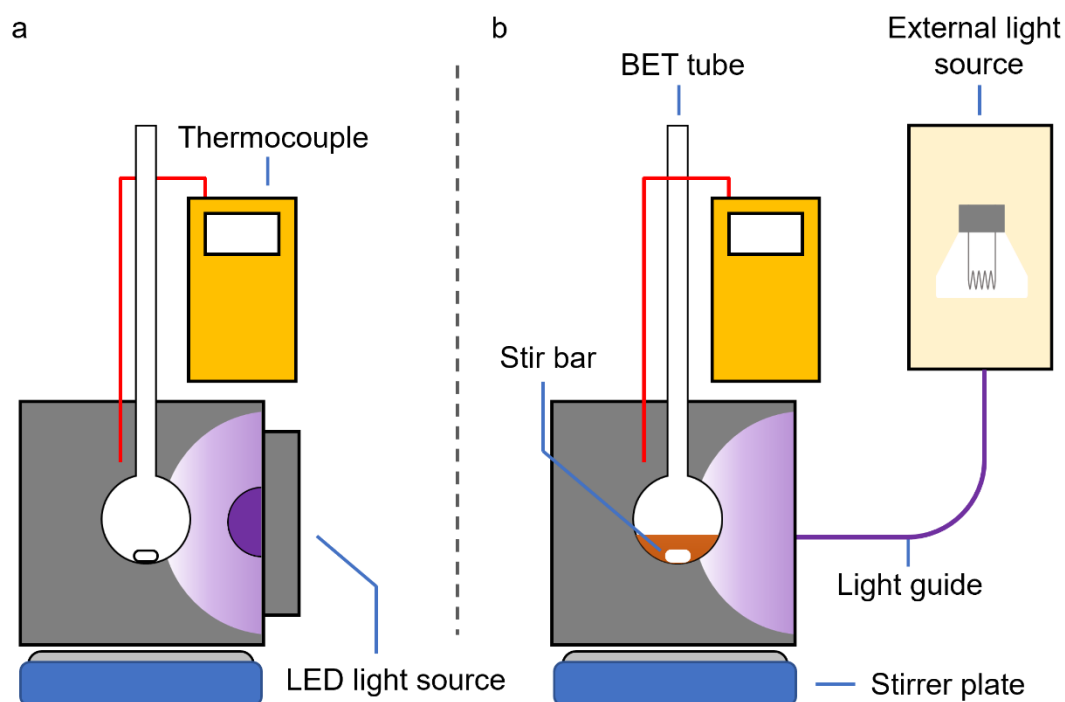


**Figure 3.5** Visual representations of photoreactor designs for constant irradiation while performing gas sorption experiments, where a) LED experimental setup; b) experimental setup with an external light source.

As most of the increase in temperature was arising from using internal light sources, an external light source was implemented instead (Figure 3.5). A UV curing system with a 100 W mercury bulb was repurposed as an external light source and fitted with a 365 nm filter, which produced a power output of 5,200 mW when fitted. A fibre optic light guide could also be fitted to the external light source, providing a direct point of



entry into the photoreactor box (Figure 3.4, c). On opposite ends of the photoreactor, slits were added to the design to allow for airflow through the box, and two external fans were fitted in a push-pull configuration. As aluminium foil did not provide a mirror surface after adhesion, mirrored acrylic sheets were cut to size to cover the interior surfaces which did not have any slits present to reflect any residual light. Finally, the internal temperature was monitored over the course of several days, which found that the internal temperature within the photoreactor remained at 28.5 °C, with less than 0.5 °C fluctuation when the UV light was on versus when the sample was under ambient conditions. With this experimental setup, a decrease in CO<sub>2</sub> uptake was observed for the solid Zn(AzDC)(4,4'-BPE)<sub>0.5</sub> material, going from 941 μmol/g under ambient conditions to 666 μmol/g while under constant irradiation, a decrease of 29%. While this was lower than the original report of 42%, which also used specialised quartz BET tubes, these results were sufficient as a proof-of-concept for a photoresponse using standard borosilicate BET tubes.

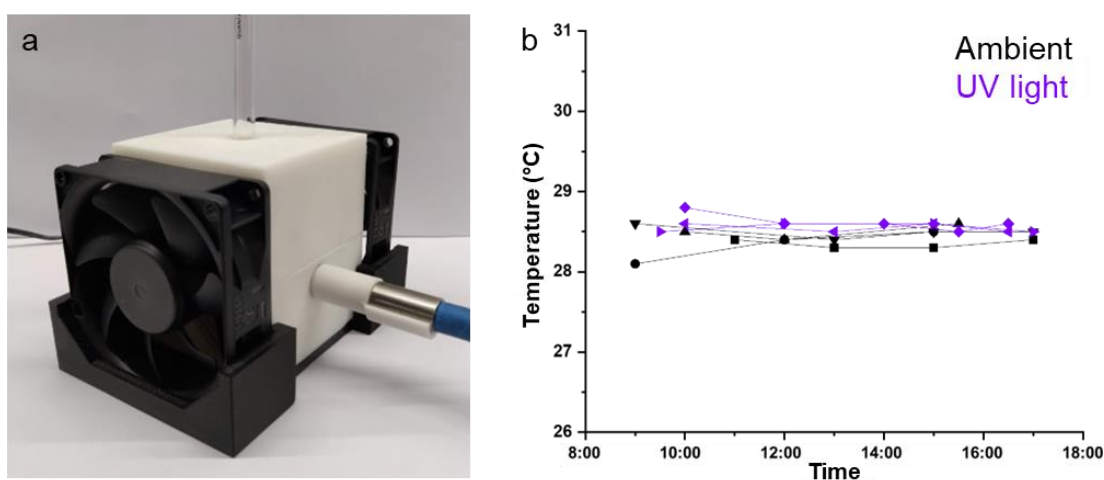


**Figure 3.6** a) The final 3D printed photoreactor design for gas sorption; b) Internal temperature monitoring of the photoreactor versus time.

### 3.3.3 Solvent Screening

Given the ever-broadening number and types of liquids used to develop PLs, this study focused on those that were recently used in another type III PL study within the Cooper group (Figure 3.7).<sup>10</sup> For screening combinations to produce a PL, CO<sub>2</sub> gas sorption was primarily used to identify whether there is an increase in uptake upon the addition of porous material to the liquid over that of the neat liquid.

One physical property that often seems to be missing from scientific reports of PLs at high wt% concentrations is the viscosity of the produced liquids. On preparing high loadings, the viscosity increases, so there needs to be a compromise between the uptake and the viscosity in the resulting PL. When the loading becomes too high, it may still be reported and classed as a liquid, but it might be too viscous to stir, which defeats the purpose of producing a liquid if it is unable to flow like a conventional liquid. With that in mind, the highest loading in this study was limited to 20 wt%.

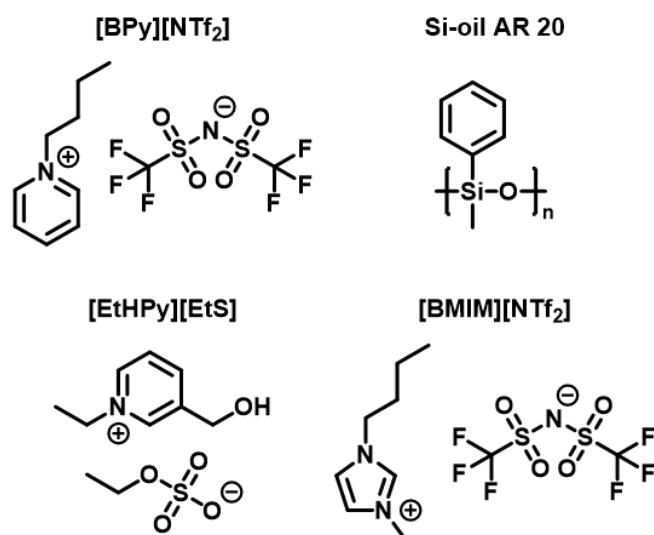


**Figure 3.7** Structures of liquids screened to form type III porous liquids: 1-butylpyridinium bis(trifluoromethanesulfonyl)imide ([BPy][NTf<sub>2</sub>]), silicone oil AR 20, 1-ethyl-3-(hydroxymethyl)pyridinium ethyl sulfate ([EtHPy][EtS]), and 1-butyl-3-methylimidazolium bis(trifluoromethylsulfonyl)imide ([BMIM][NTf<sub>2</sub>]).

Four liquids were selected for screening which included silicone oil AR 20, and ionic liquids 1-butylpyridinium bis(trifluoromethanesulfonyl)imide ([BPy][NTf<sub>2</sub>]), 1-ethyl-3-(hydroxymethyl)pyridinium ethyl sulfate ([EtHPy][EtS]) and 1-butyl-3-methylimidazolium bis(trifluoromethylsulfonyl)imide ([BMIM][NTf<sub>2</sub>]). To screen these liquids for size-exclusivity from the MOF, 12.5 wt% dispersions were prepared. The CO<sub>2</sub> uptake was measured under ambient conditions, that is without UV irradiation and in the presence of laboratory lighting, while stirring at 300 rpm. In all cases there was some improvement in CO<sub>2</sub> uptake, though results drastically varied (Figure 3.8, Table 3.1). The worst performance was the dispersion formed using [BPy][NTf<sub>2</sub>], with only a negligible improvement in uptake of 4.1 μmol/g<sub>L</sub> over the neat ionic liquid. This suggests that the ionic liquid is either entering the pores of the MOF or the liquid is interacting with the surface of the material, preventing any CO<sub>2</sub> from entering. Interestingly, this ionic liquid was one of the best examples from the type III porous liquid study using POCs as the dispersed porous material,<sup>10</sup> which leads back to the

difficulty in choosing suitable solvent systems for PLs, given trends can drastically change even if they are identified as being size-excluded in other PLs. The second ionic liquid, [EtHPy][EtS], showed a considerable improvement in CO<sub>2</sub> uptake over the neat liquid with an increase of 59%, corresponding to an increase of 25.8 μmol/g<sub>L</sub>.

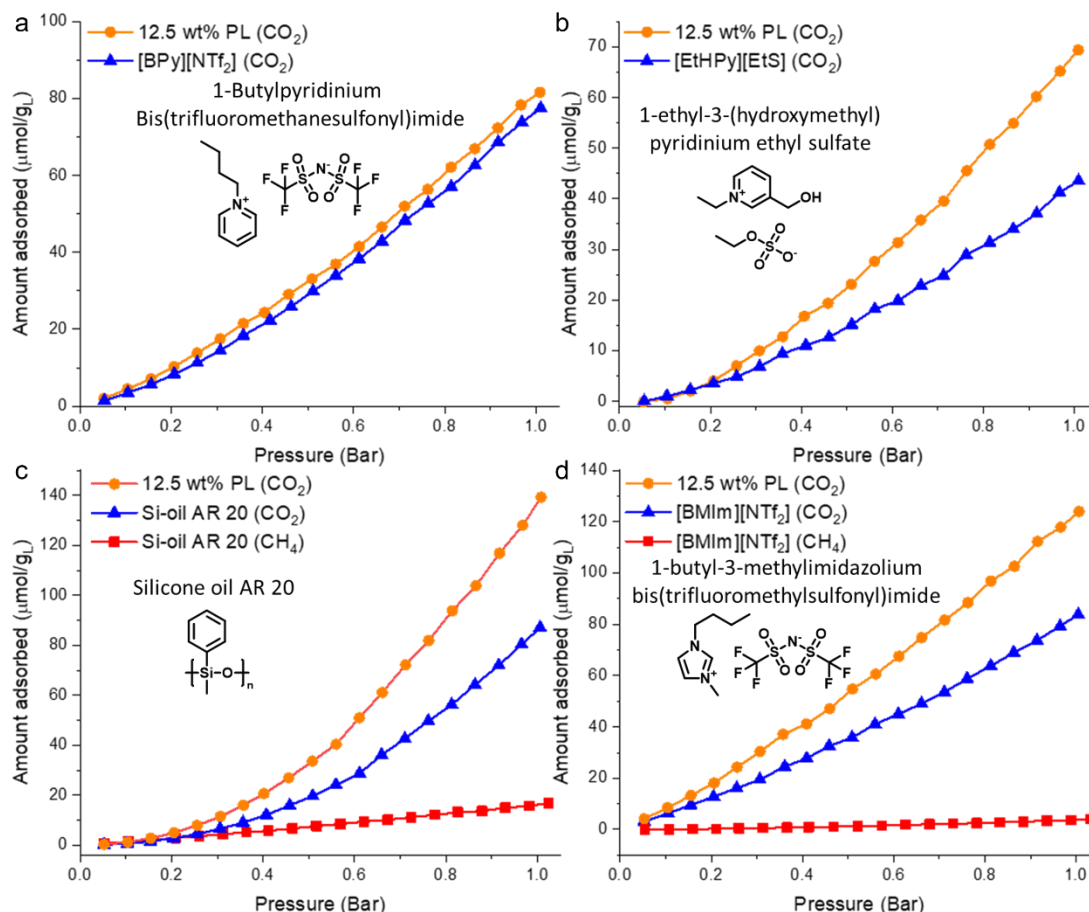


**Figure 3.8** Porous liquid screening using gas uptake measurements for the neat liquid and the resulting liquid with a 12.5 wt% loading, where a) [BPy][NTf<sub>2</sub>]; b) [EtHPy][EtS]; c) silicone oil AR 20; d) [BMIM][NTf<sub>2</sub>].

The remaining two liquids, silicone oil AR 20 and [BMIM][NTf<sub>2</sub>] both achieved significantly higher CO<sub>2</sub> uptake than the initial two ionic liquids that were screened. [BMIM][NTf<sub>2</sub>] also behaved vastly differently from the other type III POC PLs, where it was one of the worst liquids in that study. For both PLs, increases in CO<sub>2</sub> uptake were found to be 52.2 μmol/g<sub>L</sub> and 40.2 μmol/g<sub>L</sub> which equates to increases of 60% and 48% over the neat liquids for silicone oil AR 20 and [BMIM][NTf<sub>2</sub>], respectively. As these were the two highest observed CO<sub>2</sub> uptakes, with good increases over that

**Table 3.1** Summary of gas uptake measurements in neat liquids and attempts at producing porous liquids with their corresponding gas uptakes.

Sample	CO <sub>2</sub> uptake at 1 bar (μmol/g <sub>L</sub> )		Difference (μmol/g <sub>L</sub> )	CH <sub>4</sub> uptake at 1 bar (μmol/g <sub>L</sub> )
	Neat Liquid	12.5 wt% PL		12.5 wt% PL
[BPy][NTf <sub>2</sub> ]	77.4	81.5	4.1	-
[EtHPy][EtS]	43.5	69.3	25.8	-
Si-oil AR 20	87.0	139.2	52.2	16.8
[BMIM][NTf <sub>2</sub> ]	83.7	123.9	40.2	4.0

of the neat liquid, CH<sub>4</sub> uptake in the neat liquids was also investigated. In both cases there was significantly less CH<sub>4</sub> uptake than CO<sub>2</sub>, however [BMIM][NTf<sub>2</sub>] took up 4 times less CH<sub>4</sub> than silicone oil AR 20. With the desire to also access a type III PL with good CO<sub>2</sub>/CH<sub>4</sub> selectivity, a compromise had to be made between the system which had the highest CO<sub>2</sub> uptake and an ionic liquid which would take up less CH<sub>4</sub>. Moving forward it was decided that a lower CH<sub>4</sub> uptake would be preferential to try and produce a CO<sub>2</sub> selective PL, hence [BMIM][NTf<sub>2</sub>] was selected for further studies.

### 3.3.4 Photoresponsive Gas Sorption Experiments

To investigate the photoresponsive aspect of the porous liquids that are formed after dispersing the MOF in the selected ionic liquid, [BMIM][NTf<sub>2</sub>], and its effect on the overall gas uptake, a variety of samples were prepared at 5, 12.5, and 20 wt%. Samples were prepared directly in gas sorption tubes, where the MOF was weighed in the tubes and the corresponding amount of ionic liquid then added, to ensure a representative wt% was measured by preventing loss of material when loading the tubes. Samples were then sonicated and placed under continuous vacuum for 20 hours with stirring. Once a sample had been evacuated, it was placed inside of the photoreactor before running the sorption experiment – the samples were degassed between ambient and irradiated measurements.

Initial results were promising in terms of developing a photoresponsive type III PL. At all loadings (5, 12.5, and 20 wt%), an increase in CO<sub>2</sub> uptake was observed (Figure 3.9). Irradiation with UV light also showed a decrease in CO<sub>2</sub> uptake versus the samples measured under ambient conditions. The 20 wt% PL was able to adsorb the largest amount of CO<sub>2</sub>, where a decrease of 20% could be observed after irradiation

with UV light. The 12.5 wt% sample performed rather disappointingly and had adsorbed a quantity of gas much closer to that of the 5 wt% sample, rather than that of the 20 wt% as one would expect. The change in uptake upon irradiating with light was also disappointing and inconsistent with the behaviour observed for the 20 wt% sample, with only a 6% decrease in CO<sub>2</sub> uptake apparent. The 5 wt% sample behaved as expected, with an increase in CO<sub>2</sub> uptake of 38% over the neat ionic liquid, and a decrease of 21% could be observed after exposing the sample to UV light.

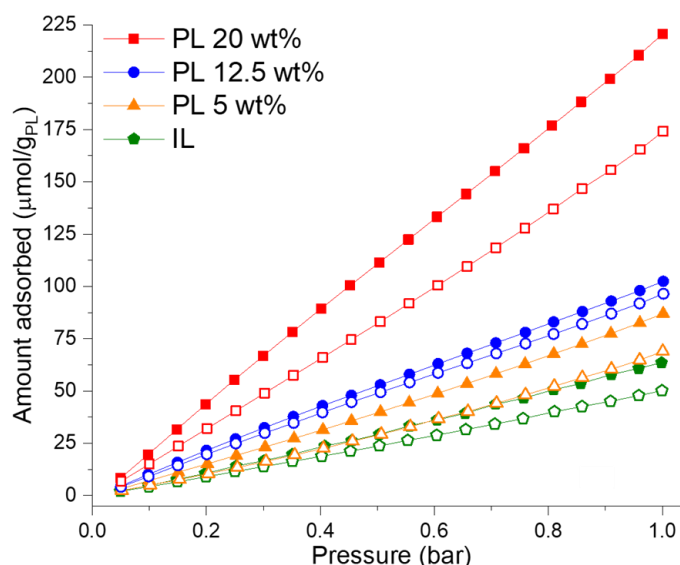


**Figure 3.9** CO<sub>2</sub> adsorption isotherms for Zn(AzDC)(4,4'-BPE)<sub>0.5</sub> [BMIM][NTf<sub>2</sub>] porous liquid at different loadings, and neat [BMIM][NTf<sub>2</sub>] ionic liquid, under ambient conditions (filled) and irradiated with UV light (empty).

Unusual activity was also observed with the neat ionic liquid when it was exposed to UV irradiation for the duration of the experiment, where a decrease in CO<sub>2</sub> uptake was also apparent (Figure 3.9). As the temperature within the box was consistent, maintaining between 28 °C and 29 °C, it seems unlikely that the observed 21% decrease in CO<sub>2</sub> uptake is associated to temperature. Unfortunately, there are very few reports of the effects of irradiating ionic liquids with UV light. A report by Rao *et al.* investigated the effects of UV light of an ionic liquid which has the same cation as this study, BMIM<sup>+</sup>, but a different anion, BF<sub>4</sub><sup>-</sup>, rather than NTf<sub>2</sub><sup>-</sup>.<sup>25</sup> Here they hypothesise the possibility of the cation undergoing structural changes as a result of forming new species with itself and the counterion. They observe new species using mass spectrometry after irradiation, along with a decrease in absorbance in the UV-Vis spectra. However, <sup>1</sup>H NMR spectroscopic analysis demonstrated no detectable

destruction or changes to the molecular structure, and the authors suggest that less than 0.5% of the material undergoes any change upon irradiation.

To determine whether a similar occurrence was happening with [BMIM][NTf<sub>2</sub>], UV-Vis and <sup>1</sup>H NMR experiments of the material were explored. To explore the material using UV-Vis spectroscopy (Figure 3.10), the material was dissolved in acetonitrile and the absorbance spectra showed very similar features to [BMIM][BF<sub>4</sub>]. These features include little to no absorption in the visible region (400 – 800 nm) and an increase in absorption as the wavelength falls below 400 nm, which likely corresponds to the  $\pi \rightarrow \pi^*$  transition. Acetonitrile is featureless until below 250 nm (note – the small change at 350 nm is due to the light source changing to the lower range wavelength during the experiment). Rather than irradiating the sample at the  $\lambda_{\text{max}}$ , the sample was irradiated with the same light source (365 nm) used to measure the photoswitching PL, allowing us to determine whether there were any changes under similar conditions as the gas sorption experiments. The sample was irradiated in 2-minute intervals, up to 14 minutes. After irradiating the sample for 2 minutes, there was a significant change in the absorbance spectra, where the  $\lambda_{\text{max}}$  at 280 nm decreased along with a decrease in absorbance between 260 nm – 330 nm. After continued irradiation, this trend continues up to 10 minutes, although there is a much slower change at 330 nm, whereas the initial  $\lambda_{\text{max}}$  at 280 nm changes very little over the course of continued irradiation. After 10 minutes there were no further appreciable changes in the spectra.

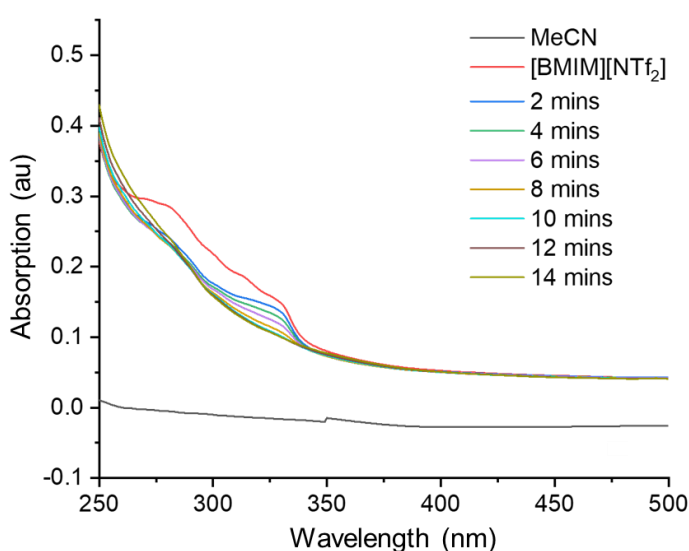


**Figure 3.10** Absorption spectra of acetonitrile and [BMIM][NTf<sub>2</sub>] in acetonitrile, before after irradiation with 2-minute intervals.

A  $^1\text{H}$  NMR spectroscopic study was also performed in acetonitrile, where the same sample was used for both the sample under ambient conditions and then irradiated for 10 minutes (Figure 3.11). In both cases, no change was observed in the  $^1\text{H}$  NMR spectra, including the sample concentration which remained constant, as determined by integrating the aromatic protons of the ionic liquid and the residual solvent signal. Although there is no conclusive evidence of mass structural change, there is evidence of a change taking place in the material which can be observed in the UV-Vis experiments, which may explain the difference in the observed  $\text{CO}_2$  uptake while the sample is being irradiated. While this change remains somewhat unexplained, it provides an advantage to this photoresponsive PL, as both the porous material and the ionic liquid can decrease the amount of  $\text{CO}_2$  adsorbed whilst being irradiated. This could lead to the possibility of known and future ionic liquids being studied further, with photoirradiation being a possible mechanism to release gas from the system.

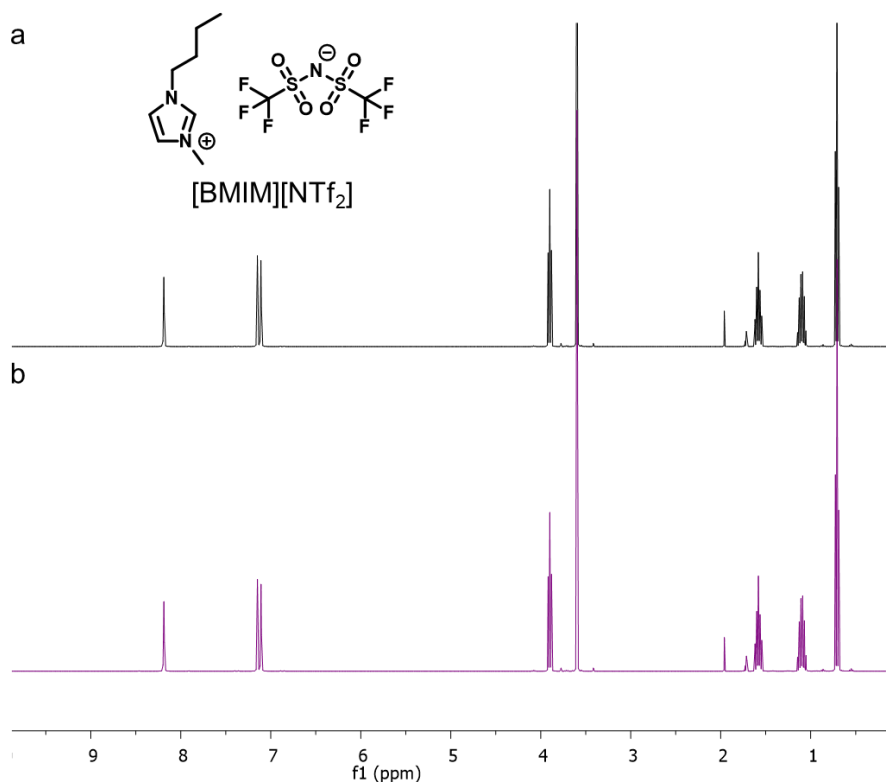


**Figure 3.11**  $^1\text{H}$  NMR spectra of [BMIM][NTf<sub>2</sub>] in acetonitrile, where a) performed under ambient conditions; b) sample irradiated for 10 minutes at 365 nm.

The inconsistent performance of the 12.5 wt% PL, at least when compared to the 5 and 20 wt% samples, was also investigated further. The initial measurements described above were performed on samples produced from different batches of the solid MOF – having followed the reported synthetic procedure of the MOF, which only yields ~500 mg of product, separate batches were required to prepare enough

samples to perform the gas sorption measurements. After observing this difference in uptake, several batches of the MOF were prepared in parallel on a double scale and were each analysed individually. PXRD analysis showed variations between each batch, along with vast variations in CO<sub>2</sub> capacity, where one sample was able to adsorb 766 μmol/g of CO<sub>2</sub>, while another had just over a third of that capacity (Figure 3.12).

After discovering these variations in the Zn(AzDC)(4,4'-BPE)<sub>0.5</sub> material, further investigations into producing a photoresponsive PL were carried out with a variety of the batches from this investigation. As there were large differences in the gas uptake in the solid MOF, samples were selected based on their CO<sub>2</sub> uptake. The batches with the highest and lowest uptakes, and one falling mid-range, were selected to investigate how these samples would affect the gas uptake and photoresponsive aspects of the corresponding PLs. The three samples that were selected to prepare PLs were: batch 1, denoted as PL1, which had the highest CO<sub>2</sub> uptake of 766 μmol/g; batch 2, denoted as PL2, had a mid-range CO<sub>2</sub> uptake of 457 μmol/g; and batch 3, denoted as PL3, which had the lowest CO<sub>2</sub> uptake of 277 μmol/g.

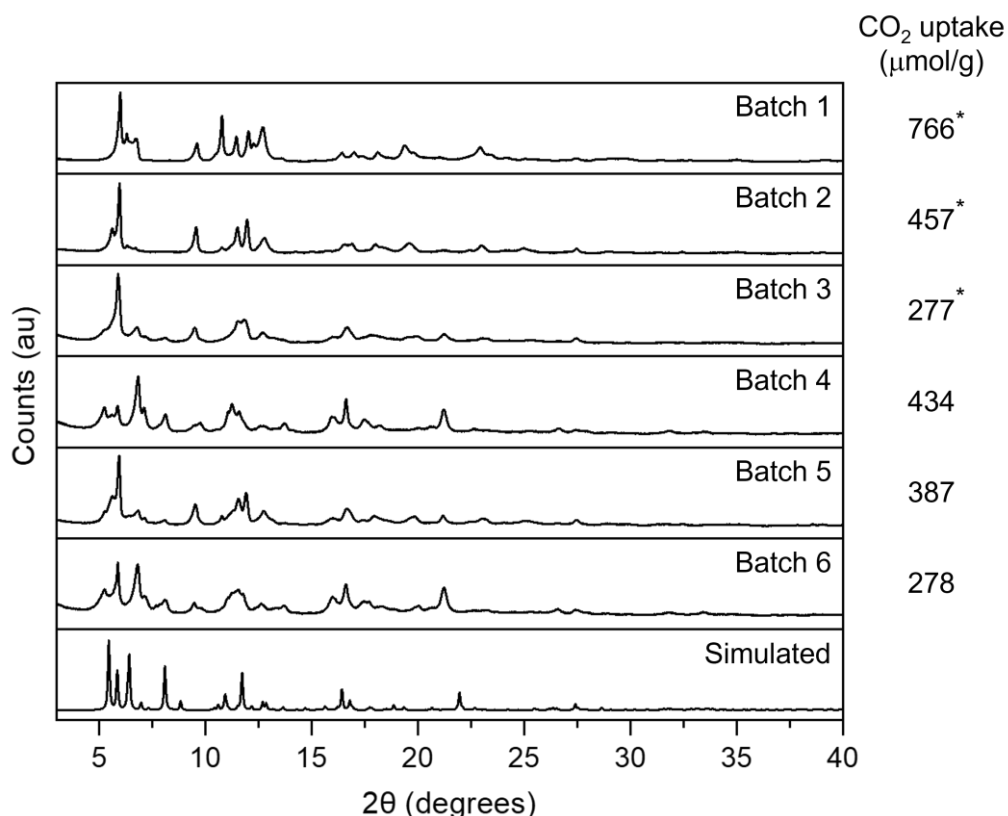


**Figure 3.12** PXRD patterns of 6 different batches of Zn(AzDC)(4,4'-BPE)<sub>0.5</sub> with their corresponding CO<sub>2</sub> uptake at 25 °C and the simulated powder pattern (CCDC code 649367). Samples marked with an asterisk (\*) were selected for further testing as porous liquids.



To ensure sufficient sample throughout the experiment and to prevent mixing any batches for various experiments, all the measurements were initially prepared as a 20 wt% PL, and once the necessary measurements had been performed on the sample, both the 12.5 and 5 wt% PLs were prepared from the same sample by diluting with the corresponding amount of ionic liquid. Once each sample was made to its respective concentration, it was sonicated for 20 minutes before being placed under continuous vacuum with stirring on the Quantachrome instrument for 20 hours, before performing further measurements. This method produced far more reliable results than the initial set of experiments (Figures 3.13-3.15), rather than comparing different wt% samples formed using different batches or mixing two batches of material, which had confirmed as potentially having large differences in uptake between batches.

In each case, the calculated, theoretical maximum gas uptake for the different PLs was compared to the experimentally measured gas uptake, for both CO<sub>2</sub> performed under ambient conditions and irradiation, and CH<sub>4</sub> under ambient conditions, at 1 bar (Tables 3.2-3.4). The theoretical maximum gas uptake can be calculated by the following equation:  $N_{PL} = W_{MOF}N_{MOF} + W_{IL}N_{IL}$ , where  $W_{MOF}$  and  $W_{IL}$  refers to the wt% proportion of the MOF and ionic liquid used to form the PL, and  $N_{MOF}$  and  $N_{IL}$  are the experimentally measured gas uptake capacities at 1 bar of the MOF and the ionic liquid.

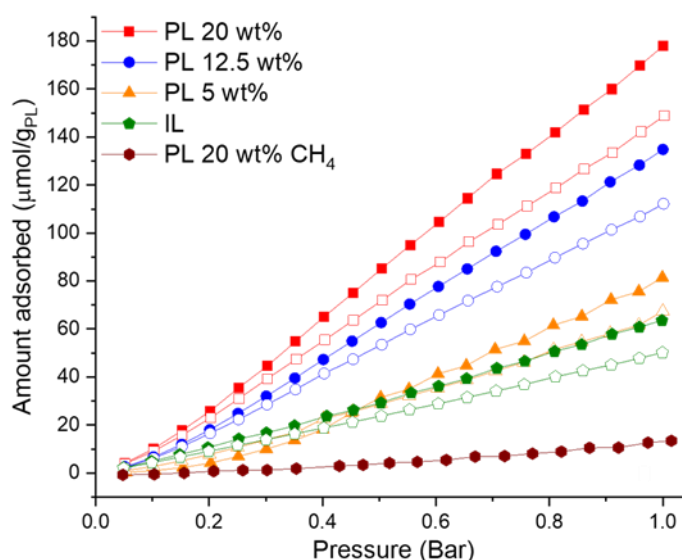


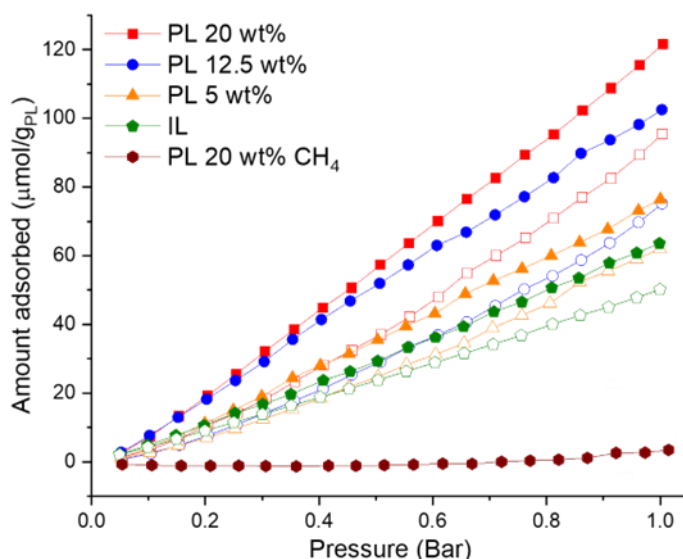
**Figure 3.13** CO<sub>2</sub> and CH<sub>4</sub> (labelled) adsorption isotherms of photoresponsive PLs prepared from batch 1, PL1, and the corresponding ionic liquid under ambient conditions (filled) and irradiated with UV light (empty).

**Table 3.2** Summary of gas uptake measurements of neat ionic liquid, Zn(AzDC)(4,4'-BPE)<sub>0.5</sub>, and the porous liquids produced from batch 1, PL1, with their corresponding gas uptakes.

Sample	CO <sub>2</sub> uptake at 1 bar (μmol/g <sub>L</sub> )		Predicted uptake at 1 bar (μmol/g <sub>L</sub> )		% of calculated uptake at 1 bar	
	Ambient	UV	Ambient	UV	Ambient	UV
PL 20 wt%	178.1	148.8	204.0	145.3	87	102
PL 12.5 wt%	134.8	112.2	151.4	109.6	89	102
PL 5 wt%	81.5	67.4	98.7	73.9	82	91
MOF	766.7	526.3	-	-	-	-
IL	63.5	50.1	-	-	-	-

Sample	CH <sub>4</sub> uptake at 1 bar (μmol/g <sub>L</sub> )		Predicted uptake at 1 bar (μmol/g <sub>L</sub> )		% of predicted uptake at 1 bar	
	Ambient	UV	Ambient	UV	Ambient	UV
PL 20 wt%	13.4	19.4	19.4	68		
MOF	81.4	-	-	-	-	-
IL	4.0	-	-	-	-	-



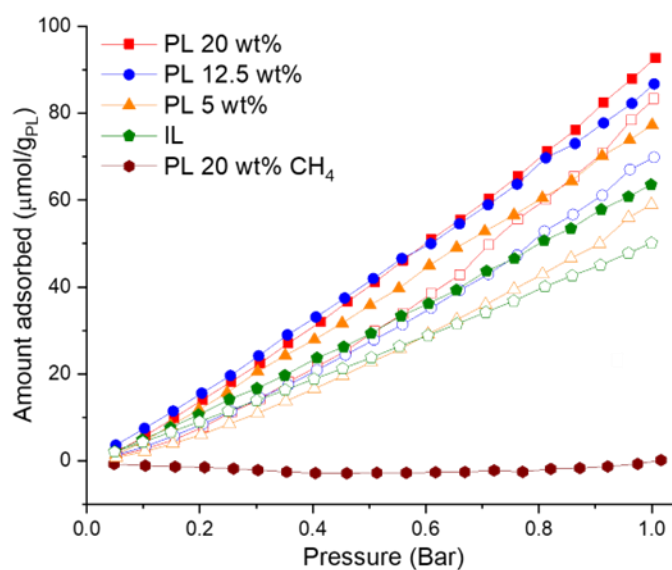
**Figure 3.14** CO<sub>2</sub> and CH<sub>4</sub> (labelled) adsorption isotherms of photoresponsive PLs prepared from batch 2, PL2, and the corresponding ionic liquid under ambient conditions (filled) and irradiated with UV light (empty).

**Table 3.3** Summary of gas uptake measurements of neat ionic liquid, Zn(AzDC)(4,4'-BPE)<sub>0.5</sub>, and the porous liquids produced from batch 2, PL2, with their corresponding gas uptakes.

Sample	CO <sub>2</sub> uptake at 1 bar (μmol/g <sub>L</sub> )		Predicted uptake at 1 bar (μmol/g <sub>L</sub> )		% of calculated uptake at 1 bar	
	Ambient	UV	Ambient	UV	Ambient	UV
PL 20 wt%	121.5	95.4	142.4	108.1	85	88
PL 12.5 wt%	102.5	75.1	112.8	86.3	90	86
PL 5 wt%	76.4	61.9	83.3	64.6	91	95
MOF	457.8	339.8	-	-	-	-
IL	63.5	50.1	-	-	-	-

Sample	CH <sub>4</sub> uptake at 1 bar (μmol/g <sub>L</sub> )	Predicted uptake at 1 bar (μmol/g <sub>L</sub> )	% of predicted uptake at 1 bar
	PL 20 wt%	3.4	12.3
MOF	45.8	-	-
IL	4.0	-	-



**Figure 3.15** CO<sub>2</sub> and CH<sub>4</sub> (labelled) adsorption isotherms of photoresponsive PLs prepared from batch 3, PL3, and the corresponding ionic liquid under ambient conditions (filled) and irradiated with UV light (empty).

**Table 3.4** Summary of gas uptake measurements of neat ionic liquid, Zn(AzDC)(4,4'-BPE)<sub>0.5</sub>, and the porous liquids produced from batch 3, PL3, with their corresponding gas uptakes.

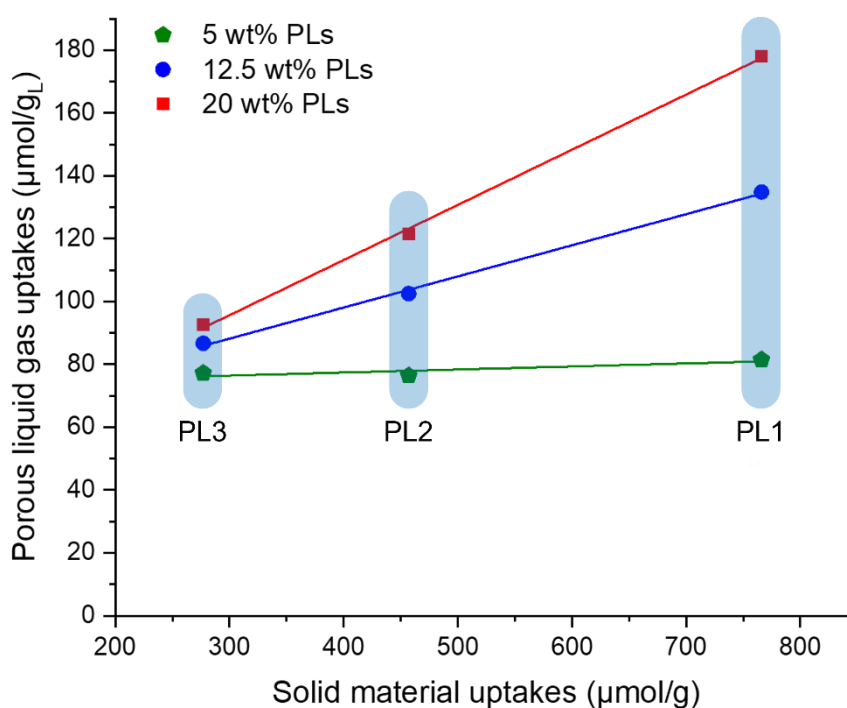
Sample	CO <sub>2</sub> uptake at 1 bar (μmol/g <sub>L</sub> )		Predicted uptake at 1 bar (μmol/g <sub>L</sub> )		% of calculated uptake at 1 bar	
	Ambient	UV	Ambient	UV	Ambient	UV
PL 20 wt%	92.7	83.3	106.4	91.3	87	91
PL 12.5 wt%	86.7	69.8	90.3	75.8	96	92
PL 5 wt%	77.2	58.9	74.2	60.4	104	97
MOF	277.9	256.0	-	-	-	-
IL	63.5	50.1	-	-	-	-

Sample	CH <sub>4</sub> uptake at 1 bar (μmol/g <sub>L</sub> )		Predicted uptake at 1 bar (μmol/g <sub>L</sub> )		% of predicted uptake at 1 bar	
	Ambient	UV	Ambient	UV	Ambient	UV
PL 20 wt%	0.14		2.9		4	
MOF	14.7		-		-	
IL	4.0		-		-	

Prior to preparing the PLs, each MOF was tested in its solid state for its CO<sub>2</sub> capacity under ambient conditions and whilst being irradiated, which produced a range of differences in CO<sub>2</sub> uptake. The best sample demonstrated a decrease of 31%, while the intermediate sample demonstrated a 25% decrease in CO<sub>2</sub> uptake, and the lowest sample had a disappointing 7% decrease in CO<sub>2</sub> uptake. As the preparation of the MOF incorporated several washing steps, it is unlikely that any unreacted precursors remained. The formation of non-porous oligomers is possible however, which could result in the observed differences in CO<sub>2</sub> capacity and produce a much smaller change in CO<sub>2</sub> uptake when the sample is irradiated, as a smaller proportion of the bulk material would be the photoresponsive porous framework. Typically, the synthesis of porous MOFs involves high temperatures above the boiling point of the solvent, which provides a degree of reversibility and enough energy to overcome any potential energy barriers that prevent the MOF from forming.<sup>26</sup> However, the reported synthetic procedure for Zn(AzDC)(4,4'-BPE)<sub>0.5</sub> uses a moderate temperature of 100 °C, and a relatively short reaction time of 24 hours.<sup>22</sup>

Another possibility for batch 3, the sample with the smallest decrease in CO<sub>2</sub> uptake while being irradiated, could be differing quantities of each ligand incorporated into the final MOF structure. While the reported structure of Zn(AzDC)(4,4'-BPE)<sub>0.5</sub> contains layers of AzDC and pillar 4,4'-BPE linkers, due to the different lengths of the components, it seems plausible that some kind of self-sorting could occur. Self-sorting in MOFs has previously been reported, where different frameworks can be produced when multiple components are used, leading to self-sorting or mixed ligand frameworks.<sup>27</sup> If the MOF was comprised of more of the shorter ligand, 4,4'-BPE, it would make sense that a smaller pore size would be produced from this material, resulting in a lower CO<sub>2</sub> capacity. The  $\lambda_{\max}$  of 4,4'-BPE occurs lower than that of AzDC, at approximately 310 nm, and corresponds to the  $\pi \rightarrow \pi^*$  transition. Irradiating the material at this wavelength, or within the shoulder of the absorption, will lead to isomerisation from *trans*  $\rightarrow$  *cis*. However, as the shoulder of the absorption spans beyond 365 nm, some isomerisation will occur at this wavelength. However, the  $\lambda_{\max}$  of AzDC is much closer to 365 nm, and therefore more likely to absorb at this wavelength resulting in more photoisomerisation will occur. This means that, if a MOF was produced with more of the 4,4'-BPE ligand, less of the material would be capable of photoisomerisation at 365 nm, which would lead to a smaller decrease in CO<sub>2</sub> uptake while irradiated.



**Figure 3.16** Summary of CO<sub>2</sub> uptakes in batches 1, 2 and 3 of the solid Zn(AzDC)(4,4'-BPE)<sub>0.5</sub> vs. the CO<sub>2</sub> uptake in the corresponding porous liquids at 5 wt% (green pentagons), 12.5 wt% (blue circles), and 20 wt% (red squares).

The PL samples, PL1, PL2, and PL3, prepared with each batch of MOF, batch 1, batch 2, and batch 3, all demonstrated an increased CO<sub>2</sub> capacity over the neat ionic liquid (Figures 3.13-3.15). Increases could be observed in all PLs, with incremental increases from 5 wt% to 20 wt%, where an increase of 91%, 180% and 45% was observed for the different batches respectively for the 20 wt% samples over the neat ionic liquid. There is also a direct correlation between the CO<sub>2</sub> uptake in the solid MOF and the resulting PL (Figure 3.16). In addition, all PLs were within 15% of their calculated CO<sub>2</sub> uptake under ambient conditions, and within 12% of the calculated uptake while being irradiated. The most successful and uniform PL of the three was PL1, which had a maximum uptake of 178 μmol/g<sub>PL</sub> CO<sub>2</sub> at 20 wt%, followed by a 16% decrease when irradiated to 148 μmol/g<sub>PL</sub>. The 12.5 wt% sample also demonstrated a 16% decrease from 134 μmol/g<sub>PL</sub> to 112 μmol/g<sub>PL</sub>. Finally, the 5 wt% sample also showed a 17% decrease from 81 μmol/g<sub>PL</sub> to 67 μmol/g<sub>PL</sub>. PL2 displayed a decrease of 19-26% upon irradiation with light, and PL3 ranged from 10-23% (Figure 3.17).

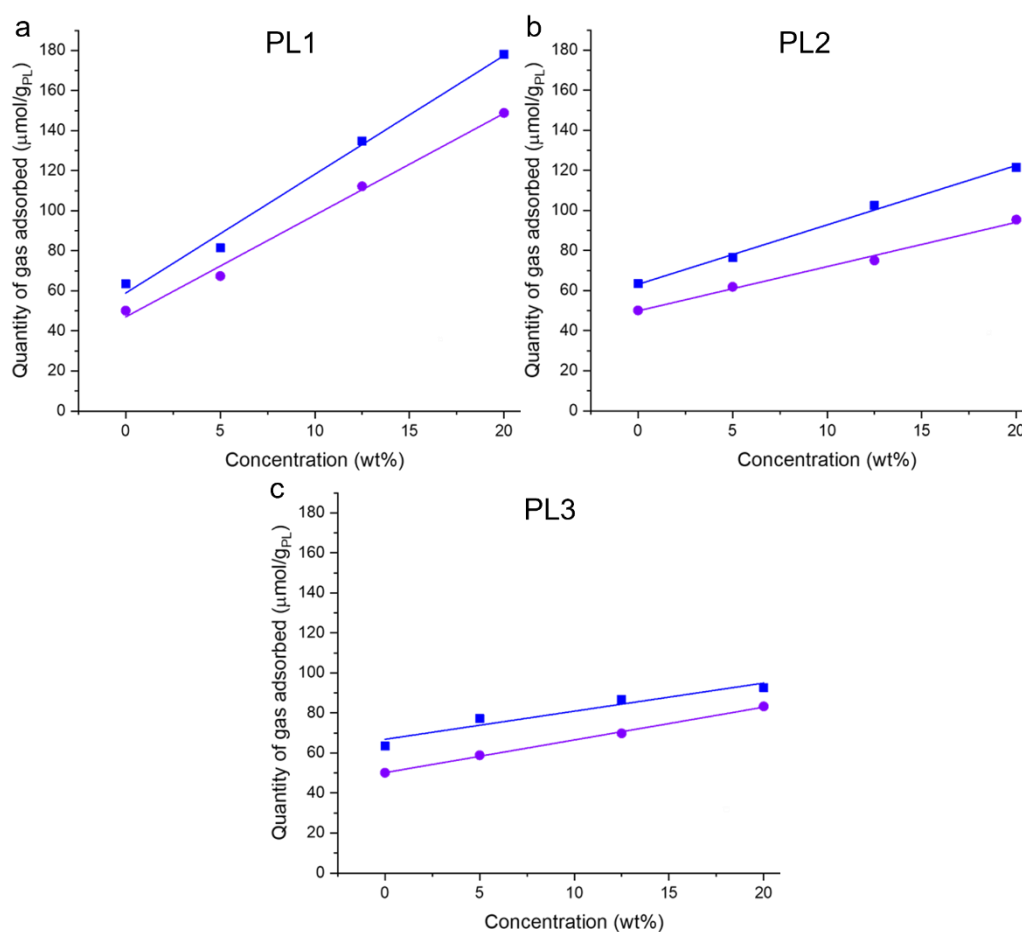


**Figure 3.17** Measured gas uptake across a range of concentrations of porous under ambient conditions (blue squares) and constant irradiation (purple circles), with the corresponding linear fit lines, where a) PL1; b) PL2; c) PL3.

Measuring the CH<sub>4</sub> uptake in the photoresponsive PL also provided some very welcome results. Across all of the PLs formed using different batches of MOF, the CH<sub>4</sub> uptake was almost non-existent, ranging from 0.14 μmol/g<sub>PL</sub> for PL3, up to 13.4 μmol/g<sub>PL</sub> for PL1. In each case, there is a 13-fold, 35-fold, and 662-fold higher capacity for CO<sub>2</sub> than CH<sub>4</sub>, for PL1, PL2, and PL3, respectively. While there are some reports of gas selective PLs,<sup>4,7,11,28</sup> this example demonstrates what we believe to be the highest CO<sub>2</sub>/CH<sub>4</sub> selectivity of any reported porous liquid to date.

Next, to explore the porous liquid's ability to be recycled through multiple gas uptake cycles, investigations looked towards the cyclability of the material. The 12.5 wt% sample of PL1 was cycled 10 times by performing sorption experiments under ambient conditions (after exposure to 450 nm blue light for 10 minutes prior to starting the experiment) and then constant UV irradiation, repeatedly (Figure 3.18). Overall, the average CO<sub>2</sub> uptake was 98 ± 2.0 μmol/g<sub>PL</sub> under ambient conditions, compared to 90 ± 1.6 μmol/g<sub>PL</sub> when the PL was exposed to UV light. This corresponds to an average decrease of 8% in CO<sub>2</sub> uptake when exposure to UV light. While this is far less than the initial experiments, which showed a decrease of 16%, we believe this is due to partial saturation of the sample, as the degas phase between the initial experiments was set to 20 hours between each consecutive run, whereas this cycling experiment was performed while the sample was kept on the analysis port which has a maximum degas time of 1 hour, resulting in lower overall gas uptakes and a lower observed change upon irradiation.

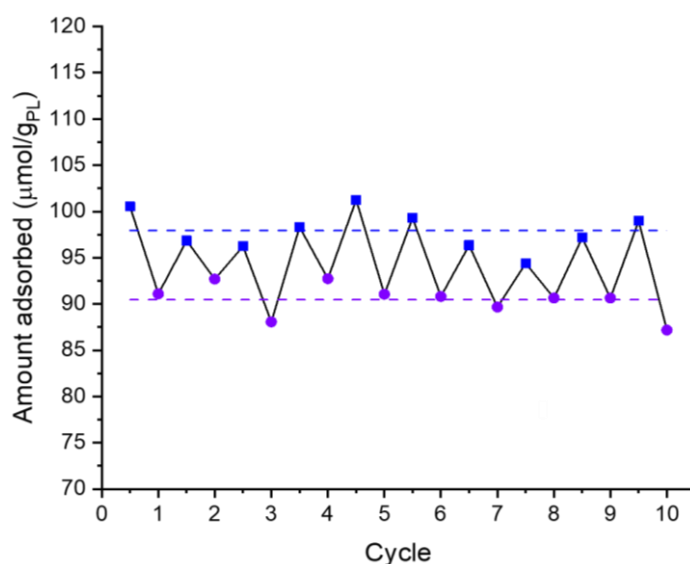


**Figure 3.18** Recycling study for CO<sub>2</sub> uptake in a 12.5 wt% Zn(AzDC)(4,4'-BPE)<sub>0.5</sub> [BMIM][NTf<sub>2</sub>] porous liquid (PL1), under UV light (violet circles), or ambient conditions (blue squares, after exposure for 450 nm light for 10 minutes), and the corresponding averages (dashed lines).

Finally, to ensure there were no changes in the bulk porous material after preparing them as PLs, including the sonication step which is known cause the reduction in particle size and in some cases material decomposition of MOFs, and to observe whether there were any changes after gas sorption, the solid material was analysed by PXRD after re-isolation (Figures 3.19-3.21). To prepare the material so it could be used on a high-throughput PXRD plate, some of the ionic liquid had to be removed from the sample. The PL formed from each batch of MOF was therefore poured onto filter paper, which absorbed some of the ionic liquid, making the sample viscous enough to sit in the shallow sample well of the PXRD plate. The remaining material was further washed with methanol (like that of the sample preparation before evacuating in a vacuum oven) and collected by filtration, and the washed solid was also analysed. In all cases, there was very little variation between the powder diffraction patterns of each MOF from the activated starting material, the concentrated PL, and methanol washed material, indicating that inclusion of the MOF into the PL and the addition of sonication had little to no effect on the framework material.

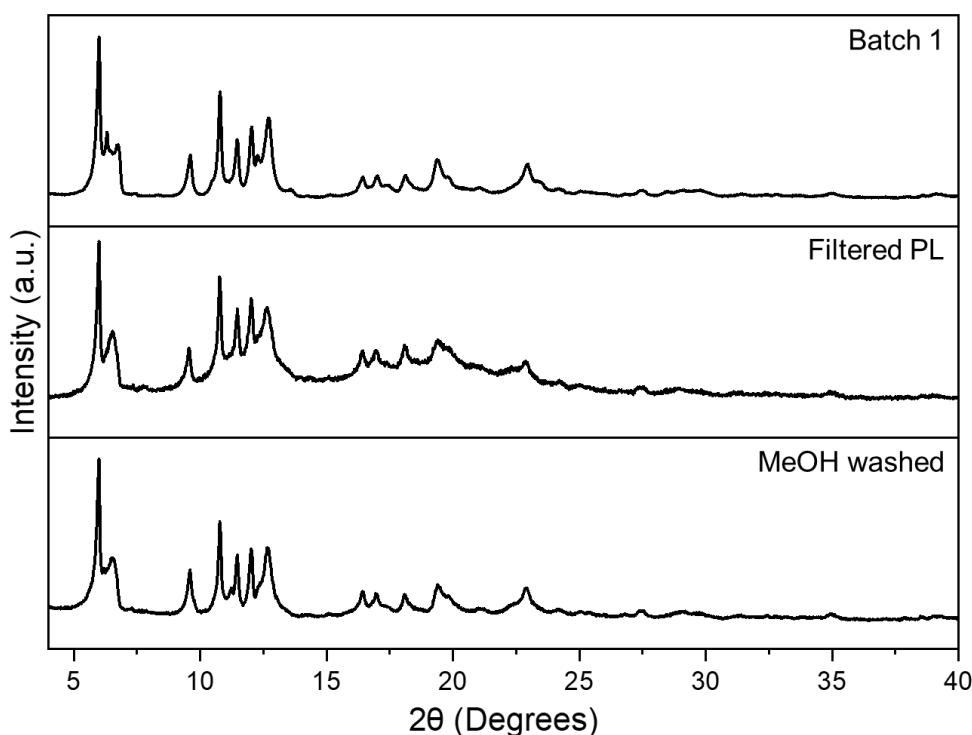


**Figure 3.19** PXRD patterns of solid Zn(AzDC)(4,4'-BPE)<sub>0.5</sub> (batch 1), the filtered porous liquid, and the sample isolated from the PL and washed with MeOH, after gas sorption experiments



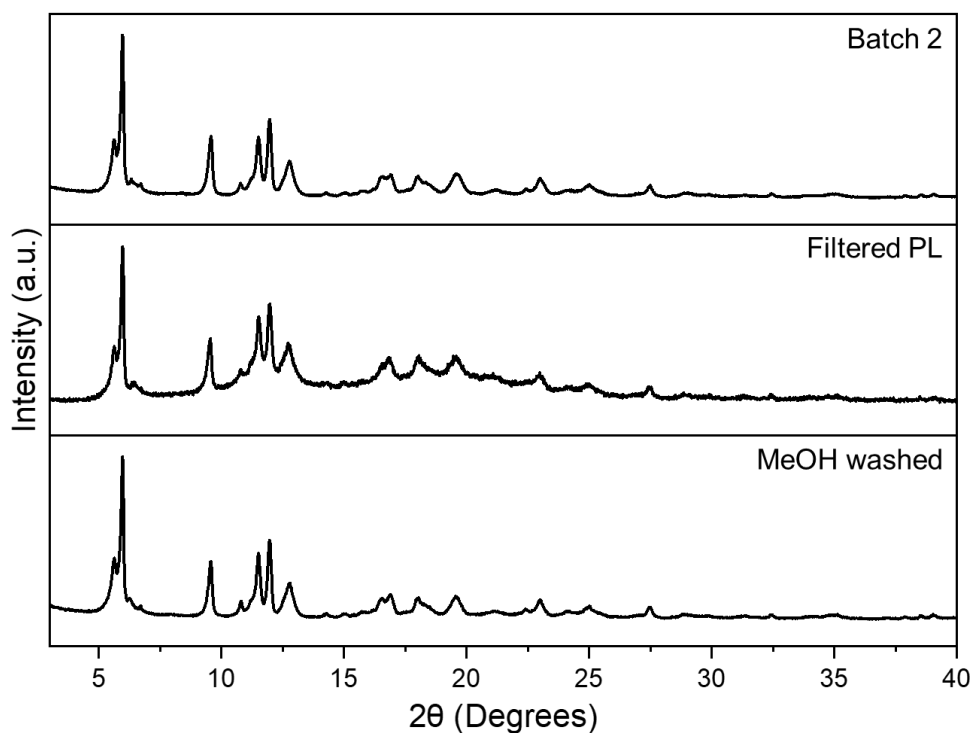


**Figure 3.20** PXR D patterns of solid  $\text{Zn}(\text{AzDC})(4,4'\text{-BPE})_{0.5}$  (batch 2), the filtered porous liquid, and the sample isolated from the PL and washed with MeOH, after gas sorption experiments.

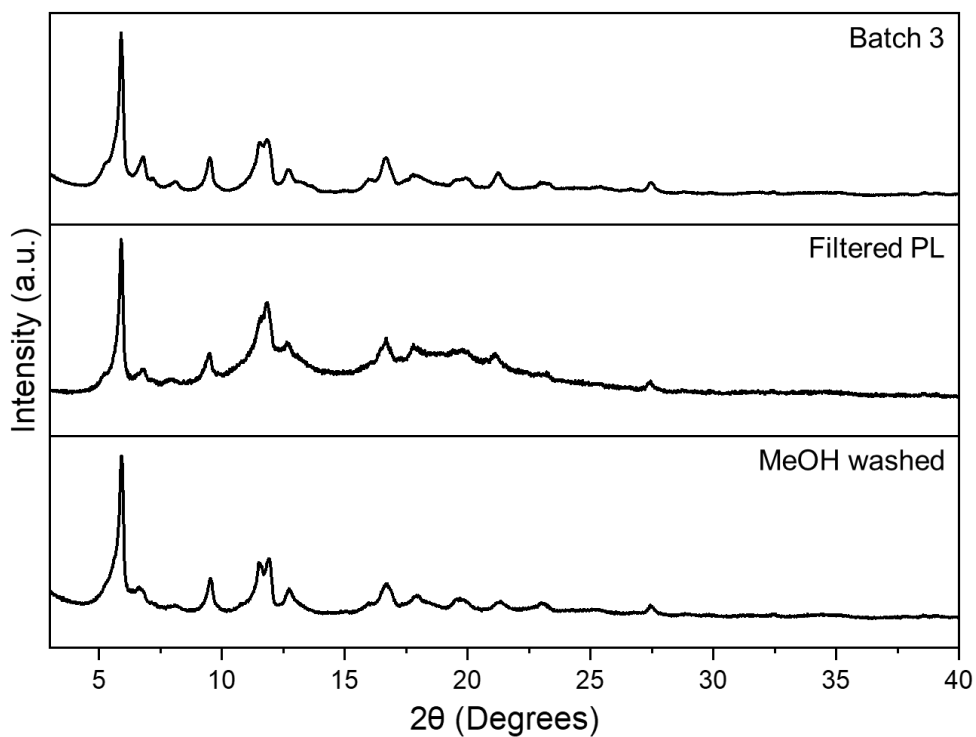


**Figure 3.21** PXR D patterns of solid  $\text{Zn}(\text{AzDC})(4,4'\text{-BPE})_{0.5}$  (batch 3), the filtered porous liquid, and the sample isolated from the PL and washed with MeOH, after gas sorption experiments.

### 3.3.5 Gas Displacement Measurements

Gas evolution experiments have proven to be very effective at giving an indication of the gas uptake in PLs, and have been utilised in many studies since their discovery.<sup>2,14,29,30</sup> Probe gases, which include CH<sub>4</sub>, CO<sub>2</sub>, Xe, and N<sub>2</sub>, have all been used, which can help demonstrate the effective pore window size. It has also been useful in identifying how different solvents can influence the gas uptake in PLs, where a recent study showed that varying the solvent, but using the same porous material, can lead to different amounts of gas being released, demonstrating a differing affinity to the material.<sup>15</sup> Gas displacement measurements use standard laboratory apparatus, which typically includes a burette, GC vials, tubing, a beaker, and probe gas, making this technique far more readily available than gas sorption instruments (Figure 3.22). Probing the release of gas can also be straight forward as the sample can be exposed to heat or sonication, or a small molecule such as chloroform can be injected into the vial to displace the gas within the pores.

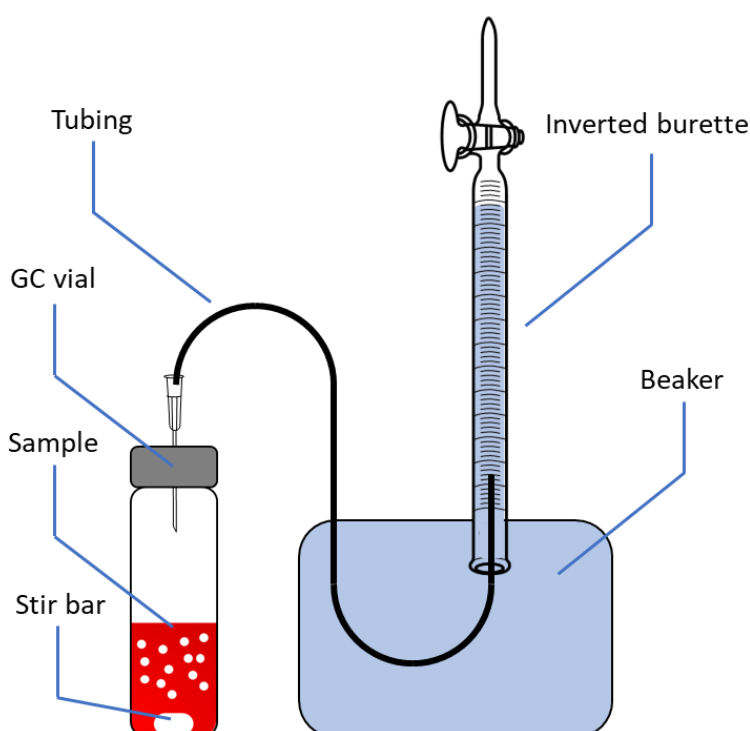


**Figure 3.22** Visual representation of the gas displacement apparatus used to measure gas release from porous liquids.

Gas displacement experiments were performed using the sample with the largest CO<sub>2</sub> uptake from the gas sorption experiments, PL1. To prepare the samples for gas displacement, CO<sub>2</sub> was bubbled through the sample at ~50 – 60 mL/min for 30 minutes. The sample cap was then replaced before preparing the sample for each

respective method of gas release (Figure 3.23). Tubing was placed into the cap, and a small amount of air was pushed through to remove any residual water from the tubing and to set the start point prior to taking the initial measurement. When removing the syringe, a small amount of silicone grease was applied to the lid to ensure no further air could enter the sample during the experiment. The starting measurement was then taken, and each sample was given 30 minutes before the end point was taken. For the PL sample, four measurements for each release mechanism were attempted, that is, UV irradiation, sonication, and heating (80 °C), and one final measurement was performed for chemical displacement (0.4 mL of  $\text{CHCl}_3$ ). For the neat ionic liquid, three measurements were taken for each release mechanism, and again, a single measurement was performed for chemical displacement (0.4 mL of  $\text{CHCl}_3$ ). Chemical displacement measurements were carried out using chloroform as the displacement solvent and measured in 0.2 mL increments up to 1 mL, and in both cases any volume above 0.4 mL showed no substantial increase in the gas displaced other than that which corresponded to the volume of  $\text{CHCl}_3$  added to the sample.

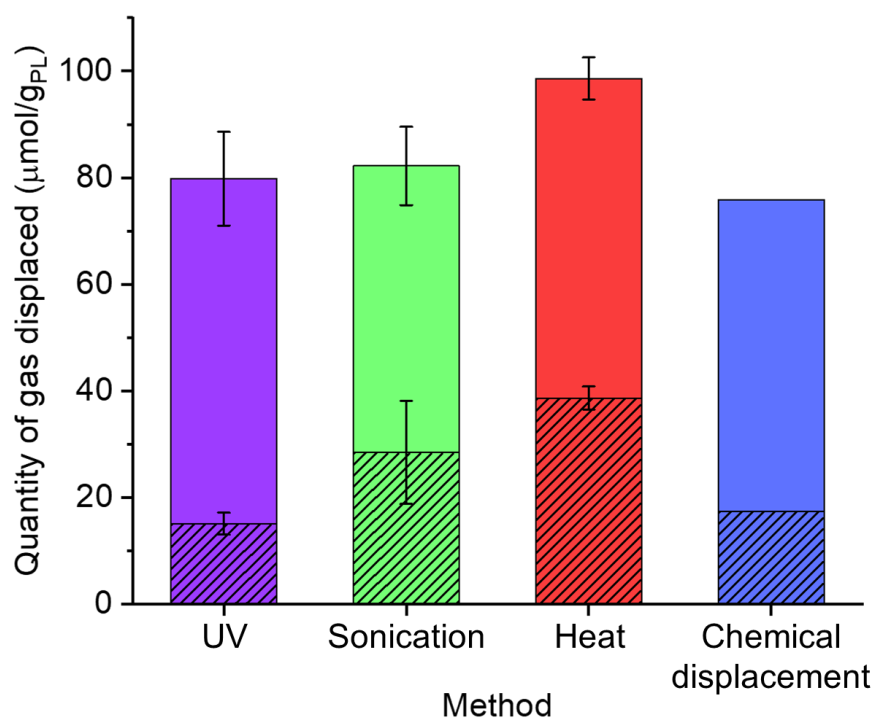


**Figure 3.23**  $\text{CO}_2$  displacement experiments from the 12.5 wt% porous liquid PL1 (solid bars), and the ionic liquid, [BMIM][NTf<sub>2</sub>] (dashed lines), using different mechanisms of release, including UV irradiation, sonication, heating (80 °C), and chemical displacement (0.4 mL  $\text{CHCl}_3$ ). The corresponding standard deviations for each sample over multiple experiments are also shown on their respective bars.

In all cases, the PL displayed improvements over that of the neat ionic liquid, with more than two times as much gas displaced for all mechanisms (Figure 3.23, Tables 3.5-3.6). While heating the sample to 80 °C resulted in the highest amount of displaced gas, the neat ionic liquid also released the largest amount of gas when using the same method compared to the others, which resulted in the lowest percentage increase displayed by the PL of 157%. Sonication also displayed a similar percentage increase of 192% over the neat ionic liquid, although a slightly lower total gas displacement. Chemical displacement performed well, although surprisingly it displaced the lowest overall amount of gas compared to the other methods, where the PL showed an increase of 341%. Arguably, UV irradiation displayed the greatest increase of gas displaced on going from the neat ionic liquid to the PL – while the PL displaced the 3<sup>rd</sup> lowest volume of gas overall in the study, the increase over that of the neat liquid was 426%.

**Table 3.5** Gas evolution data for 12.5 wt% PL1 prepared from batch 1 of the MOF, at 298 K. Calculations are based on 2.82 g of material.

Method	Volume evolved (mL)	Mean volume evolved (mL)	Gas uptake ( $\mu\text{mol/g}_{\text{PL}}$ )
UV	4.95	$5.05 \pm 0.55$	$79.8 \pm 8.78$
	5.20		
	4.25		
	5.80		
Sonication	5.90	$5.20 \pm 0.46$	$82.2 \pm 7.33$
	5.10		
	4.60		
	5.20		
Heat	6.40	$6.23 \pm 0.24$	$98.6 \pm 3.92$
	6.50		
	5.85		
	6.20		
Chemical displacement	4.80	4.80	75.9

**Table 3.6** Gas evolution data for the ionic liquid [BMIM][NTf<sub>2</sub>]. Calculations are based on 5.11 g of material.

Method	Volume evolved (mL)	Mean volume evolved (mL)	Gas uptake ( $\mu\text{mol/g}_{\text{PL}}$ )
UV	1.90	$1.73 \pm 0.23$	$15.1 \pm 2.05$
	1.90		
	1.40		
Sonication	2.80	$3.26 \pm 1.11$	$28.5 \pm 9.69$
	2.20		
	4.80		
Heat	4.70	$4.43 \pm 0.25$	$38.7 \pm 2.17$
	4.10		
	4.50		
Chemical displacement	2.40	2.40	17.4

### 3.4 Conclusions

Through the course of this study, the development of a photoresponsive type III porous liquid has been achieved. While the CO<sub>2</sub> uptake in the bulk MOF material used in this study varies, experimenting with several batches of this material has continually demonstrated its ability to be translated into a porous liquid. This was demonstrated using specialised gas sorption instruments and simpler gas displacement experiments.

Overall, it has been demonstrated that a significant increase in CO<sub>2</sub> capacity can be achieved through the creation of porous liquids, where this example remains competitive against similar type III porous liquid systems. It has also been shown that this new porous liquid has a very high selectivity towards CO<sub>2</sub> over CH<sub>4</sub>, with a 13 times higher capacity for CO<sub>2</sub> than CH<sub>4</sub>. This remains to be one of the highest selectivity demonstrated in any porous liquid to date. It is also the first proof-of-concept report of a photoresponsive porous liquid that is capable of releasing gas from the material upon exposure to UV irradiation.

As this is the first photoresponsive porous liquid, it opens the possibilities for new porous liquids to be developed from stimuli-responsive responsive materials.

Systems that utilise fewer precursors or discrete porous molecules, such as a photoresponsive organic cages, rather than a multi-component framework material, may lead to a more reproducible porous liquid with a consistent gas capacity. The selectivity of these materials may also be utilised in the future, where these materials could be incorporated into flowable sorbents for gas separation processes. One could imagine a system where a gas could be flowed through this system, before being irradiated to remove a portion of the gas from the material, and then being recycled back for re-loading. Modification of the porous material and adjustment of the internal pore size could lead to the discovery of selective materials towards other sorbates.

## 3.5 Experimental Details

### 3.5.1 General Synthetic and Analytical Methods

**Materials:** 4-Nitrobenzoic acid, [BMIM][NTf<sub>2</sub>] and zinc nitrate were purchased from Sigma-Aldrich, *trans*-1,2-bis(4-pyridyl)ethylene was purchased from Fluorochem, and all chemicals were used as received. Other solvents were reagent or HPLC grade purchased from Fisher Scientific.

**NMR:** <sup>1</sup>H and <sup>13</sup>C Nuclear magnetic resonance spectra were recorded using an internal deuterium lock for the residual protons in DMSO-d<sub>6</sub> (δ 2.50 ppm and 39.52 ppm) at ambient probe temperature on a Bruker Avance 400 (400 MHz/101 MHz) instrument. <sup>1</sup>H NMR data are presented as follows: chemical shift, peak multiplicity (s = singlet, d = doublet, t = triplet, q = quartet, m = multiplet, br = broad, app = apparent), coupling constants (*J*/ Hz), and integration. Chemical shifts are expressed in ppm on a δ scale relative to δ<sub>DMSO</sub> (2.50 ppm and 39.52 ppm) and coupling constants, *J*, are given in Hz

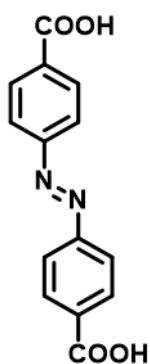
**PXRD:** Laboratory powder X-ray diffraction data were collected in transmission mode on samples held on thin Mylar film in aluminium well plates on a Panalytical X'Pert PRO MPD equipped with a high-throughput screening (HTS) XYZ stage, X-ray focusing mirror and PIXcel detector, using Ni-filtered Cu Kα radiation. Data were measured over the range 4–40° in ~0.013° steps over 60 minutes.

**3D Printers:** A Form 3 resin printer from Formlabs was used to print the photoreactor and probe mount in white resin (GPWH04). Prints were washed for 15 minutes in an IPA bath and then cured for 30 minutes at 60 °C. A Gigabot 3+ thermoplastic printer from re:3D was used to print the fan mounts for the photoreactor using black PLA (RS stock 832-0264).

**Design:** Autodesk Fusion 360 was used to design the prints for this project.

### 3.5.2 Synthesis and Characterisation

#### 4,4'-(diazene-1,2-diyl)dibenzoic acid



Material was synthesised following the procedure reported by Lyndon *et al.*<sup>23</sup> 4-Nitrobenzoic acid (15.00 g, 89.8 mmol) was added to a solution of sodium hydroxide (51.0 g, 1.28 mol, in 225 mL water), and the solution was gently heated until the solid dissolved. Glucose (100 g, 55.5 mmol) was dissolved in 150 mL water and gently heated until the solid dissolved. The warm glucose solution was then added slowly, portionwise, to the solution at 50 °C, where the solution initially formed a yellow precipitate, before turning brown upon further addition of glucose. The mixture was left to stir overnight at room temperature. Methanol was added to the solution until a light brown precipitate formed. The precipitate was collected by filtration, and dissolved in water followed by acidification with acetic acid (~20 mL), before being collected by filtration once more to yield a light pink precipitate. The product was washed with an excess of water and then dried under vacuum for several hours to yield the final product (6.50 g, 24.0 mmol, 53%).

<sup>1</sup>H NMR (400 MHz, DMSO)  $\delta_{\text{H}}$  8.16 (d,  $J = 8.7$  Hz, 4H), 8.01 (d,  $J = 8.7$  Hz, 4H). No trace of acid peak. <sup>13</sup>C NMR (101 MHz, DMSO)  $\delta_{\text{H}}$  166.67, 154.17, 133.53, 130.71, 122.85.

#### Zn(AzDC)(4,4'-BPE)<sub>0.5</sub>

Material was synthesised following the procedure reported by Chen *et al.* using a 2x scale.<sup>22</sup> Zn(NO<sub>3</sub>)<sub>2</sub>·6H<sub>2</sub>O (0.56 g, 1.87 mmol), 4,4'-(diazene-1,2-diyl)dibenzoic acid (0.50 g, 1.87 mmol) and *trans*-1,2-bis(4-pyridyl)ethylene (0.17 g, 0.93 mmol) were suspended in DMF (200 mL) and heated in a 500 mL Duran bottle at 100 °C for 24 hours. The red crystals were then collected by filtration, washed with DMF and hexane, and dried in air, yielding the final product as a red solid (0.65- 0.79 g, 1.05- 1.28 mmol, 56-68 % based on C<sub>27.5</sub>H<sub>31.5</sub>N<sub>5.5</sub>O<sub>7</sub>Zn).

Prior to solid gas sorption measurements samples were left to stir in MeOH for 1 hour, before filtering and heating to 150 °C under dynamic vacuum for at least 24h.



### 3.5.3 Light-Responsive Porous Liquid Gas Adsorption Experimental Setup

**Gas Sorption Analysis:** Gas sorption measurements on porous liquids and ionic liquids were measured on a Quantachrome Nova 4200e. Solid and liquid samples were degassed separately in a vacuum oven overnight at 150 °C before being added to 9 mm BET tubes with a small glass stir bar (6 mm x 5 mm), and then sonicated for 10 minutes. Porous liquid samples were then degassed under dynamic vacuum while stirring overnight before backfilling with helium. Samples were then weighed after degassing and placed on the analysis port. Sorption measurements were then performed at room temperature while stirring at 300 RPM. Adsorption settings were as follows: 20 pressure points from 0.05 to 1.0 bar in 0.05 increments; pressure tolerance = 0.05 mmHg; equilibration time = 1800 seconds; equilibration timeout = 5400 seconds.<sup>10</sup>

To analyse samples while irradiating with UV-light, a custom-made 3D printed reactor was designed with mirror coated internal walls (acrylic mirror, 3mm thick) fitted with an external light source (Omniculture S1000, fitted with a 365 nm filter) and a light guide to maximise sample exposure during the experiment. As the sample needed to be stirred during the measurement to ensure equilibration and saturation, a stirrer plate was placed under the reactor box while operating. Two external 40 mm fans mounted either side in a push-pull configuration against the reactor walls with slits allow air to pass through the reactor. Temperature within the box was monitored with a thermocouple and points were taken at several times over the day over several experiments and was found to maintain a temperature between 28 and 29 °C which fluctuated less than 1 °C, regardless of whether the light source was on or not (Figure 3.6, b). During the experiment, the UV light source was set to the maximum intensity and was continuous throughout. For 'ambient' conditions, the sample was irradiated with a blue (450 nm) LED for 10 minutes prior to starting the experiment.

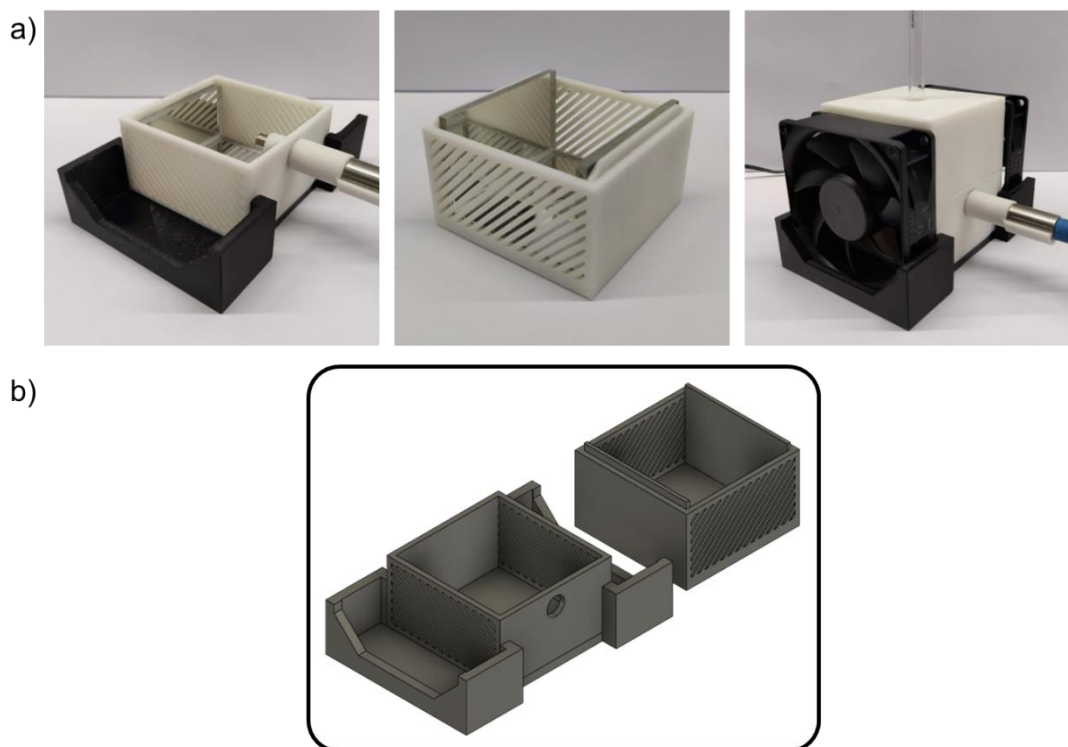


**Figure 3.24** a) 3D printed reactor for light-responsive sorption; b) 3D design of light box for sorption setup.

### 3.5.4 Gas Evolution Experimental Setup

**Gas Uptake and Evolution Studies:** Samples of PLs and ionic liquids were tested with gas purchased from BOC with research grade carbon dioxide (N5.0) in GC headspace vials (22 mm x 45 mm screw top, 10 mL, Fisher Scientific). All samples were exposed to a flow of gas bubbled through the liquid and measurements conducted at room temperature (20 – 25 °C) in a temperature-controlled laboratory. Prior to making up the porous liquid sample and carrying out any measurements, both the MOF and ionic liquid were heated to 150 °C in a vacuum oven overnight.

The flow rate of gas was measured using a Gilmont calibrated flowmeter (tube size 0, Gilmont EW-03201-22) with a stainless-steel float on a scale of 1-100. The flow of gas used was in the region that was previously reported for PLs<sup>14</sup> and the rate was set to ~50-60 mL/min. Samples were left for 30 minutes under continuous bubbling before measuring gas displacement.

Gas evolution was measured by displacement of water in an inverted burette (0.1 mL graduations) which was placed in a beaker of water connected to a GC vial containing the sample *via* a needle and tubing. Prior to exposing the sample to the selected method, a syringe of air was pushed into the sample vial to remove any residual water in the tube and to set the start point prior to taking the initial measurement. A small

amount of vacuum grease was applied to the cap to ensure no holes created by the needle affected the measurement. Measurements were repeated a total of 4 times on the PL1 sample and 3 times on ionic liquid sample for each release method, but only once for chemical displacement measurements on both samples (Tables 3.5-3.6). Gas evolution measurements were taken after 30 minutes of their corresponding method of release.

### 3.6 References

- 1 N. O'Reilly, N. Giri and S. L. James, *Eur. J. Chem.*, 2007, **13**, 3020–3025.
- 2 N. Giri, M. G. Del Pópolo, G. Melaugh, R. L. Greenaway, K. Rätzke, T. Koschine, L. Pison, M. F. C. Gomes, A. I. Cooper and S. L. James, *Nature*, 2015, **527**, 216–220.
- 3 H. Liu, B. Liu, L. C. Lin, G. Chen, Y. Wu, J. Wang, X. Gao, Y. Lv, Y. Pan, X. X. Zhang, X. X. Zhang, L. Yang, C. Sun, B. Smit and W. Wang, *Nat. Commun.*, 2014, **5**, 1–7.
- 4 B. D. Egleston, A. Mroz, K. E. Jelfs and R. L. Greenaway, *Chem. Sci.*, 2022, **13**, 5042–5054.
- 5 B. D. Egleston, K. V. Luzyanin, M. C. Brand, R. Clowes, M. E. Briggs, R. L. Greenaway and A. I. Cooper, *Angew. Chemie Int. Ed.*, 2020, **59**, 7362–7366.
- 6 S. Aguado, G. Bergeret, C. Daniel and D. Farrusseng, *J. Am. Chem. Soc.*, 2012, **134**, 14635–14637.
- 7 B. Lai, J. Cahir, M. Y. Tsang, J. Jacquemin, D. Rooney, B. Murrer and S. L. James, *ACS Appl. Mater. Interfaces*, 2021, **13**, 932–936.
- 8 W. Shan, P. F. Fulvio, L. Kong, J. A. Schott, C. L. Do-Thanh, T. Tian, X. Hu, S. M. Mahurin, H. Xing and S. Dai, *ACS Appl. Mater. Interfaces*, 2018, **10**, 32–36.
- 9 J. Cahir, M. Y. Tsang, B. Lai, D. Hughes, M. A. Alam, J. Jacquemin, D. Rooney and S. L. James, *Chem. Sci.*, 2020, **11**, 2077–2084.
- 10 A. Kai, B. D. Egleston, A. Tarzia, R. Clowes, M. E. Briggs, K. E. Jelfs, A. I. Cooper and R. L. Greenaway, *Adv. Funct. Mater.*, 2021, **31**, 2106116.
- 11 H. Mahdavi, S. J. D. Smith, X. Mulet and M. R. Hill, *Mater. Horizons*, 2022, **9**, 1577–1601.
- 12 R. L. Martin and M. Haranczyk, *Chem. Sci.*, 2013, **4**, 1781–1785.
- 13 O. K. Farha, I. Eryazici, N. C. Jeong, B. G. Hauser, C. E. Wilmer, A. A. Sarjeant, R. Q. Snurr, S. T. Nguyen, A. Ö. Yazaydin and J. T. Hupp, *J. Am. Chem. Soc.*, 2012, **134**, 15016–15021.
- 14 R. L. Greenaway, D. Holden, E. G. B. Eden, A. Stephenson, C. W. Yong, M. J. Bennison, T. Hasell, M. E. Briggs, S. L. James and A. I. Cooper, *Chem. Sci.*, 2017, **8**, 2640–2651.

- 15 R. J. Kearsey, B. M. Alston, M. E. Briggs, R. L. Greenaway and A. I. Cooper, *Chem. Sci.*, 2019, **10**, 9454–9465.
- 16 G. T. Rochelle, *Science*, 2009, **325**, 5948, 1652–1654.
- 17 P. R. Gogate and A. B. Pandit, *Ultrason. Sonochem.*, 2004, **11**, 105–117.
- 18 O. Renier, G. Bousrez, K. Stappert, M. Wilk-Kozubek, B. Adranno, H. Pei, E. T. Spielberg, V. Smetana and A. V. Mudring, *Cryst. Growth Des.*, 2020, **20**, 214–225.
- 19 Z. Li, H. Wang, M. Chu, P. Guan, Y. Zhao, Y. Zhao and J. Wang, *RSC Adv.*, 2017, **7**, 44688–44695.
- 20 E. A. Kelly, N. Willis-Fox, J. E. Houston, C. Blayo, G. Divitini, N. Cowieson, R. Daly and R. C. Evans, *Nanoscale*, 2020, **12**, 6300–6306.
- 21 D. Statman and I. Jánossy, *J. Chem. Phys.*, 2003, **118**, 3222.
- 22 B. Chen, S. Ma, E. J. Hurtado, E. B. Lobkovsky and H. C. Zhou, *Inorg. Chem.*, 2007, **46**, 8490–8492.
- 23 R. Lyndon, K. Konstas, B. P. Ladewig, P. D. Southon, P. C. J. Keperter and M. R. Hill, *Angew. Chemie Int. Ed.*, 2013, **52**, 3695–3698.
- 24 J. Park, D. Yuan, K. T. Pham, J. R. Li, A. Yakovenko and H. C. Zhou, *J. Am. Chem. Soc.*, 2012, **134**, 99–102.
- 25 L. Rao, W. Wei, Z. Xia, F. Li, F. Yang and K. Zhou, *Asian J. Phys. Chem. Sci.*, 2017, **4**, 1–12.
- 26 N. Stock and S. Biswas, *Chem. Rev.*, 2012, **112**, 933–969.
- 27 F. J. Rizzuto and J. R. Nitschke, *J. Am. Chem. Soc.*, 2020, **142**, 7749–7753.
- 28 M. Z. Ahmad and A. Fuoco, *Curr. Res. Green Sustain. Chem.*, 2021, **4**, 100070.
- 29 B. D. Egleston, K. V. Luzyanin, M. C. Brand, R. Clowes, M. E. Briggs, R. L. Greenaway and A. I. Cooper, *Angew. Chemie Int. Ed.*, 2020, **59**, 7362–7366.
- 30 C. W. Chang, I. Borne, R. M. Lawler, Z. Yu, S. S. Jang, R. P. Lively and D. S. Sholl, *J. Am. Chem. Soc.*, 2022, **144**, 4071–4079.



## **Chapter 4**

### **Melt-Quenched Porous Organic Cage Glasses**

## 4.1 Preface

Porous organic cages (POCs) are a molecular type of porous material, which have recently been instrumental in the discovery of porous liquids, that is, a liquid with permanent intrinsic porosity. Since the discovery of porous liquids, organic cages have been incorporated into numerous systems, with multiple examples of type II (that is, a porous material dissolved in a size-excluded solvent) and type III (that is, a porous material dispersed in a size-excluded solvent) porous liquids. While type I (neat liquids consisting of molecules that contain an internal cavity) have been discovered, there are very few examples that incorporate organic cages into this type of material. This is likely due to the inherent instability of imine based porous organic cages, which are fairly susceptible to decomposition, and are very often reported to decompose prior to melting.

In this chapter, we aim to explore the melting of organic cages to gain a greater understanding of whether a neat liquid organic cage could be a possibility. In the process of this research several cages were found to successfully melt, and glass transitions were identified. The melt-quenched organic cage glasses were then further explored for their gas sorption, where one example exhibited greater gas capacities than the as-synthesised parent cage. Another well-known POC was also discovered to have unusual thermal transitions, which leads to a complete loss in porosity and has yet to be reported for any imine based organic cage.

The work in the first portion of this chapter has been published (M. C. Brand, F. Greenwell, R. Clowes, B. D. Egleston, A. Kai, A. I. Cooper, T. D. Bennett, and R. L. Greenaway, *Melt-quenched Porous Organic Glasses*, *J. Mat. Chem. A*, **2021**, 9, 19807). The work within the latter part of this chapter has been compiled and is being prepared for publication (M. Brand, F. Greenwell, A. I. Cooper, T. D. Bennett, and R. L. Greenaway, *Thermal Conversion of a Porous Organic Cage into a Polymeric Organic Glass or Extended Crystalline Framework*).

Synthesis and characterisation were carried out by M. Brand, F. Greenwell, and R. Greenaway. Gas sorption and gas high-throughput experiments were carried out by M. Brand and R. Clowes. Electron microscopy experiments were carried out by B. Egleston and A. Kai. Computational studies were permed by K. Jelfs and A. Moroz (Imperial College). Project guidance was provided by R. Greenaway, T. Bennett, and A. Cooper. An Optical DSC450 and imaging station was loaned from Linkam Scientific.



## 4.2 Glasses

Glasses are a class of material which we are all very familiar with, whether that is for general day-to-day applications such as our phone screens, or even more specialised applications such as bulletproof windows and optical fibres.<sup>1</sup> One of the most desirable and widely used features is the transparent nature of glass while remaining solid-like. Glasses also share similar properties to the corresponding crystal such as the density, and thermal properties.<sup>2</sup> Though, unlike crystals, glasses exhibit a much broader melting point range and lack long range order which makes them isotropic and more liquid-like. Glasses remain one of the materials where the practical applications have outweighed the scientific understanding. This leaves glasses with a broad and somewhat vague definition, for example, an early definition described them as “*an inorganic product of fusion which has been cooled to a rigid condition without crystallizing*” by the American Society of Testing Materials.<sup>2</sup> This definition also spans to the general population within the Oxford Dictionary.<sup>3</sup> Of course, our understanding means that this cannot be the definition as many organic glasses are now known.<sup>4</sup> Additionally, there are other methods of producing glasses which avoids high temperatures, such as sol-gel processes that use a chemical process, and chemical vapour deposition which avoids fusion of the constituent materials.<sup>5</sup> A

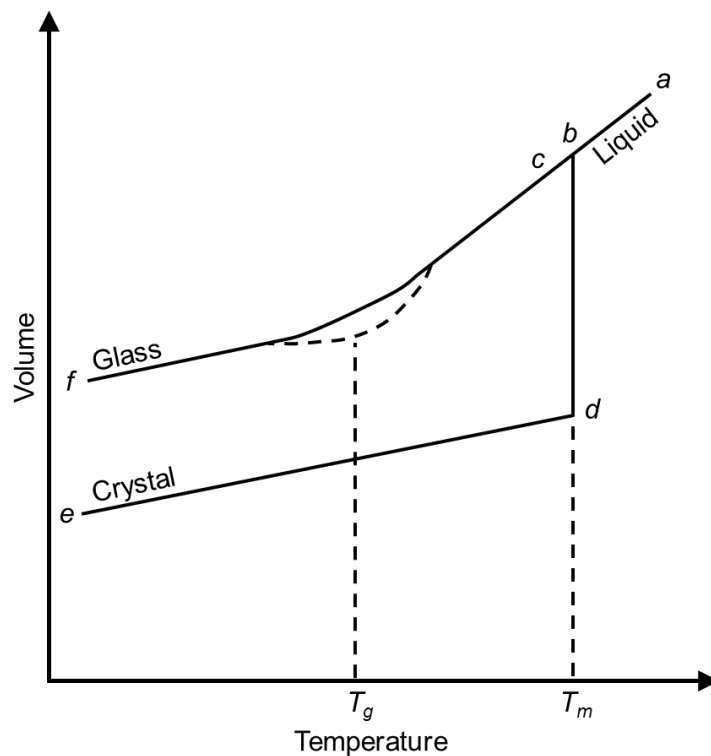


**Figure 4.1** Volume-temperature diagram for a glass and crystal forming liquid. Reproduced with permissions from ref (6).

simpler and more accurate definition of a glassy state may be “*an amorphous solid material, which can be observed by the absence of sharp Bragg peaks in X-ray diffraction*”. However, this definition may remain too broad as other amorphous solids, such as microcrystals, could still be categorised under this definition. The results in this chapter will focus solely on glasses formed from the liquid state and melt-quenching.

The glass transition can be explained in terms of a volume-temperature (V-T) diagram which demonstrates how the atomic rearrangement can occur to form a glass or a crystal (Figure 4.1).<sup>6</sup> Consider a sample of material at a temperature above its melting point ( $T_m$ ), at point *a*. At this point, the material exists in liquid form as there is sufficient thermal energy to maintain this state. As the temperature decreases to the  $T_m$ , the energy of the system decreases, and the atomic rearrangement also begins to slow. At this point, *b*, the sample is in a thermodynamic equilibrium between the liquid and an infinitely small number of crystals. As the temperature of the sample becomes lower than the  $T_m$ , at point *c*, the sample can take two possible pathways, the first being crystallisation. Crystallisation can occur if the sample is cooled at a rate where atomic rearrangement can readily occur, however, the sample must have a sufficient number of nuclei and have an appropriate crystal growth rate. On further cooling, the crystal follows the *d* to *e* pathway, resulting in a decrease in volume and crystal formation. It is also important to note that the points *abd* can occur over a range of temperatures rather than a singular point.<sup>2</sup> Alternatively, if the sample is cooled below the  $T_m$  and crystallisation does not occur, the sample can move into a supercooled liquid state. This can arise if the sample is cooled at a high rate. This results in the sample becoming more viscous, and molecules become less mobile and are unable to rearrange, trapping it in a liquid-like structure.<sup>7</sup> The point at which the supercooled liquid becomes solid, *i.e.*, the glass state, is the glass transformation range, creating the glass *f*. Although the glass transformation will occur over a temperature range, it is typically reported as a single temperature of the transition, the glass transition temperature,  $T_g$ , which is the steepest point within the transition region. Once a material has undergone a glass transition and is in the glass state, reheating the material will return it to the supercooled liquid state, passing through the glass transformation region, which can be observed in a heat-cool-heat differential scanning calorimetry (DSC) scan, although, the transition does not follow the same path as it does on cooling. If the heating and cooling are performed at the same rate, then the glass transition temperature will be very similar.<sup>8</sup>

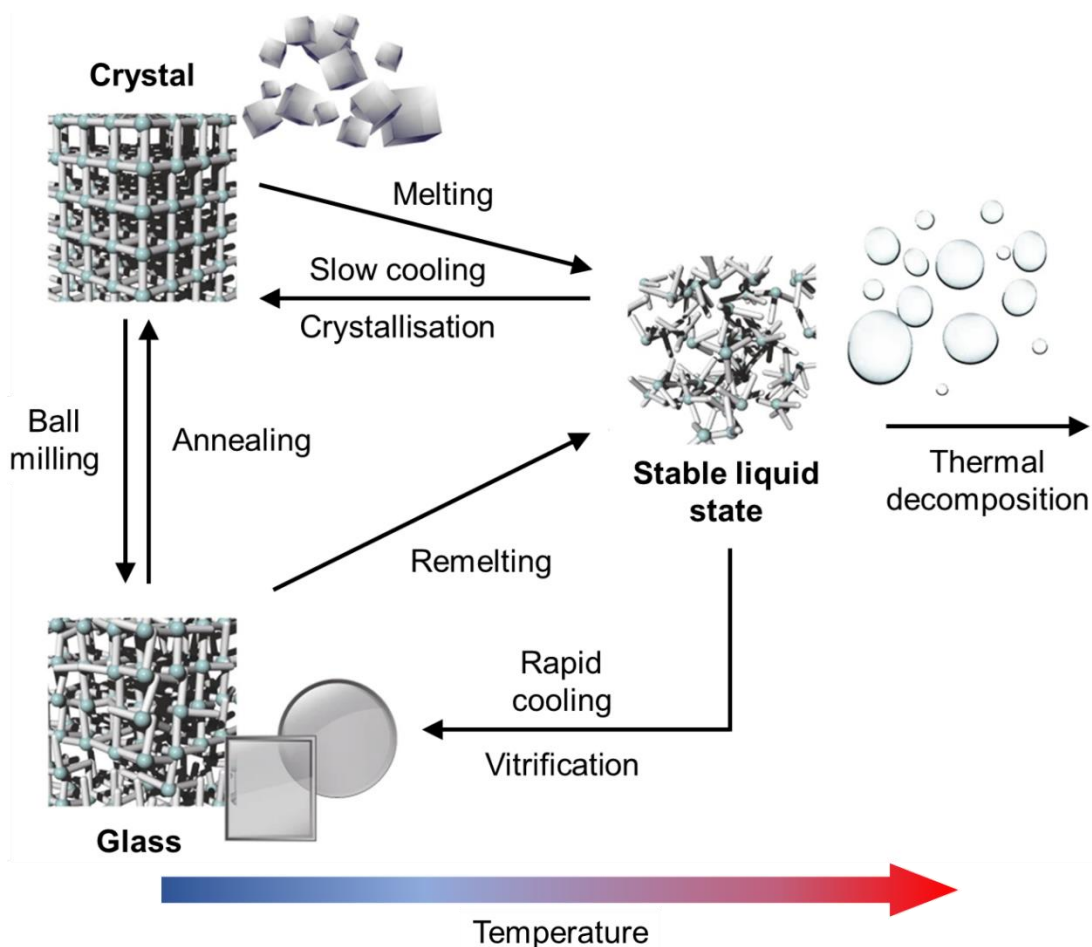


**Figure 4.2** Various routes to produce crystals, glasses, and liquids. Reproduced with permissions from ref (4).

### 4.3 Type 1 Porous Liquids

First conceptualised by O'Reilly *et al.*, a type 1 porous liquid (PL) is a material where its constituent molecules contain an internal cavity, or pore, with a scaffold rigid enough to prevent collapse if the cavity remains unoccupied, and the auxiliary structure cannot fill the cavities of neighbouring molecules.<sup>9</sup> One possibility to approach a true type 1 PL is by utilising supramolecular materials, such as crown ethers or calixarenes, which can be tailored to have a more favourable shape; however, these molecules typically have shallow cavities and are highly flexible which can prevent them from accepting a guest molecule and increases the likelihood of intermolecular penetration. To date, there are far fewer examples of type 1 PLs than both type 2 and type 3, ultimately demonstrating how difficult it is to produce these types of system.<sup>10</sup>

One of the earliest reported attempts to produce a type 1 PL was by Giri *et al.*, where POCs were utilised and functionalised with alkyl chains to lower the melting point of

the material, potentially producing a liquid POC.<sup>11</sup> Typically, imine based POCs are often reported as being somewhat unstable and will decompose prior to melting, making this the first series of meltable organic cages.<sup>12,13</sup> The synthesis of several alkyl-decorated cages, with melting points ranging from 50 °C to 198 °C, was reported. While these results were a promising pathway towards a type 1 PL, they found that all of the materials were non-porous in the solid state, and exhibited no porosity in the liquid state. They then proposed that the loss in porosity was due to interpenetration from the alkyl chains entering the cavities of neighbouring cages. To try and alleviate this problem, a computational study was carried out using bulkier auxiliary groups with *t*-butyl functionality attached to the terminus of the long alkyl chains.<sup>14</sup> During this study they found that the functionalised chains entered the cavities of the neighbouring materials significantly slower than that of the unbranched chains, however, the interpenetration was more thermodynamically favoured which demonstrated that none of these materials would exhibit porous behaviour.

Since these two initial reports of attempting to produce a PL by functionalising POCs with long chains, other groups have also sought to proceed with similar methods which have proven far more successful in creating porous variants. The first successful example of creating a type 1 PL was reported by Ma *et al.*, where they used modified metal organic cages (MOCs).<sup>15</sup> In this study they report the use of MOCs, based off of a trialdehyde (5,5',5''-(benzene-1,3,5-triyl)tripicolinaldehyde), zinc metal ions, and poly(ethylene glycol) (PEG) functionalised anilines, with two chain lengths, 4 and 19 units long, where the PEG chains have ionic liquid functionality (Figure 4.3, a). Only the longer 19-unit chain produced a liquid at room temperature, while the shorter chain meant the MOC remained solid. To identify whether the pores remained empty, positron annihilation lifetime spectroscopy (PALS) was used. This technique can determine the average pore size by measuring the lifetime of positrons, which can then be compared to calculated pore diameters. Similar studies on type 3 PLs have also demonstrated the capabilities of PALS.<sup>12</sup> The experimental results suggest that the cavity remains structurally intact and is empty, unlike that of the alkylated organic cages. They attribute this to the imidazolate terminal and triflimide producing strong ionic bonds, preventing the long chains from entering the cavity of neighbouring molecules. Additional studies also go on to suggest that the pore remains empty as a PL, by exposing the samples to a range of isomers of propanol and butanol, which further demonstrates the pore size and its capability of selectively binding branched isomers over the linear alternative. Finally, after exploring the gas selective capabilities, they go on to investigate the absorption of chlorofluorocarbons

(CFCs) into the PL. Here they identify three CFC's that are capable of being bound within the PL, with an order of affinity  $\text{CFCl}_3 > \text{CF}_2\text{Cl}_2 > \text{CF}_3\text{C}$ , demonstrating that these gases can be absorbed without the use of solvents and were able to go through multiple cycles of absorption without the PL showing any signs of decomposition.

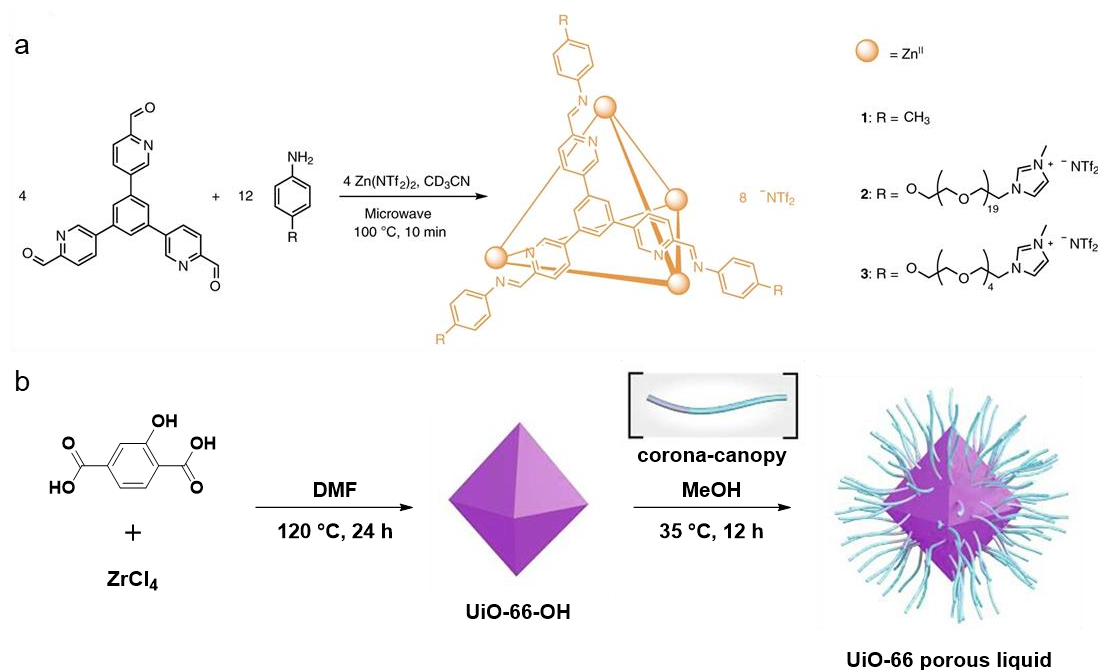


**Figure 4.3** a) Preparation of metal organic cages and type 1 porous liquid derived from a metal organic cage incorporating ionic liquid functionality; b) Synthetic approach to produce UiO-66-OH and the corresponding corona-canopy porous liquid. Figure (a) Reproduced with permissions from ref (15), figure (b) Reproduced with permissions from ref (16).

Another recent example has also broadened the possibilities by decorating a porous material with long functional groups. This work, by Wang *et al.*, focused on creating a type 1 PL by post-synthetic modification of a MOF, UiO-66, which is synthesised from terephthalic acid and zirconium oxide clusters.<sup>16</sup> In this case, a modified variant of the MOF was synthesised using 2-hydroxyterephthalic acid, to create UiO-66-OH, where the addition of hydroxyl groups allowed the material to undergo a condensation reaction with an organosilane (OS) (3-(trihydroxysilyl)-1-propanesulfonic acid), creating UiO-66-OH-OS (Figure 4.3, b). After the synthesis of the silane derived MOF, a series of polyether amines were added to create the corresponding UiO-66-PL, where the liquid is described as its approximate molecular weight, *i.e.*, UiO-66-M2070, where M2070 is a polyether monoamine of approximately 2000 molecular weight, creating a 'corona-canopy' system. This system is tethered via ionic bonding, creating a liquid at room temperature, and changing the polyether amine canopy

species produces liquids of variable viscosities. To identify whether the material remains porous, gas uptake measurements were performed with CO<sub>2</sub> and compared to the pure oligomer corona-canopy species, up to 10 bar. In all cases, they observed an increase in CO<sub>2</sub> uptake in the PL, ranging from an increase of 32% up to 144%. They claim that this broad range is due to some of the polyether amines having flexible chains, while others are more complex causing them to become entangled, leading to more difficult gas transportation.

#### **4.4 Melt-Quenched Porous Organic Cage Glasses**

##### **4.4.1 Screening the Thermal Properties of Porous Organic Cages**

Recently, there have been several discoveries identifying new phases which connect families of porous material through topological disorder. This includes the liquid states of porous MOFs<sup>4</sup> and MOCs.<sup>15</sup> With the introduction of MOFs and MOCs with accessible liquid states, rather than thermal decomposition, more investigations have focused on the liquid state of materials, and subsequently the discovery of the glass state of these materials came to light. Some of these materials with a glass state include a subclass of MOFs called zeolitic imidazolate frameworks (ZIFs), which were developed by Bennett *et al.* Here they identified several ZIFs that could exist as a liquid, with a melting point of ca. 400 °C, and on cooling of the liquid, formed materials with no long range order but retained the short range connectivity of the crystalline solid-state material, that is, they formed a glass.<sup>17,18</sup> These materials were also found to maintain some porosity when compared to the crystalline parent material. Glasses also offer an additional benefit over their crystalline counterpart as they can be cast into transparent, bulk, mechanically stable materials.

POCs have been very successful with their implementation into type 2 and 3 PLs (that is, solutions of porous material in a size-excluded solvent, and suspensions of porous materials in a size-excluded solvent, respectively) (Figure 4.4). However, to move towards type 1 PLs (that is, neat liquids formed from molecules containing permanent cavities) using POCs, we need far more understanding of these materials in their liquid state. POCs would make excellent candidates for type 1 PLs, at least on paper, due to their solution-processability and discrete shape-persistent nature. Though there have been many studies investigating these materials in their crystalline and amorphous states,<sup>19</sup> through disruption of the crystal packing, there are very few studies on the melting of POCs, other than those previously mentioned, which focused on functionalised organic cages decorated with alkylated chains.<sup>11</sup> To the best of our knowledge, there are no other studies investigating the liquid state of

POCs. This is possibly due to the nature of the dynamic chemistries involved in the synthesis of these materials, such as imine condensations, which can often make these materials difficult to isolate from solution.<sup>20</sup> The reversible nature of the imine bond can also give these materials a degree of instability, where decomposition can readily occur in the presence of water, or they can be susceptible to collapse when the material is desolvated.<sup>21</sup> While organic cages have been well documented over the past two decades, they are often reported without any melting behaviours or are often identified as decomposing prior to any solid-liquid transition occurring.<sup>12,22,23</sup> The reports that include any melting properties tend to include information obtained from a DSC trace without any further evidence to suggest that the peak they identify corresponds to the melting transition, as opposed to any other endothermic transformation, for example, by including data gathered by visual melting points or using an imaging DSC apparatus.

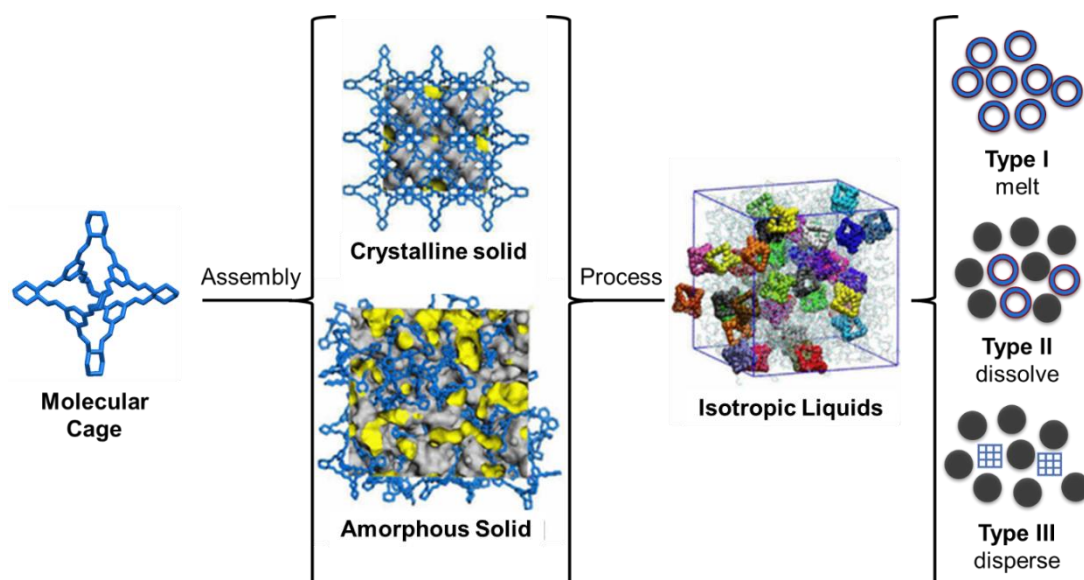


**Figure 4.4** Possible avenues of porous organic cages to form a crystalline solid, amorphous solid, or isotropic porous liquids (categorised as type I, type II, and type III).

To allow for melting to occur in organic cages, a number of design strategies can be implemented to minimise the chance of decomposition, and therefore lead to a solid-liquid transition. One of these methods involves reducing the imine bonds, removing the reversible nature by forming a more stable amine. While this can create a more stable cage, the increased flexibility can often lead to a loss in shape-persistence, which in turn leads to a loss in porosity due to collapse of the internal cavity. This was demonstrated in the case of **CC3** where all 12 imine bonds were successfully reduced to form **RCC3**.<sup>24</sup> To counteract the collapsing that occurs through reduction, and to reintroduce some porosity into materials, they can then be modified by conversion to

aminal or amide bonds (Figure 4.5).<sup>24,25</sup> This can be achieved through the addition of a simple aldehyde such as acetone or formaldehyde, or a bulky substituent with acid halide functionality. Alternatively, as described earlier, melting can be achieved through the addition of long alkyl substituents to the outer structure of the cage. While experimentally they found an almost complete loss in porosity in these cages,<sup>11</sup> a computational study predicted that the cage decorated with pentyl functionality would retain 30% of its porosity.<sup>14</sup>

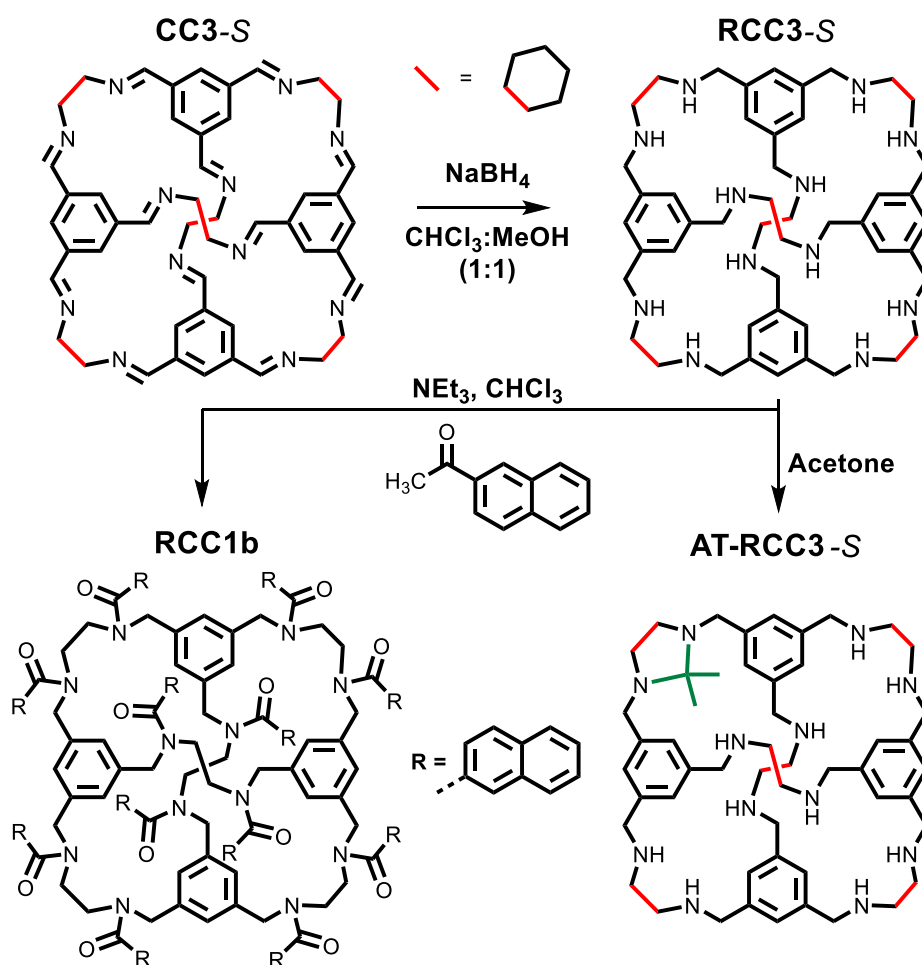


**Figure 4.5** Reaction schemes for the synthesis of **RCC3-S**, **AT-RCC3-S**, and **RCC1b**.<sup>24,25</sup>

With those considerations, a series of structurally related organic cages were selected to investigate whether they had a melting point ( $T_m$ ), or whether thermal decomposition ( $T_d$ ) occurs before the melting onset. Initially, five cages were selected to screen for melting behaviour with a mixture of imine and amine functionality, no external functionalisation, alkyl functionalisation, and aromatic functionalisation. This included **CC3**, the reduced variant **RCC3**, acetone-tied **RCC3** as **AT-RCC3**, functionalised **RCC1** (Tri<sup>4</sup>Di<sup>6</sup> cage formed from TFB and ethylenediamine) with naphthyl-amide as **RCC1b**, and pentyl substituted imine cage **nC<sub>5</sub>-CC** (Figure 4.6).



After performing preliminary investigations into their thermal properties, **CC3** was removed from this part of the study after exhibiting different behaviour – further studies are carried out in the later part of this chapter.

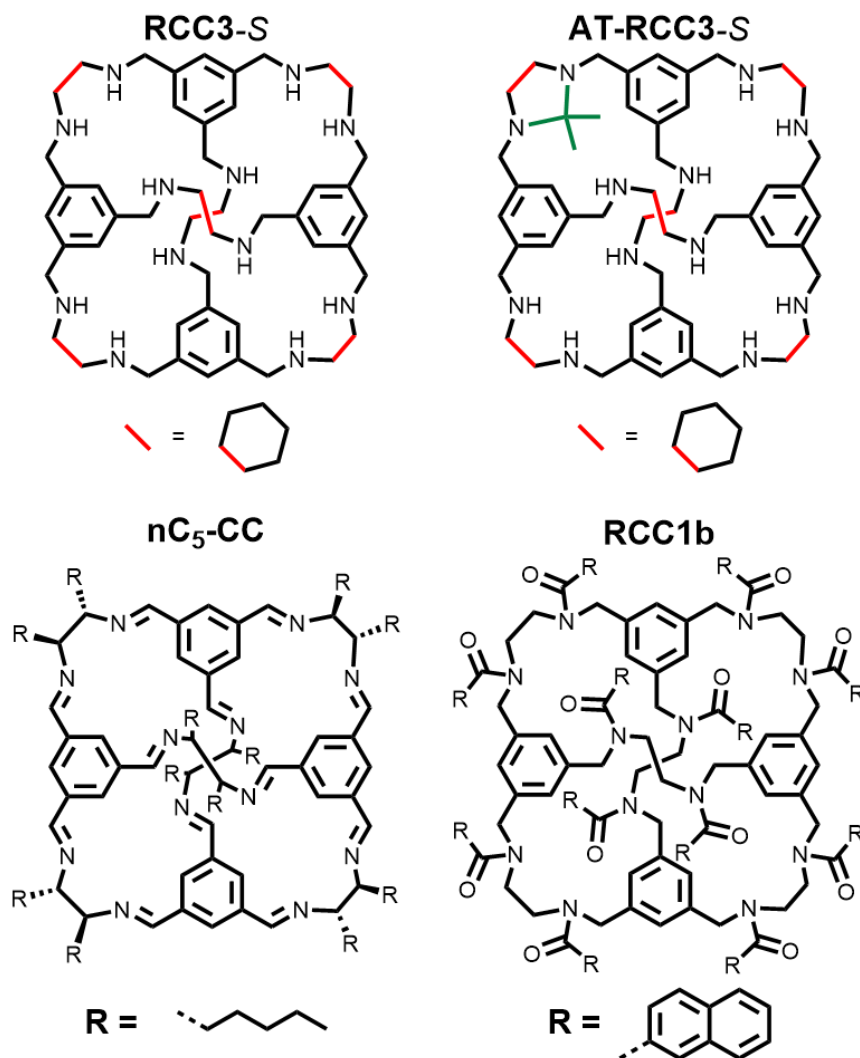


**Figure 4.6** Structures of the organic cages studied for melting and glass formation.

All materials synthesised with a chiral diamine were prepared with *S,S*-cyclohexanediamine (*S,S*-CHDA), and the resulting cage species typically have the nomenclature corresponding with the chirality, *i.e.*, **CC3** formed using *S,S*-CHDA is named **CC3-S**. However, for simplicity, they will be referred to as **CC3**, **RCC3**, and **AT-RCC3** for this portion of the chapter. All four cages were synthesised as per literature procedures and were isolated by either rapid solvent removal or rapid precipitation using solvent exchange. The corresponding synthetic procedures can be found in the experimental section of this chapter. All cages were found to be in an amorphous arrangement when analysed by powder x-ray diffraction (PXRD), except

for **AT-RCC3** which had some signals present in the PXRD pattern indicating some degree of crystallinity (Figure 4.11).

Once synthesised, the cages were dried in a vacuum oven with elevated temperatures (90 °C for all materials, except for **RCC3** which required 130 °C) under reduced pressure, and were continually monitored until no considerable weight loss was observed by thermogravimetric analysis (TGA). This was to ensure any observed endotherms or exotherms in the DSC traces were not due to a loss of solvent. Thermal decomposition temperatures were also extracted from the TGA traces, where the  $T_d$  is reported at the temperature where the gradient begins to change prior to the onset of bulk weight loss. All four samples exhibited very minor decreases in the weight % up until the decomposition temperatures starting at 280 °C for **nC<sub>5</sub>-CC** ranging up to 350 °C for **AT-RCC3** (Figure 4.6).

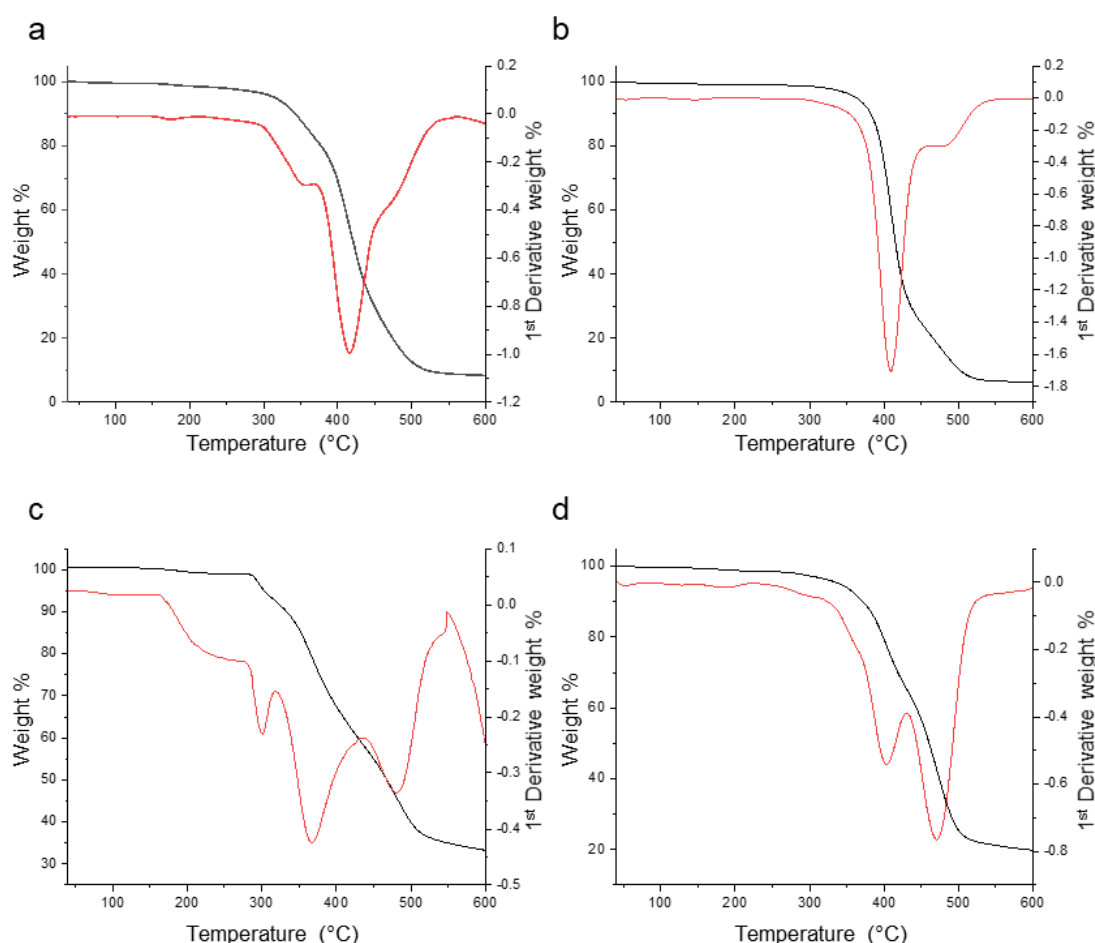


**Figure 4.7** TGA traces (black) and the corresponding 1<sup>st</sup> derivative (red) of a) **RCC3** desolvated at 130 °C; b) **AT-RCC3** desolvated at 90 °C; c) **nC<sub>5</sub>-CC** desolvated at 90 °C; d) **RCC1b** desolvated at 90 °C.

DSC studies were then carried out on all four samples, revealing a variety of complex behaviours upon heating (Figure 4.8). Samples were initially heated to a point

approximately 20 °C below their  $T_d$  to ensure no sample decomposition would occur during the scan. A broad endotherm can be observed in **RCC3** in the region of 100 – 200 °C, followed by a second sharp endotherm at approximately 270 °C occurring before the onset of mass loss. The DSC trace for **AT-RCC3** and **RCC1b** also show endothermic features starting at approximately 130 °C and 230 °C, respectively. The scan for **nC<sub>5</sub>-CC** also displays two separate peaks, one endotherm in the region of 140-170 °C, which is then followed by a sharp exotherm at 190 °C.

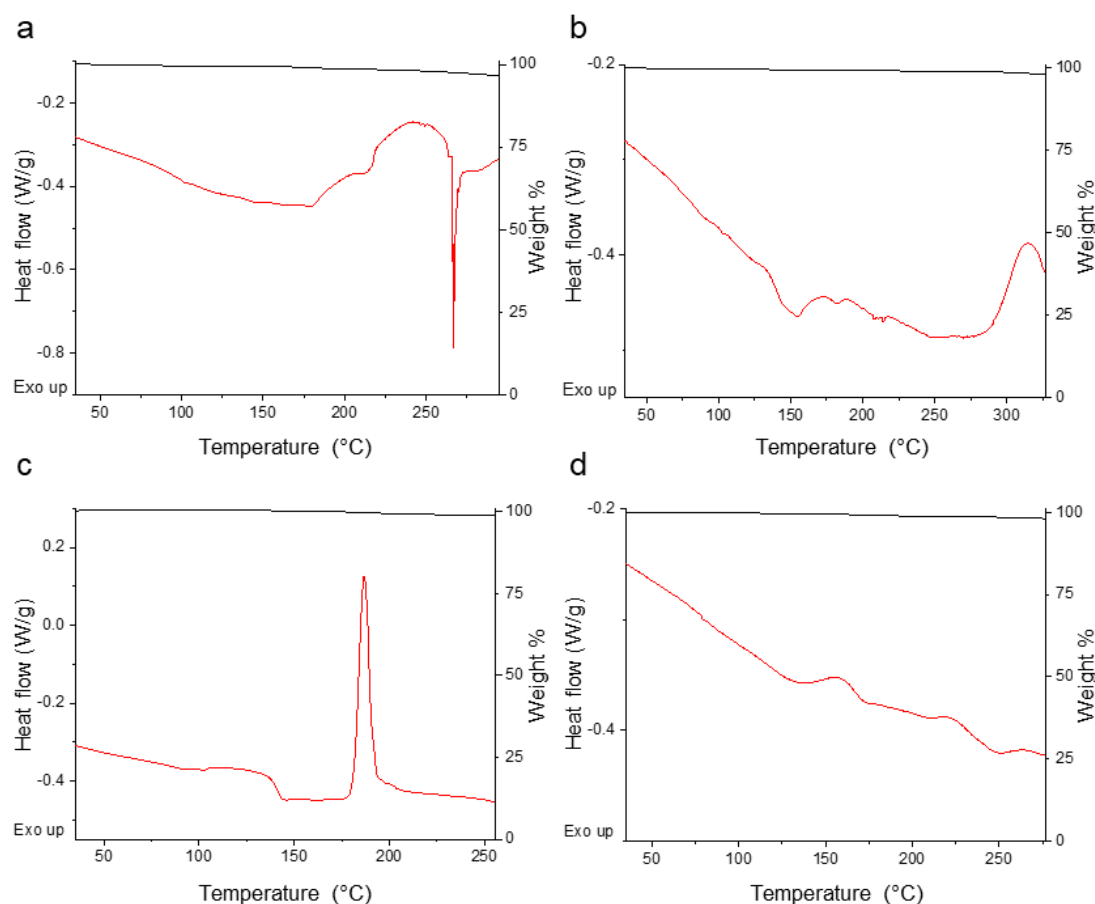


**Figure 4.8** Initial DSC traces (red) and the corresponding TGA curve (black) of a) **RCC3** heated to 300 °C; b) **AT-RCC3** heated to 330 °C; c) **nC<sub>5</sub>-CC** heated to 260 °C; d) **RCC1b** heated to 280 °C.

To confirm whether any of the endotherm peaks produced were a result of melting, melting point apparatus was used to monitor the sample from room temperature up to the broad endotherm temperatures. Melting points were identified in all cases, where all three of the reduced variants exhibited a very broad melting range of approximately 100 °C, between the onset of melting and the final liquid state of the material (Table 4.1). This corresponds to the broad endotherm peaks identified in the initial DSC traces, confirming these are a result of melting. The imine sample, **nC<sub>5</sub>-CC** had a considerably smaller melting range of 20 °C. This is likely due to the

differences between amorphous and crystalline materials. Crystalline materials typically exhibit sharp, well-defined melting points due to their long-range order, meaning local environments are the same, hence the thermal energy required for melting is uniform. On the other hand, amorphous solids lack long-range order (and arguably even more so with flexible organic cages), and the local environment is non-uniform and differing amounts of thermal energy is required to overcome the different interactions within that material. A visual demonstration of the broad melting behaviour of **RCC3** between 100-200 °C was recorded using an optical DSC (Figure 4.9), the full recording can be found at *J. Mater. Chem. A*, 2021, **9**, 19807–19816, as a supplementary movie.

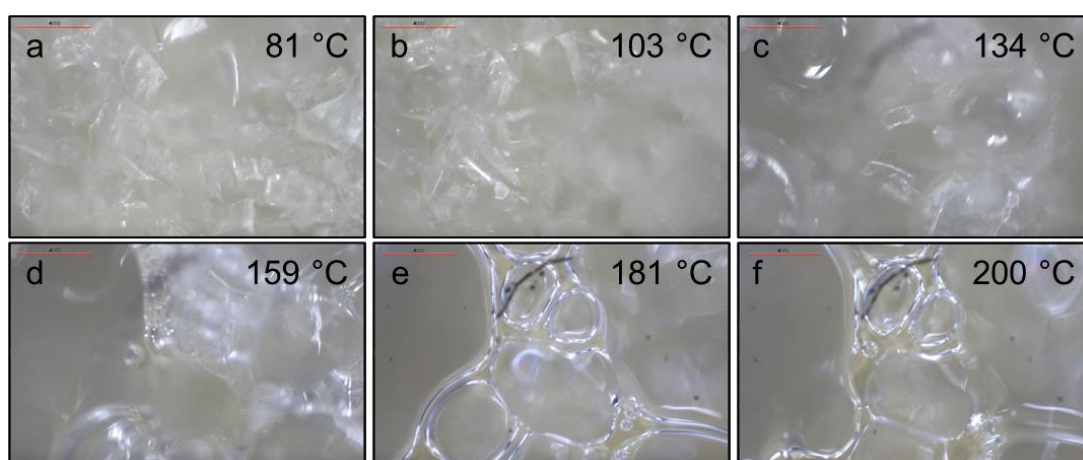


**Figure 4.9** Images taken at different temperatures from a recording on an optical DSC in the melting range of **RCC3**, where a) 81 °C; b) 103 °C; c) 134 °C; d) 159 °C; e) 181 °C; f) 200 °C.

To try and identify some of the other endothermic and exothermic features in the DSC traces, further analysis of the heated sample was completed, which included  $^1\text{H}$  NMR spectroscopy and PXRD. The  $^1\text{H}$  NMR spectra showed little to no change in the heated samples of **AT-RCC3**, and **RCC1b**, whereas **RCC3** and **nC<sub>5</sub>-CC** became insoluble after heating to 300 °C and 260 °C, respectively. One possibility is that the exotherm identified by DSC of **nC<sub>5</sub>-CC** is a polymerisation of the cage species occurring from cross-linking due to the dynamic nature of imine bonds. All samples also remained amorphous, with no traces of any signals in the PXRD patterns.

A second series of DSC experiments were then performed to a temperature below their respective decomposition temperatures and any exotherms identified in the initial set of experiments. Samples were then cycled through a heat-cool (HC) and a heat-cool-heat (HCH) cycle, with the same rate of heating and cooling (10 °C/min). On the cooling downscan in the DSC, several of the samples had clear indications

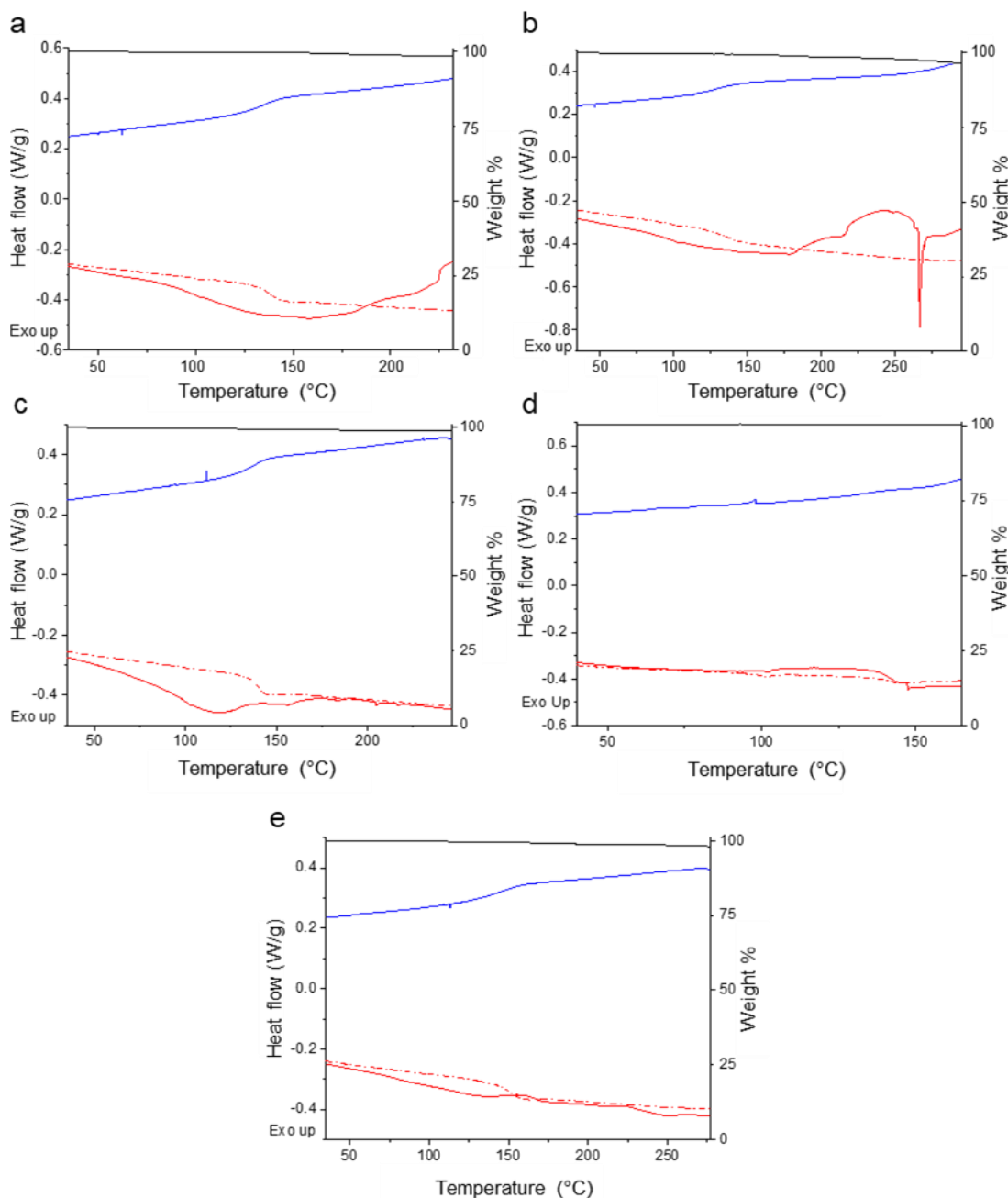


**Figure 4.10** DSC traces and corresponding TGA curve (black) subjected to heat-cool-heat (HCH) cycles, where the initial upscan is shown as a solid red line, downscan as a blue line, and second upscan as a dashed red line, of a) **RCC3** cycle to 250 °C; b) **RCC3** cycle to 300 °C; c) **AT-RCC3** cycle to 250 °C; d) **nC<sub>5</sub>-CC** cycle to 170 °C; e) **RCC1b** cycle to 280 °C.

that a glass transition was taking place. The data for **RCC3** clearly shows a reversible glass transition at 138 °C, which can be seen on the downscan and the reverse on the second upscan (Figure 4.10). A glass transition can also be observed in **RCC1b** and **AT-RCC3**, whereas this is not seen in **nC<sub>5</sub>-CC**. The  $T_g$  of both **RCC3** and **AT-RCC3** occurs at the same temperature, which can be rationalised by both cages having an identical exterior (Table 4.1). **AT-RCC3** only varies by the incorporation of

the internal aminal functionalisation (through the addition of acetone), which appears to have no effect on the phase transition, possibly because of its location which has little effect on the surface of the molecule.

**Table 4.1** Summary of the thermal decomposition onsets ( $T_d$ ) from TGA, melting point ranges ( $T_m$ ) based on visual observations and DSC, and glass transitions ( $T_g$ ) from DSC, for a range of organic cages.

Organic cage	$T_d / ^\circ\text{C}$	$T_m / ^\circ\text{C}$	$T_g / ^\circ\text{C}$	Notes
<b>RCC3-S</b>	ca. 300	100-200	138	Second sharp endotherm at 270 °C
<b>AT-RCC3-S</b>	350	150-250	138	-
<b>RCC1b</b>	300	150-250	150	-
<b>nC<sub>5</sub>-CC</b>	280	170-190	N/A	Sharp exotherm at 190 °C

Further analysis of the materials of the second series of DSC experiments found **RCC3**, **AT-RCC3**, and **RCC1b** to have remained amorphous after melting, whereas **nC<sub>5</sub>-CC** contained Bragg peaks indicating crystallisation upon cooling from its liquid state (Figure 4.11). Analysis by <sup>1</sup>H NMR spectroscopy of the glassy materials also indicated that no structural change had occurred to **RCC3** or **nC<sub>5</sub>-CC**, with both spectra corresponding to the starting cage. Some signal broadening was noted for **RCC1b** compared to the pre-processed cage, which may be due to the naphthylamide functionality (Figure 4.15). Analysis of **AT-RCC3** showed the most difference between all the heated samples, where the glassy material became mostly insoluble. However, <sup>1</sup>H NMR analysis on some of the small amount of sample that dissolved suggested that the acetal functionality had been lost and the material had been converted back to **RCC3** (Figure 4.13). This loss in acetal functionality has previously been reported where **AT-RCC3** will slowly convert back to **RCC3** over time in CDCl<sub>3</sub>.<sup>24</sup> Given a small portion of this sample was soluble, it only represents a small portion of the sample which may have reverted to **RCC3** in solution rather than by heating. Further analysis by Raman spectroscopy of both the pre-processed **AT-RCC3** and the glassy material found similar characteristics throughout, which suggests that the loss of the acetal functionality did not occur due to the heating, but rather is reverting back to **RCC3** when in solution.

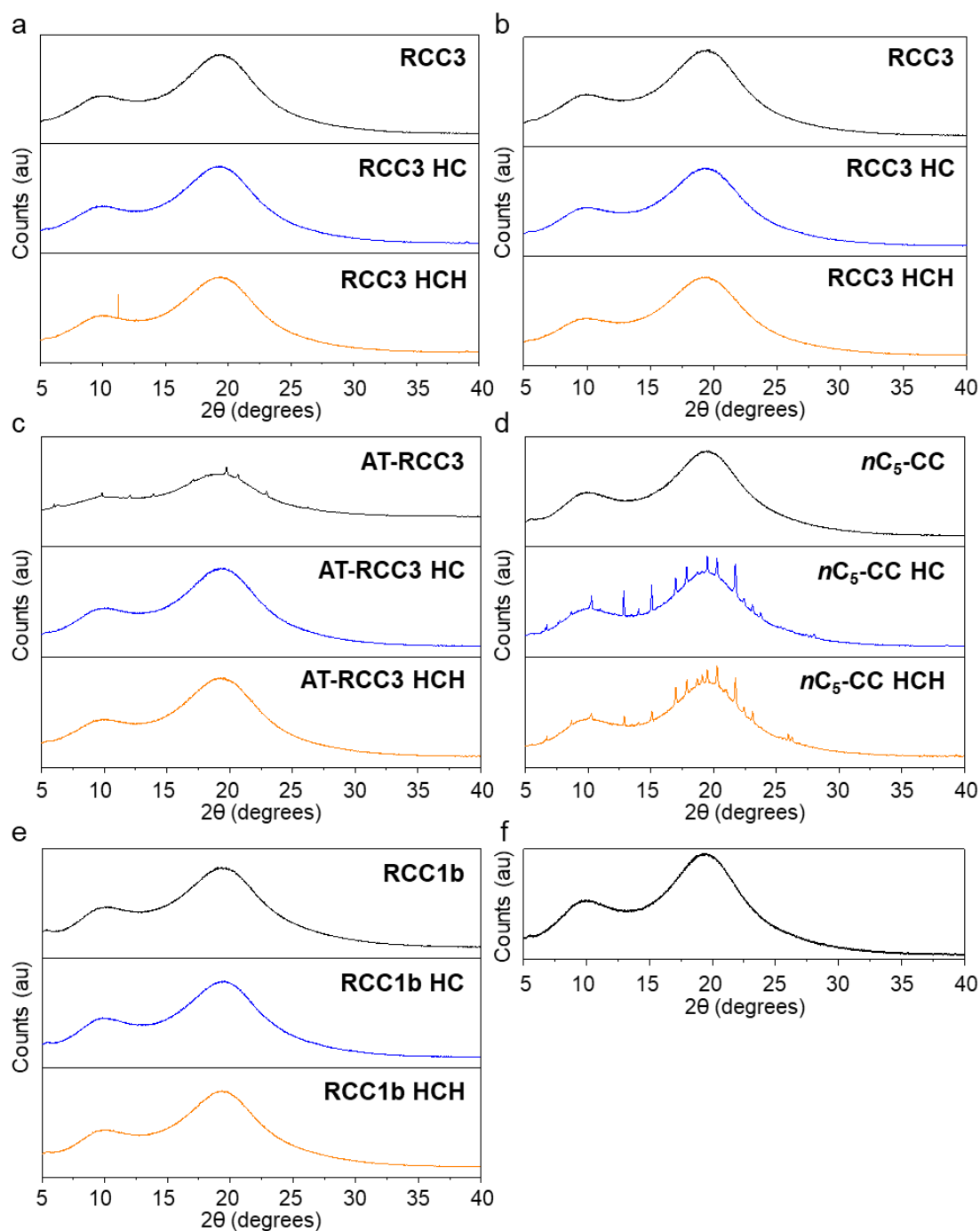


**Figure 4.11** Stacked PXRDs of cage samples, prior to heating (black), after a heat-cool (HC) cycle (blue), and after a heat-cool-heat (HCH) cycle (orange), where a) **RCC3**, with HC and HCH to 250 °C; b) **RCC3**, with HC and HCH to 300 °C; c) **AT-RCC3**, with HC and HCH to 250 °C; d) ***nC*<sub>5</sub>-CC**, with HC and HCH to 170 °C; e) **RCC1b**, with HC and HCH to 280 °C; f) blank sample of an empty well of the 96-well ProxiPlate.

In the case of **RCC3**, vastly different behaviours were observed between both temperatures. In these examples, the sample was initially heated to 300 °C and then 250 °C in the second series of experiments. For the former sample, it was found that the material remained insoluble when attempting to dissolve in  $\text{CDCl}_3$  and a

CDCl<sub>3</sub>/CD<sub>3</sub>OD mixture (Figure 4.12). However, the cage heated to the lower temperature was found to readily dissolve and was identical to the pre-processed cage. This suggests that a polymeric glass had been formed at the higher temperature. In both instances, the material remained amorphous after heating.

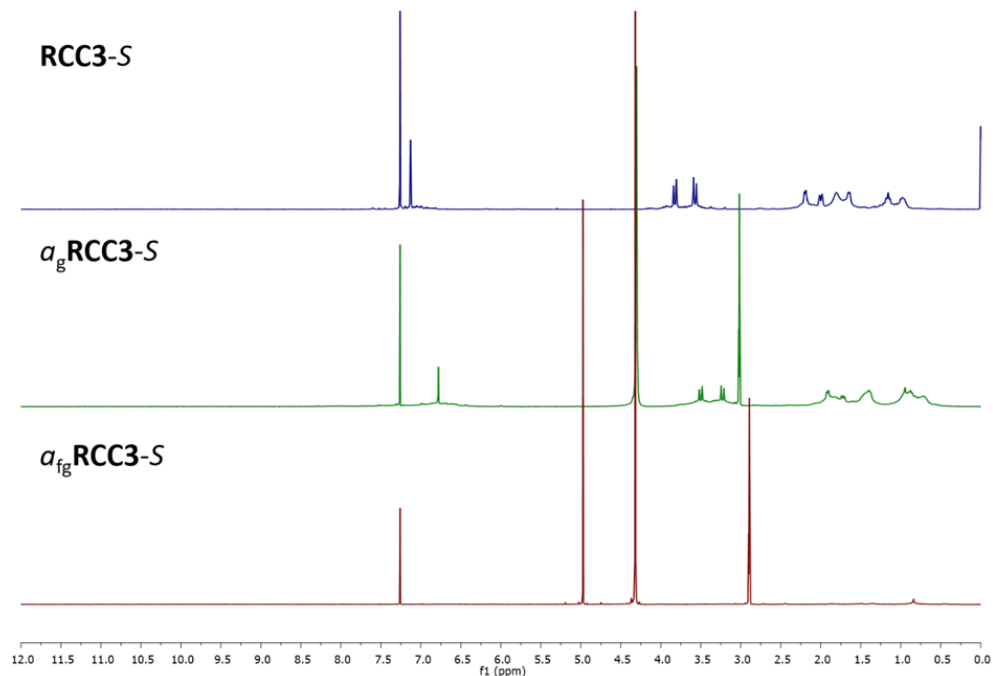


**Figure 4.12** Stacked <sup>1</sup>H NMR spectra of **RCC3-S** (CDCl<sub>3</sub>), **a<sub>g</sub>RCC3-S** (CDCl<sub>3</sub>:d<sub>4</sub>-MeOD), and **a<sub>fg</sub>RCC3-S** (CDCl<sub>3</sub>:d<sub>4</sub>-MeOD).

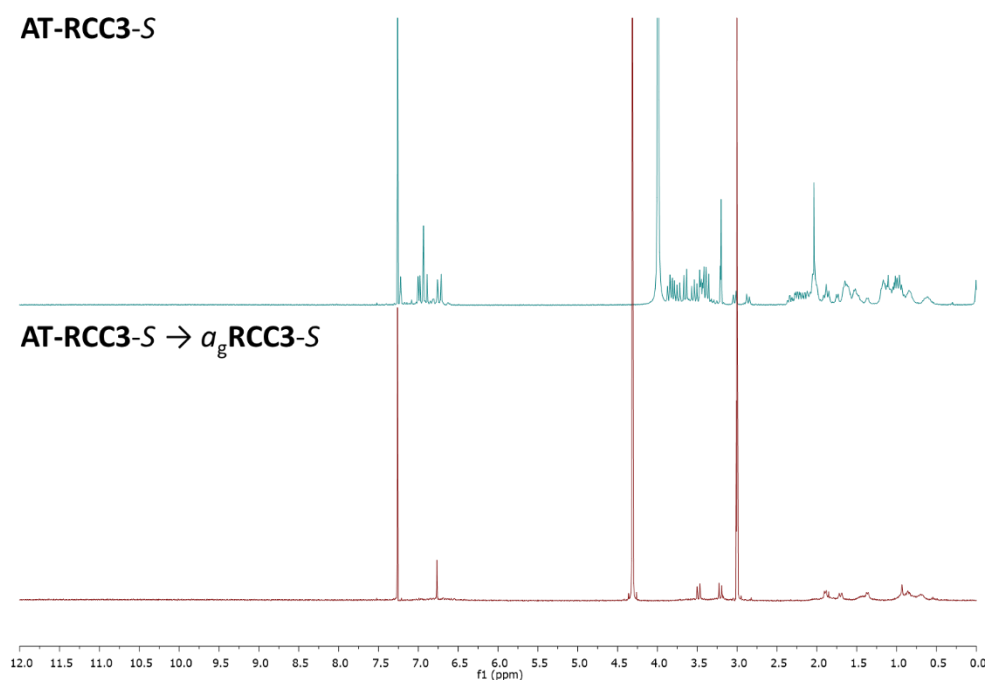


**Figure 4.13** Stacked <sup>1</sup>H NMR spectra of **AT-RCC3-S** (CDCl<sub>3</sub>:d<sub>4</sub>-MeOD) and the glass formed from heating and cooling **AT-RCC3-S** (CDCl<sub>3</sub>:d<sub>4</sub>-MeOD).



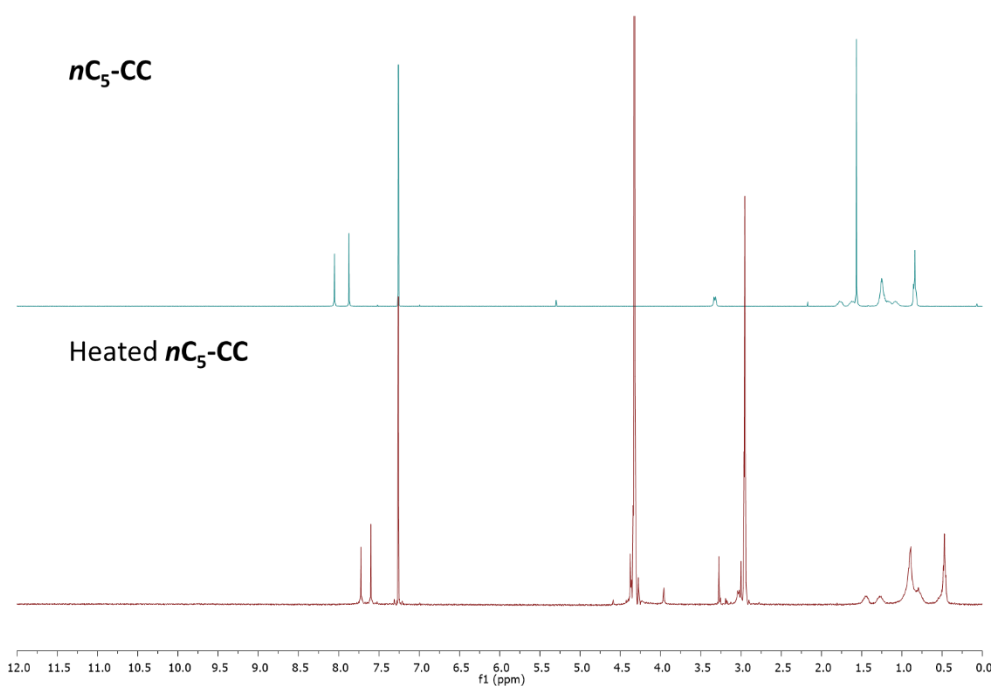


**Figure 4.14** Stacked <sup>1</sup>H NMR spectra of *nC<sub>5</sub>-CC* before (CDCl<sub>3</sub>), and after (CDCl<sub>3</sub>:d<sub>4</sub>-MeOD), a heat-melt-cool cycle to 170 °C.

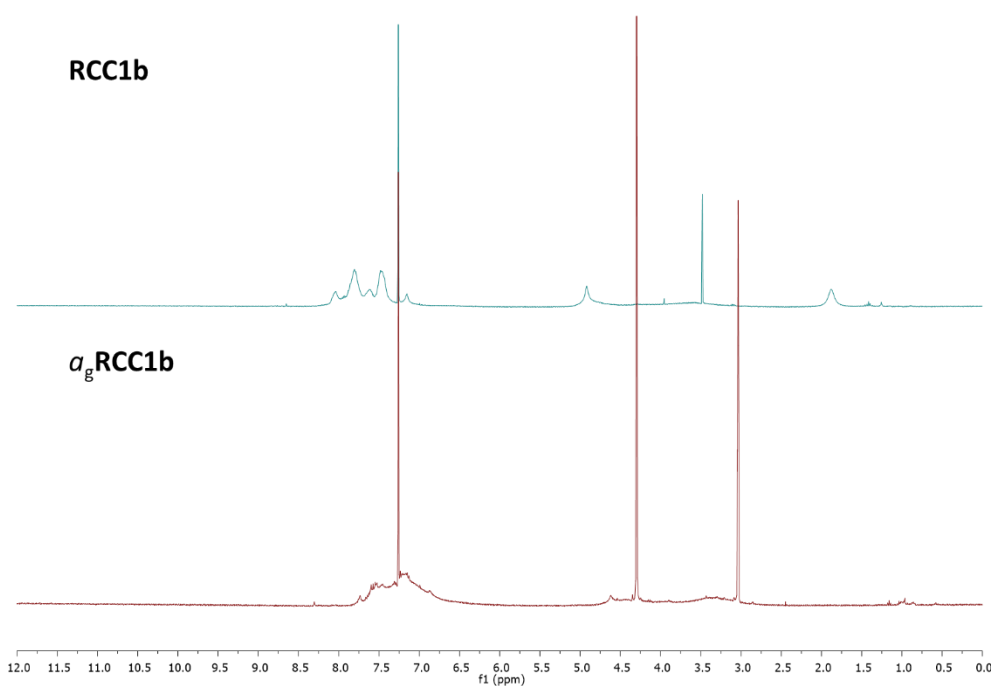


**Figure 4.15** Stacked <sup>1</sup>H NMR spectra of *RCC1b* (CDCl<sub>3</sub>) and *a<sub>g</sub>RCC1b* (CDCl<sub>3</sub>:d<sub>4</sub>-MeOD).

Optical images also proved very useful in identifying samples that had formed a melt-quenched glass (Figure 4.16). Samples were all visually inspected after heating while still in their DSC pans using a microscope. **AT-RCC3** and **RCC1b** both formed

optically transparent materials after heating, while **nC<sub>5</sub>-CC** remained opaque, and **RCC3** produced two visually different glassy materials. The first heated, to 300 °C, had created a dome shape from foaming, while the sample heated to 250 °C produced a transparent glassy material. This foaming behaviour after heating beyond the observed exotherm seen in the DSC trace is possibly due to the loss of a gas on polymerisation, which would also explain its insolubility. Another possibility is that the observed exotherm is the release of strongly bound gaseous molecules, either from within the cage cavities (physisorption) or from a carbamate formed from CO<sub>2</sub> bound with the free amine (chemisorption),<sup>26</sup> although this is less likely to explain the formation of insoluble material.

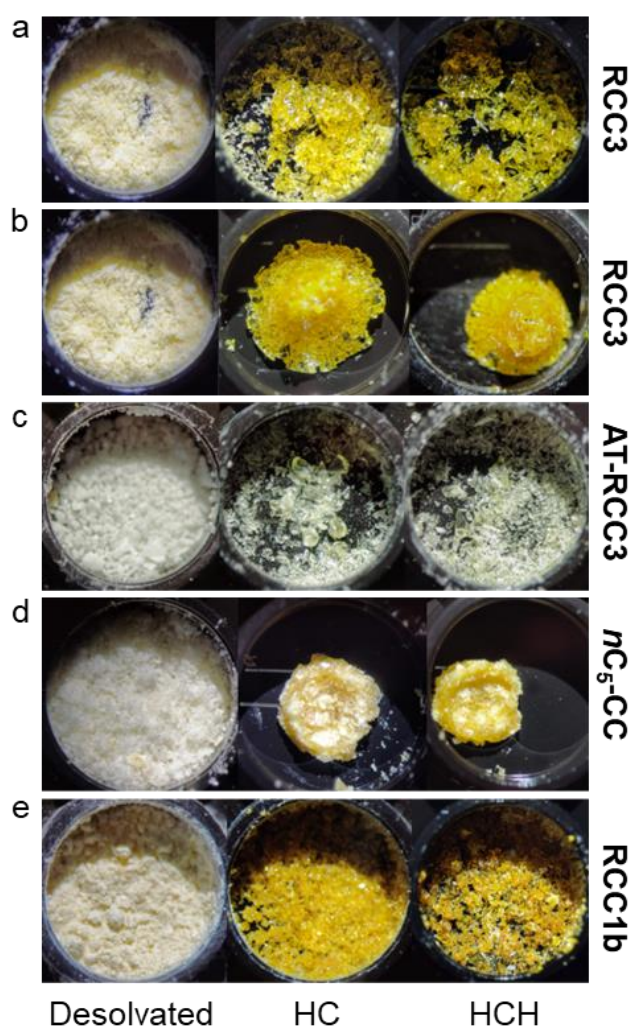


**Figure 4.16** Stacked optical images of cage sample, prior to heating (left), after a heat-cool (HC) cycle (middle), and after a heat-cool-heat (HCH) cycle (right), where a) **RCC3**, with HC and HCH to 250 °C; b) **RCC3**, with HC and HCH to 300 °C; c) **AT-RCC3**, with HC and HCH to 250 °C; d) **nC<sub>5</sub>-CC**, with HC and HCH to 170 °C; e) **RCC1b**, with HC and HCH to 280 °C

Glasses formed in the DSC studies will be referred to as  $a_g\text{RCC3}$ ,  $a_g\text{AT-RCC3}$ , and  $a_g\text{RCC1b}$ ; the foamed glass is referred to as  $a_{fg}\text{RCC3}$  (where  $a$  indicates amorphous, and the subscript  $g$  and  $fg$  a glass or foamed glass, respectively). As  $n\text{C}_5\text{-CC}$  failed to show any glass behaviour it was not investigated any further in this study.

#### 4.4.2 High-Throughput Gas Sorption of Cage Glasses

High-throughput screening can accelerate the discovery of materials, ranging from synthesis through to processing and formulation, and characterisation. There are many commercially available synthesis platforms available from companies such as Chemspeed<sup>27</sup> and Unchained Labs,<sup>28</sup> and other research groups developing alternatives such as the ‘*mobile robotic chemist*’ using a Kuka robot.<sup>29</sup> While these platforms are time effective in terms of reduced researcher effort, the initial cost for many research groups remains too high. However, there are some lower-cost alternatives, such as an open access liquid-handling robot which utilises Lego,<sup>30</sup> and the Chemputer.<sup>32</sup> While some analytical methods also lend themselves to being high-throughput due to the use of either autosamplers or microplates, such as NMR, LC-MS, UV-Vis, IR, and PXRD, some techniques are much more difficult to run in a rapid and high-throughput manner, such as gas sorption. Gas sorption experiments typically take several hours to complete (granted, samples could be run at a single pressure measurement to save time), require a considerable amount of material, and only a maximum of 4-6 samples can be measured in parallel depending on the

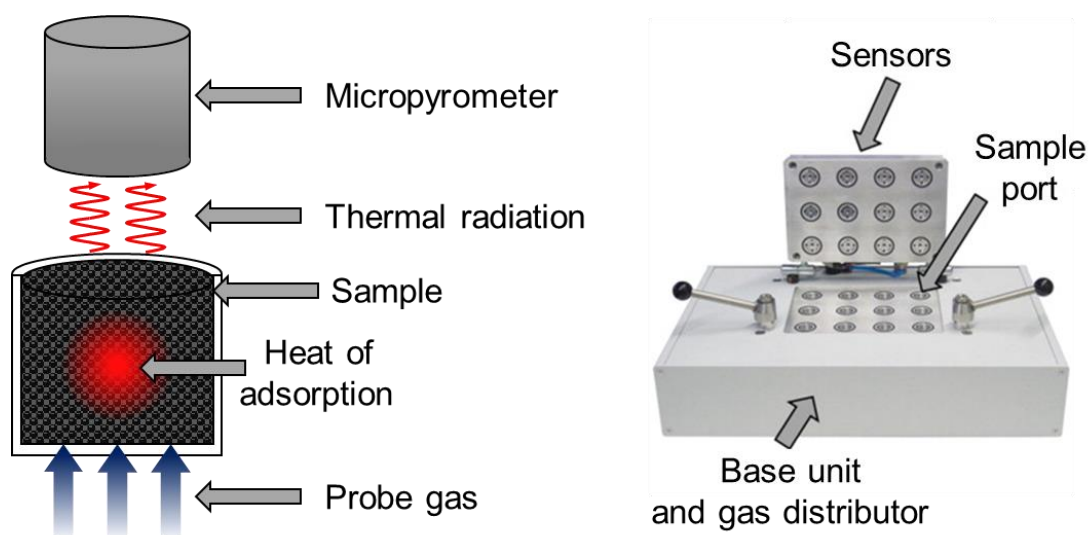


**Figure 4.17** Schematic demonstrating the Infrisorb-12 instrument. Reproduced with permissions from refs (31) and (32).

equipment used. To date, there are only a few examples of high-throughput approaches for screening the gas uptake in porous materials. One of the instruments, an 'infrisorb-12' (Figure 4.17),<sup>31,32</sup> is capable of running 12 samples simultaneously and uses butane as a probe gas. Each sample is continually monitored with a micropyrometer, which measures the temperature over the course of the experiment. As butane is injected into the sample chamber the thermal response of the samples is measured, which can then be used to evaluate the porosity of the material. In this case, MOFs were used to demonstrate the capabilities of the instrument and three new materials were identified, which were later confirmed by full sorption characterisation. In our experience, butane provides a high heat of adsorption, giving rise to a larger thermal response on physisorption, with porous materials allowing it to be detected more easily than smaller temperature differences that other probe gases produce, such as CO<sub>2</sub> and CH<sub>4</sub>. Though, one of the limiting factors is the size of butane, which has a kinetic diameter of 4.3 Å, preventing this method from identifying microporous materials with a pore diameter smaller than 0.43 nm.

Another instrument that has been designed was produced by Wildcat Discovery Technologies and is capable of running 28 samples with a variety of gases.<sup>33</sup> Software can control system valves allowing each sample to run in sequence over time, and each sample has a calibrated volume of gas and a pressure transducer. The gas is then cycled over the sample at least 15 times to ensure a uniform gas-phase composition. After equilibrium, the pressure is measured again and allows the gas uptake to be extrapolated from the change in pressure. They also state that mass spectrometry or gas chromatography could be used to measure the composition of the gas after reaching equilibrium. This provides the additional benefit of allowing samples to be measured under a variety of gases, including gas mixtures, allowing the user to test samples under real world conditions such as post-combustion conditions.

The Cooper group have developed their own in-house high-throughput instrument, which is capable of running 96 small-scale samples simultaneously using a 96-well ProxiPlate (Figure 4.18), which can also be used for PXRD analysis, and has previously been used in the discovery of organic polymers for photocatalysis.<sup>34</sup> The measurements can theoretically be performed with the majority of gases, where any bottled gas could be attached to the system, however the most commonly used within the group are CO<sub>2</sub>, N<sub>2</sub>, CH<sub>4</sub>, Kr, and Xe. Like the infrisorb-12 instrument, this also exploits the heat generated by a sample when gas is adsorbed, but rather than a

pyrometer, a thermal imaging camera is used to detect changes in temperature. The software which was produced for this instrument allows each well in the sample holder to be measured separately, and takes a base temperature reading from the plate itself which can then be subtracted from the temperature changes observed in the samples.

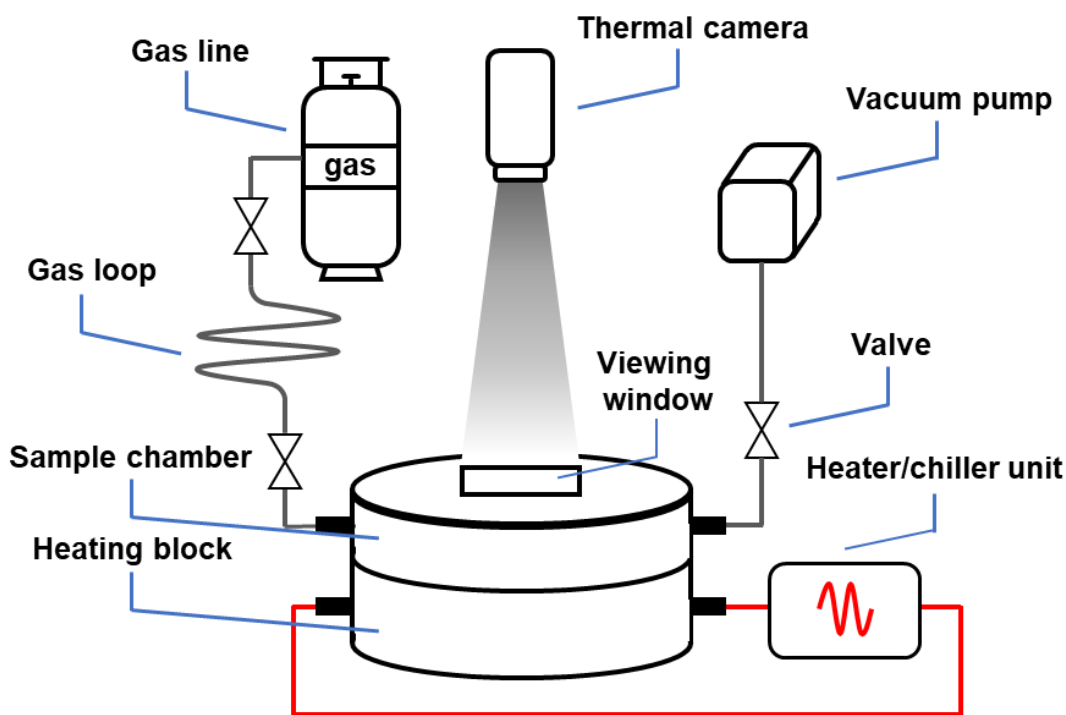


**Figure 4.18** Schematic showing the custom high-throughput gas sorption instrument.

The instrument itself is composed of several key parts shown in Figure 4.18, the first being the sample chamber. The sample chamber contains a viewing window which is made from zinc selenide glass – this type of glass is commonly used in IR components and lenses which allows the thermal imaging camera to detect temperature changes. The camera is then mounted in a fixed position 30 cm above the window. On the underside of the sample chamber is a heating block connected to a silicone-bath circulator, allowing the temperature to be controlled. Using the software, the valves can be manually controlled allowing evacuation of the sample chamber and the gas line. The valves can then be closed prior to performing measurements on the samples. Prior to analysis, samples are evacuated for 24 hours under continuous vacuum whilst maintaining the sample at an elevated temperature (80 °C). On performing the analysis, the temperature is set at 25 °C, the vacuum line and both gas line valves are closed, and the camera is set to record. The gas loop is then loaded with the probe gas by opening one side of the loop. After a few seconds the initial valve is closed and the secondary valve is opened, allowing gas to fill the sample chamber. The sample is then left to equilibrate back to the set temperature

(approx. 300 seconds), before repeating with additional doses of gas. The sample can then be evacuated from the probe gas to then undergo further testing with additional gases or opened to air.

The data produced by the software and thermal imaging camera provides the time and temperature of each sample well taken by the thermal camera, *i.e.*, each position on the 96-well plate. The base temperature of the plate can then be deducted from the sample temperature providing the change in temperature for each sample over time. The initial dose of gas provides the largest change in temperature, due to the pores within the material being empty after evacuation. This results in the secondary dose and thereafter have significantly lower temperature changes due to partly filled pores.

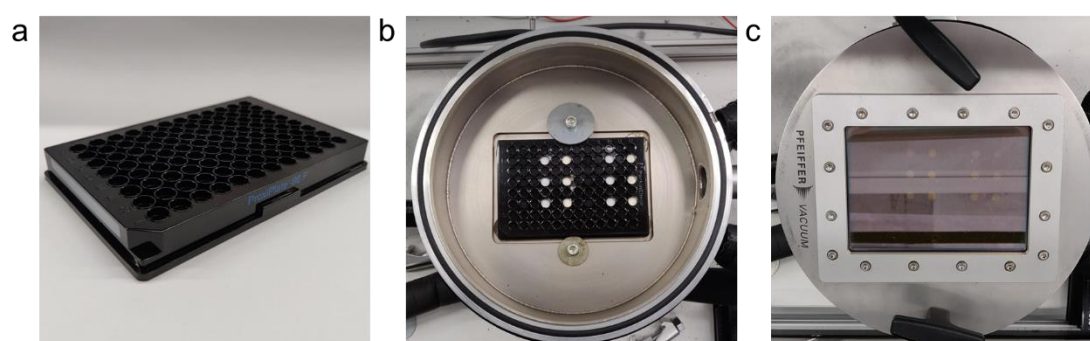


**Figure 4.19** a) Photo of the 96-well ProxiPlate used for high-throughput gas sorption; b) ProxiPlate mounted inside the high-throughput gas sorption instrument; and c) birds eye view of the sealed sample chamber of the high-throughput gas sorption instrument.

High-throughput thermal gas sorption studies were carried out on the four glass samples,  $a_g\mathbf{RCC3}$ ,  $a_{tg}\mathbf{RCC3}$ ,  $a_g\mathbf{AT-RCC3}$ , and  $a_g\mathbf{RCC1b}$ . At first,  $\text{CO}_2$  was used as the adsorbate, where the temperature difference was compared between the pre-processed cage, heat-cool glasses, and heat-cool-heat glasses. These initial results found that  $a_g\mathbf{RCC3}$ ,  $a_g\mathbf{AT-RCC3}$ , and  $a_g\mathbf{RCC1b}$  all showed considerably less temperature change compared to the pre-processed cages, where  $a_g\mathbf{AT-RCC3}$  showed almost no temperature change once the background had been deducted (Figure 4.20). However,  $a_g\mathbf{RCC3}$  and  $a_g\mathbf{RCC1b}$  did show minor temperature changes with approximately  $0.5\text{ }^\circ\text{C}$  change from the baseline. Both glasses, *i.e.*, the glass from the heat-cool process, and the sample reheated above the  $T_g$  in the heat-cool-heat process, showed little variation from one another, demonstrating the loss of porosity and/or the inaccessibility to the internal cavity of the cages. The behaviour of  $a_{tg}\mathbf{RCC3}$  demonstrated some positive results compared to the other glasses - both the heat-

cool and heat-cool-heat foamed glasses showed a greater temperature change of approximately 2 °C, versus the pre-processed cage which exhibited a temperature change of approximately 1.2 °C. The foamed glass was then tested with a range of additional probe gases which included CH<sub>4</sub>, Xe, and nC<sub>4</sub>H<sub>10</sub> (Figure 4.21). These gases were selected because of their different kinetic diameters where CO<sub>2</sub> = 3.3 Å, CH<sub>4</sub> = 3.8 Å, Xe = 3.96 Å, and nC<sub>4</sub>H<sub>10</sub> = 4.6 Å. With all probe gases, the foamed glass and the reheated foamed glass showed a larger temperature change compared to the pre-processed cage, although the difference in temperature between them decreases on increasing kinetic diameter of the probe gas (Figure 4.20). (Note – samples *a<sub>g</sub>RCC3*, and *a<sub>fg</sub>RCC3* were performed in separate experiments, hence the temperature change for **RCC3** is not identical)

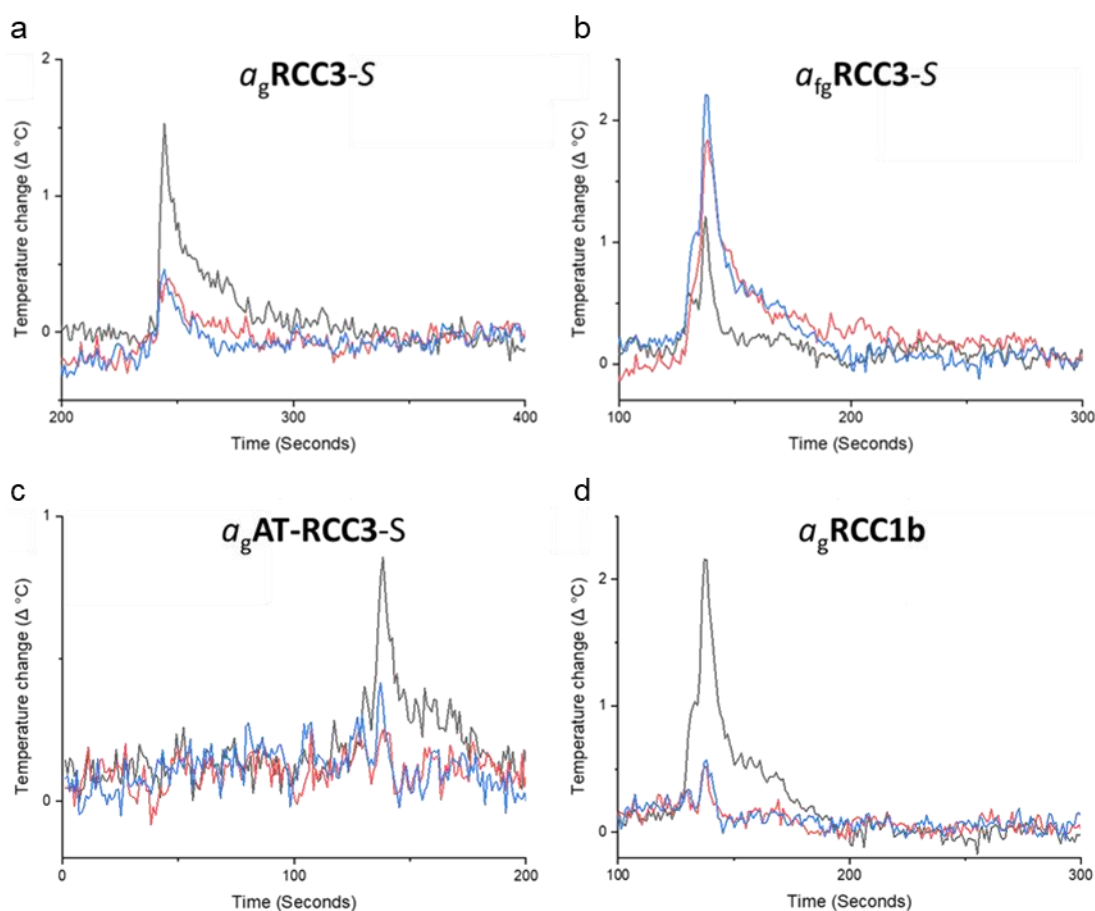


**Figure 4.20** High-throughput thermal CO<sub>2</sub> uptake measurements where amorphous pre-processed cages are in black, melt-quenched glasses in red, and samples reheated above the *T<sub>g</sub>* in blue; a) **RCC3** and *a<sub>g</sub>RCC3*; b) **RCC3** and *a<sub>fg</sub>RCC3*; c) **AT-RCC3** and *a<sub>g</sub>AT-RCC3*; d) **RCC1b** and *a<sub>g</sub>RCC1b*. Only the first CO<sub>2</sub> addition is shown here for clarity.

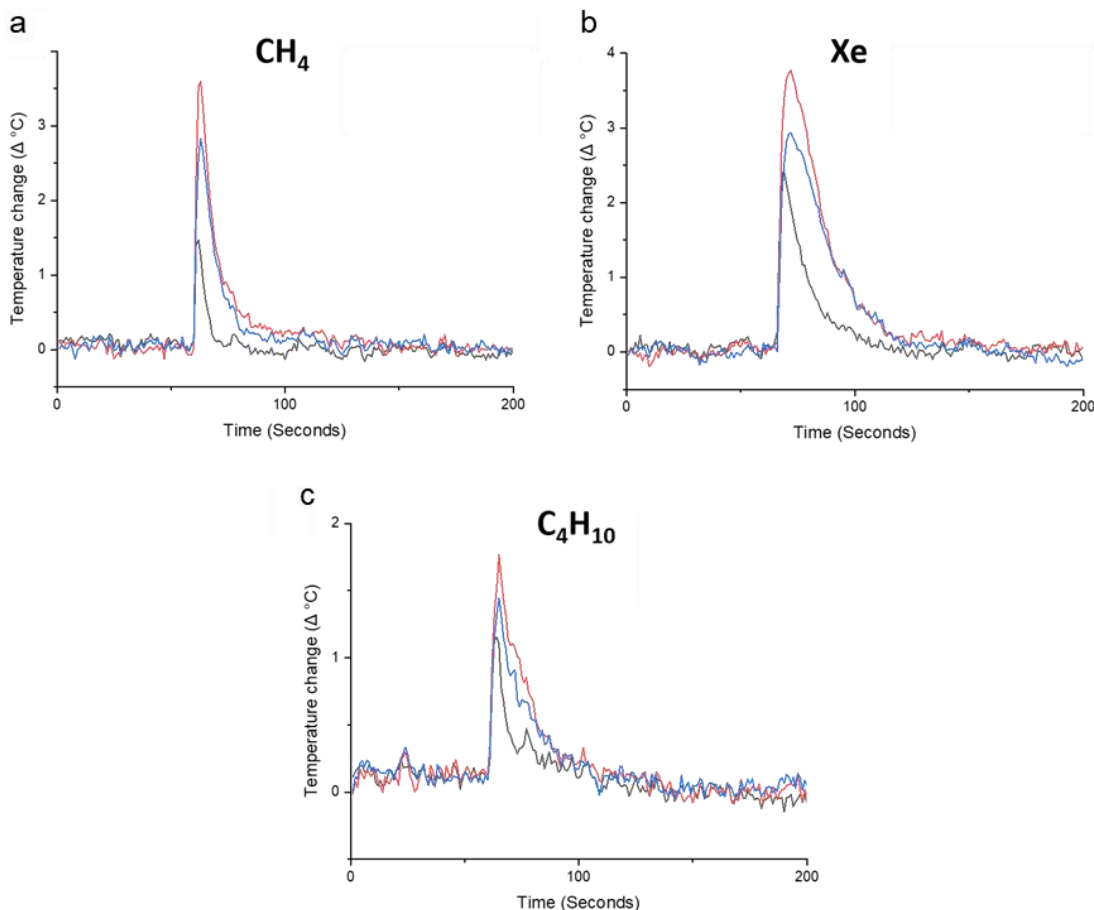


**Figure 4.21** High-throughput gas uptake measurements on **RCC3** and  $a_{T_g}$ **RCC3**, where amorphous pre-processed cages are in black, melt-quenched glasses in red, and samples reheated above the  $T_g$  in blue; a)  $\text{CH}_4$ ; b) Xe; c)  $\text{C}_4\text{H}_{10}$ . Only the first gas addition is shown here for clarity.

After identifying a potentially porous cage glass during the high-throughput thermal gas sorption studies, which found that  $a_{T_g}$ **RCC3** produced a larger temperature change versus the as-made cage, further gas sorption experiments were carried out. As the high-throughput methodology only requires a small amount of sample, in the region of 10 mg, a larger quantity of material had to be processed for analytical gas sorption; this would ideally be in the region of 50-100 mg, and due to the material not being very porous, a higher quantity of sample was preferential. A scale-out approach was therefore taken to obtain enough material for these studies, where DSC pans were filled with ~10 mg of sample and heated to their appropriate temperatures to obtain both  $a_g$ **RCC3** and  $a_{T_g}$ **RCC3**. The data obtained from this scale-out also showed slight variations from the original DSC traces, in particular, the second endotherm of  $a_{T_g}$ **RCC3** could be seen as a wider peak, rather than the sharp peak which is observed in the original DSC trace (Figure 4.22) – these variations are likely due to the scale-out being performed on a different instrument with different DSC pans.



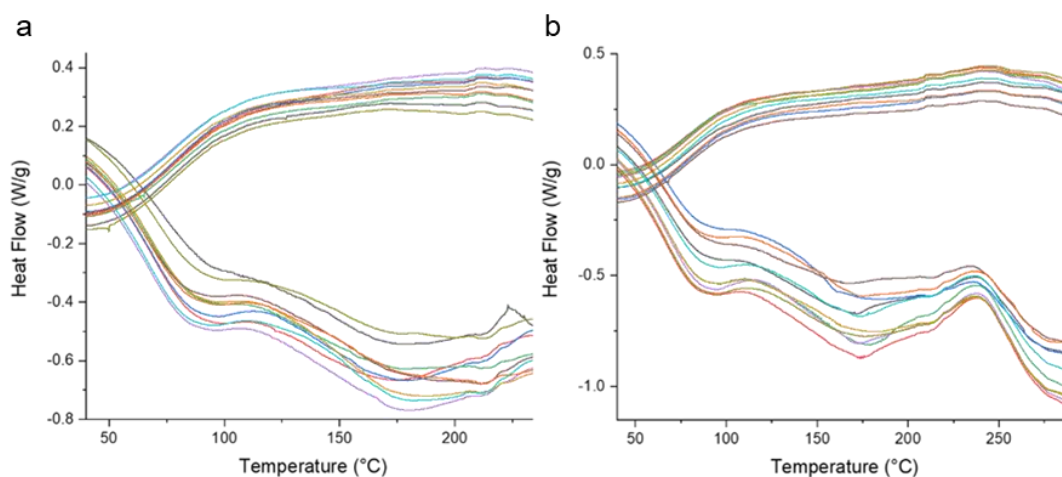


**Figure 4.22** DSC traces of the scale-out of **RCC3** after being subjected to a heat-cool cycle to a) 250 °C ( $a_g\mathbf{RCC3}$ ); b) 300 °C ( $a_{fg}\mathbf{RCC3}$ ).

Gas sorption studies were carried out on **RCC3**,  $a_g\mathbf{RCC3}$ , and  $a_{fg}\mathbf{RCC3}$ , with a variety of gases which included  $\text{N}_2$  (77 K),  $\text{CH}_4$  (273 K),  $\text{CO}_2$  (273 K) and  $\text{Xe}$  (273 K) (Figure 4.23). Given **RCC3** lacks shape-persistence, the collapse of the cage cavity would be expected, which occurs because of the flexibility of the amine bonds. This lack of shape-persistence is likely to follow through to the glass materials too, hence it was unlikely that high surface areas or high gas uptakes would be achieved in the glasses formed from **RCC3**. None of the materials exhibited high BET surface areas, where **RCC3**,  $a_g\mathbf{RCC3}$ , and  $a_{fg}\mathbf{RCC3}$  were 15, 25 and 13  $\text{m}^2 \text{g}^{-1}$ , respectively. Pore size distributions also showed very little variation between the pre-processed cage and the glasses, although  $a_g\mathbf{RCC3}$  displayed the largest pore volume, which is also supported by the isotherms (Figure 4.24). As the uptakes are low it is difficult to draw quantitative conclusions for all gases, although, there are some general trends throughout (Table 4.2). In the cases of  $\text{CO}_2$ ,  $\text{CH}_4$ , and  $\text{N}_2$ , there is a significant increase in gas uptake at 1 bar for  $a_g\mathbf{RCC3}$  versus **RCC3**, with a  $\sim 17$  fold increase for  $\text{CH}_4$ . Xenon was the only gas in this study where  $a_g\mathbf{RCC3}$  did not exceed the gas uptake of the pre-processed **RCC3**. This is perhaps due to the extrinsic porosity that occurs between cage molecules, while the glass likely exists with a higher density, hence less apparent extrinsic porosity is exhibited in this material. Interestingly, the results of the high-throughput thermal gas uptake do not directly correspond to the quantitative gas sorption experiments. This emphasises that the high-throughput methodology should only be used as a screening approach, as differences in colour, well-plate coverage, and specific heat capacity for each sample can affect the measured temperature change.

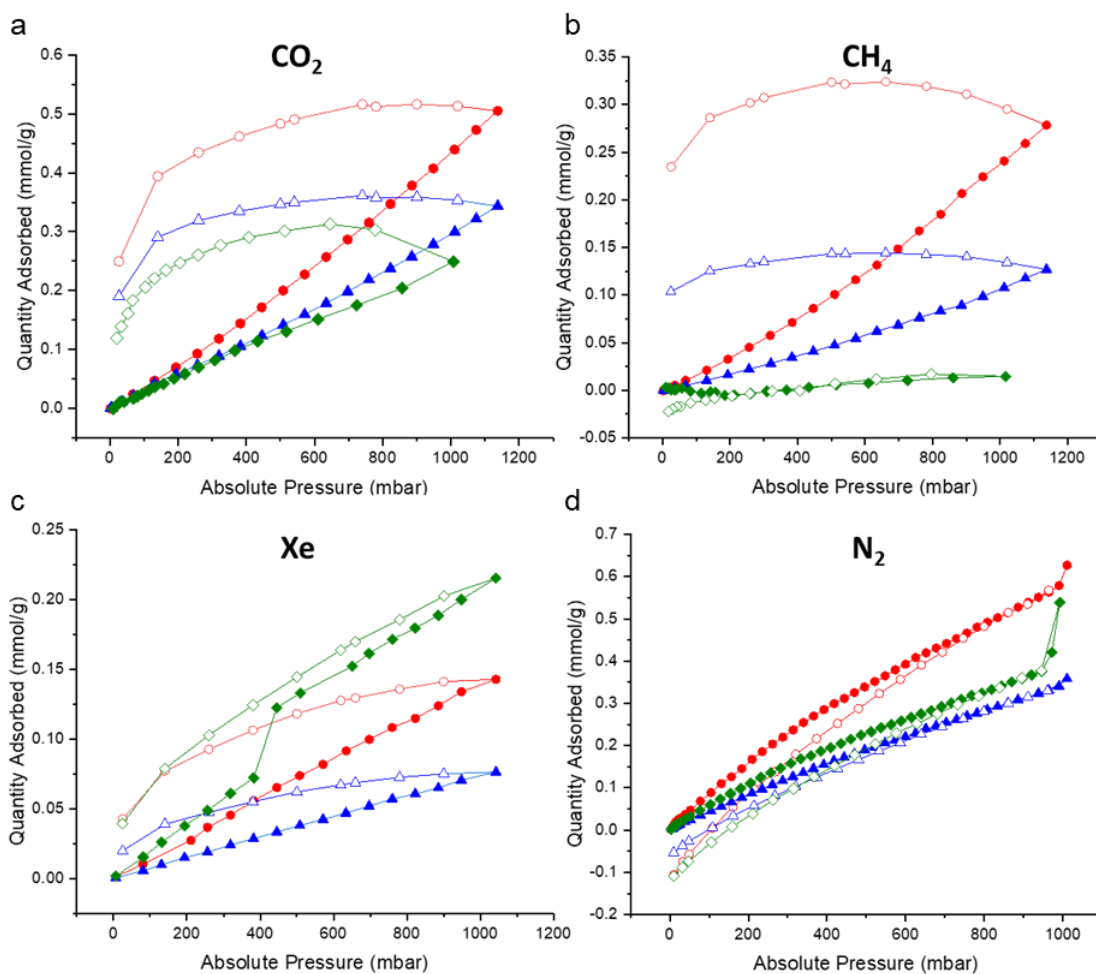


**Figure 4.23** Adsorption (filled) and desorption (empty) isotherms for **RCC3** (green),  $a_g$ **RCC3** (red),  $a_{fg}$ **RCC3** (blue): (a)  $\text{CO}_2$ , 273 K; (b)  $\text{CH}_4$ , 273 K; (c) Xe, 273 K; (d)  $\text{N}_2$ , 77 K.

**Table 4.2** Comparison of gas uptakes of **RCC3**,  $a_g$ **RCC3**, and  $a_{fg}$ **RCC3** with  $\text{CO}_2$  (273 K),  $\text{CH}_4$  (273 K), Xe (273 K), and  $\text{N}_2$  (77 K) at 1 bar.

Material	$\text{CO}_2$ (mmol g <sup>-1</sup> )	$\text{CH}_4$ (mmol g <sup>-1</sup> )	Xe (mmol g <sup>-1</sup> )	$\text{N}_2$ (mmol g <sup>-1</sup> )
<b>RCC3</b>	0.25	0.014	0.22	0.54
$a_g$ <b>RCC3</b>	0.44	0.24	0.14	0.63
$a_{fg}$ <b>RCC3</b>	0.30	0.11	0.088	0.34

While the gas uptake for the glass materials is relatively low, the increasing gas uptake is encouraging as a potential method to produce potential separation materials. These glasses also the proof-of-concept that melt-quenched glasses can be formed from organic cages at relatively low temperatures versus materials such

as PIM-1 which requires temperatures up to 440 °C.<sup>35</sup> The gas uptakes are also comparable to previously reported ZIF glasses. For example,  $a_g\text{RCC3}$  has a  $\text{CO}_2$  uptake of  $9.8 \text{ cm}^3 \text{ g}^{-1}$  (273 K, 1 bar) and a  $\text{CH}_4$  uptake of  $5.4 \text{ cm}^3 \text{ g}^{-1}$ , whereas  $a_g\text{ZIF-62}(\text{Co})$  has a  $\text{CO}_2$  uptake of  $17 \text{ cm}^3 \text{ g}^{-1}$  (273 K, 1 bar)<sup>36</sup> and  $a_g\text{ZIF-76-mblm}$  has a  $\text{CH}_4$  uptake of  $6 \text{ cm}^3 \text{ g}^{-1}$  (273 K, 1 bar).<sup>37</sup>

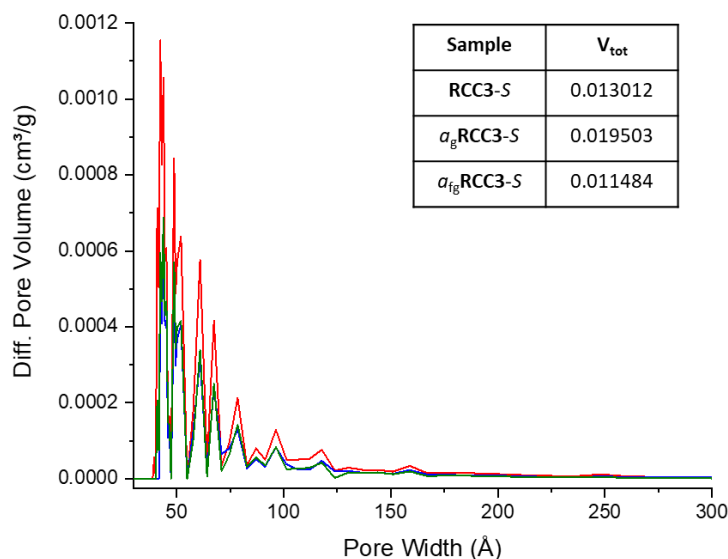


**Figure 4.24** Pore size distribution curves obtained from the  $\text{N}_2$  adsorption branch of the isotherm at 77 K of **RCC3** and glass samples using non-negative regularization model. Red -  $a_g\text{RCC3}$  (prepared at 250 °C), blue -  $a_{fg}\text{RCC3}$  (prepared at 300 °C), and green - **RCC3** (as prepared).

#### 4.4.3 The Curious Case of CC3

As previously mentioned in 4.4.1, **CC3** was part of the initial melting study but was investigated separately due to its different behaviour observed from the other cages screened. While there was another imine-based cage in the screen,  $n\text{C}_5\text{-CC}$ , which was unsuccessful in forming melt-quenched glasses, **CC3** did show early signs of glass formation. However, it was unable to form a liquid prior to decomposition, while for the other four cages in the study, glasses were formed from the liquid state.

When **CC3** was initially prepared, it was found to contain both crystalline and amorphous components, so in order to get a broader understanding of what is occurring with the material, both a crystalline and amorphous sample of **CC3** were prepared. In this portion of the chapter, *R,R*-CHDA was used to synthesise **CC3-R**, but will be referred to as **CC3** throughout. Amorphous **CC3** has previously been reported and can be prepared by freeze-drying in chloroform – the amorphous material was shown to exhibit increased gas uptake compared to crystalline **CC3**,

which arises from inefficient packing creating more extrinsic porosity between molecules, versus that of the window-to-window arrangement in crystalline **CC3**.<sup>38</sup>

**CC3** was prepared by a known layering procedure, which is able to produce a highly crystalline material. PXRD analysis confirmed that a crystalline material had been isolated, which was compared to a simulated diffraction pattern from single crystal data of **CC3**( $\alpha$ ) (Figure 4.25).<sup>12</sup> Amorphous **CC3** was also prepared from the same batch of material, where crystalline **CC3** was dissolved in chloroform at an approximate concentration of 10 mg mL<sup>-1</sup>. Small volumes (1-2 mL) of this solution was added to 14 mL vials, which was ample enough solution to cover the base of the vial, before freezing in liquid nitrogen. Overloading the vials resulted in the chloroform being removed too slowly, allowing crystallisation to occur, whereas a thin layer allowed for sufficiently fast removal of solvent to prevent crystallisation. This process was repeated numerous times to obtain enough material for full analysis, where each sample was analysed by PXRD to ensure amorphisation had occurred before combining the bulk material (Figure 4.25). SEM data was also used in conjunction with the PXRD to confirm crystallinity and amorphisation of **CC3**, which is discussed later in the chapter.

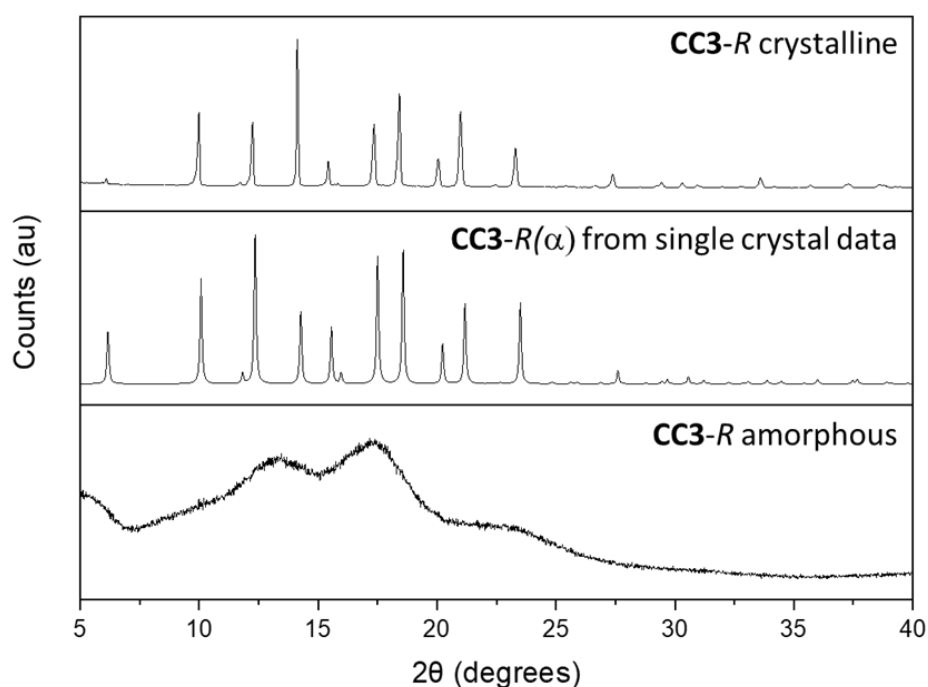


**Figure 4.25** Stacked PXRDs of **CC3** samples: **CC3** crystalline (top); **CC3** simulated powder pattern from single crystal data (middle, CCDC code 720850); and **CC3-R** amorphous (bottom).

Crystalline **CC3** was then dried in a vacuum oven at 100 °C until no significant mass loss was observed, whereas amorphous **CC3** was sufficiently dry from freeze-drying,

both of which was confirmed by TGA analysis (Figure 4.26). In both cases, the TGA traces were featureless, up to the decomposition temperatures which varied slightly depending on whether it was crystalline ( $T_d = 425\text{ °C}$ ) or amorphous ( $T_d = 400\text{ °C}$ ), confirming that the samples were free of any additional solvent, hence any features in the subsequent DSC traces are not a result of solvent loss.

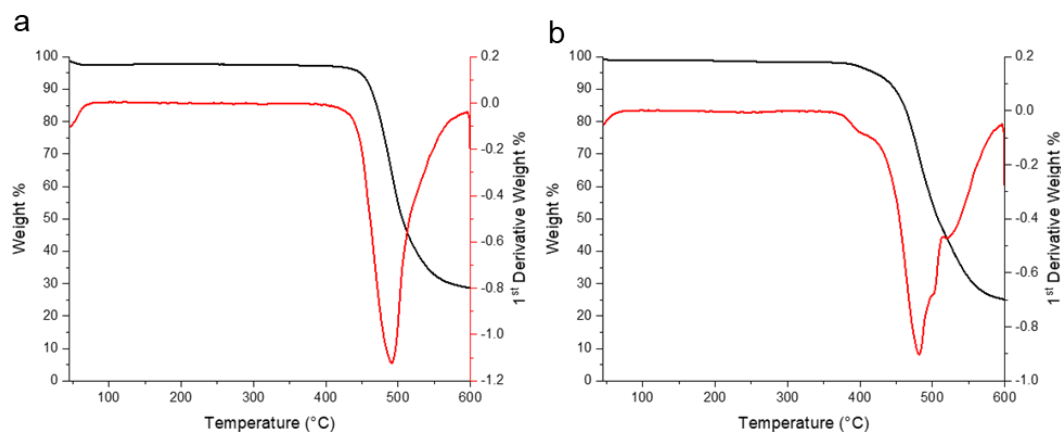


**Figure 4.26** TGA traces (black) and the corresponding 1<sup>st</sup> derivative (red) of desolvated **CC3** samples, where a) crystalline **CC3** and b) amorphous **CC3**.

DSC studies were then carried out on the desolvated crystalline **CC3** and amorphous **CC3** samples (Figure 4.27). In both cases, samples were heated to 380 °C, which is at least 20 °C below their thermal decomposition temperatures, and a variety of different features were observed. The first feature observed in the crystalline **CC3** sample was a broad endotherm at 175 °C, followed by a large broad exotherm at approximately 320 °C, on the upscan. The cooling downscan showed no significant features with a steady gradient from 380 °C down to ambient temperature. When performed with a heat-cool-heat cycle there were also no features identified in the second upscan, including no additional exotherms. With amorphous **CC3**, similar features were also observed. However, the first endotherm occurs at a slightly lower temperature, at approximately 160 °C, and is much sharper than the crystalline alternative. In addition, the exotherm also behaves differently, where it appears that there are two separate exotherms which merge into one, the first with a centre point at 310 °C and the maximum on the 'second' peak at 345 °C. The cooling downscan in this case did display a change in gradient, indicative of a glass transition which occurs at 250 °C. This glass transition can also be seen on the second upscan in the heat-cool-heat cycle, but again, there were no additional exotherms.

To investigate what was occurring with each of the DSC features, further experiments were performed where the temperatures were set to before and after the identified

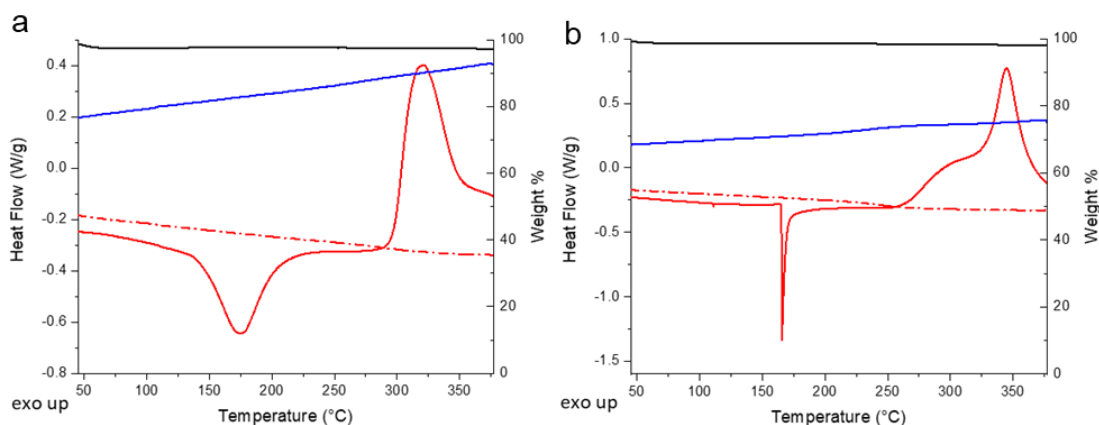


**Figure 4.27** DSC traces of desolvated **CC3** samples subjected to heat-cool-heat (HCH) cycles to 380 °C, with corresponding TGA curves (black). The initial upscan is shown as a solid red line, downscan as a blue line, and second upscan as a dashed red line: a) crystalline **CC3**; b) amorphous **CC3**.

features from the traces. Further analysis was then carried out using  $^1\text{H}$  NMR and infrared (IR) spectroscopy, optical images, and PXRD.  $^1\text{H}$  NMR spectroscopy was performed on each sample after heating crystalline **CC3** in DSC pans to the following temperatures: 120 °C, 220 °C, 270 °C, and 380 °C, where the 380 °C was also performed as a heat-cool and a heat-cool-heat (Figure 4.28); and amorphous **CC3** to the following temperatures: 140 °C, 190 °C, 250 °C, 310 °C, and 380 °C, where the 380 °C was also performed as a heat-cool and a heat-cool-heat (Figure 4.29). No change in crystalline **CC3** was observed in the  $^1\text{H}$  NMR spectra up to 270 °C, where the cage is clearly still present. However, once the samples are heated beyond the exotherm observed at 320 °C, the sample became completely insoluble in  $\text{CDCl}_3$ . This is possibly due to the formation of an insoluble polymer. The behaviour of amorphous **CC3** also followed a similar trend, where before and after the initial endotherm, cage is still clearly present in the  $^1\text{H}$  NMR spectra. The first difference becomes apparent when the sample was heated to just before the first exotherm, observed at 310 °C. Here, the sample started to become insoluble, though the small quantity that dissolved in  $\text{CDCl}_3$  was still representative of **CC3**. Finally, just like how the crystalline material became insoluble, the amorphous sample also became insoluble in both the heat-cool and heat-cool-heat cycles to the higher temperature, where no traces of cage could be observed in the spectra. The combination of the formation of insoluble materials, and the exothermic features in the DSC traces, suggests the formation of a cross-linked extended polymeric material, with the latter being known to be indicative of cross-linking.

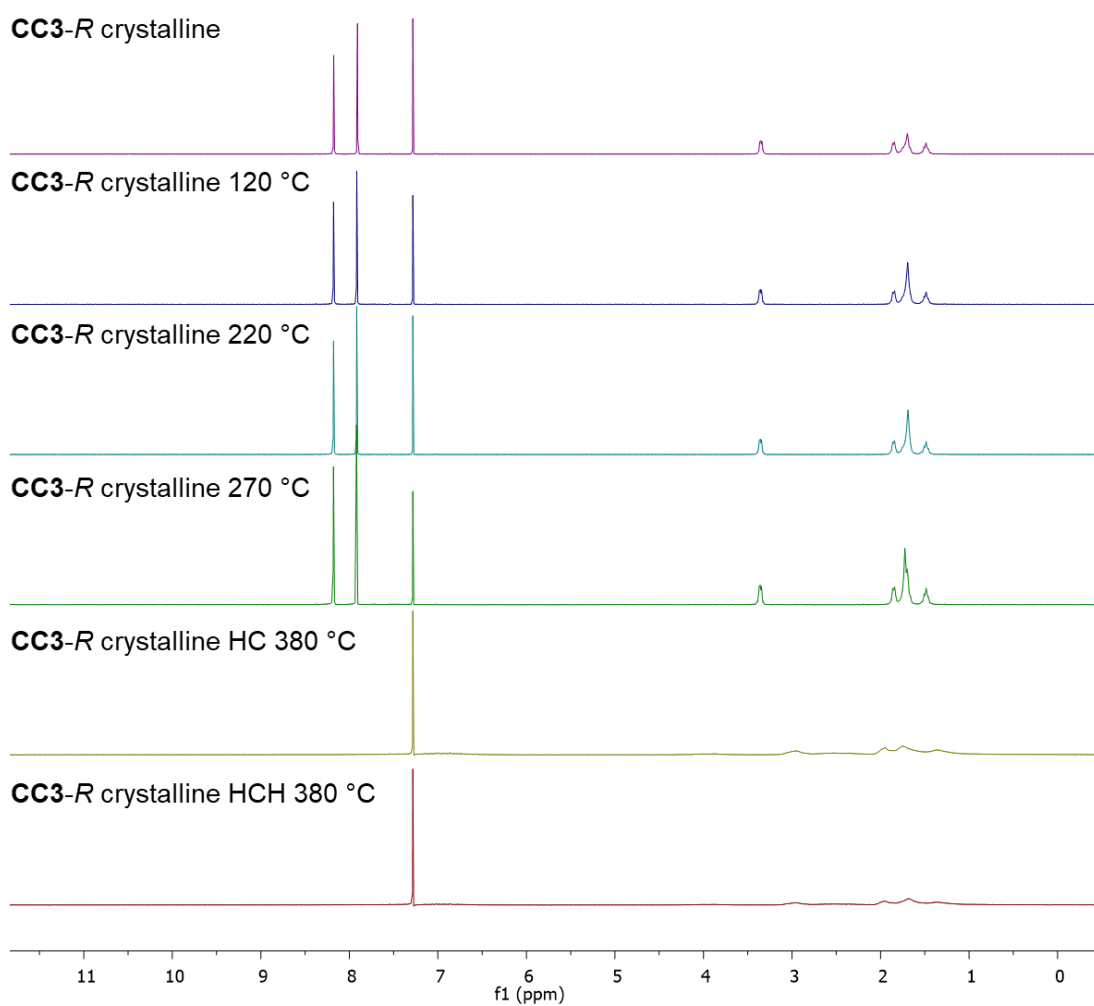


**Figure 4.28** Stacked <sup>1</sup>H NMR spectra of **CC3-R** crystalline (CDCl<sub>3</sub>). From top to bottom, **CC3-R** crystalline, heated to 120 °C, 220 °C, 270 °C, heat-cool (HC) cycle to 380 °C, and heat-cool-heat (HCH) cycle to 380 °C.

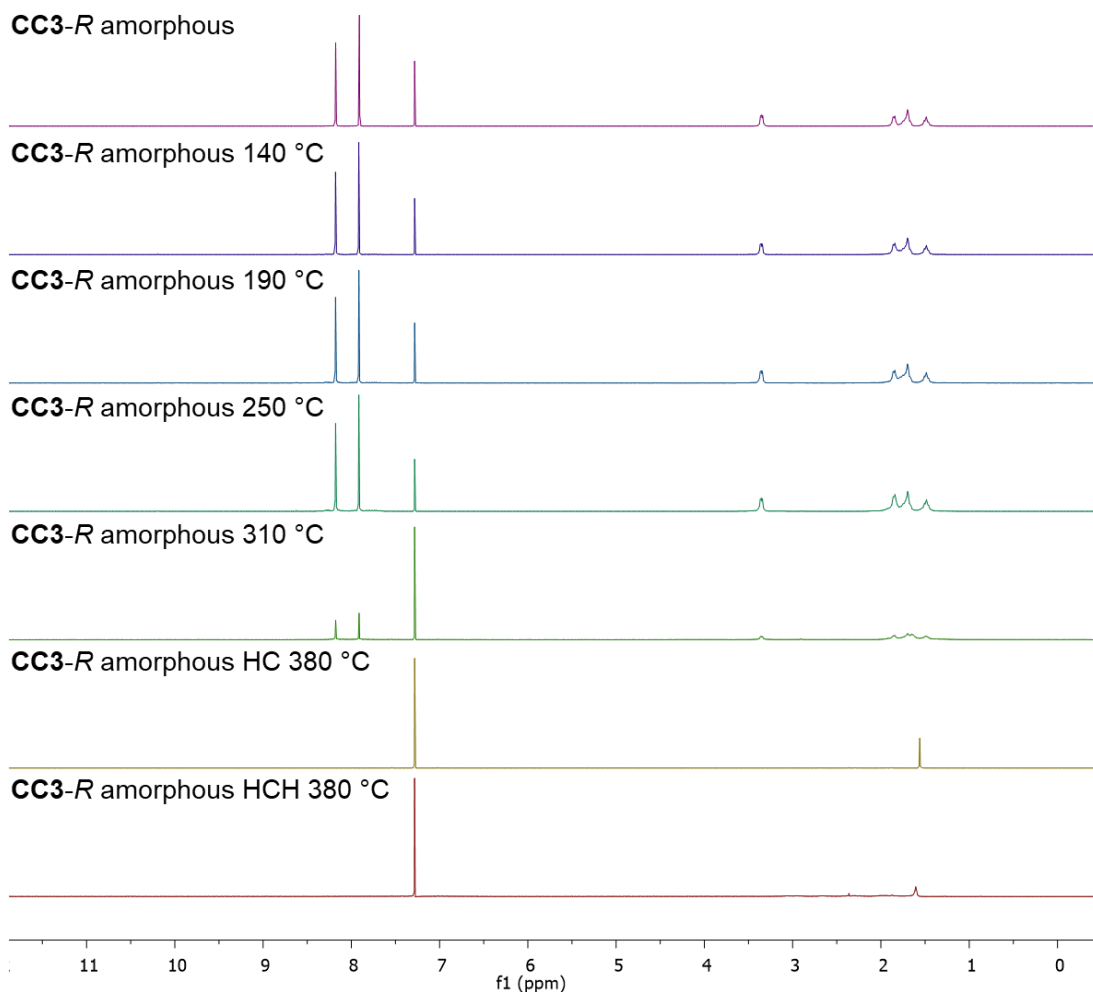


**Figure 4.29** Stacked  $^1\text{H}$  NMR spectra of **CC3-R** amorphous ( $\text{CDCl}_3$ ). From top to bottom, **CC3-R** amorphous, heated to 140 °C, 190 °C, 250 °C, 310 °C, heat-cool (HC) cycle to 380 °C, and heat-cool-heat (HCH) cycle to 380 °C.

Infrared (IR) spectroscopy provided a little more insight on what is happening when these materials are heated at elevated temperatures (Figures 4.30-4.31). **CC3** itself has very few functional groups, with aromatic rings, imines, and cyclohexane functionality, which makes the IR spectrum very useful for identifying any changes in the material. In the IR spectrum of **CC3**, two signals can be observed at  $2924\text{ cm}^{-1}$  and  $2852\text{ cm}^{-1}$ , which correspond to the C-H stretch on the cyclohexyl ring, and can also be seen in (1*R*,2*R*)-cyclohexane-1,2-diamine (CHDA). The imine C=N functionality at  $1642\text{ cm}^{-1}$ , can also be observed in an analogous control molecule (formed by the reaction of TFB with three cyclohexanamines), and stretches at  $1450\text{ cm}^{-1}$  and  $1347\text{ cm}^{-1}$ , which are likely a combination of C-H stretches from the aromatic ring and CHDA along with C-N stretches. In both cases the IR spectra are very similar. On heating to just before the exotherm, all of the identified stretches are at the same wavenumber, which include those at  $2924\text{ cm}^{-1}$ ,  $2852\text{ cm}^{-1}$ ,  $1642\text{ cm}^{-1}$ ,  $1598\text{ cm}^{-1}$ ,



1450  $\text{cm}^{-1}$  and 1347  $\text{cm}^{-1}$ . When amorphous **CC3** is heated to the midpoint of the first observed exotherm, there is a slight change in the material, with an increase in absorbance at 1598  $\text{cm}^{-1}$ , although the other peaks are still apparent. Once the materials have been heated beyond the exotherm however, the CDHA stretches at 2924  $\text{cm}^{-1}$  and 2852  $\text{cm}^{-1}$  are still present, but the imine stretch at 1642  $\text{cm}^{-1}$  is no longer present and stretches at 1598  $\text{cm}^{-1}$  and 1347  $\text{cm}^{-1}$  become far more prominent.

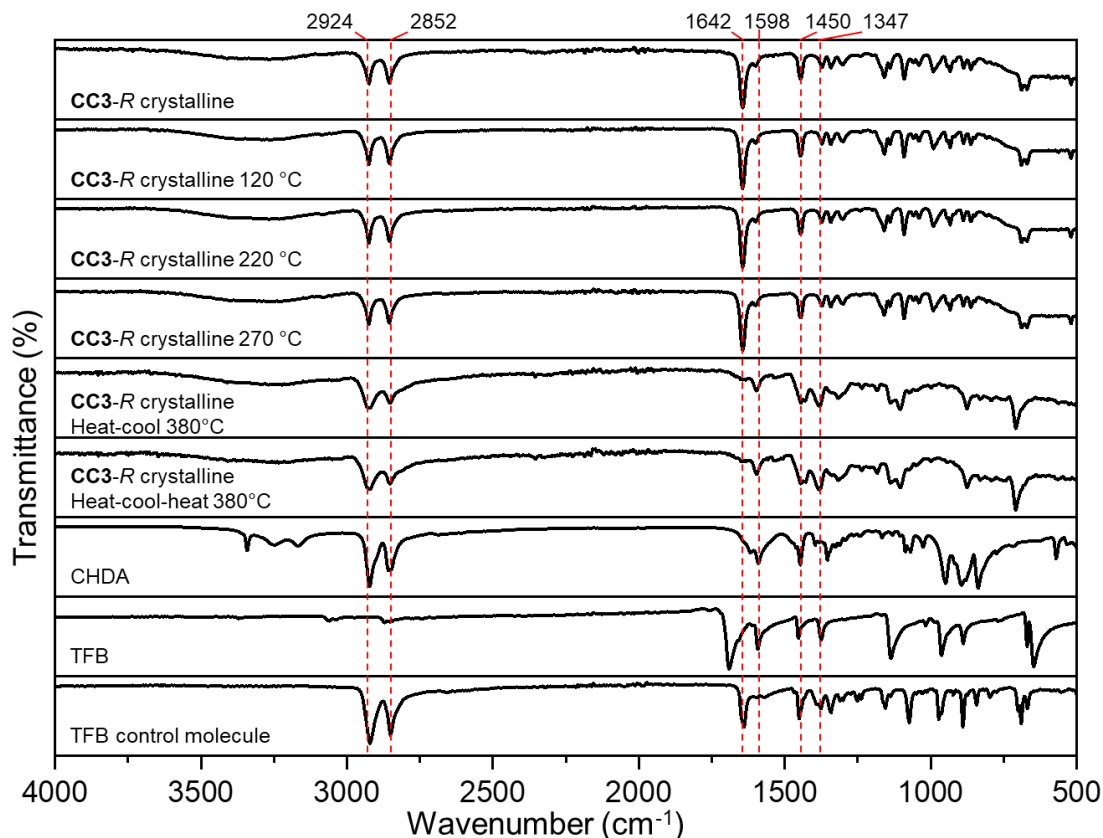


**Figure 4.30** Stacked FTIR spectra of crystalline **CC3** and starting materials. From top to bottom, **CC3-R** crystalline, heated to 120 °C, 220 °C, 270 °C, heat-cool cycle to 380 °C, heat-cool-heat cycle to 380 °C, (1*R*,2*R*)-cyclohexane-1,2-diamine (CHDA), 1,3,5-triformylbenzene (TFB), and a TFB control molecule (TFB combined with cyclohexanamine to form benzene-1,3,5-triyl)tris(*N*-cyclohexylmethanimine)).

The loss of the C=N stretch suggests that the imine functionality has been lost, which could occur through either a reversible reaction back to its starting materials, or if the material has undergone further intra- or intermolecular reactions with either itself or other molecules (potentially free gas molecules). The first possibility seems unlikely since CHDA or TFB is not observed in the  $^1\text{H}$  NMR spectra. There are also no indications that an aldehyde is being formed in the IR spectra, as there are no C=O stretches in the aldehyde region around 1700  $\text{cm}^{-1}$ . The second possibility also seems unlikely, given the samples are heated in sealed DSC pans which are under a flow of

$N_2$ , and there are no traces of impurities or any other compounds in the  $^1H$  NMR spectra. The more likely possibility is an imine cross-linking reaction. This could be a [2+2] cycloaddition of the imines between neighbouring cage molecules or an intramolecular reaction within the same cage molecule, resulting in the loss of the imine functionality, although the former would more likely explain the formation of insoluble material (Figure 4.32). The IR spectra would also support this theory with the increase in absorbance at  $1347\text{ cm}^{-1}$ , where if a [2+2] cycloaddition is occurring then there would be more C-N stretches within the material. In addition, there are no new peaks that would indicate the formation of this cycloaddition as the product would be a tertiary amine and no N-H stretch would be visible.

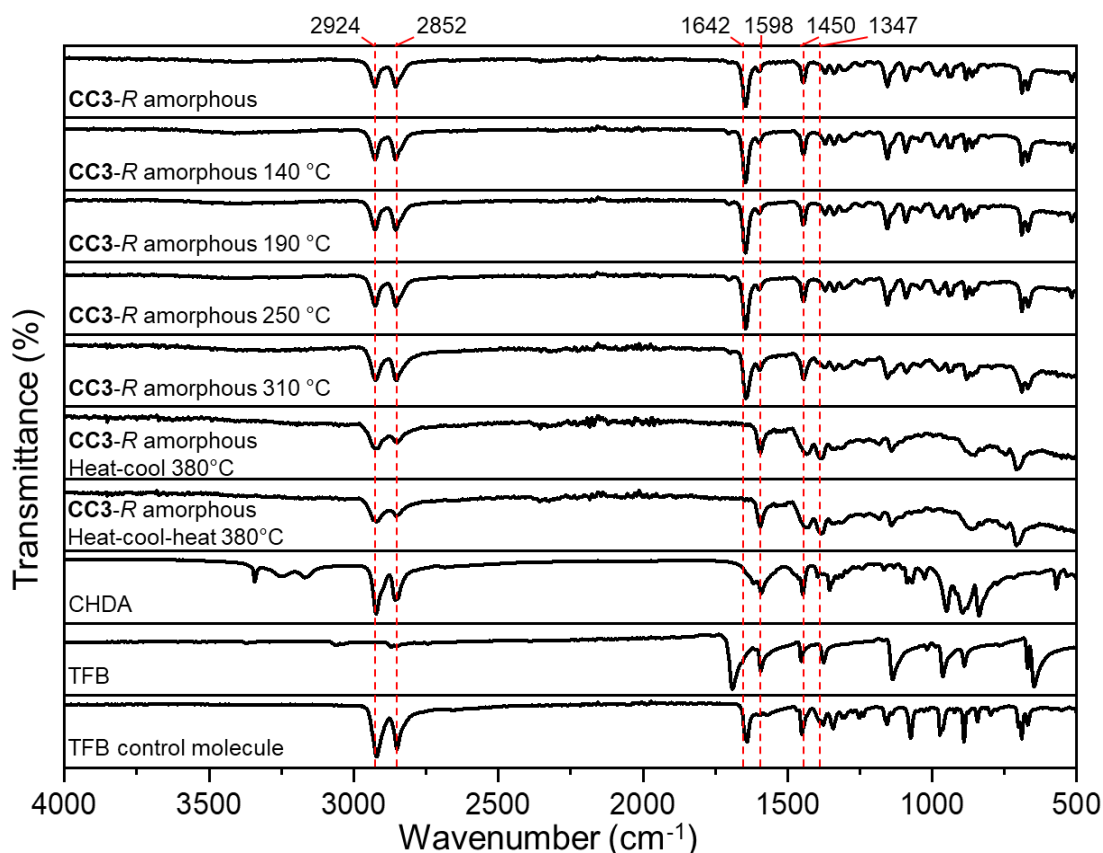


**Figure 4.31** Stacked FTIR spectra of amorphous **CC3** and starting materials. From top to bottom, **CC3-R** amorphous, heated to  $140\text{ }^\circ\text{C}$ ,  $190\text{ }^\circ\text{C}$ ,  $250\text{ }^\circ\text{C}$ ,  $310\text{ }^\circ\text{C}$ , heat-cool cycle to  $380\text{ }^\circ\text{C}$ , heat-cool-heat cycle to  $380\text{ }^\circ\text{C}$ , (1*R*,2*R*)-cyclohexane-1,2-diamine (CHDA), 1,3,5-triformylbenzene (TFB), and a TFB control molecule (TFB combined with cyclohexanamine to form benzene-1,3,5-triyl)tris(*N*-cyclohexylmethanimine)).

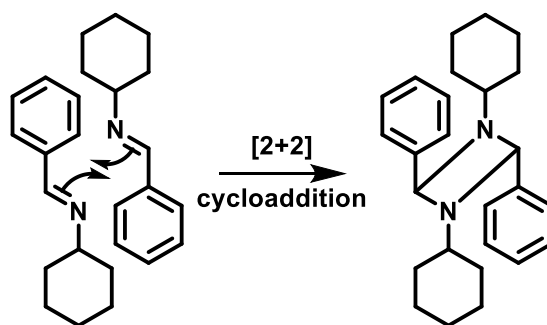


**Figure 4.32** Possible reaction mechanism of **CC3** units for the [2+2] cycloaddition occurring upon heating **CC3** to 380 °C.

Analysis of the materials by PXRD also uncovered some unexpected results. As with the other types of analysis of these materials, very little difference was observed with the crystalline material on heating beyond the initial endotherm up to 270 °C, with **CC3**( $\alpha$ ) seen throughout without the addition of any new signals, although there are changes in signal intensities. However, once the material has been heated beyond the observed exotherm, the PXRD pattern changes dramatically, with **CC3**( $\alpha$ ) no longer apparent (Figure 4.33). This pattern is recognisable in both the heat-cool and heat-cool-heat cycles, indicating that an additional upscan with heating does not affect the material further. The resulting material has a PXRD pattern that contains three distinct low angle signals at 6, 15, and 18°, almost resembling those that are produced by covalent-organic frameworks and polymers. Optical images were also taken at each temperature and are shown against their corresponding PXRD pattern, where there is a gradual colour change up to 270 °C, from a colourless to off-white, whereas the heat-cool and heat-cool-heat to 380 °C forms a yellow powder and a light brown powder, respectively. The loss of crystallinity and formation of a species with low angle diffraction patterns also supports the intermolecular cross-linking theory, rather than an intramolecular species which in theory should maintain a similar PXRD pattern to the starting material as there would only be a small change to the internal cavity, like that of **FT-RCC3** and **AT-RCC3** which maintain similar PXRD patterns with **RCC3**.<sup>24</sup>

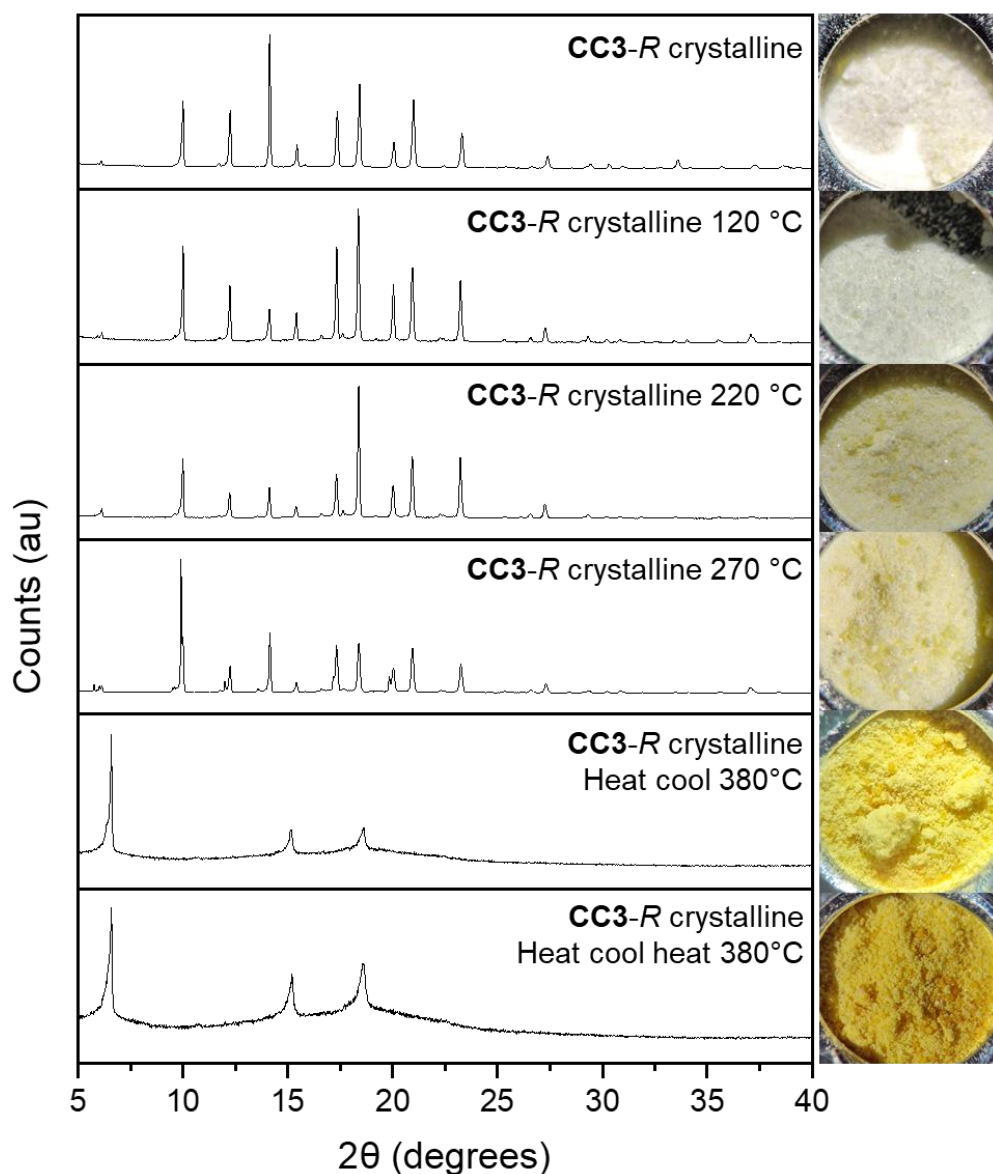


**Figure 4.33** Stacked PXRD patterns and optical images of crystalline **CC3** heated to different temperatures. From top to bottom, **CC3** crystalline, heated to 120 °C, 220 °C, 270 °C, heat-cool (HC) cycle 380 °C, and heat-cool-heat (HCH) cycle 380 °C.

Unfortunately, very little information could be extracted from the PXRD patterns of the amorphous **CC3** samples, other than in this case the material remains amorphous after increasing the material to all temperatures, which is consistent with the observed glass transitions after heating to 380 °C (Figure 4.34). Visually, the amorphous **CC3** existed as colourless flakes after freeze drying, which were maintained throughout. Colour changes could also be seen, similar to those for crystalline **CC3**, although the colour changes were more dramatic, forming yellow flakes after heating to 250 °C, orange flakes at 310 °C, and brown material after heating to 380 °C.

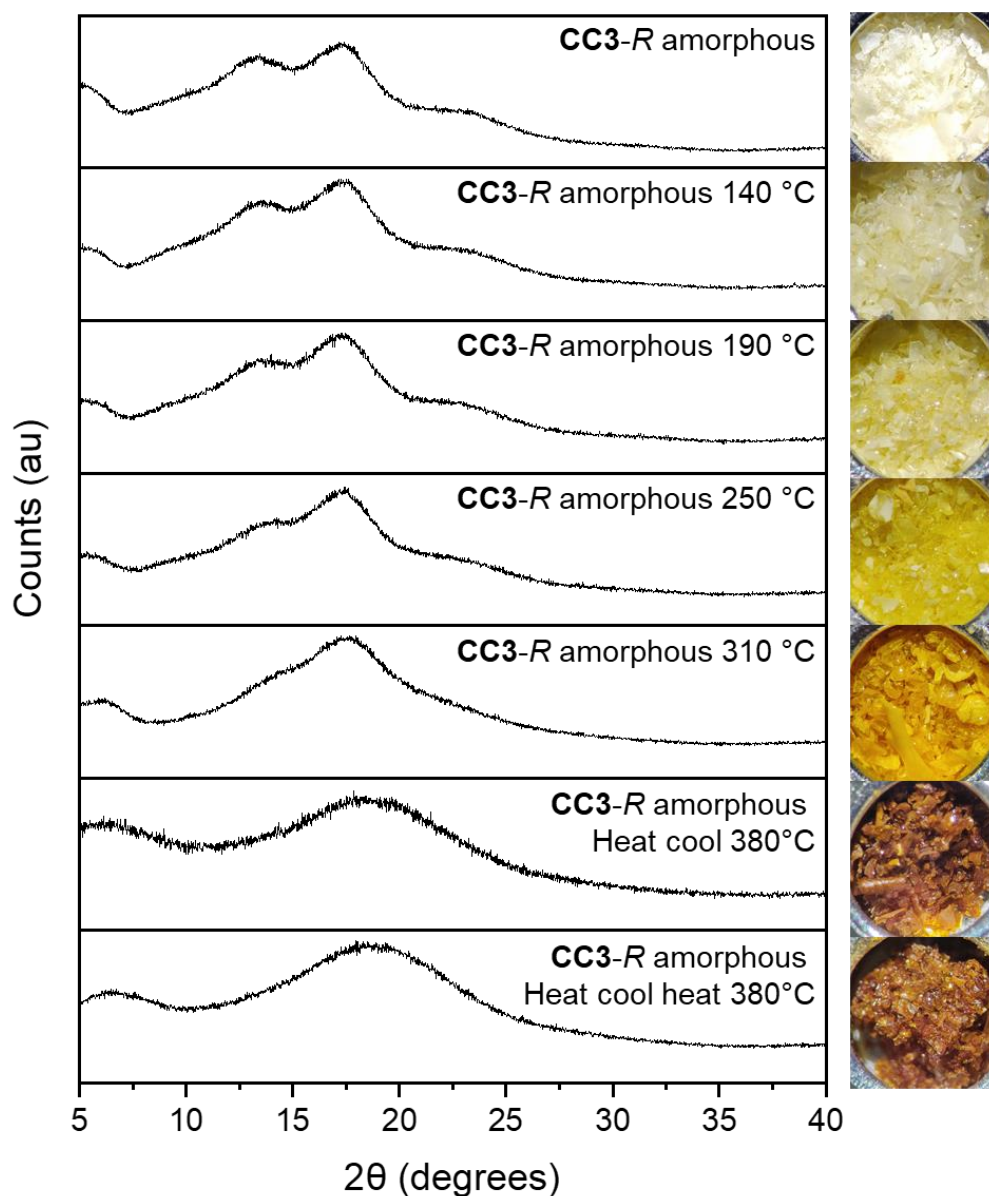


**Figure 4.34** Stacked PXRD patterns and optical images of amorphous **CC3** heated to different temperatures. From top to bottom, **CC3-R** amorphous, heated to 140 °C, 190 °C, 250 °C, 310 °C, heat-cool (HC) cycle to 380 °C, heat-cool-heat (HCH) cycle to 380 °C.

Scanning electron microscopy (SEM) was also utilised to gather insight into whether there were physical transformations of the bulk material once they had been heated past the exotherms to 380 °C (Figure 4.35). Crystalline **CC3** forms octahedral crystallites, which can be observed at 8.5 kx magnification with sizes in the region of 10  $\mu\text{m}$ . Once the material has been heated to 380 °C, the octahedral crystallites are still maintained and can be observed with well-defined edges and little variation in size. This shows that the internal structure of the crystallites is changing when exposed to these conditions, giving rise to different crystal lattice planes, and hence the variation in the observed PXRD pattern. This also supports the theory of

intermolecular cross-linking, as the individual cages pack together in a window-to-window configuration in **CC3**( $\alpha$ ), and conversion from a single molecular species to a species with long range order can occur while the crystal topology remains unchanged. As expected, for amorphous **CC3** there are no well-defined crystallites and the sample appears as much larger, poorly defined flakes, which also translates to the material once it has been heated past the exotherm to 380 °C.

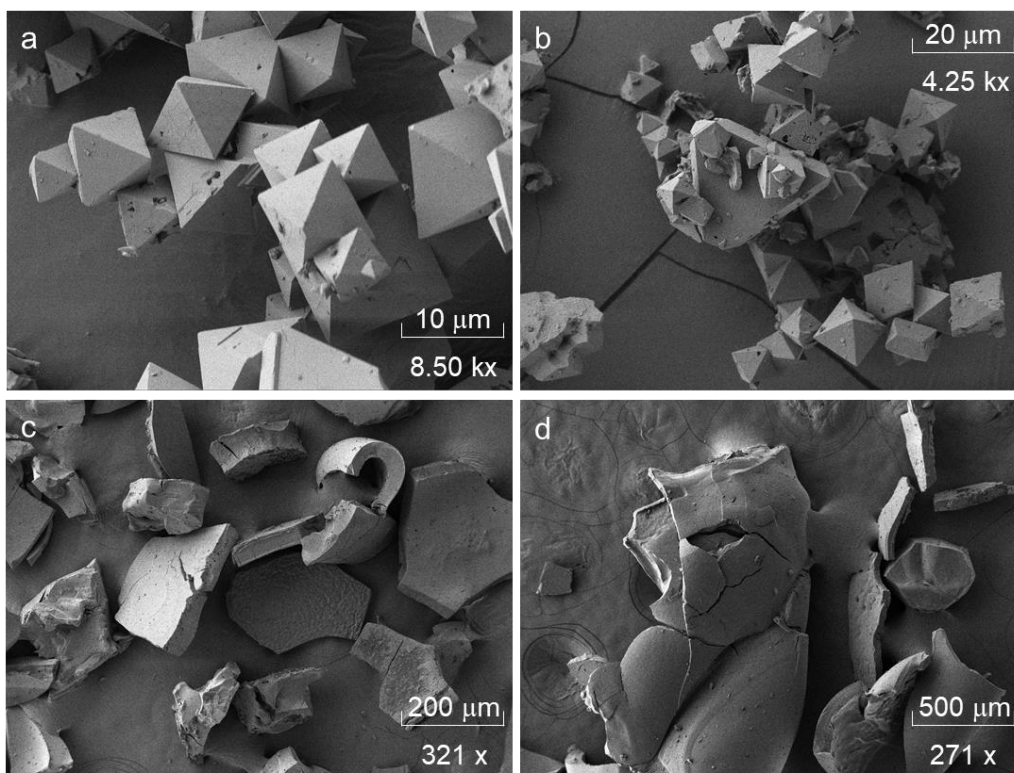


**Figure 4.35** SEM images of **CC3**, where a) **CC3** crystalline; b) **CC3** crystalline after a heat-cool cycle to 380 °C; c) **CC3** amorphous; d) **CC3** amorphous after a heat-cool cycle to 380 °C.

To investigate whether these new materials, **CC3<sub>M</sub>** (insoluble material from crystalline **CC3** after HC to 380 °C) and **a<sub>g</sub>CC3** (amorphous **CC3** after HC to 380 °C), had any different gas sorption properties to **aCC3** and **CC3**( $\alpha$ ), a scale-out approach was used like in the previous study where multiple DSC sequences were performed to obtain approximately 100 mg of sample. In the process of performing the ~10 runs for each sample of amorphous **CC3** and crystalline **CC3**, in both cases, there were several samples which did not exhibit the initially observed endotherm in the DSC trace. When the DSC pans were removed from the sample holder, it could be seen that several of the pan lids had inflated or were still flat like when they were first sealed (Figure 4.36). These pans were then compared to the DSC traces, and a general trend was found where those which had flat pan lids corresponded with those with

small endothermic features, and those with inflated lids corresponded to those with larger endothermic features. This suggests that the endothermic feature observed in the initial DSC studies of amorphous **CC3** and crystalline **CC3** is due to some gas being expelled from the material.

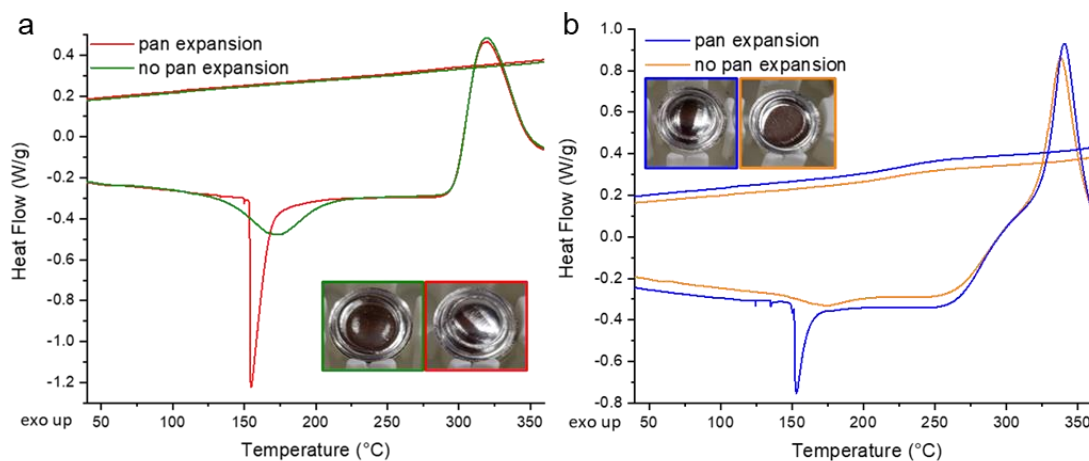


**Figure 4.36** DSC traces of **CC3** subjected to a heat-cool cycle to 380 °C. Traces in both cases are from the bulk of their respective material. a) crystalline **CC3**, where red shows a large endotherm and pan expansion, and green shows a smaller endotherm with a flat pan lid; b) amorphous **CC3**, where blue shows a large endotherm with pan expansion, and orange shows a smaller endotherm and no pan expansion.

Gas sorption experiments for the amorphous and crystalline **CC3** followed the trends that are previously reported for this material, in that the amorphous material generally demonstrated higher gas uptake than the crystalline counterpart (Figure 4.37, Table 4.3).<sup>37</sup> In the initial report of this behaviour, they conclude that this occurs because inefficient packing leads to more extrinsic porosity, hence the material has enhanced uptake. This can be observed for CO<sub>2</sub>, H<sub>2</sub>, and N<sub>2</sub>, although different behaviour is seen with CH<sub>4</sub>. This could be explained by the inefficient packing creating regions of empty space, which may have openings smaller than the kinetic diameter of CH<sub>4</sub>, which is larger than the other three probe gases, and hence the CH<sub>4</sub> is unable to enter these cavities making the apparent gas uptake lower than that of the crystalline material.

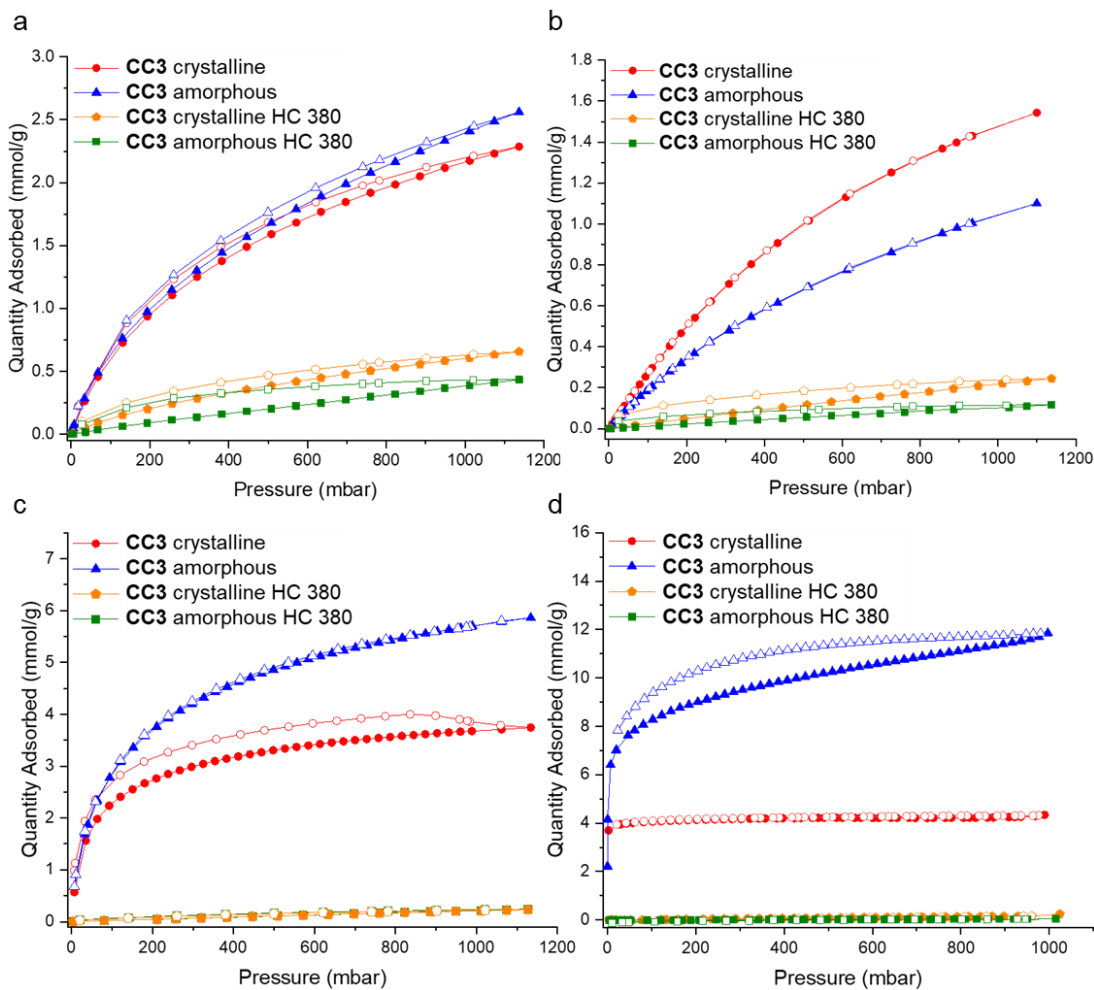


**Figure 4.37** Adsorption (filled) and desorption (empty) isotherms of **CC3** crystalline (red), **CC3** amorphous (blue), **CC3** crystalline heat-cool 380 °C (orange), and **CC3** amorphous heat-cool 380 °C (green), where a) CO<sub>2</sub> isotherm at 273 K; b) CH<sub>4</sub> isotherm at 273 K; c) H<sub>2</sub> isotherm at 77 K; d) N<sub>2</sub> isotherm at 77 K.

Both the **CC3<sub>IM</sub>** and **a<sub>g</sub>CC3** showed a significant decrease in gas uptake. With measurements performed at 273 K, both materials were able to adsorb some quantity of gas, although substantially lower than that of the pre-processed **aCC3** and **CC3(α)**, where the **CC3<sub>IM</sub>** material showed a decrease of 72% and 85% for CO<sub>2</sub> and CH<sub>4</sub>, respectively. The **a<sub>g</sub>CC3** material showed an even larger decrease of 84% and 90% for CO<sub>2</sub> and CH<sub>4</sub>, respectively. Both materials also performed extremely poorly for H<sub>2</sub> and N<sub>2</sub>, with little to no gas uptake observed, whereas these were the highest uptakes for the pre-processed materials, **aCC3** and **CC3(α)**. A decrease was observed in the heated crystalline material of 94% for both gases, and a decrease of 96% and >99% for the heated amorphous material for H<sub>2</sub> and N<sub>2</sub>, respectively. These results also support the possibility of intermolecular cross-linking – if cross-linking has occurred as proposed, then the free space between the individual cages could be occupied or



there could be restricted cavity access, making the material impermeable to gas and the uptake significantly reduced.

**Table 4.3** Comparison of gas uptakes of crystalline **CC3** (red), amorphous **CC3** (blue), crystalline **CC3** heat-cool (HC) 380 °C (orange), and amorphous **CC3** heat-cool (HC) 380 °C with CO<sub>2</sub> (273 K), CH<sub>4</sub> (273 K), H<sub>2</sub> (273 K), and N<sub>2</sub> (77 K) at 1 bar.

Material	CO <sub>2</sub> (mmol g <sup>-1</sup> )	CH <sub>4</sub> (mmol g <sup>-1</sup> )	H <sub>2</sub> (mmol g <sup>-1</sup> )	N <sub>2</sub> (mmol g <sup>-1</sup> )
<b>CC3-R</b> crystalline	2.17	1.47	3.66	4.34
<b>CC3-R</b> amorphous	2.41	1.04	5.70	11.85
<b>CC3-R</b> <sub>IM</sub>	0.60	0.21	0.21	0.24
<b>a<sub>g</sub>CC3-R</b>	0.38	0.10	0.20	0.04

While the effect of heating both **aCC3** and **CC3(α)** is not completely understood at this stage, the experimental data points towards cross-linking between cage molecules, through the loss of imine bonds observed in the IR spectra. The disappearance of the characteristic **CC3(α)** signals in the PXRD pattern, also suggests the possibility that an extended framework with long-range order has been produced. The cross-linking theory is also supported by the complete loss of porosity, where access to the intrinsic and extrinsic pores would be blocked by the formation of new bonds between neighbouring cages, rather than intramolecular cross-linking which would still have extrinsic pores (Figure 4.38).

**CC3** has often been reported as being temperature stable up to its decomposition temperature, where an evident change is occurring in the material which results in a dramatic change in the properties of the material. A large exothermic feature can also be observed in the initial glass study with **nC<sub>5</sub>-CC**. This was initially thought to be due to the formation of an insoluble polymer, however, it may be a similar cross-linking polymerisation that is theorised in the case of **CC3** because of the similar imine functionality. Further investigation into **nC<sub>5</sub>-CC** was not performed due to the difficulty of producing a crystalline sample arising from the flexible pentyl chains on the exterior of the cage.

This project investigating the changes of **CC3** when subjected to high temperatures is still ongoing. Our computational collaborators (Dr Austin Mroz, Jelfs Group, Imperial College London) are currently investigating whether the PXRD patterns fit reported structures of COFs and polymers to try and identify the extended structure. Additionally, they are modelling the possibility of these cages undergoing cross-linking between cages as proposed earlier, in an attempt to replicate the observed long-range order, to allow simulated powder patterns to be compared with the experimental PXRD patterns.

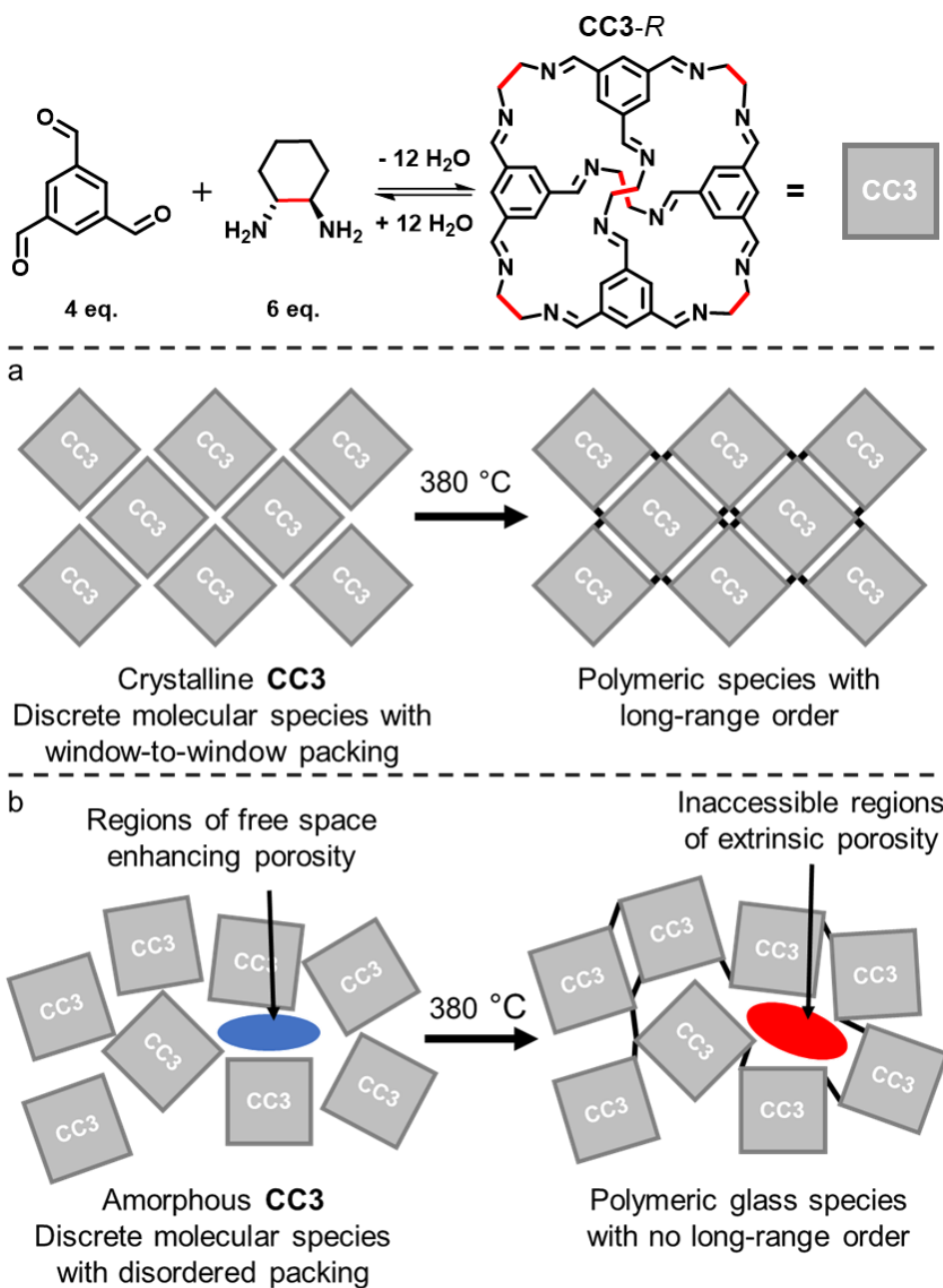


**Figure 4.38** Schematic of the synthesis of **CC3**, along with theorised cross-linking reactions when exposed to high temperatures, where a) crystalline **CC3** forming a polymeric species with long-range order; b) amorphous **CC3** forming a polymeric glass species.

## 4.5 Conclusions

Although the observed gas uptakes are low for the organic cage glasses, especially when they are compared to the plethora of MOFs, COFs, and ZIFs, which have reported BET surface areas above  $500 \text{ m}^2 \text{ g}^{-1}$ , they are comparable to previously reported ZIF glasses. The newly reported glass variety of **RCC3**,  $a_g\text{RCC3}$ , has a  $\text{CO}_2$  uptake of  $9.8 \text{ cm}^3 \text{ g}^{-1}$  at 1 bar, 273 K, which is in the same order of magnitude of  $a_g\text{ZIF-62}(\text{Co})$  with an uptake of  $17 \text{ cm}^3 \text{ g}^{-1}$  under the same conditions. Additionally, the  $\text{CH}_4$  uptake of  $5.4 \text{ cm}^3 \text{ g}^{-1}$  at 1 bar, 273 K, is almost directly comparable to  $a_g\text{ZIF-76-mblm}$  which has an uptake of  $6 \text{ cm}^3 \text{ g}^{-1}$  under the same conditions.

The increase in porosity is very encouraging for potential uses of these materials, while also creating new opportunities for future POCs. The increase in methane uptake is exciting and changing the properties of a material by changing its physical state has potential for gas separations. Though some materials have emerged as promising platforms for gas separations, such as polymers of intrinsic microporosity (PIMs), they are currently unable to be produced from the liquid state and require a solvent for processing, whereas meltable organic cages with the ability to form a glass could be cast directly from the liquid state. In principle, this could irradiate the need for solution processing and creates the possibility to form membranes or other separation media directly from the liquid state of the material, while also producing a more stable and less soluble material.

The thermal properties of imine cages have also been explored, and exothermic transitions were identified in both cases. The current combination of data indicates that intermolecular cross-linking is occurring, arising from the imine functionality leading to molecular cages becoming connected, where in the case of crystalline **CC3** it can lead to long-range order, comparable to that of a COF. This phenomenon demonstrates the importance of using a wider range of analysis to characterise the thermal properties of these materials, as opposed to just TGA, so that important features are not missed and the material's stability is more thoroughly understood.

## 4.6 Experimental Details

### 4.6.1 General Synthetic and Analytical Methods

**Materials:** Chemicals were purchased from Sigma-Aldrich, Fluorochem, TCI-UK, or Manchester Organics. Solvents were reagent or HPLC grade purchased from Fisher Scientific. All chemicals and solvents were used as received unless specified.

**Synthesis:** All reactions were stirred magnetically using Teflon-coated stirring bars. Where heating was required, the reactions were warmed using a stirrer hotplate with heating blocks with the stated temperature being measured externally to the reaction flask with an attached probe. Removal of solvents was done using a rotary evaporator.

**NMR Spectra:** <sup>1</sup>H Nuclear magnetic resonance (NMR) spectra were recorded using an internal deuterium lock for the residual protons in CDCl<sub>3</sub> ( $\delta = 7.26$  ppm) at ambient probe temperature on a Bruker Avance 400 (400 MHz) instrument. NMR data are presented as follows: chemical shift, integration, peak multiplicity (s = singlet, d = doublet, t = triplet, q = quartet, m = multiplet, br = broad, app = apparent) and coupling constants ( $J$  / Hz). Chemical shifts are expressed in ppm on a  $\delta$  scale relative to  $\delta_{\text{CDCl}_3}$  (7.26 ppm) and coupling constants,  $J$ , are given in Hz.

**HRMS:** High resolution mass spectrometry (HRMS) was carried out using an Agilent Technologies 6530B accurate-mass QTOF Dual ESI mass spectrometer (MeOH + 0.1% formic acid, 0.25 mL/min, capillary voltage 4000 V, fragmentor 225 V) in positive-ion detection mode.

**MPt:** Obtained using Stuart SMP10 digital melting point apparatus and are reported uncorrected.

**TGA:** Thermogravimetric analysis (TGA) was carried out using a PerkinElmer TGA 8000 with an automated vertical overhead thermobalance. The sample was heated in ceramic sample pans under nitrogen at a rate of 10 °C/min to 600 °C.

**DSC:** Differential scanning calorimetry (DSC) was performed on a TA instruments Discovery DSC. Heating and cooling rates were set at 10 °C/min up to the desired temperature. Samples were equilibrated at 20 °C before heating. Once the set upper temperature had been reached, samples were held at that temperature for 5 minutes before cooling. Measurements were performed under a flow of nitrogen set at 50 mL/min. Samples were prepared in air in Tzero aluminium hermetic pans and sealed with Tzero hermetic lid with pin hole (blue set).

For scale up of **RCC3-S** for gas sorption, a TA instruments Q2000 was used. Heating and cooling rates were set at 10 °C/min up to the desired temperature. Samples were equilibrated at 20 °C before heating. Once the set upper temperature had been reached, samples were held at that temperature for 5 minutes before cooling. Measurements were performed under a flow of nitrogen set at 50 mL/min. Samples were prepared in air in Tzero aluminium pans with Tzero lid (black set).

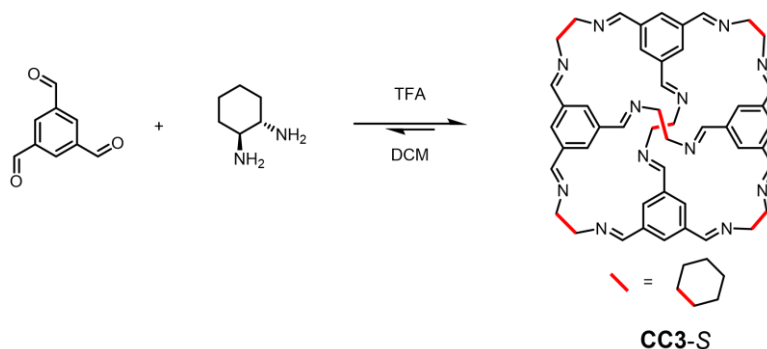
**PXRD:** Laboratory powder X-ray diffraction (PXRD) data were collected in transmission mode on samples held on a black opaque 96-shallow well microplate (ProxiPlate-96 Black) on a Panalytical X'Pert PRO MPD equipped with a high-throughput screening (HTS) XYZ stage, X-ray focusing mirror and PIXcel detector, using Ni-filtered Cu K $\alpha$  radiation. Data were measured over the range 4–40° in ~0.013° steps over 60 minutes.

**High-Throughput Gas Sorption Analysis:** High-throughput gas sorption was performed on a custom platform. A thermal camera is mounted above a sorption chamber and records the temperature change associated with gas adsorption/desorption. Samples were loaded into a 96-well ProxiPlate and degassed under vacuum whilst heating at 80 °C overnight and then left to equilibrate at 25 °C and maintained with a temperature-controlled oil heating unit. Whilst recording, the adsorbate gas is charged into the sorption chamber with approximately a 70 mbar dose. Samples were left to equilibrate for approximately 3 minutes before consecutive dosing. Data interpretation – 7 empty wells were averaged and used as a temperature change reference. This reference value was deducted from the measured temperature change in the sample wells giving temperature change in the samples.

**Gas Sorption Analysis:** Surface areas were measured by nitrogen sorption at 77 K. Samples were degassed offline at 90 °C for 15 h under dynamic vacuum (10<sup>-5</sup> bar) before analysis, followed by degassing on the analysis port under vacuum. Isotherms were measured using a Micromeritics 2020 volumetric adsorption analyzer. Gas uptake measurements for CH<sub>4</sub>, CO<sub>2</sub>, and Xe were taken at a temperature of 273 K, stabilized using a circulating water chiller/heater, and N<sub>2</sub> were taken at a temperature of 77 K.

## 4.6.2 Synthesis and Characterisation of Organic Cages

### CC3-S



**CC3-S** was prepared according to the procedure previously reported by Jones *et al.*<sup>39</sup> DCM (50 mL) was added onto 1,3,5-triformylbenzene (TFB, 2.5 g, 15.41 mmol, 4.0 eq.), being careful so as to not disturb the solid, followed by the addition of trifluoroacetic acid (50  $\mu$ L). A solution of (1*S*,2*S*)-cyclohexane-1,2-diamine (*S,S*-CHDA, 2.64 g, 23.12 mmol, 6.0 eq.) in DCM (50 mL) was then carefully layered on top, and the reaction capped and left undisturbed for 5 days. The resulting crystals were collected by filtration, washed with methanol, and dried *in vacuo* to afford **CC3-S** as a colourless solid (2.96 g, 2.65 mmol, 68%).

**<sup>1</sup>H NMR** (400 MHz, CDCl<sub>3</sub>:d<sub>4</sub>-MeOD)  $\delta_{\text{H}}$  8.02 (12H, s), 7.79 (12H, s), 3.28–3.21 (12H, m), 1.77–1.64 (12H, m), 1.56 (24H, br s), 1.41–1.27 (12H, m); **HRMS** (ES+) calc. for C<sub>72</sub>H<sub>84</sub>N<sub>12</sub> 1116.6936, found [M+2H]<sup>2+</sup> 559.3411; **CHN** calc for C<sub>72</sub>H<sub>84</sub>N<sub>12</sub>: C, 77.4; H, 7.6; N, 15.0%. Found C, 74.5; H, 7.5; N, 14.6%. Data in accordance with literature values.<sup>19</sup>

### CC3-R

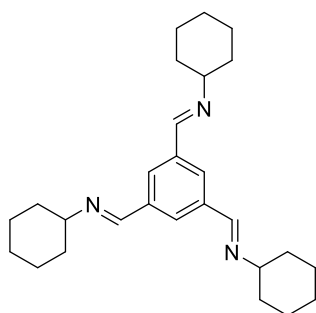
To prepare **CC3-R**, the procedure above was followed with (1*R*,2*R*)-cyclohexane-1,2-diamine, and yielded a colourless solid (3.09 g, 2.76 mmol, 71%).

**<sup>1</sup>H NMR** (500 MHz, CDCl<sub>3</sub>)  $\delta_{\text{H}}$  8.15 (12H, s), 7.89 (12H, s), 3.34–3.32 (12H, m), 1.84–1.82 (12H, m), 1.68 (24H, br s), 1.49–1.44 (12H, m).

To prepare **CC3-R** as an amorphous sample, **CC3-R** was dissolved in DCM at a concentration of ca. 10 mg/mL and 1-2 mL of sample was added to a 14 mL glass vial. The sample was then rapidly frozen by submerging the sample in liquid nitrogen.

The frozen sample was placed in an insulated drying flask and attached to an SP Scientific VirTis Sentry 2.0 freeze drier with the temperature set to  $-70\text{ }^{\circ}\text{C}$  with reduced pressure. The sample was left on high vacuum for 48 hours, yielding the recovered product as **CC3-R** amorphous. This process was scaled out and repeated several times to obtain enough sample for the scope of this project.

### 1,1',1''-(Benzene-1,3,5-triyl)tris(*N*-cyclohexylmethanimine) - TFB control molecule

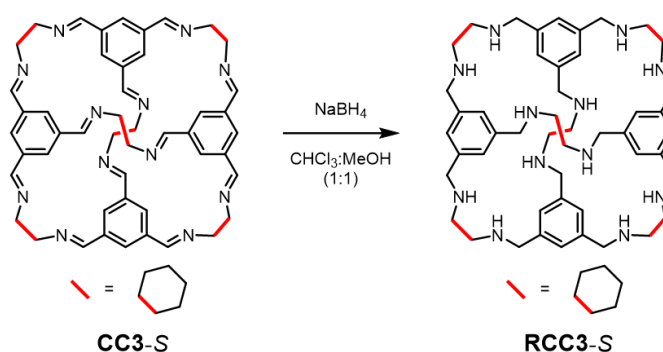


1,1',1''-(Benzene-1,3,5-triyl)tris(*N*-cyclohexylmethanimine) was prepared according to the procedure previously reported by Greenaway *et al.*<sup>13</sup> To a solution of 1,3,5-triformylbenzene (TFB, 1.0 g, 6.16 mmol, 1.0 eq.) in DCM (100 mL) was added cyclohexylamine (2.12 mL, 18.50 mmol, 3.0 eq.) and the resulting solution was stirred at rt overnight before being concentrated *in vacuo*. The

resulting solid was dried in the vacuum oven at  $90\text{ }^{\circ}\text{C}$  to afford the desired product as an off-white solid (2.20 g, 5.4 mmol, 88%).

**$^1\text{H NMR}$**  (400 MHz,  $\text{CDCl}_3$ )  $\delta_{\text{H}}$  8.37 (s, 3H), 8.10 (s, 3H), 3.20 (tt,  $J = 10.5, 4.0$  Hz, 3H), 1.90 – 1.79 (m, 6H), 1.79 – 1.65 (m, 9H), 1.58 (m, 6H), 1.45 – 1.31 (m, 6H), 1.31 – 1.22 (m, 3H).  **$^{13}\text{C NMR}$**  (101 MHz,  $\text{CDCl}_3$ )  $\delta_{\text{C}}$  158.0, 137.5, 129.3, 70.1, 34.5, 25.8, 25.0. Data in accordance with literature values.<sup>13</sup>

### RCC3-S

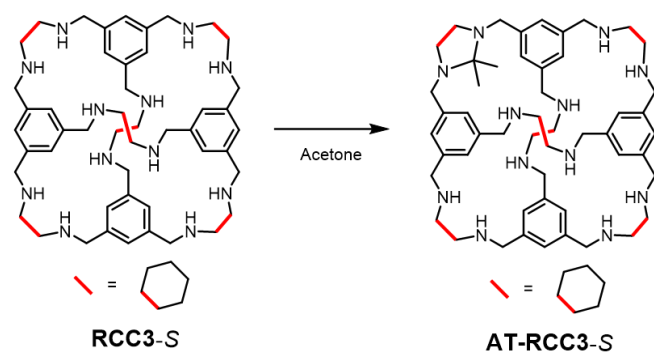


To a solution of **CC3-S** (5.0 g, 4.50 mmol, 1.0 eq.) in a mixture of  $\text{CHCl}_3$ :MeOH (1:1 v/v, 300 mL) was added  $\text{NaBH}_4$  (5.42 g, 143.18 mmol, 32.0 eq.) under  $\text{N}_2$ . The

resulting solution was stirred at room temperature overnight before the addition of water (10 mL). After stirring for a further 12 h, the solvent was removed *in vacuo*. The crude solid was partitioned between CHCl<sub>3</sub> and water, before the aqueous layer was extracted with CHCl<sub>3</sub> (3 x 50 mL). The combined organic layers were washed with water (3 x 100 mL), dried (Na<sub>2</sub>SO<sub>4</sub>), and concentrated *in vacuo* to afford a pale-yellow foam which was ground into a solid (5.2 g, 4.55 mmol, quant.).

**<sup>1</sup>H NMR** (400 MHz, CDCl<sub>3</sub>) δ<sub>H</sub> 7.13 (12H, s), 3.82 (12H, d, *J* = 14.0 Hz), 3.57 (12H, d, *J* = 14.1 Hz), 2.20 (12H, d, *J* = 8.9 Hz), 2.00 (12H, d, *J* = 12.7 Hz), 1.65 (12H, d, *J* = 8.4 Hz), 1.20 – 1.12 (12H, m), 1.02 – 0.92 (12H, m); **HRMS** (ES+) calc. for C<sub>72</sub>H<sub>108</sub>N<sub>12</sub> 1140.8814, found [M+H]<sup>+</sup> 1141.8632 and [M+2H]<sup>2+</sup> 571.4356; **CHN** calc for C<sub>72</sub>H<sub>108</sub>N<sub>12</sub>: C, 75.7; H, 9.6; N, 14.7%. Found C, 71.4; H, 8.8; N, 13.9%. Data in accordance with literature values.<sup>24</sup>

### AT-RCC3-S

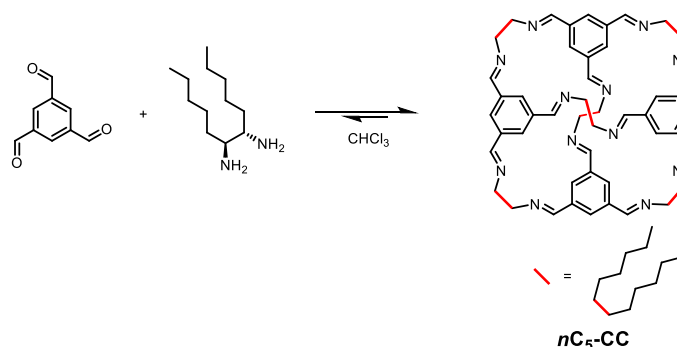


**RCC3-S** (2.65 g, 2.32 mmol, 1.0 eq.) was dissolved in acetone (160 mL) and left to stand overnight. The colourless crystals were collected by filtration and washed with acetone, before drying *in vacuo* to afford a colourless solid (1.48 g, 1.25 mmol, 53%).

**<sup>1</sup>H NMR** (400 MHz, CDCl<sub>3</sub>:d<sub>4</sub>-MeOD) δ<sub>H</sub> 7.22 – 6.71 (12H, m), 3.87 – 2.85 (24H, m), 2.34 – 0.61 (66H, m); **HRMS** (ES+) calc. for C<sub>75</sub>H<sub>112</sub>N<sub>12</sub> 1180.9127, found [M+H]<sup>+</sup> 1181.8979 and [M+2H]<sup>2+</sup> 591.4521; **CHN** calc for C<sub>75</sub>H<sub>112</sub>N<sub>12</sub>: C, 76.2; H, 9.6; N, 14.2%. Found C, 74.5; H, 9.3; N, 14.1%. Data in accordance with literature values.<sup>24</sup>



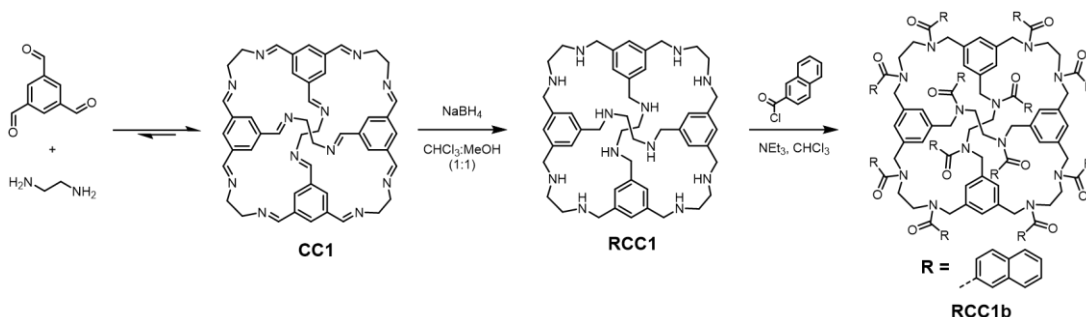
## ***n*C<sub>5</sub>-CC**



A solution of 1,3,5-triformylbenzene (TFB, 1.36 g, 8.42 mmol, 4.0 eq.) and (6*S*,7*S*)-dodecane-6,7-diamine (3.04 g, 15.17 mmol, 7.2 eq., synthesised according to previous literature methods<sup>11</sup>) in  $\text{CHCl}_3$  (43 mL) was refluxed for 6 days before being allowed to cool to room temperature. The crude reaction was concentrated *in vacuo* before acetone was added to precipitate a pale brown solid which was collected by filtration. The solid was subsequently re-dissolved in a mixture of DCM/MeOH (1:1, 100 mL), insoluble precipitates were removed by filtration, and the DCM was carefully removed *in vacuo* until an off-white solid precipitated. The resulting solid was collected by filtration and dried further *in vacuo* to afford ***n*C<sub>5</sub>-CC** as an off-white solid (55 mg, 0.034 mmol, 2%).

**<sup>1</sup>H NMR** (400 MHz,  $\text{CDCl}_3$ )  $\delta_{\text{H}}$  8.05 (12H, s), 7.87 (12H, s), 3.33 (12H, dd,  $J = 5.8, 2.6$  Hz), 1.84 – 1.70 (12H, m), 1.69 – 1.58 (12H, m), 1.33 – 1.01 (72H, m), 0.84 (36H, t,  $J = 6.9$  Hz); **HRMS** (ES+) calc. for  $\text{C}_{108}\text{H}_{168}\text{N}_{12}$  1634.3541, found  $[\text{M}+\text{H}]^{2+}$  818.1655; **CHN** calc for  $\text{C}_{108}\text{H}_{168}\text{N}_{12}$ : C, 79.4; H, 10.4; N, 10.3%. Found C, 78.3; H, 10.2; N, 10.0%. Data in accordance with literature values.<sup>11</sup>

## **RCC1b**



A solution of 1,3,5-triformylbenzene (3.0 g, 18.5 mmol, 4.0 eq.) was dissolved in DCM (920 mL) and transferred into a 5 L jacketed reactor. A solution of ethylenediamine (1.9 mL, 28.4 mmol, 6.1 eq.) dissolved in DCM (680 mL) was then added dropwise to

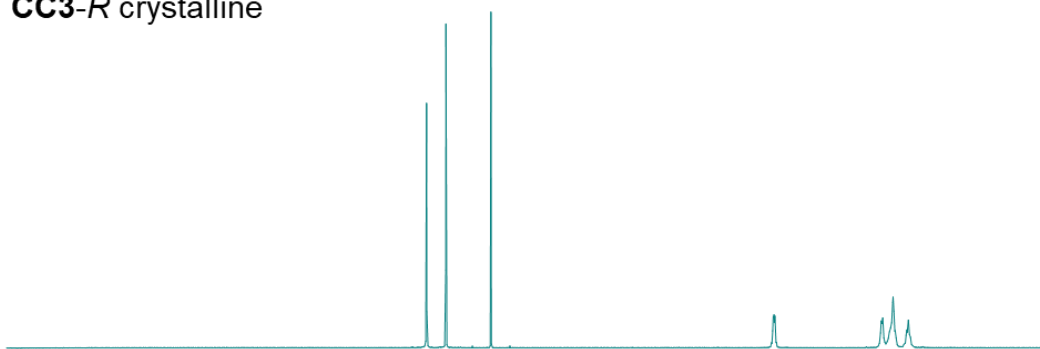
the TFB solution at 0 °C over 48 hours, with overhead mechanical stirring. The resulting reaction mixture was filtered to remove any insoluble precipitate, and carefully concentrated *in vacuo* (water bath maintained below 20 °C), but not to dryness. Hexane was added to the concentrated solution to precipitate **CC1** which was collected by filtration to afford a **CC1** as a colourless solid (3.18 g, 4.01 mmol, 87%), and used directly without further purification.

**CC1** (1.6 g, 2.01 mmol, 1.0 eq.) was dissolved in a mixture of CHCl<sub>3</sub>/MeOH (1:1, 120 mL) by stirring, before NaBH<sub>4</sub> (2.44 g, 64.56 mmol, 32.0 eq.) was added batchwise under N<sub>2</sub>. After complete addition, the reaction was stirred at room temperature for 18 h before the addition of water (5 mL). The mixture was stirred for a further 18 h before being concentrated *in vacuo*, and the resulting solid sonicated in CHCl<sub>3</sub>. The filtrate was collected and concentrated *in vacuo* to afford **RCC1** as a colourless foamed solid (1.65 g, 0.20 mmol, quant.) which was used directly to form **RCC1b**.

Triethylamine (2.56 mL, 18.36 mmol, 15.0 eq.) was added to a solution of **RCC1** (1.0 g, 1.22 mmol, 1.0 eq.) in anhydrous CHCl<sub>3</sub> (100 mL) under N<sub>2</sub> at 0 °C. After 15 min, a solution of naphthoyl chloride (2.94 g, 15.42 mmol, 12.6 eq.) in anhydrous CHCl<sub>3</sub> (50 mL) was added dropwise. The resulting mixture was allowed to warm to room temperature and stirred for 6 days before being concentrated *in vacuo*. To the crude material was added THF (100 mL) and the slurry sonicated, before the colourless triethylamine hydrochloride salts were removed by filtration. The resulting orange filtrate was concentrated *in vacuo*, before the solid was stirred in MeOH (40 mL). The filtrate was decanted off the solid, and the washing repeated a further 4 times, before the solid was collected by filtration and dried *in vacuo* to afford **RCC1b** as a pale-yellow solid (1.39 g, 0.52 mmol, 42%).

**<sup>1</sup>H NMR** (400 MHz CDCl<sub>3</sub>) δ<sub>H</sub> 8.06 – 7.15 (96H, m), 4.91 (24H, br s), 3.63 (24H, br s); **HRMS** (ES+) calc. for C<sub>180</sub>H<sub>144</sub>N<sub>12</sub>O<sub>12</sub> 2666.1060, found [M+2Na]<sup>2+</sup> 1356.0058; **CHN** calc for C<sub>180</sub>H<sub>144</sub>N<sub>12</sub>O<sub>12</sub>: C, 81.1; H, 5.4; N, 6.3%. Found C, 78.3; H, 5.4; N, 6.5%. Data in accordance with literature values.<sup>25</sup>

**CC3-R** crystalline



**CC3-R** amorphous

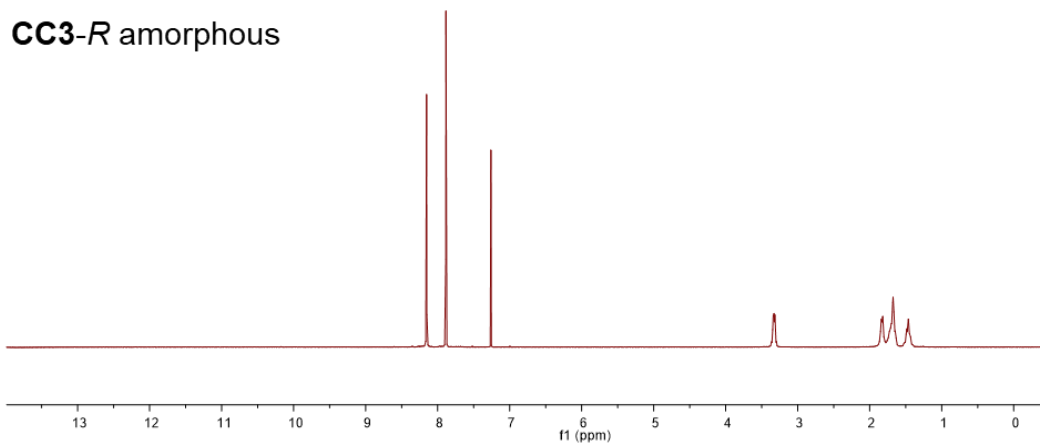


**Figure 4.39** <sup>1</sup>H NMR (CDCl<sub>3</sub>) spectra of **CC3** in their crystalline (top) and amorphous (bottom) states.

## 4.7 References

- 1 J. C. Mauro, C. S. Philip, D. J. Vaughn and M. S. Pambianchi, *Int. J. Appl. Glas. Sci.*, 2014, **5**, 2–15.
- 2 A. K. Varshneya and J. C. Mauro, *Fundamentals of inorganic glasses*, Elsevier, Third., 2019.
- 3 glass, n.1 : Oxford English Dictionary, <https://www.oed.com/view/Entry/78752?rskey=u9UPWz&result=1#eid>, (accessed 27 January 2022).
- 4 T. D. Bennett and S. Horike, *Nat. Rev. Mater.*, 2018, **3**, 431–440.
- 5 A. Gujral, L. Yu and M. D. Ediger, *Curr. Opin. Solid State Mater. Sci.*, 2018, **22**, 49–57.
- 6 M. D. Ediger, C. A. Angell and S. R. Nagel, *J. Phys. Chem.*, 1996, **100**, 13200–13212.
- 7 P. G. Debenedetti and F. H. Stillinger, *Nature*, 2001, 410, 259–267.
- 8 V. Belostotsky, 2014, arXiv:1409.2906.
- 9 N. O'Reilly, N. Giri and S. L. James, *Eur. J. Chem.*, 2007, **13**, 3020–3025.
- 10 D. Wang, Y. Xin, D. Yao, X. Li, H. Ning, H. Zhang, Y. Wang, X. Ju, Z. He, Z. Yang, W. Fan, P. Li, Y. Zheng, D. C. Wang, Y. Y. Xin, D. D. Yao, X. Q. Li, H. M. Zhang, Y. D. Wang, Z. J. He, W. D. Fan, Y. P. Zheng, H. L. Ning, X. Q. Ju, Z. Y. Yang and P. P. Li, *Adv. Funct. Mater.*, 2022, **32**, 2104162.
- 11 N. Giri, C. E. Davidson, G. Melaugh, M. G. Del Pópolo, J. T. A. Jones, T. Hasell, A. I. Cooper, P. N. Horton, M. B. Hursthouse and S. L. James, *Chem. Sci.*, 2012, **3**, 2153–2157.
- 12 T. Tozawa, J. T. A. Jones, S. I. Swamy, S. Jiang, D. J. Adams, S. Shakespeare, R. Clowes, D. Bradshaw, T. Hasell, S. Y. Chong, C. Tang, S. Thompson, J. Parker, A. Trewin, J. Bacsa, A. M. Z. Slawin, A. Steiner and A. I. Cooper, *Nat. Mater.*, 2009, **8**, 973–978.
- 13 R. L. Greenaway, D. Holden, E. G. B. Eden, A. Stephenson, C. W. Yong, M. J. Bennison, T. Hasell, M. E. Briggs, S. L. James and A. I. Cooper, *Chem. Sci.*, 2017, **8**, 2640–2651.
- 14 G. Melaugh, N. Giri, C. E. Davidson, S. L. James and M. G. Del Pópolo, *Phys.*

- Chem. Chem. Phys.*, 2014, **16**, 9422–9431.
- 15 L. Ma, C. J. E. Haynes, A. B. Grommet, A. Walczak, C. C. Parkins, C. M. Doherty, L. Longley, A. Tron, A. R. Stefankiewicz, T. D. Bennett and J. R. Nitschke, *Nat. Chem.*, 2020, **12**, 270–275.
  - 16 D. Wang, Y. Xin, X. Li, F. Wang, Y. Wang, W. Zhang, Y. Zheng, D. Yao, Z. Yang and X. Lei, *Chem. Eng. J.*, 2021, **416**, 127625.
  - 17 T. D. Bennett, Y. Yue, P. Li, A. Qiao, H. Tao, N. G. Greaves, T. Richards, G. I. Lampronti, S. A. T. Redfern, F. Blanc, O. K. Farha, J. T. Hupp, A. K. Cheetham and D. A. Keen, *J. Am. Chem. Soc.*, 2016, **138**, 3484–3492.
  - 18 T. D. Bennett, J. C. Tan, Y. Yue, E. Baxter, C. Ducati, N. J. Terrill, H. H. M. Yeung, Z. Zhou, W. Chen, S. Henke, A. K. Cheetham and G. N. Greaves, *Nat. Commun.*, 2015, **6**, 1–7.
  - 19 T. Hasell, S. Y. Chong, K. E. Jelfs, D. J. Adams and A. I. Cooper, *J. Am. Chem. Soc.*, 2012, **134**, 588–598.
  - 20 M. E. Briggs, K. E. Jelfs, S. Y. Chong, C. Lester, M. Schmidtman, D. J. Adams and A. I. Cooper, *Cryst. Growth Des.*, 2013, **13**, 4993–5000.
  - 21 K. E. Jelfs, X. Wu, M. Schmidtman, J. T. A. Jones, J. E. Warren, D. J. Adams and A. I. Cooper, *Angew. Chemie Int. Ed.*, 2011, **50**, 10653–10656.
  - 22 M. Liu, L. Chen, S. Lewis, S. Y. Chong, M. A. Little, T. Hasell, I. M. Aldous, C. M. Brown, M. W. Smith, C. A. Morrison, L. J. Hardwick and A. I. Cooper, *Nat. Commun.*, 2016, **7**, 1–9.
  - 23 M. Mastalerz, *Chem. Commun.*, 2008, 4756–4758.
  - 24 M. Liu, M. A. Little, K. E. Jelfs, J. T. A. Jones, M. Schmidtman, S. Y. Chong, T. Hasell and A. I. Cooper, *J. Am. Chem. Soc.*, 2014, **136**, 7583–7586.
  - 25 J. L. Culshaw, G. Cheng, M. Schmidtman, T. Hasell, M. Liu, D. J. Adams and A. I. Cooper, *J. Am. Chem. Soc.*, 2013, **135**, 10007–10010.
  - 26 H. Koizumi, K. Takeuchi, K. Matsumoto, N. Fukaya, K. Sato, M. Uchida, S. Matsumoto, S. Hamura and J. C. Choi, *Commun. Chem.*, 2021, **4**, 1–7.
  - 27 Chemspeed Technologies AG - Official Website -, <https://www.chemspeed.com/>, (accessed 3 February 2022).
  - 28 Life Science Tools | Unchained Labs, <https://www.unchainedlabs.com/>,

(accessed 3 February 2022).

- 29 B. Burger, P. M. Maffettone, V. V. Gusev, C. M. Aitchison, Y. Bai, X. Wang, X. Li, B. M. Alston, B. Li, R. Clowes, N. Rankin, B. Harris, R. S. Sprick and A. I. Cooper, *Nature*, 2020, **583**, 237–241.
- 30 L. C. Gerber, A. Calasanz-Kaiser, L. Hyman, K. Voitiuk, U. Patil and I. H. Riedel-Kruse, *PLOS Biol.*, 2017, **15**, e2001413.
- 31 P. Wollmann, M. Leistner, W. Grählert, O. Throl, F. Dreisbach and S. Kaskel, *Microporous Mesoporous Mater.*, 2012, **149**, 86–94.
- 32 P. Wollmann, M. Leistner, U. Stoeck, R. Grünker, K. Gedrich, N. Klein, O. Throl, W. Grählert, I. Senkovska, F. Dreisbach and S. Kaskel, *Chem. Commun.*, 2011, **47**, 5151–5153.
- 33 J. A. Mason, T. M. McDonald, T. H. Bae, J. E. Bachman, K. Sumida, J. J. Dutton, S. S. Kaye and J. R. Long, *J. Am. Chem. Soc.*, 2015, **137**, 4787–4803.
- 34 Y. Bai, L. Wilbraham, B. J. Slater, M. A. Zwijnenburg, R. S. Sprick, and A. I. Cooper, *J. Am. Chem. Soc.* 2019, 141, **22**, 9063–9071
- 35 H. Yin, Y. Z. Chua, B. Yang, C. Schick, W. J. Harrison, P. M. Budd, M. Böhning and A. Schönhals, *J. Phys. Chem. Lett.*, 2018, **9**, 2003–2008.
- 36 L. Frentzel-Beyme, M. Kloß, R. Pallach, S. Salamon, H. Moldenhauer, J. Landers, H. Wende, J. Debus and S. Henke, *J. Mater. Chem. A*, 2019, **7**, 985–990.
- 37 C. Zhou, L. Longley, A. Krajnc, G. J. Smales, A. Qiao, I. Erucar, C. M. Doherty, A. W. Thornton, A. J. Hill, C. W. Ashling, O. T. Qazvini, S. J. Lee, P. A. Chater, N. J. Terrill, A. J. Smith, Y. Yue, G. Mali, D. A. Keen, S. G. Telfer and T. D. Bennett, *Nat. Commun.*, 2018, **9**, 1–9.
- 38 S. Jiang, J. T. A. Jones, T. Hasell, C. E. Blythe, D. J. Adams, A. Trewin and A. I. Cooper, *Nat. Commun.*, 2011, **2**, 1–7.
- 39 J. T. A. Jones, T. Hasell, X. Wu, J. Bacsá, K. E. Jelfs, M. Schmidtman, S. Y. Chong, D. J. Adams, A. Trewin, F. Schiffman, F. Cora, B. Slater, A. Steiner, G. M. Day and A. I. Cooper, *Nature*, 2011, **474**, 367–371.

## **Chapter 5**

### **Conclusions and Future Outlook**

## 5.1 Conclusions

Since the discovery of POCs in the latter part of the 2000's,<sup>1,2</sup> researchers have developed a plethora of new examples with a wide variety of shapes and sizes. Due to the inherent properties that some POCs possess, such as intrinsic porosity and window size, they have been used in a vast array of applications which includes molecular sensors,<sup>3</sup> molecular separations,<sup>4</sup> and gas storage.<sup>5</sup> More recently, POCs have proven to be invaluable in the discovery of porous liquids,<sup>6</sup> and continue to prove their effectiveness in these types of materials.<sup>7,8</sup> However, the rate of discovery remains low when compared to materials such as metal-organic frameworks, with newer cages often only containing small changes to known systems.<sup>9</sup> With new computational methods being developed, a wider range of materials can be screened without the need for laboratory based experiments, removing a large amount of the trial-and-error that the traditional approaches take.<sup>10,11</sup>

In chapter 2, the development of a new variation of POC has been investigated, with the aid of computational modelling. While the number of POCs continue to increase year after year, many are based on incremental changes to static components, resulting in small variations in size and topology. In this chapter, the exploration into cages that can undergo a structural change was investigated, more specifically, those that undergo a structural change in response to light through the incorporation of photochromic molecules. To achieve this, computational models were produced using azobenzene-derived precursors, which were then subjected to various screening processes, followed by modelling of isomerised variants of those cages. Upon identifying successful candidates, azobenzene-derived aldehyde precursors were synthesised and subjected to various screens with different partner amines. Two cages were successfully isolated, a Tet<sup>3</sup>Di<sup>6</sup> and Tri<sup>2</sup>Di<sup>3</sup> species, and fully characterised with 1D and 2D NMR experiments. The photophysical properties of these cages were investigated, including the quantum yield, photostationary state, and thermal half-lives. These cages were shown to be capable of photoisomerisation, where the cages were found to have a *trans* to *cis* isomerisation which ranged from 62% up to 78% determined through UV-vis experiments, and thermal half-lives ranging from 40 hours up to 367 hours.

During the development of photoresponsive cages, it was envisioned that they could be used in combination with a size-excluded solvent to produce a photoresponsive porous liquid. In chapter 3, a proof-of-concept study was therefore carried out to investigate the possibility of a photoresponsive porous liquid. The newly developed photoresponsive organic cages were not fully developed to a point where they could



be utilised in either a type II or type III porous liquid. As an alternative system, a known photoresponsive MOF was used in combination with an ionic liquid to produce a new porous liquid. During this study, 3D printing was employed to produce a reactor capable of irradiating porous liquid samples during gas sorption measurements. This new porous liquid was found to have a vastly increased CO<sub>2</sub> capacity over that of the neat ionic liquid, with increases of up to 180%. Additionally, this porous liquid exhibits a very high CO<sub>2</sub>/CH<sub>4</sub> selectivity, where the porous liquid is able to adsorb 13-times more CO<sub>2</sub> than CH<sub>4</sub>, making it one of, if not, the most selective porous liquid to date. Irradiation of the porous liquid sample with 365 nm light also found a modest decrease in CO<sub>2</sub> capacity, compared to those under ambient conditions, which shows the successful incorporation of a photoresponsive MOF creating the first reported photoresponsive porous liquid.

Finally, in chapter 4, an exploration into the incorporation of porous organic cages into type I porous liquids was explored. While the melting of organic cages is typically avoided, due to the stability issues that imines have, in some of the initial investigations, several cages were explored to determine whether melting was possible. During this process several cages were found to be able to melt, where three of these cages were found to have a glass transition. These materials were then explored as melt-quenched organic cage glasses to determine whether there were varying properties compared to the as-synthesised cages. One of glasses was found to have improved gas uptake with N<sub>2</sub>, CO<sub>2</sub>, and CH<sub>4</sub> compared to the amorphous pre-processed cage. While the gas uptakes for this organic cage glass remains low compared to MOFs, COFs and ZIFs, it is almost directly comparable to some recently reported MOF glasses.<sup>12,13</sup> This has the potential to introduce porosity into a more stable and less soluble glass, with the potential of removing solvent processing to form other materials such as membranes or separation media.

## 5.2 Future Work

The study of new photoresponsive organic cages in chapter 2 was very successful. However, further experiments that would have really investigated the potential of these materials would have been gas sorption. Within that study, computational models were generated with each cage undergoing a single isomerisation, from pure *trans* to pure *cis*. In these experiments, the relative energies were determined and found that they increase with each consecutive isomerisation. With each of these isomers, there is a change in cavity diameter which occurs because of the cage

changing shape. The larger cage in this study Tet<sup>3</sup>Di<sup>6</sup> found an overall increase in cavity diameter from 4.4 Å in the lowest energy conformation, up to 6.4 Å when the cage is fully isomerised. Gas sorption studies on this material could yield some interesting possibilities, where an ambient sample should theoretically take up a lower quantity of gas, and then an irradiated sample could have a higher gas capacity based on the cavity diameter. Furthermore, with each isomerisation of the cage, the window size also changes. This could open the possibility of changing selectivity, or a selective capture and release mechanism, for example, if a larger molecule is able to fit within the cage under irradiation where the cage windows slightly increase in size, exposure with blue light could potentially reduce the window size causing the guest to become trapped. The smaller cage in this study Tri<sup>2</sup>Di<sup>3</sup> shows the opposite correlation with regards to cavity size, where a relatively small cavity diameter of 2.2 Å undergoes a complete pore collapse with no cavity diameter. This could also have some interesting porosity measurements, with an on or off gas sorption based on the conditions. One of the issues that face these studies is how much irradiation these materials can withstand, so as a proof-of-concept, gas sorption measurements could be carried out with gases that typically use low temperatures, such as N<sub>2</sub> or H<sub>2</sub>. These cages were shown to lose all signals in the <sup>1</sup>H NMR spectra after continuous exposure, whereas the photoresponsive MOF in chapter 3 was shown to maintain the same PXRD pattern to that of the parent material after continuous light exposure. This would make it very difficult to produce any type of gas isotherm with continuous exposure. However, utilising low temperatures would allow the sample to be irradiated for a period before material decomposition, and then lowering the temperature of the sample resulting in a significantly longer thermal half-life (especially at 77 K), though the thermal half-lives of the solid materials is unknown. This would mean the sample would not need continuous exposure over the course of the experiment, though it limits the type of gases that could be used. Alternatively, slightly lower temperature isotherms could take place, for example at 0 °C, which would open the opportunity for more probe gases to be tested, with a slightly higher thermal half-life, though some sample reversion would be expected over the course of the experiment.

Another possibility would be to synthesise organic cages that include photochromic molecules that have a higher energy barrier, so that reversion is only possible by photons rather than ambient temperature, such as diarylethenes. In theory, this could create a cage that would only isomerise based on the wavelength it was exposed to without converting back to the most stable conformation. This could produce a cage that has two distinct isomers, with the possibility of having different pore sizes, leading

to a cage with the ability to turn on and off gas uptake through irradiation at different wavelengths. Having a cage with two thermally stable isomers would also remove the need for continuous exposure to light, reducing the possibility of decomposition.

Given the successful implementation of organic cages into type II and type III porous liquids, it would also be an interesting possibility to create another photoresponsive porous liquid. However, there would be the added difficulty of choosing a solvent that is both size-excluded and one that maintains a moderate thermal half-life for the cage materials. This could be lessened through short bursts of irradiation during the gas sorption measurements, which could serve two purposes, the first being the maintenance of the photoisomerised state, allowing measurements to be taken of the isomerised photoresponsive porous liquid. Secondly, it would reduce the possibility of material decomposition which occurs from longer periods of irradiation. If decomposition was to occur, then there would be the possibility of investigating the more stable amine variants, by reducing the imine bonds, though this may lead to a significant reduction of gas uptake, as seen in other POCs.

Finally, the production of melt-quenched organic cage glasses from the liquid state was successful, though all the examples explored within chapter 4 that produced glass transitions were reduced variants. Both imine-based organic cage examples that were studied underwent an unexpected exothermic transition, which is thought to be some form of thermally-induced cross-linking. Given **CC3** produces a sample where reflections can be observed in the powder pattern after this exothermic transition, it provides some guidance on how to proceed. There are ongoing experiments being performed by our computational collaborators to see whether molecular modelling can provide an answer to the structure of the material that is produced. This collaboration is currently producing models with various cross-linking mechanisms to the neighbouring molecules to produce powder patterns to see whether they replicate those observed experimentally. In addition to this, variable temperature powder X-ray diffraction experiments are in the process of being completed to try and observe whether there are any intermediate states during this exothermic process, which may provide some answers on the process that is happening.

### 5.3 References

- 1 P. Skowronek and J. Gawronski, *Org. Lett.*, 2008, **10**, 4755–4758.
- 2 T. Tozawa, J. T. A. Jones, S. I. Swamy, S. Jiang, D. J. Adams, S. Shakespeare, R. Clowes, D. Bradshaw, T. Hasell, S. Y. Chong, C. Tang, S. Thompson, J. Parker, A. Trewin, J. Bacsá, A. M. Z. Slawin, A. Steiner and A. I. Cooper, *Nat. Mater.*, 2009, **8**, 973–978.
- 3 L. Tapia, I. Alfonso and J. Solà, *Org. Biomol. Chem.*, 2021, **19**, 9527–9540.
- 4 J. H. Zhang, S. M. Xie, M. Zi and L. M. Yuan, *J. Sep. Sci.*, 2020, **43**, 134–149.
- 5 G. Zhang, O. Presly, F. White, I. M. Opperl and M. Mastalerz, *Angew. Chemie Int. Ed.*, 2014, **53**, 1516–1520.
- 6 P. F. Fulvio and S. Dai, *Chem*, 2020, **6**, 3263–3287.
- 7 R. L. Greenaway, D. Holden, E. G. B. Eden, A. Stephenson, C. W. Yong, M. J. Bennison, T. Hasell, M. E. Briggs, S. L. James and A. I. Cooper, *Chem. Sci.*, 2017, **8**, 2640–2651.
- 8 A. Kai, B. D. Egleston, A. Tarzia, R. Clowes, M. E. Briggs, K. E. Jelfs, A. I. Cooper, R. L. Greenaway, A. Kai, B. D. Egleston, R. Clowes, M. E. Briggs, A. I. Cooper, R. L. Greenaway, A. Tarzia and K. E. Jelfs, *Adv. Funct. Mater.*, 2021, **31**, 2106116.
- 9 R. L. Greenaway, V. Santolini, M. J. Bennison, B. M. Alston, C. J. Pugh, M. A. Little, M. Miklitz, E. G. B. Eden-Rump, R. Clowes, A. Shakil, H. J. Cuthbertson, H. Armstrong, M. E. Briggs, K. E. Jelfs and A. I. Cooper, *Nat. Commun.*, 2018, **9**, 1–11.
- 10 E. Berardo, L. Turcani, M. Miklitz and K. E. Jelfs, *Chem. Sci.*, 2018, **9**, 8513–8527.
- 11 V. Santolini, M. Miklitz, E. Berardo and K. E. Jelfs, *Nanoscale*, 2017, **9**, 5280–5298.
- 12 L. Frenzel-Beyme, M. Kloß, R. Pallach, S. Salamon, H. Moldenhauer, J. Landers, H. Wende, J. Debus and S. Henke, *J. Mater. Chem. A*, 2019, **7**, 985–990.
- 13 C. Zhou, L. Longley, A. Krajnc, G. J. Smales, A. Qiao, I. Erucar, C. M. Doherty, A. W. Thornton, A. J. Hill, C. W. Ashling, O. T. Qazvini, S. J. Lee, P. A. Chater,

N. J. Terrill, A. J. Smith, Y. Yue, G. Mali, D. A. Keen, S. G. Telfer and T. D. Bennett, *Nat. Commun.*, 2018, **9**, 1–9.